ADVANCED STEEL CONSTRUCTION

An International Journal

Volume 21 Number 1

February 2025

CONTENTS

Technical Papers

Website: *http://www.hkisc.org*
ISSN 1816-112X
Science Citation Index Expanded, Materials Science Citation Index and ISI Alerting
Cover: Jewel Changi Airport, Singapore. Photo@ Liu Yao-Peng
e-copy of IJASC is free to download at "www.ascjournal.com" in internet and mobile apps.

ADVANCED STEEL CONSTRUCTION

VOL.21, NO.1 (2025)

ADVANCED STEEL CONSTRUCTION

an International Journal

ISSN 1816-112X

Volume 21 Number 1 *February 2025*

ISSN 1816-112X

Science Citation Index Expanded, Materials Science Citation Index and ISI Alerting

Advanced Steel Construction
an international journal

Cover: Jewel Changi Airport, Singapore. Photo@ Liu Yao-Peng
e-copy of IJASC is free to download at "www.ascjournal.com" in internet and mobile apps.

General Information
Advanced Steel Construction, an international journal

Aims and scope

The International Journal of Advanced Steel Construction provides a platform for the publication and rapid dissemination of original and up-to-date research and technological developments in steel construction, design and analysis. Scope of research papers published in this journal includes but is not limited to theoretical and experimental research on elements, assemblages, systems, material, design philosophy and codification, standards, fabrication, projects of innovative nature and computer techniques. The journal is specifically tailored to channel the exchange of technological know-how between researchers and practitioners. Contributions from all aspects related to the recent developments of advanced steel construction are welcome.

Subscription inquiries and change of address. Address all subscription inquiries and correspondence to Member Records, IJASC. Notify an address change as soon as possible. All communications should include both old and new addresses with zip codes and be accompanied by a mailing label from a recent issue. Allow six weeks for all changes to become effective.

The Hong Kong Institute of Steel Construction
HKISC
c/o Prof. SL Chan,
Unit 209B, Photonics Centre, No. 2 Science Park East Avenue,
Hong Kong Science Park, Shatin, N.T., Hong Kong, China.
Tel: 852- 3595 6150 Fax: 852- 3619 7238
Email: ceslchan@connect.polyu.hk Website: *http://www.hkisc.org/*
ISSN 1816-112X
Science Citation Index Expanded, Materials Science Citation Index and ISI Alerting

ISSN 1816-112X

Science Citation Index Expanded, Materials Science Citation Index and ISI Alerting

Advanced Steel Construction
an international journal

VOLUME 21 NUMBER 1 **February 2025**

Technical Papers

Advanced Steel Construction – Vol. 21 No. 1 (2025) 1–20
DOI:10.18057/IJASC.2025.21.1.1

WIND RESISTANCE PERFORMANCE AND REINFORCEMENT MEASURES OF STANDING SEAM METAL ROOFS BASED ON WIND TUNNEL TESTS

Wen-Bing Han [1], Jing-Zhen Chen [2,*], Bo Yang [1], Hua-Chang Liu [2], Kai-Fang Lv [2], Chu-Huang Huang [2] and Mohamed Elchalakani [3]

[1] *School of Civil Engineering, Chongqing University, Shapingba District, Chongqing 400045, China*
[2] *China Construction Fourth Engineering Division Corp., LTD, Xiamen 361000, China*
[3] *Department of Civil, Environmental and Mining Engineering, University of Western Australia, Crawley, WA 6009, Australia*
** (Corresponding author: E-mail: 1578339351@qq.com)*

ABSTRACT

As an important building envelope structure, metal roofs have been widely used in various large-scale buildings because of their unique advantages such as beautiful shape, lightweight nature, flexibility, and exceptional strength. However, there are still some gaps in the existing research on the wind resistance performance of metal roof systems, which poses a serious threat to life and property. To address this gap, this paper conducted wind tunnel tests of long-span standing seam metal roofs. The basic wind pressure of 0.95 kN/m^2, which is once every 100 years. The wind-induced response of the metal roofs under varying wind speeds and wind directions was simulated by the wind tunnel tests, which involved the measurement and analysis of the load distribution characteristics, equivalent wind loads, and wind vibration coefficients. The experimental results were used to determine the design wind load for the metal roofing structure and to conduct the wind vibration calculations. The results indicated that in regions experiencing high negative wind pressure, the results obtained from extreme value analysis marginally exceeded those obtained through the peak factor method. The stress characteristics and instability modes of metal roofs in strong wind environments were summarized, and the factors affecting the wind resistance performance of metal roofs were analyzed. The reinforcement measures for wind resistance design of metal roofs were proposed, it serves as a theoretical guide and scientific foundation for the future development of similar metal roof structures.

ARTICLE HISTORY

Received: 12 June 2024
Revised: 17 December 2024
Accepted: 20 December 2024

KEYWORDS

Large span metal roofs;
Wind tunnel tests;
Wind resistance performance;
Finite element analysis;
Reinforcement measures

1. Introduction

The metal roof serves as a crucial exterior maintenance structure boasting notable advantages of beautiful appearance, lightweight construction, corrosive resistance, and facilitation of installation [1-3]. Its significance extends beyond mere aesthetics, encompassing essential functions like waterproofing, thermal insulation, and decorative purposes within building structures [4,5]. Generally, metal roofing is exposed to a variety of complex loads, including alternating wind loads, temperature variations, and precipitation [6-9]. It is not uncommon for metal roofing to be damaged by wind loads, safety concerns such as metal roofing flying off and collapsing have also attracted considerable attention [10-13]. Therefore, it is imperative to investigate the dynamic response of metal roofs to wind-induced vibrations, and it will also promote the application and development of metal roofs in regions susceptible to typhoons [14,15].

With the increase in extreme weather events, the wind resistance of metal roof structures has gradually attracted attention. Numerous scholars have studied the mechanical properties of metal roofing under wind loads by experiments and numerical analysis [16,17]. Baskaran et al. [18] conducted wind tunnel tests to examine three prevalent standing seam metal roofing structures and proposed a simplified design method for assessing the wind-bearing capacity of metal roofing. Schroter et al. [19] predominantly explored the key factors affecting the wind-bearing capacity of roof panels through static testing. Xu et al. [20] utilized a combination of experimental trials and numerical simulations. The results indicated that the key parameters influencing the wind-bearing capacity included the bite-bearing capacity of lock joints and fixed supports within roof panels. Farquhar et al. [21] conducted small-scale uniform uplift and wind tunnel tests on a standing seam roof model. A pressure coefficient capable of correlating uniform uplift failure pressures with the actual wind pressures was proposed. Compared with the traditional sliding supports, the wind load capacity and failure mode of the metal roof system using the novel sliding support with high tensile and wind resistance are improved [22]. Sinno et al. [23] also studied the wind resistance of standing seam roofing panels through experiments, it is indicated that the pivotal determinants affecting wind resistance capacity are the connections between individual roof panels and the supports linking these panels. Li et al. [24] investigated the influence of various parameters (e.g., purlin spacing, roof slab thickness, and slab width) on the wind uplift resistance of standing seam roofing slabs through theoretical analysis. Based on an effective method to evaluate the wind resistance behavior of standing seam metal systems, the wind-induced structural response of the system was investigated experimentally and numerically, including the displacement of metal plates, stress, and the reaction force of clips [25,26].

Numerous investigations have been conducted to evaluate the wind-bearing capacity of metal roofing under dynamic loading conditions. Simiu et al. [27], Petrov et al. [28], and Suresh et al. [29] specifically investigated the impact of various wind loads on the fatigue performance of metal roofing, and a methodology for calculating wind-induced fatigue damage was proposed. Additionally, Myuran et al. [30,31] focused on the mechanical properties of metal roof panels subjected to cyclic wind loads through experimental tests and proposed a new anti-fatigue design method for metal roof panels. Given the wind vibration vulnerability of standing seam metal roof systems, the failure process of roof systems under wind load was analyzed considering fatigue damage, and the vulnerability of different types of roof systems was compared [32,33]. Habte and Homles et al. [34,35] conducted dynamic loading tests on full-size standing seam metal roof panels and discussed the effects of roof panel type and specimen design on wind-bearing capacity. Luo et al. [36] explored the dynamic response of large-span metal roofs under repeated wind loads through dynamic loading tests, indicating that the new type of metal roofing structure exhibits favorable seismic performance. The latest application of Computational Fluid Dynamics technology (CFD) in wind field analysis and its comparison with traditional wind tunnel experiments are discussed, and it is shown that the use of CFD provides good calculation accuracy [37]. The application and future development of CFD in wind resistance design of metal roofing in high-rise buildings are summarized [38,39]. Aiming at the design of metal roofing, Baskaran et al. [40,41] carried out a series of fatigue tests. The wind resistance performance of various roof structures under repeated wind loads and the bolted joint performance is evaluated. A new method for calculating the wind-bearing capacity of lightweight metal roofing is proposed.

Currently, significant advancements have been made in the wind resistance of metal roofs, encompassing areas such as wind pressure distribution, roof shape optimization, dynamic response, aeroelastic performance, support connections, and purlin fastening systems, as well as the durability and corrosion resistance of roofing materials [1,16,26]. Moreover, wind tunnel testing remains fundamental for understanding wind loads and optimizing roof design, with the development of more accurate scale models to improve the simulation of complex roof geometries [2,9,15,32]. Combining the wind tunnel test results with the structural response models, the wind resistance of the roofs under wind loads is comprehensively analyzed. Computational Fluid Dynamics (CFD) has become a critical method for studying wind loads, with growing emphasis on the interaction between wind and structures, considering factors such as vortex shedding, flow separation, and the resulting pressure variations [37,39]. This is especially crucial for understanding the aeroelastic behavior of metal roofs and for designing systems that reduce wind-induced vibrations or instabilities. The combined advancements in wind tunnel testing and CFD have exhibited a profound impact on the design and optimization of metal roofs. These

developments contribute to the updating of international design standards and codes, ensuring that they more accurately reflect wind load predictions based on advanced testing and simulation methods [10,25,37].

Compared with the traditional roof system, the standing seam metal roof system can effectively release temperature-induced stress, in which the rolling edge of the adjacent roof plate is occluding with the support riser through the electric locking machine, and then the support is bolted to the purlin [17,21,42]. Extensive investigations have been conducted on the wind-resistant design of metal roofing, including both experimental tests and theoretical analysis. Various wind exposure test methods (e.g., ASTM E1592 [43], ANSI/ FM 4474 [44], and UL 1897 [45]) for standing seam roofing systems were proposed. However, the existing design specifications lack comprehensive determinations for the design wind loads of standing seam roofing, primarily due to the complexity and diversity of metal roofing loads. Based on the metal roof project of the Xiamen International Expo Center (XIEC), this paper focuses on the wind resistance performance of large-span metal roofs under wind loads by the wind tunnel tests, which advances the application and development of metal roofing within large-span building structures.

2. Project overview

The project is situated southwest of the intersection of Binhai East Avenue and Xiang 'an Tunnel, Xiamen City, which is the coastal core area of Xiamen East Sports Exhibition New City. The conference center project covers a total area of 107439318 m^2, a total construction area of 231100 m^2, an above-ground construction area of 169000 m^2, a building height of 68.55 m, featuring its most expansive span at 81 m, belonging to a class of high-rise buildings. Additionally, the design mandates consideration of a basic wind pressure occurrence once in a century, adding complexity to the overall roof design. The installation process poses challenges in ensuring adherence to the design scheme for the overall linear shape, while simultaneously meeting the stringent quality requirements for wind resistance and leak prevention. The overall layout of the project is illustrated in **Fig. 1**, including the conference center, exhibition hall (3W), land-side exhibition hall (2.4W), sea-side exhibition hall (2.4W), login hall, corridor, belvedere and warehouse.

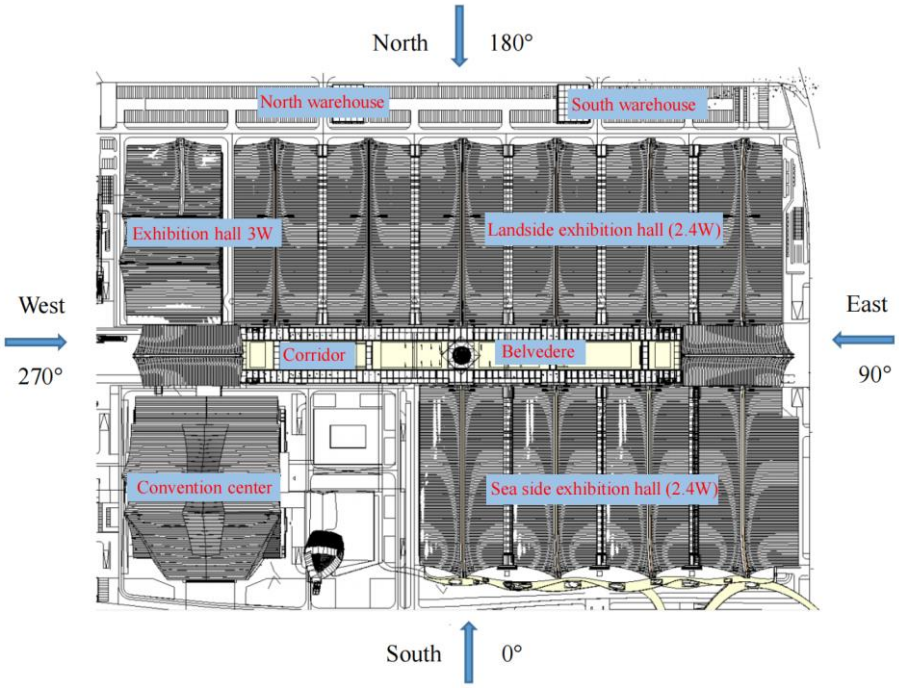

Fig. 1 Overall layout of Xiamen International Expo Center

The model of the conference center is depicted in **Fig. 2**. The primary framework comprises steel frames (reinforced concrete columns) and steel trusses. The warehouse adopts a portal frame and steel truss structure, while the flooring incorporates a combination of composite steel plates and concrete slabs. The roofing systems include a double metal roofing system, a single daylighting roofing system, a drainage gutter system, an eaves gutter system, and connections featuring aluminum plates for eaves and gutters. The roofing system structure in this project is up to 9 layers, the overall height of the structural layer ranging from approximately 850 mm to 1000 mm. The roofing shape ascends 31 meters above the highest structural layer, and the cornice roof extends as far as 6 m beyond the lower facade. Notably, the maximum curvature of the roofing surface exceeds 1/22. The formation of the curved surface primarily relies on the roofing steel structure line, roofing purlin line, ridge eaves line, and the surface layer comprised of metal plates, aluminum plates, and honeycomb plates.

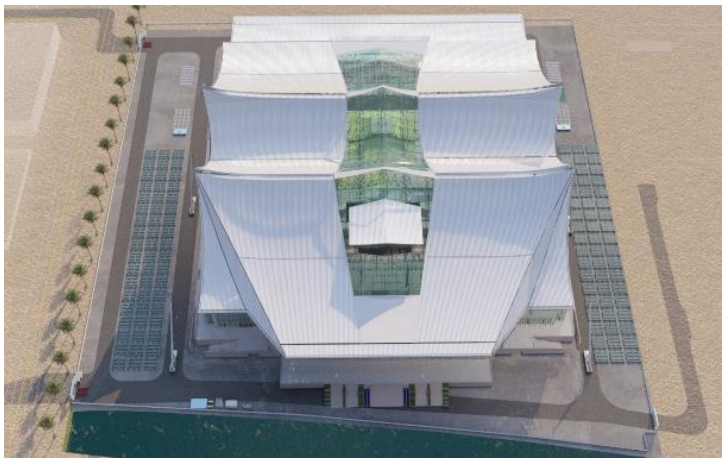

Fig. 2 Global view of the conference center

3. Wind tunnel test

3.1. Model and measuring point arrangement

Due to the intricate design of the conference center, the existing specifications lack the corresponding body shape coefficient and wind vibration coefficient for this distinctive building structure. It is necessary to conduct wind tunnel tests and wind vibration calculations for the metal roofing of the conference center to ensure the safety, cost-effectiveness, and soundness of the structural design, as well as to fulfill the design criteria for wind-resistant uplift. To simulate the wind loads of long-span metal roofs under different wind speeds, a wind tunnel test platform was constructed, which can simulate the airflow conditions and the stress distributions experienced by the metal roofing under different wind speeds.

The wind tunnel test model of metal roofing is a rigid model, which is made of glass fiber reinforced plastic, Plexiglas, and ABS plastic according to the geometric similarity, and certain components were produced using 3D printing technology. The scale of the model is 1:220, as shown in **Fig. 3**. The test is carried out in the CGB-2 wind tunnel laboratory (test section 8 m×5 m). The maximum plugging area of the model is about 1.25 m^2, with a corresponding maximum plugging ratio of 3.2%, which met the requirement not greater than 5% in JGJ/T 338-2014 (Standard for wind tunnel test of buildings and structures) [46]. The dimensionless parameters such as the wind pressure coefficient obtained from the wind tunnel test can be directly applied to the design of building structures.

(a) Front view (b) Back view

Fig. 3 Wind tunnel test model

Table 1
Summary of measuring points

Number	Object	Total number of points	Description
1	Conference center	1034	
2	Exhibition hall of 3W	544	
3	Landside exhibition hall of 2.4W	466	3 exhibition halls: L1, L2, L3
4	Seaside exhibition hall of 2.4W	478	3 exhibition halls: H1, H2, H3
5	Entrance hall	402	
6	Belvedere	16	
7	Corridor	84	
8	North warehouse	98	2 warehouses: B1, B2
Total		5108	

Table 1 summarizes the all measuring points layout. This paper focuses on elucidating the arrangement of measuring points within the conference center. A total of 1034 measuring points in the conference center including the upper surface of the upper metal roofing (A:56, B:43, C43, D:51, E:51, F:49, G:49, H:38, J:38, K:36), upper surface of lower metal roofing (M:18, N:16, P:56), lower surface of upper metal roofing (AX: 54, KX: 16), and lower surface of lower metal roofing (AX:54, KX:16, PX:56).

3.2. Experimental program and test method

3.2.1. Wind tunnel tests and equipment

The experiment was conducted within the confines of the CGB-2 boundary layer wind tunnel laboratory. The enclosed test section spans a length of 34 meters, with a cross-section measuring 8 m in width and 5 m in height. The maximum wind speeds up to 35 m/s, and the reference wind speed of the testing flow field is measured and monitored by micro pressure gauges. A Dandy 4-channel hot wire anemometer system is used to simulate the atmospheric boundary layer in the wind field. The wind pressure measurement process involved an electronic scanning valve, a data acquisition board, and a proprietary signal acquisition and data processing software, constituting a comprehensive wind pressure measurement and recording system.

3.2.2. Wind field simulation

Based on the surrounding topography and geomorphic characteristics, the geomorphic roughness index (α) is determined as 0.12. The basic wind pressure once in 100 years is 0.95 kN/m^2, which is equivalent to the wind speed (U_0) of 38.99 m/s at a height of 10 m above the ground. Wind speed at different heights above the ground is described using Eq. (1).

$$U_z = U_0 \left(Z/Z_0\right)^{\alpha} \tag{1}$$

Where U_0 is the average wind speed at the height of 10 m above the ground, the 50-year recurrence period, U_z is the average wind speed at the height of Z from the ground.

During the wind tunnel test, the wind speed profile is simulated and verified by the multifunctional simulation device at the wind entrance and the rough element situated at the bottom wall of the wind tunnel. The measured wind speed curves at different heights away from the bottom wall of the wind tunnel are shown in **Fig. 4 (a)**, and are compared with the theoretical curves calculated by Eq. (1). It is found that the relative error is minimal, which indicates that the wind tunnel simulation is in good agreement with test results.

In the atmospheric boundary, the airflow comprises numerous eddies of varying intensity, and turbulence is a key parameter to characterize the intensity of eddies. Turbulence decreases with the increase of the altitude above the ground, which is related to the average wind speed, time interval, and ground roughness. According to the GB 50009-2012 (Load code for the design of building structures) [47], the variation of turbulence with height is described by Eq. (2).

$$I_u = I_{10}\left(\frac{Z}{10}\right)^{-\alpha} \tag{2}$$

Where Z is the height from the ground, I_{10} is 10 m high nominal turbulence. The turbulence simulated by the wind tunnel is shown in **Fig. 4 (b)**, it is found that the simulation results are close to the theoretical calculated value of Eq. (2). The accurate simulation of the wind tunnel flow field provides a significant guarantee for the reliability of average wind pressure and fluctuating wind pressure measurement.

To verify the accuracy of the scale model and wind tunnel settings, the correctness of the scale model was confirmed by ensuring geometric similarity, Reynolds number similarity, and dynamic similarity. The accuracy of the wind tunnel settings was validated through flow field testing, environmental monitoring, and boundary effect control. Additionally, the reliability of the experiment was further validated by comparing it with theoretical predictions, conducting repeated tests, and cross-checking with field tests.

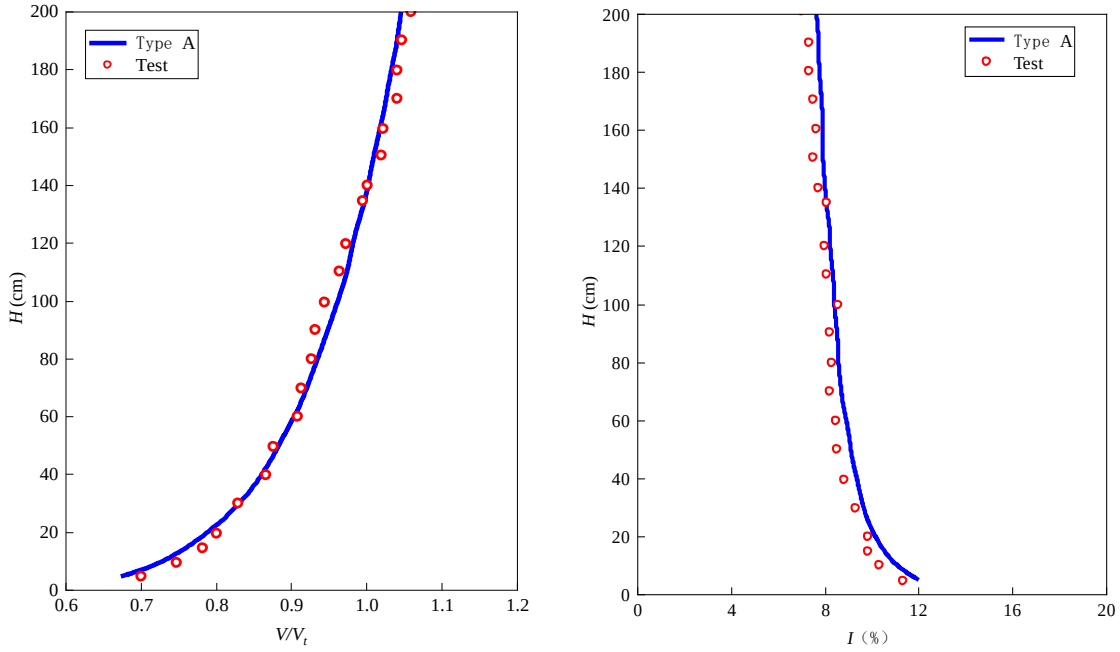

(a) Wind speed profile (b) Turbulence intensity profile

Fig. 4 Class A atmospheric boundary characteristics simulated by wind tunnel test

3.2.3. Test method

Following the completion of the atmospheric boundary layer simulation in the wind tunnel, the model is installed on the turntable in the test section of the wind tunnel. During the wind tunnel test, each wind direction angle constitutes a distinct load condition, with a 15° interval for wind direction changes. The wind direction angles from 0° to 360°, including 24 distinct load conditions. As shown in **Fig. 1**, the wind direction angle of 0° and the rotation center are defined, and the wind direction of each load condition is increased counterclockwise for one cycle around the rotation center.

3.3. Analysis of the test results

3.3.1. Wind pressure coefficient

While both dynamic wind pressure and static wind pressure wind tunnel tests employ rigid models, the testing methodologies and contents differ significantly. Dynamic wind pressure test uses an electronic scanning valve and a data acquisition system to capture the pressure spectrum at each measuring point in a period in the wind field simulating turbulence, to obtain the wind pressure coefficient. According to the international test standards, the dynamic wind pressure sampling time should be equivalent to 10 minutes, and the data samples collected must be enough to obtain real statistical data. The wind pressure coefficient of each measuring point is determined in line with JGJ/T 338-2014 [46], as shown in Eq. (3).

$$C_{pi} = \frac{p_i - p_\infty}{0.5\rho v_\infty^2} \tag{3}$$

Where the C_{pi} represents the wind pressure coefficient of a specific measuring point i on the building surface; P_i is the wind pressure value of measuring point i; P_∞ is the static pressure of the reference point; V_∞ is the wind speed at the reference point. For this test, V_∞= 12.4 m/s, and the reference point is situated at the model height of 0.6 m, corresponding to the real height of 132 m. According to the similarity principle, the dimensionless parameters of the model are consistent with the real structure, so the C_{pi} on the model is the average wind pressure coefficient of the corresponding point on the real structure.

3.3.2. Mean wind pressure

For this wind tunnel test, the geomorphic index (α) is 0.12, the height of the wind speed reference point H is 132 m, and the basic wind pressure (w_0) is 0.95 kN/m^2 once every 100 years. The reference wind pressure can be calculated using Eq. (4a). Where z_i represents the body shape coefficient of any point, and the local body shape coefficient corresponding to each measuring point (μ_{zi}) is obtained by Eq. (4b).

$$W_r = \mu_{zr} w_0 = 1.284 \times \left(\frac{132}{10}\right)^{0.24} \times 0.95 = 2.266 \left(\mathrm{kN/m^2}\right) \tag{4a}$$

$$\mu_{zi} = \left(\frac{132}{z_i}\right)^{0.24} \tag{4b}$$

In wind resistance design, it is imperative to account for the maximum wind pressure under each wind direction while considering the predominant local wind direction. For the awning test area, both the upper and lower surfaces experience simultaneous wind loading, and the wind pressure difference should be considered in the design. The wind pressure difference is defined as the wind pressure on the upper surface minus that on the lower surface, and the positive and negative signs of the wind pressure are the same as that of the upper surface. The net wind pressure coefficient (C_{pms}) of each measurement point can be calculated using Eq. (5). Where C_{pu} and C_{pl} denote the wind pressure coefficient of the upper and lower surface, respectively.

$$C_{pms} = \sqrt{\sum_{k-1}^{N} \left(C_{pu} - C_{pl}\right)^2 \Big/ \left(N-1\right)} \tag{5}$$

For the awning test area, the upper and lower surfaces have been superimposed, and the numbering rule of the test points after combined is to change the number to lowercase to show the difference, such as the test points S9 and SX9 are denoted as s9 after superimposed. Taking the metal roof of the conference center as an example, the wind pressure coefficient and body shape coefficient of each measuring point under various wind direction angles are analyzed and calculated, the results are listed in **Table 2**.

During periods of heightened average wind pressure on the roofing, the wind direction angles associated with positive and negative wind pressure for the same measuring point differ. For the upper surface of the roof, the average maximum positive wind pressure reaches 1.00 kN/m², accompanied by a corresponding maximum body shape coefficient of 0.62, at that time the wind direction angle is 315°. At a wind angle of 240°, the maximum negative wind pressure (-4.80 kN/m²) is achieved, and the body shape coefficient is -2.85. For the whole conference center, the point of the west facade ridge curtain wall (O22) experiences the maximum positive wind pressure of 1.68 kN/m², with a shape coefficient of 0.92 and a wind direction of 285°. The maximum negative wind pressure (-4.84 kN/m²) occurs at the measuring point (P13) on the upper surface of the lower roof, the corresponding body shape coefficient is -3.05, and the wind direction is 225°. As shown in **Fig. 5**, the distribution of average wind pressure under different wind pressure coefficients and body shape coefficients is shown. It can be found that with the increasing wind pressure coefficient and body shape coefficient, the positive and negative average wind pressure increases linearly, and its increasing law conforms to a plane.

Table 2
Summary of the test results with average wind pressure

Measure distribution		Positive wind pressure				Negative wind pressure			
Location	Point ID	Wind pressure coefficient (C_{pi})	Average wind pressure (kN/m²)	Shape coefficient (Zi)	Wind direction (°)	Wind pressure coefficient (C_{pi})	Average wind pressure (kN/m²)	Shape coefficient (Zi)	Wind direction (°)
The upper roof covers the upper surface	A1	0.29	0.66	0.41	285	-1.52	-3.43	-2.15	45
	B4	0.44	1.00	0.62	315	-1.15	-2.61	-1.66	285
	C10	0.34	0.77	0.47	330	-1.66	-3.77	-2.29	60
	D51	0.24	0.54	0.29	300	-1.03	-2.32	-1.25	300
	E47	0.11	0.24	0.14	285	-1.17	-2.64	-1.42	75
	F19	0.43	0.97	0.51	345	-1.20	-2.73	-1.41	225
	G9	0.34	0.77	0.42	30	-1.54	-3.50	-1.81	30
	H2	0.37	0.85	0.46	195	-1.55	-3.50	-2.07	240
	J1	0.32	0.73	0.39	165	-1.22	-2.75	-1.49	30
	K36	0.06	0.14	0.08	165	-2.12	-4.80	-2.85	240
The lower roof covers the upper surface	M3	0.25	0.56	0.35	210	-1.27	-2.89	-1.79	270
	N10	0.21	0.49	0.30	165	-0.91	-2.07	-1.29	270
	P13	0.15	0.35	0.22	165	-2.13	-4.84	-3.05	225
The lower surface of the roof	AX41	0.61	1.37	0.91	330	-0.56	-1.27	-0.85	300
	KX10	0.24	0.54	0.33	165	-1.22	-2.77	-1.67	225
	PX1	0.45	1.01	0.65	255	-0.67	-1.53	-0.99	210
Belvedere	Z1	0.79	1.80	1.05	285	-1.72	-3.91	-2.23	30
West elevation ridge curtain wall	Q22	0.74	1.68	0.92	285	-1.40	-3.18	-1.75	210
	S17	0.68	1.55	0.87	285	-0.76	-1.72	-1.08	165
East elevation ridge curtain wall	R22	0.71	1.62	0.89	60	-1.31	-2.98	-1.92	315
	T17	0.64	1.46	0.82	60	-0.98	-2.21	-1.91	300
South facade curtain wall	U23	0.72	1.63	1.15	60	-0.96	-2.17	-1.88	15
North facade curtain wall	V23	0.51	1.15	0.82	225	-0.49	-1.12	-0.97	210
West side canopy	W5	0.55	1.24	0.85	285	-0.76	-1.71	-1.17	165
East side canopy	Y7	0.56	1.26	0.86	75	-0.91	-2.06	-1.41	300

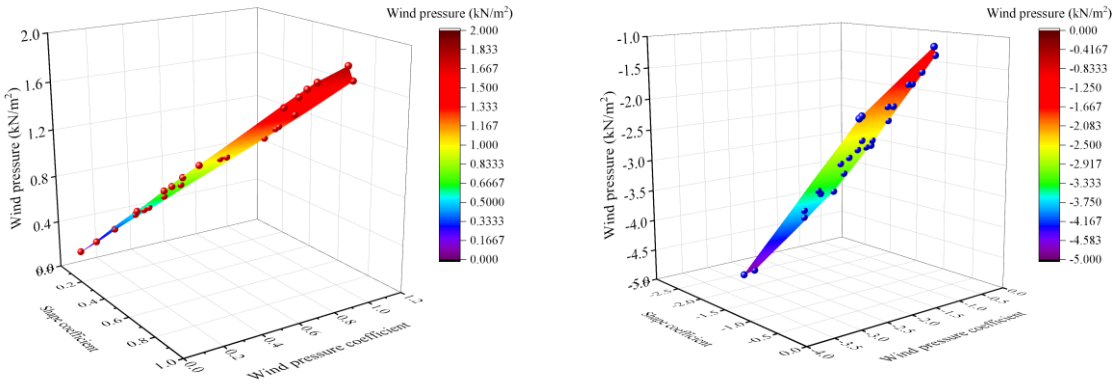

(a) Positive wind pressure (b) Negative wind pressure

Fig. 5 Distribution of average wind pressure

3.3.3. Isogram of body shape coefficient

Fig. 6 takes the body shape coefficient of the upper surface of the roof of the conference center as an example and shows the contour distribution diagram when the shape coefficient reaches the ultimate values under positive and negative wind pressure. When the wind direction is 315°, the contour lines of the body shape coefficient concentrate on the roof surface, depicting predominantly negative wind pressure across most areas, as shown in **Fig. 6 (a)**. Notably, within the southern portion of the conference center, there exist more areas experiencing positive wind pressure, resulting in relatively sparse contour lines. As shown in **Fig. 6 (c)**, when the wind direction is 210°, the distribution of contour lines for the shape coefficient on the upper roof surface reveals three primary areas. The northern and southern sides of the roof primarily encounter positive wind pressure zones, whereas the central part predominantly experiences negative wind pressure, significantly influenced by variations in wind direction angles.

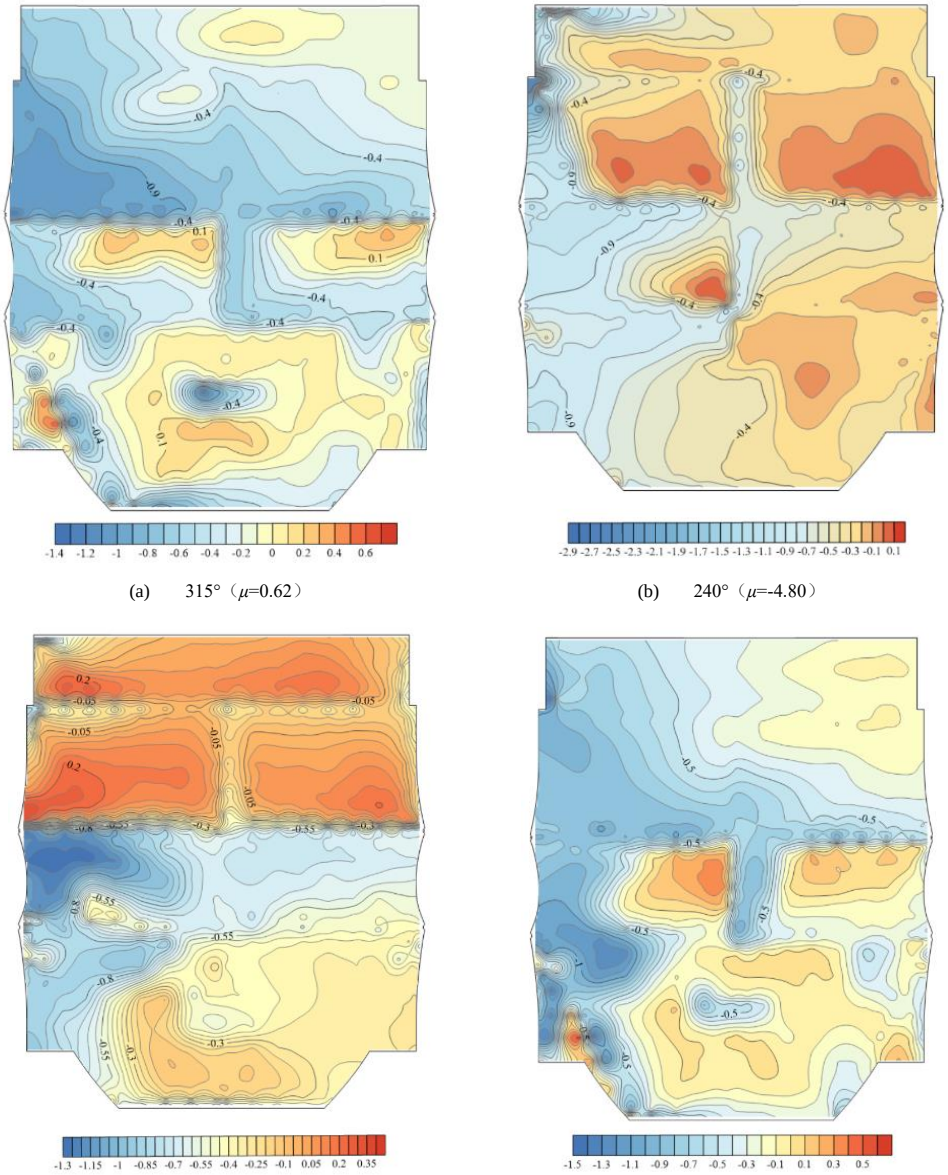

(a) 315°（μ=0.62） (b) 240°（μ=-4.80）

(c) 210°（μ=0.08） (d) 300°（μ=-2.23）

Fig. 6 Distribution of body shape coefficient at different wind direction angles

4. Standard wind load of the enclosure structure

4.1. Comparison of calculation methods

At present, there are two main methods to calculate the standard wind load of the metal roof envelope structure, including the peak factor method (PFM) and the extreme value analysis method (EAM). Compared to other methods, the PFM and EAM have unique advantages in the wind resistance design of metal roofs. Utilizing statistical analysis and empirical formulas, these methods are highly effective in addressing extreme fluctuations, uneven distribution, and complex local effects of wind loads, making them widely adopted in engineering practice. By providing a more accurate assessment of extreme wind loads, they help ensure the safety and stability of metal roofs under severe wind conditions. In contrast, traditional formula-based methods and standard approaches typically fail to fully capture extreme wind loads and the dynamic response of the structure. As a result, they are not suitable for all types of structures, particularly those that require consideration of extreme wind speeds and dynamic effects. The following two methods are used for analysis and calculation.

4.1.1. Peak factor method (PFM)

Fluctuating wind pressure is an important factor for the design of curtain walls, roof plates, and connectors, so it is necessary to analyze the wind pressure coefficient and wind load at each point after considering the wind pressure fluctuation. According to the probability and statistical theory, and ensuring a 99.98% reliability rate, the maximum positive and negative values of the fluctuating wind pressure coefficient (C_p) of the metal roof of the conference center can be determined using the Eqs. (6).

$$C_{P\max} = \overline{C}_{pi} + 3.5C_{pi} \tag{6a}$$

$$C_{P\min} = \overline{C}_{pi} - 3.5C_{pi} \tag{6b}$$

As a common enclosed building structure, the internal pressure of the conference center itself should be considered when calculating the standard wind load. Corresponding to the positive and negative conditions of the outer surface, the local body shape coefficient of the internal pressure of the building is -0.2 and 0.2, respectively. Therefore, the design wind load value of the envelope structure should be superimposed on the wind pressure of the outer surface and the inner surface, which can be calculated using Eqs. (7).

$$W_i^{\max} = (\overline{C}_{pi} + 3.5C_{pi})W_r + 0.2\beta_{gz}\mu_z W_0 \tag{7a}$$

$$W_i^{\min} = (\overline{C}_{pi} - 3.5C_{pi})W_r - 0.2\beta_{gz}\mu_z W_0 \tag{7b}$$

Where the W_i is designed wind load of the envelope structure, W_r is the wind pressure value of the outer surface obtained by the wind tunnel test, and the basic wind pressure once in 100 years is W_0. The wind vibration coefficient is defined

as $\beta_{gz}=1+2gI_{10}(z/10)^{-\alpha}$, and 0.12 is taken for class A landform I_{10}, μ_z is the local body shape coefficient corresponding to each measuring point

4.1.2. Extreme value analysis method (EAM)

The Gumbel fitting method assumes that the ultimate value of the wind pressure coefficient conforms to the Gumbel distribution, that is, the extreme value type I distribution, and the distribution function is shown in Eq. (8). Where μ and β are the positional and scale parameters of Gumbel distribution, respectively.

$$F(x)=\exp[(-\exp(-\frac{x-\mu}{\beta})] \tag{8}$$

The time history of the wind pressure coefficient is divided into n subsamples of equal length. Within each subsample, the maximum and minimum values are extracted and subsequently arranged in ascending order. Lieblein BLUE (Best Linear Unbiased Estimator) method was used to determine the distribution coefficients μ and β. The average Gumbel distribution is taken to estimate the extreme value wind pressure, as shown in Eq. (9).

$$E(x)=\mu+\gamma\beta \tag{9}$$

Where γ=0.5772 signifies the Euler-Mascheroni constant. The BLUE algorithm is widely used in wind speed and extreme value wind pressure statistics. Notably, the BLUE algorithm holds prominence in statistical analyses of wind speed and extreme value wind pressure, garnering endorsement from both the ASCE specifications. The wind load value of the outer surface obtained through the EAM also needs to consider the correction of the internal pressure. This correctional approach aligns with the methodology delineated in Eq. (7).

4.1.3. Comparison of the calculated results

Two typical positions B40 (the middle position) and E33 (the windward angle area) of L1 in the exhibition hall (2.4W) under the wind angle of 135° were taken respectively to compare and analyze the rationality of the two calculation methods, as shown in **Fig. 7**. It is observed that the two methods exhibit close agreement within the Gaussian distribution region. For the non-Gaussian distribution region, the EAM shows more reasonable results. The wind pressure curves of the two measuring points are enveloped in the range of positive and negative wind pressure curves obtained by EAM. However, for E33 in the corner region, the upper limit of the wind pressure line calculated by the PFM significantly deviates from the actual wind pressure time history curves.

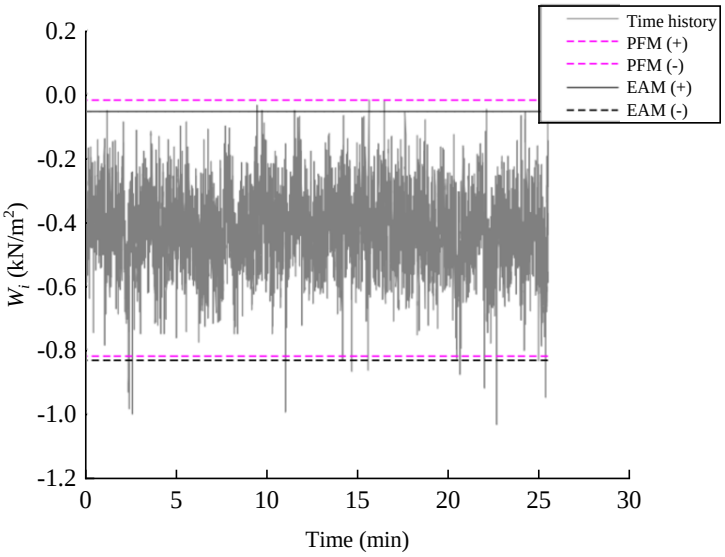

(a) B40

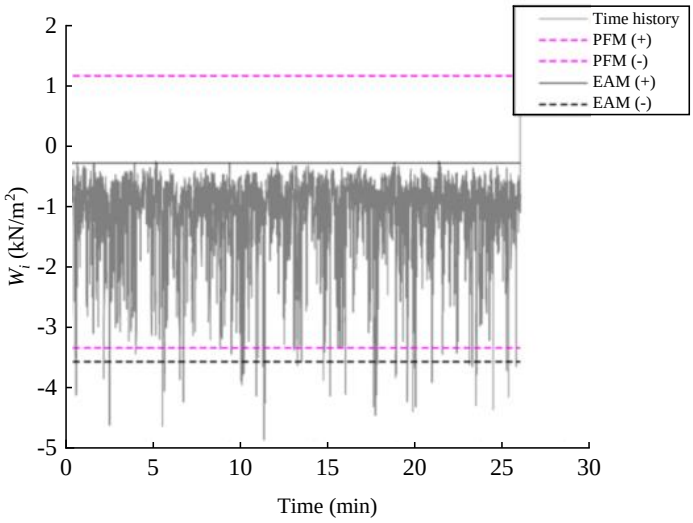

(b) E33

Fig. 7 Comparison of calculation results of two statistical methods

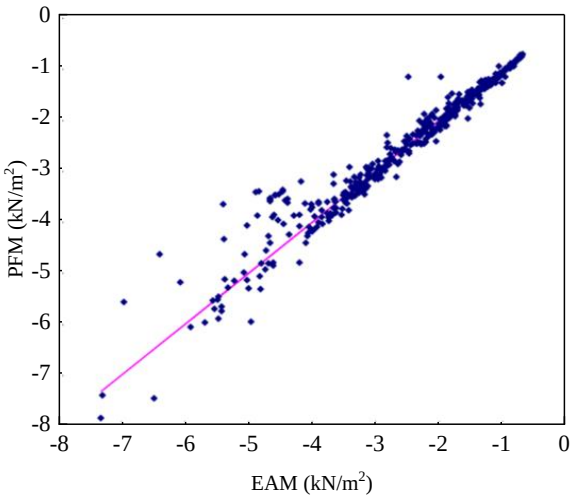

Fig. 8 Comparison of extreme wind pressure

Fig. 8 depicts the comparison of the extreme negative wind pressure in the design wind load of the L1 enclosure structure of the exhibition hall (2.4W). Notably, the calculated results from the two methods exhibit a close correspondence. For the area of high negative wind pressure, the results of the EAM are marginally higher than that of the PFM. For low negative wind pressure regions, the results of PFM are slightly greater than that of EAM. Therefore, it is safe to use the envelope results of the two methods in the calculation of the standard wind load of the enclosure structure, ensuring a comprehensive and conservative consideration of extreme conditions.

4.2. Standard value of wind load

The measurement points exhibit significant positive and negative values of the standard wind load of the conference center at various wind angles and the corresponding results are presented in **Table 3**. It is found that the measuring points and wind direction angles of the roof with pronounced pulsating positive and negative wind pressures are various. For the upper roof surface, at measuring point F20, the maximum pulsating positive wind pressure reaches 3.15 kN/m², occurring at a wind direction angle of 0°. The peak pulsating negative wind pressure (-9.69 kN/m²) is recorded at 270°, accompanied by a wind pressure coefficient of -4.25. For the entire conference center, the maximum pulsating positive wind pressure (4.83 kN/m²) appears at the measuring point (R29) of the roof ridge curtain wall on the east elevation, where the wind pressure coefficient is 1.86 and the wind direction angle is 60°. Additionally, the maximum pulsating negative wind pressure (-9.69 kN/m²) is identified at the measuring point (K1) on the upper surface of the upper roof, where the associated wind pressure coefficient is -4.255 and the wind direction angle is 255°.

The distribution of roof wind pressure has been extensively verified through wind tunnel tests and wind pressure measurements, and studies have shown that areas such as the edges, corners, and ridges of the roof generally experience higher wind pressure. These results align with both experimental data and theoretical models, especially when considering factors such as wind direction, roof geometry, and aerodynamic effects. The uneven distribution of metal roof wind pressure is mainly affected by the geometric shape of the roof, wind flow interference, local eddy currents, as well as wind speed and direction.

Table 3
Test results of pulsating wind pressure

Location	Pulsating positive wind pressure				Pulsating negative wind pressure			
	Point ID	Wind pressure coefficient	Wind pressure (kN/m²)	Wind direction (°)	Point ID	Wind pressure coefficient	Wind pressure (kN/m²)	Wind direction (°)
The upper roof covers the upper surface	A1	0.94	2.68	300	A11	-2.91	-8.57	30
	B14	1.03	2.90	300	B2	-2.64	-6.10	300
	C4	0.87	2.52	45	C5	-3.02	-7.08	60
	D51	0.70	2.20	315	D33	-2.45	-5.27	315
	E47	0.63	2.06	345	E10	-3.01	-6.48	75
	F20	1.11	3.15	0	F32	-2.72	-5.86	300
	G20	0.34	3.11	345	G36	-3.15	-7.18	30
	H11	0.86	2.57	210	H31	-2.66	-6.08	240
	J1	0.96	2.81	150	J30	-3.03	-6.53	30
	K36	0.68	2.12	45	K1	-4.25	-9.69	270
The lower roof covers the upper surface	M1	0.67	2.07	195	M18	-3.02	-7.06	270
	N9	0.59	1.89	195	N1	-1.88	-4.59	270
	P20	0.55	1.81	45	P40	-4.10	-9.38	240
The lower surface of the roof	AX53	1.10	3.02	30	AX22	-1.88	-4.05	75
	KX2	0.62	1.97	195	KX1	-2.42	-5.78	225
	PX1	0.97	2.75	255	PX38	-1.38	-3.66	75
Belvedere	Z1	1.59	3.61	285	Z5	-4.33	-8.46	45
West elevation ridge curtain wall	Q51	1.40	3.77	285	Q29	-2.52	-6.03	210
	S17	1.20	3.31	285	S14	-1.54	-3.49	30
East elevation ridge curtain wall	R29	1.86	4.83	60	R23	-3.59	-8.37	165
	T22	1.74	4.54	60	T46	-1.98	-4.27	300
South facade curtain wall	U23	1.47	3.83	30	U2	-1.74	-4.18	15
North facade curtain wall	V23	1.01	2.79	225	V2	-1.06	-2.61	210
West side canopy	W5	0.97	2.19	285	W1	-2.58	-3.59	165
East side canopy	Y3	1.85	4.20	60	Y1	-2.91	-3.89	45

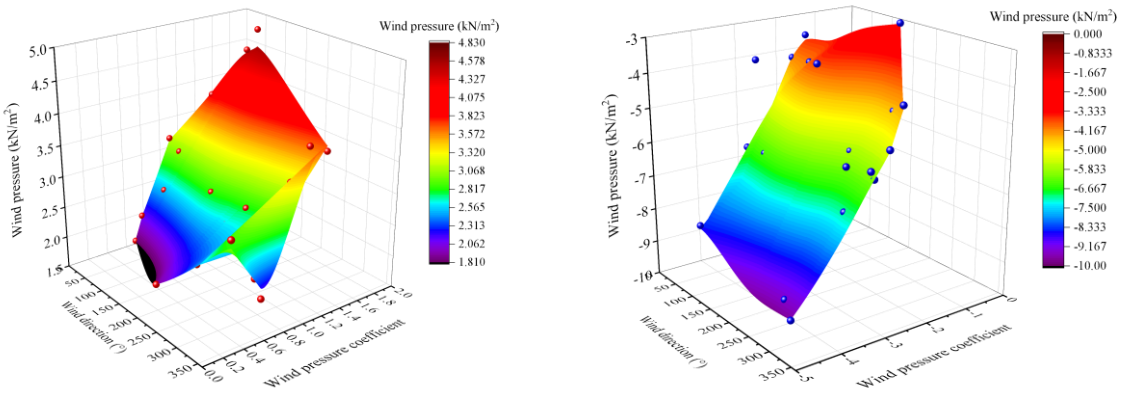

(a) Positive wind pressure (b) Negative wind pressure

Fig. 9 Distribution of pulsating wind pressure

Fig. 9 also shows the relationship between pulsating wind pressure wind direction angle and wind pressure coefficient. It can be found that the variation law of pulsating wind pressure with wind direction angle is not obvious, because different wind direction will cause significant differences in wind loads at different parts. However, the increase of the wind pressure coefficient shows a linear increase trend, which further indicates that the wind pressure coefficient plays a key role in the wind load value of metal roofs.

4.3. Isogram of wind vibration coefficient

As depicted in **Fig. 10,** the wind vibration coefficient of the upper surface of the roof of the conference center is taken as an example. The distribution diagram illustrates the culmination of the body shape coefficient under both pulsating positive and negative wind pressures. It is found that when the wind direction angle is 0°, the isogram distribution of wind vibration coefficient on the roof surface exhibits a relatively scattered pattern **(Fig. 10a)**, and the isogram distribution is positive in most areas, there are notable negative areas only in the southern sector of the conference center, resulting in a comparatively sparse isogram distribution. As shown in **Fig. 10(d)**, when the wind direction angle is 315°, the isogram distribution of the wind vibration coefficient on the upper surface of the roof predominantly manifests two distinct areas. The southern side of the roof mainly shows the cross-distribution of positive and negative wind vibration coefficients, whereas the northern part primarily displays a positive wind vibration coefficient area. This variation is heavily contingent on the specific direction of the wind angle.

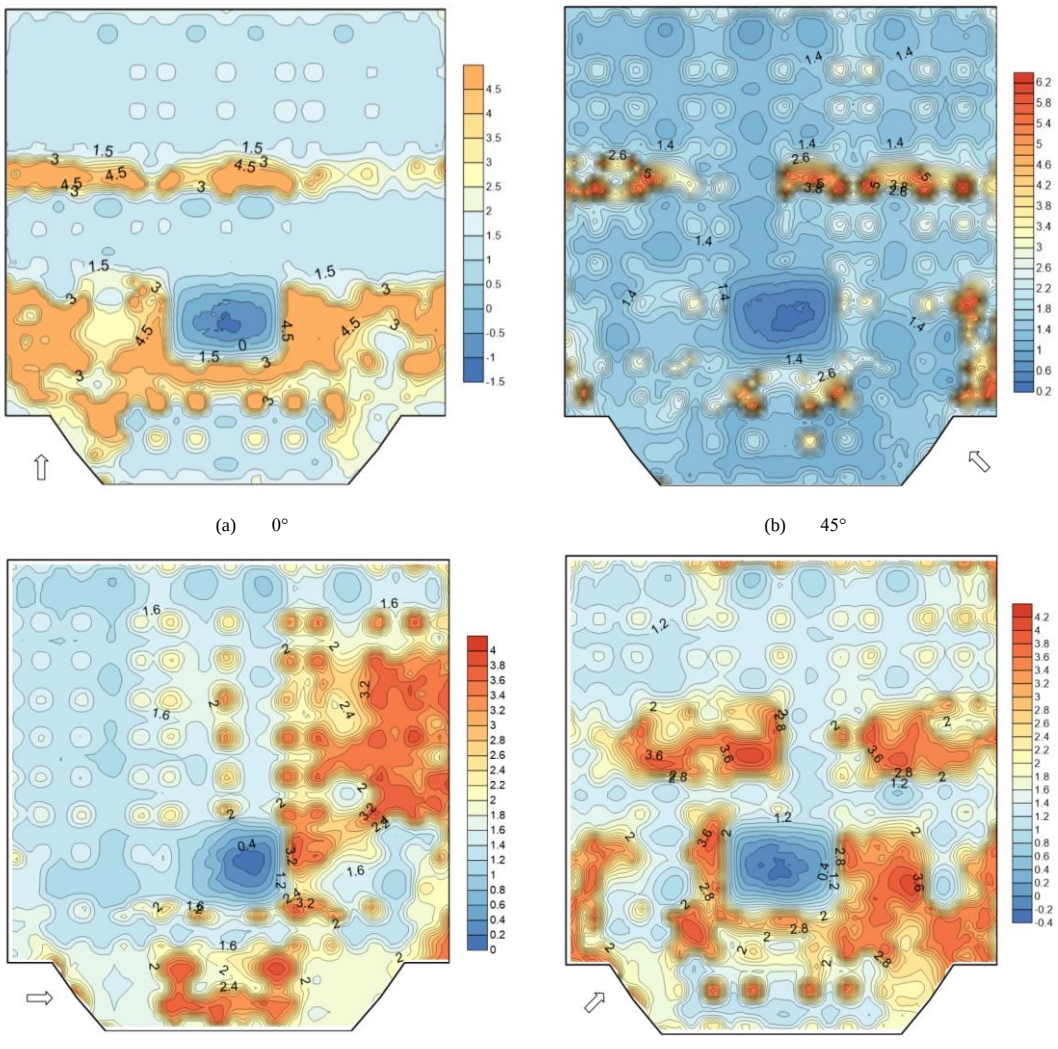

(a) 0° (b) 45°

(c) 270° (d) 315°

Fig. 10 Distribution of wind vibration coefficient

5. Wind vibration calculation and result analysis

5.1. Wind vibration calculation principle

The method employed for analyzing the time history of structural wind vibration responses involves discretizing the structure through the fundamental principles of finite element analysis. The time history of wind load was applied on the corresponding element node and the response of the structure was by directly solving the motion equation in the time domain. While the calculation results obtained through the time domain method align more closely with reality compared to the linear method in the frequency domain, it is typically reserved for critical projects or research verification.

The algorithms utilized in the time domain method can be categorized into direct integration and mode superposition methods. The direct integration method encompasses linear acceleration techniques, *Wilson-θ*, *Runge-Kutta*, and *Newmark-β* methods. In this study, the *Newmark-β* method is specifically employed to compute the time history of the roof structure, tailored to its unique characteristics. The concept of equivalent static wind load is proposed to facilitate engineering applications. When this equivalent load acts on the structure as a static load, the resultant structural response corresponds to the maximum value observed under actual wind load conditions. The equivalent static wind load is commonly expressed as the product of static wind load and wind vibration coefficient (λ). This coefficient accounts for the amplification effect of fluctuating wind loads on structural responses. The load wind vibration coefficient is defined using Eqs. (10).

$$\lambda = \frac{P_e}{\overline{P}} = \frac{\overline{P} + P_d}{\overline{P}} = 1 + \frac{P_d}{\overline{P}} \tag{10a}$$

$$P_d = gm(z)\omega_1^2\varphi(z)\sigma_1 \tag{10b}$$

Where λ is the wind vibration coefficient, P_e is the equivalent static wind load, $\overline{P}$ Is the static wind load, P_d is the dynamic wind load, g is the peak factor, generally g=2.5, $m(z)$ is the total mass of z height, ω_1 is the circular frequency of the first vibration mode. $\varphi(z)$ is the first-order mode coefficient of the structure at the height of z, and σ_1 is the root mean square of the generalized displacement of the first mode.

In the wind vibration time history analysis of intricate spatial structures, several challenges arise when applying the defined load wind vibration coefficient as per the code. i) Due to the presence of multiple vibration modes in complex spatial structures, the selection of the appropriate vibration modes is difficult. ii) The acceleration response of each joint can be obtained in the FE analysis of wind vibration. If the acceleration response is used to calculate the wind vibration coefficient, only the maximum inertia force can be obtained without considering the wind vibration background component. The wind vibration coefficient calculation method stipulated essentially includes the additional force arising from the wind vibration background component and the resonance component in the code. iii) The specification for the wind vibration coefficient typically employs a single mass block to account for the vibration of the vibrating body. Consequently, in cases where the force transmission path of the vibrating body in the direction of wind pressure is unclear, substituting the mass block becomes impractical, rendering the determination of the load wind vibration coefficient unattainable.

The displacement wind vibration coefficient is a type of effective wind vibration coefficient, determined by the ratio of the maximum displacement to the average displacement response of a structure. The displacement wind vibration coefficient has been applied successfully in high-rise buildings and roof structures dominated by first-order modes. The displacement response includes the background and resonance component of wind vibration. The maximum displacement (U_{max}) generated by dynamic wind load can be calculated using Eq. (11).

$$U_{\max} = \overline{U} + g\sigma_u \tag{11}$$

Where the mean displacement is denoted by, and σ_u is the mean square of displacement. The maximum displacement vector generated by the dynamic wind load is assumed to be equal to the displacement vector generated by the equivalent static load, the displacement wind vibration coefficient can be derived from the definition of the specification. The static equilibrium formulation of the structure under the action of average wind load and equivalent static wind load is shown in Eqs. (12).

$$[K]\{\overline{U}\} = [\overline{P}] \tag{12a}$$

$$[K]\{\overline{U} + g\sigma_u\} = [P_e] \tag{12b}$$

Then the displacement wind vibration coefficient is shown in Eqs. (13).

$$\{\beta\} = \frac{[K]\{\overline{U} + g\sigma_u\}}{[K]\{\overline{U}\}} \tag{13a}$$

$$\beta_i = \frac{P_{ei}}{\overline{P_i}} = \frac{\sum_{j=m,\, j\neq i}^{n} k_{ij}(\overline{U}_j + g\sigma_{uj}) + k_{ii}(\overline{U}_i + g\sigma_{ui})}{\sum_{j=m,\, j\neq i}^{n} k_{ij}\overline{U}_j + k_{ii}\overline{U}_i} \tag{13b}$$

Where j is the adjacent joint i, and k_{ii} and k_{ij} are diagonal and non-diagonal elements of row i of the total rigid matrix. If the following two proportional parameters α_1 and α are introduced, the displacement wind vibration coefficient of joint i can be expressed as Eq. (14a).

$$\beta_i = \frac{\alpha_1 + 1}{\alpha_2 + 1} \cdot \frac{\overline{U}_i + g\sigma_{ui}}{\overline{U}_i} \tag{14a}$$

$$\alpha_1 = \frac{\sum_{j=m,\, j\neq i}^{n} k_{ij}(\overline{U}_j + g\sigma_{uj})}{(\overline{U}_i + g\sigma_{ui})k_{ii}} \tag{14b}$$

$$\alpha_2 = \frac{\sum_{j=m,\, j\neq i}^{n} k_{ij}\overline{U}_j}{\overline{U}_i k_{ii}} \tag{14c}$$

Notably, when the average displacement of each joint is large enough compared to the mean square, or the mean square of each joint is in the same proportion to the average. At this time, the wind vibration coefficient obtained from the definition of load wind vibration coefficient is consistent with the displacement wind vibration coefficient, as shown in Eq. (15).

$$\beta_i = \frac{\overline{U}_i + g\sigma_{ui}}{\overline{U}_i} \tag{15}$$

The application conditions of the displacement wind vibration coefficient are that the mean displacement is large enough relative to the mean square, or the basic configuration of the displacement dynamic and the static response have high similarity. Consequently, this method proves effective for structures predominantly vibrating in the first-order mode but is deemed unsuitable for large-span spatial structures with multi-order modes. To address this, a novel approach combining the Load Response Correlation (LRC) method and the Inertial Wind Load method is proposed to account for the equivalent static wind load on structures. Because the equivalent wind load of background response calculated by the load-response correlation method can obtain different equivalent wind load values for each response of each member, it is difficult to apply this method in large-span roofing structures.

According to the engineering practice, this paper puts forward a simplified calculation method for load wind vibration coefficient, which has obtained favorable outcomes in practical applications. The mean square of acceleration obtained from FE analysis was used to calculate the maximum inertial force of the structure. Simultaneously, the mean square of fluctuating wind pressure is employed to assess the maximum wind vibration force on the structure. The load wind vibration coefficient can be simplified using Eq. (16).

$$\lambda_i = 1 + \frac{g\sqrt{(m_i\sigma_i)^2 + (C_{pi}W_rA_i)^2}}{\overline{C}_{pi}W_rA_i} \tag{16}$$

Where m_i is the total mass of the vibrating body corresponding to the i joint; the mean square of the acceleration of i joint obtained from the σ_i time-course analysis; C_{pi} and C_{pi} are the average wind pressure coefficient and the root

mean square wind pressure coefficient, respectively. *Wr* is the reference point wind pressure; A_i is the corresponding area of wind pressure acting on the *i* joint; *g* is the peak factor.

Structural damping must be specified in structural dynamic analysis. In this paper, Rayleigh structural damping is adopted, as shown in Eq. (17). Where *C* is the total damping matrix of the system; *M* is the mass matrix of the structure; *K* is the stiffness matrix of the structure; α and β are constants in Rayleigh damping.

$$C = \alpha M + \beta K \tag{17}$$

The values of α and β cannot be directly acquired from the real structure but can be derived from the damping ratio of the structure. ξ_i is the damping ratio relative to the *i*-order mode of the structure. If ω_i is the frequency of the *i*-th mode of the structure, the relationship between ξ_i and α and β can be expressed using Eq. (18). It is generally believed that the ξ is constant in a certain structural natural vibration frequency range, so given the ξ and two frequencies within this range, α and β can be obtained, and the ξ of the steel structure is 0.02.

$$\xi_i = \frac{\alpha}{2\omega_i} + \frac{\beta\omega_i}{2} \tag{18}$$

The sampling frequency of pulsating wind pressure measurement in the wind tunnel test is 31.5 Hz, with a sampling interval of 0.0032 s. According to the test wind speed ratio of 1:4.28 and the model scale ratio of 1:220, the test time ratio of 1:51.3 can be obtained, and the actual sampling time interval is 0.164 s. The wind pressure coefficient at each measuring point of the structure can be calculated using Eq. (19).

$$C_{pi}(t) = \frac{P_i(t)}{P_0 - P_\infty} \tag{19}$$

Where C_{pi} represents the wind pressure coefficient at the measuring point *i*, P_i denotes the wind pressure acting at that same point, P_0 and P_∞ refer to the total pressure and static pressure at the reference height during the test, respectively. For the wind tunnel test of the roof structure, the reference point is located at a height of 0.6 m, and considering the model scale of 1:220, the actual height of the reference point is 132 m. Using a basic wind pressure of 0.95 kN/m^2, the wind pressure time history corresponding to the measurement point in the actual building can be calculated by obtaining the C_{pi}(t) time history for each point, as shown in Eq. (20).

$$P_i(t) = C_{pi}(t) \times 1.284 \times \left(\frac{132}{10}\right)^{0.24} \times 0.95 = C_{pi}(t) \times 2.66(\mathrm{kN/m}) \tag{20}$$

Following the determination of the Finite element (FE) model, the wind load time history data at each measuring point undergoes spatial interpolation to formulate P_i(t) at individual stress joints. The control area (A_i) of each stress joint is calculated according to the coordinate relationship within the FE model. Due to the complexity of the structure, the wind load value of each joint can be decomposed into *x*, *y* and *z* directions, as illustrated in Eqs. (21). Where A_{xi}, A_{yi} and A_{zi} represent the projected areas in the *x*, *y* and *z* directions, respectively.

$$F_{xi}(t) = P_i(t) \times A_{xi} \tag{21a}$$

$$F_{yi}(t) = P_i(t) \times A_{yi} \tag{21a}$$

$$F_{zi}(t) = P_i(t) \times A_{zi} \tag{21c}$$

The wind load time history of each joint in *x*, *y* and *z* directions is applied to the FE model of the roof structure to calculate the wind-induced dynamic response. The time domain calculation method employed the *Newmark-β* method. The displacement response time history (U_i) and acceleration response time history (α_i) of each joint can be obtained, and the displacement mean square (σ_{ui}) and acceleration root mean square ($\sigma_{\alpha i}$) can be calculated through statistics. The wind load of all joints is accumulated to determine the overall wind load of the roof in the *z* direction, and the overall wind vibration coefficient (β_f) of the roof structure is calculated, as shown in Eq. (22). Where, F and $\overline{F}$ are the cumulative values of the equivalent and average wind load, respectively.

$$\beta_f = F/\overline{F} \tag{22}$$

5.2. Calculation model

In this calculation, 3D3S and other models established previously were used and imported into ANSYS software through interface files. **Fig. 11** shows the FE model of the conference center, in which the total number of joints is 72951. Notably, 2803 joints and 50,343 rods within the model are directly exposed to the influence of wind loads.

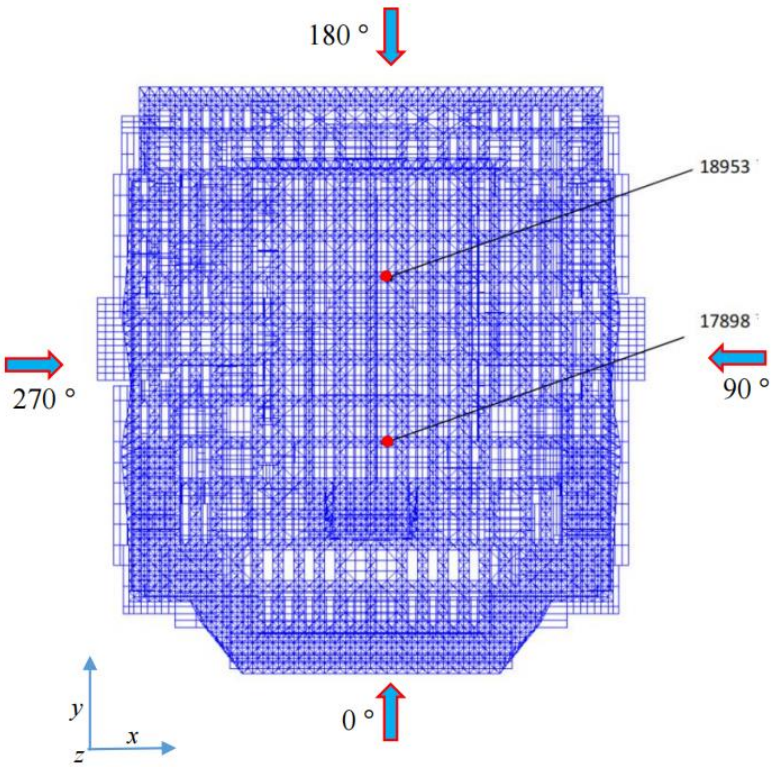

(a) Top view

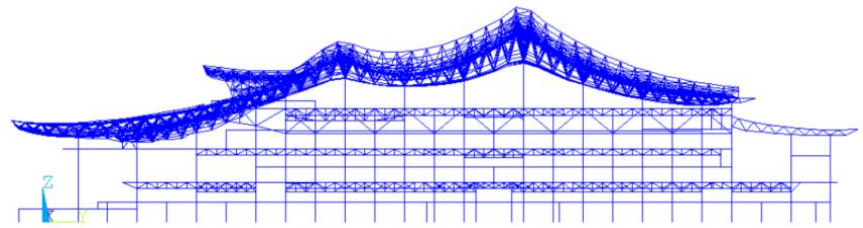

(b) East elevation view

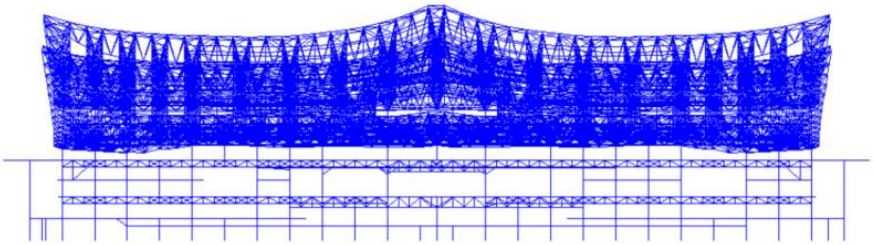

(c) South elevation view

Fig. 11 Finite element model of conference center roofing structure

5.3. Analysis of wind vibration calculation results

The displacement time history of typical joints of the metal roofing structure, namely joints 18953 and 17898 (**Fig. 11**), under 0° wind direction is obtained by calculation, as depicted in **Fig. 12**. It can be found that under this wind direction, the predominant displacement at the joint occurs in the positive *z*-direction (vertical). The displacement in the *x* direction (sideways) and the *y* direction (downwind) is nearly negligible.

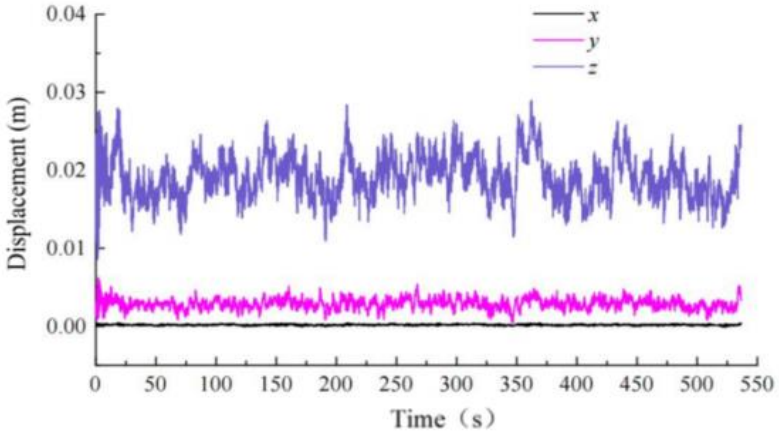

(a) Joint of 18953

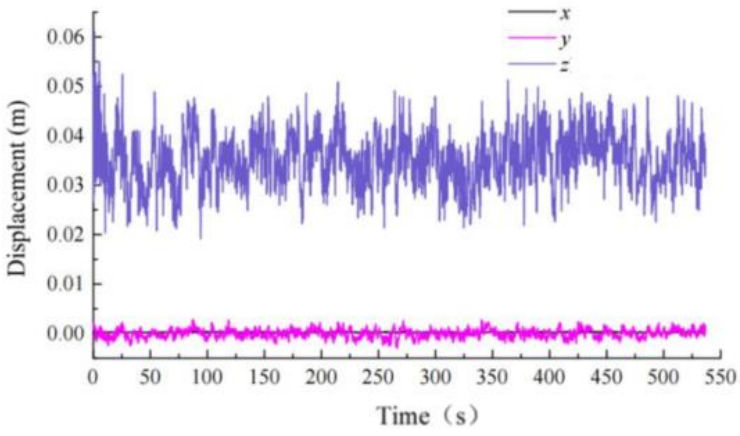

(b) Joint of 17898

Fig. 12 Displacement time history of typical joints at 0° wind direction

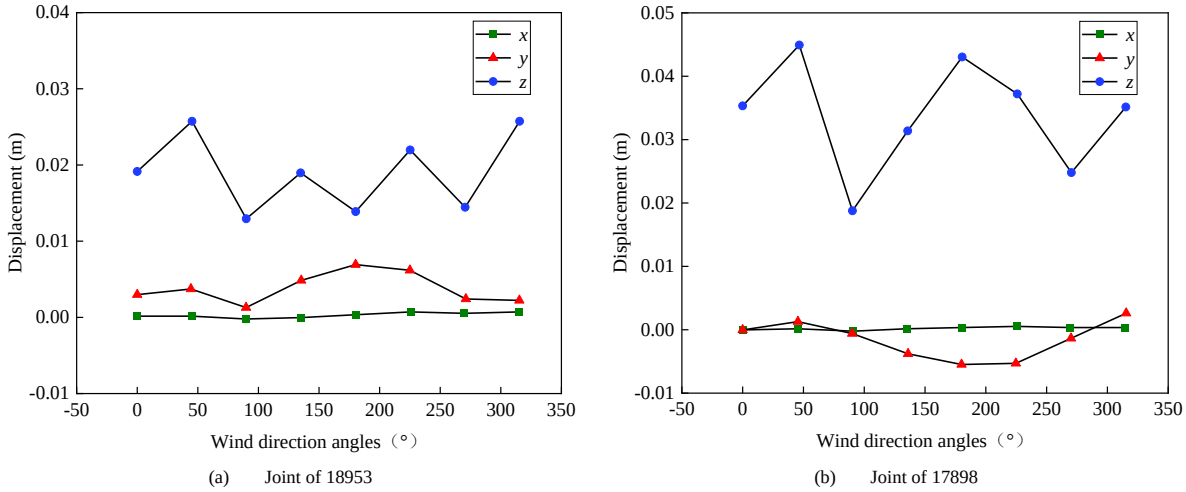

Fig. 13 The average displacement of typical joints under various wind directions

Taking the joints 18953 and 17898 of the metal roofing structure as typical examples, the average displacements under various wind directions are illustrated in **Fig. 13**. The results indicated that the primary displacement of these joints occurs in the *z*-direction (vertical), while displacements in the *x* and *y* directions are nearly negligible. In the *z*-direction displacement of this joint 18953, all displacements are oriented upward. Notably, the largest displacements are observed at wind angles of 45° and 315°, indicating that the metal roofing structure withstands greater wind loads near the position of this joint.

The forces F_x, F_y and F_z of each joint in the *x*, *y* and *z* directions were calculated, with the wind direction angle defined as depicted in **Fig. 11(a)**, which is consistent with the definition in the FE analysis. The average wind load and equivalent wind load values for each joint at wind angles of 0°, 45°, 90°, 135°, 180°, 225°, 270° and 315° can be directly applied to 3D3S structural design software.

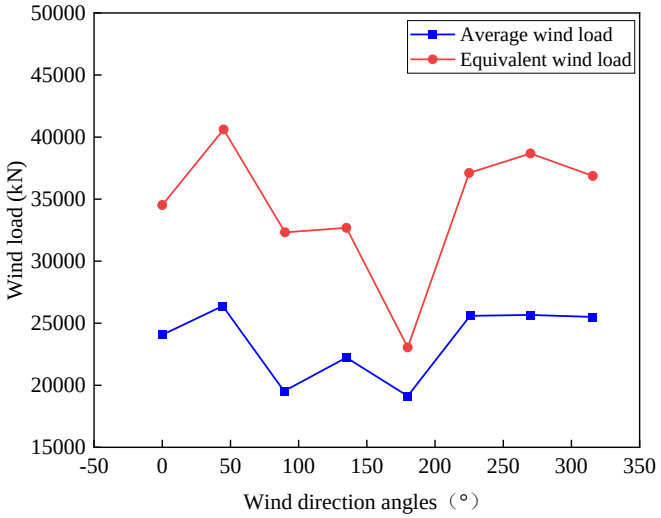

Fig. 14 Wind loads in the *z* direction of the metal roofing

Fig. 14 shows the variation trend of the wind load in the *z*-direction with the different wind direction angles. The average wind load and equivalent wind load for 2803 upper roof joints in the *z*-direction were obtained in the FE calculation. The wind load has taken into account the wind load area, and its unit is kN/m^2. The basic wind pressure utilized in the calculations is 0.95 kN/m^2, which is once in 100 years. **Table 4** presents all the calculated results for the *z*-direction, it can be indicated that the equivalent wind load and the average wind load in the *z*-direction reach the positive peak at a wind direction angle of 45°, and the wind vibration coefficient corresponding to the ultimate wind load is determined to be 1.54.

Table 4
Overall wind loads of conference center roof structure

Wind direction	Equivalent wind load	Average wind load	Vibration
0	34546	24072	1.44
45	40598	26333	1.54
90	32307	19588	1.65
135	32655	22127	1.48
180	23100	19191	1.20
225	37159	25712	1.45
270	38594	25734	1.50
315	36946	25524	1.45

Fig. 15 also presents the average wind load and equivalent wind load values in the *x* and *y* directions for the metal roof panel of the conference center. The wind load acting on the roof structure in the *z*-direction surpasses that in the other two directions. Specifically, the minimum equivalent wind load in the *x* direction is approximately -1200 kN, occurring at a wind direction angle of 90°. The minimum equivalent wind load in the *y* direction is about -17000 kN with a wind direction angle of 180°. The minimum equivalent wind load in the *z* direction is approximately -23100 kN at a wind direction angle of 180°. The maximum equivalent wind load in the *z* direction exceeds 40598 kN and the wind angle is 45°. It is indicated that the ability of the roof to withstand wind load in the *z* direction plays a critical role, which should be considered in the design.

6. Wind damage and strengthening measures of metal roofs

6.1. Discussion on wind damage

Metal roofing systems have been developing continuously with the diversification of roofing applications and the change in structural requirements. Roofing in the service process also appeared to be a variety of engineering problems, as a light discontinuous and large-span metal roof structure wind resistant problem is more prominent. This issue is not confined to coastal areas experiencing the force of strong typhoons; it is prevalent even in inland regions. **Fig. 16** shows the typical failure mode of metal roofs in China [48,49]. The severe weather events have drawn considerable attention due to safety concerns, including incidents of metal roofs being dislodged and collapsing during rainstorms.

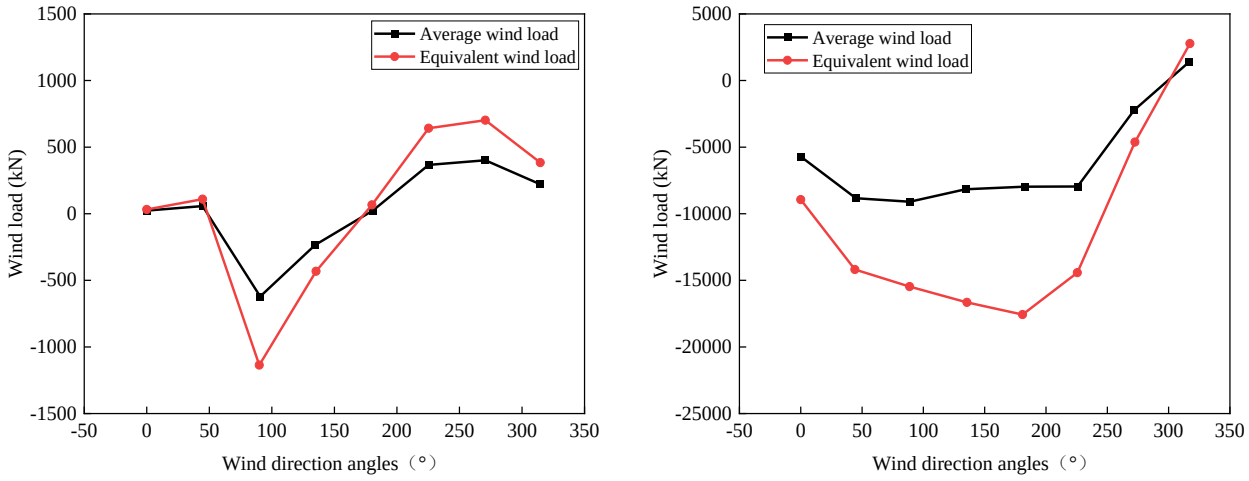

(a) *x* (b) *y*

Fig. 15 Wind load in *x* and *y* directions of the roof structure

(a) Terminal of the capital airport (b) Wuhan Tianhe airport

(c) Suzhou industrial park station (d) Zhanjiang Olympic sports center

Fig. 16 Typical failure modes of metal roofing [48,49]

Table 5
Wind disaster statistics of metal roofing

Time	Project name	Wing load	Failure modes	Roof selection
2010.09	Xiamen Institute of Technology Gymnasium	Super typhoon	The molded steel plate was lifted and the purlin was not damaged	Pressed steel sheet metal roofing
2010.12	Terminal T3 of Capital Airport	Wind speed is 26 m/s, Force 10 gale	Part of the roof metal sheet was torn off by the strong wind	Aluminum magnesium manganese vertical locking metal roofing
2011.11	Terminal T3 of Capital Airport	Wind speed is 24 m/s, Force 9 gale	The roof of Terminal D area was partially torn off by strong winds	
2013.03	Terminal T3 of Capital Airport	Wind speed is 30 m/s, Force 11 gale	The roof in the northeast corner of the international area of the terminal was partially lifted, and the glass cotton of the roof insulation layer was blown off	
2012.08	Suzhou Railway Station Park	Force 10 gale	15 aluminum, magnesium, and manganese plates were thrown open	
2013.08	Wuhan Tianhe Airport T2 terminal	Force 12 gale	The metal plate of the T2 roof was lifted off a corner, and the thermal insulation quilt was blown off by strong winds	
2018.03	Nanchang Changbei Airport Terminal T2	Wind speed is 29.5 m/s, Force 11 gale	The external suspended ceiling material at the T2 overhanging eaves is dropped as a whole, and the roof panel at the arc is large.	

The typical wind damage accidents of metal roofing are listed in **Table 5**. It is found that the damage to the roof system is mainly caused by the following reasons: (i) The design of the roof wind bearing capacity is insufficient; (ii) Insufficient strength in the support and purlin connections; (iii) Failure of the connection between the joint and the bite of the roof plate. The analysis of a large number of roofing accidents reveals that the wind resistance capacity of metal roofing systems primarily depends on the robustness of the supports. Wind disaster investigation shows [50,51] that the damage of standing seam roofing systems is mostly the separation of the roof plate and the fixed support at the lock joint, while the connection between the support and the purlin is still basically intact.

According to the analysis of the causes of the above-mentioned wind damage on the metal roofing, it is found that the phenomenon of wind damage on the roof is mostly caused by the disconnection of the connection between the metal roof plate and the fixed support. When subjected to negative wind pressure, the roof plate initially exhibits an upward arch deformation, as illustrated in **Fig. 17**. In instances of excessive wind suction, this can result in the detachment of the roof plate from the support, leading to damage or severance of the support and the connection with the roofing purlin.

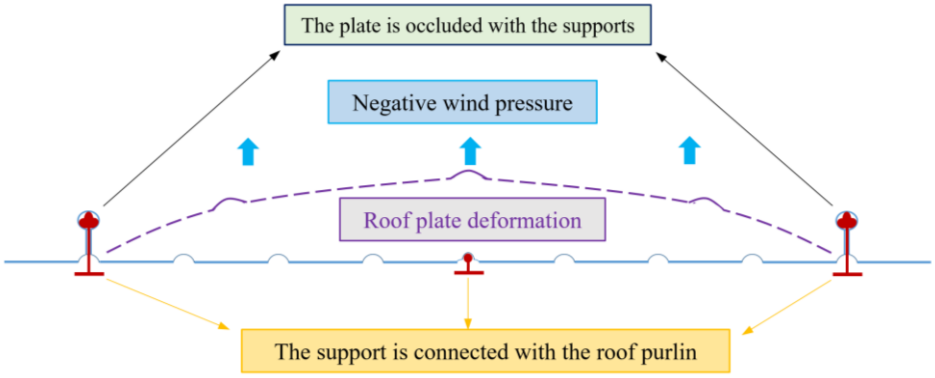

Fig. 17 The wind load transfer way of standing seam metal roofing plate

The examination of the wind resistance performance of metal roofing mainly includes the following key aspects. i) The main load of metal roof under wind load is divided into gas pressure, friction force, and suction force. The gas pressure mainly acts on the roof, the friction operates primarily on the contact surface between the roof and the wind load, and the suction predominantly affects the bottom plate of the roofing. When the wind speed is higher, the pressure and suction on the roof intensify, whereas friction remains relatively constant. Therefore, metal roofing primarily experiences a complex stress state of bending-compression and bending-torsion under a strong wind environment. ii) Various instabilities may manifest in metal roofs when exposed to intense wind conditions, encompassing local buckling, global buckling, and local shear failure. Notably, global buckling stands out as the most prevalent form of instability in such scenarios. iii) The wind resistance performance of metal roofing is affected by many factors, including roof form, material selection, structural design, connection and support system, and the overall roofing load.

6.2. Reinforcement measures of wind resistance

6.2.1. Wind resistance design principles

Under the action of wind loads, the structural surface will form negative wind pressure or trigger structural resonance, which will cause various metal roof damage phenomena. **Fig. 18** illustrates the typical wind resistance mechanism of metal roofing subjected to wind loads. The wind resistance design principles of metal roofing mainly include the following aspects.

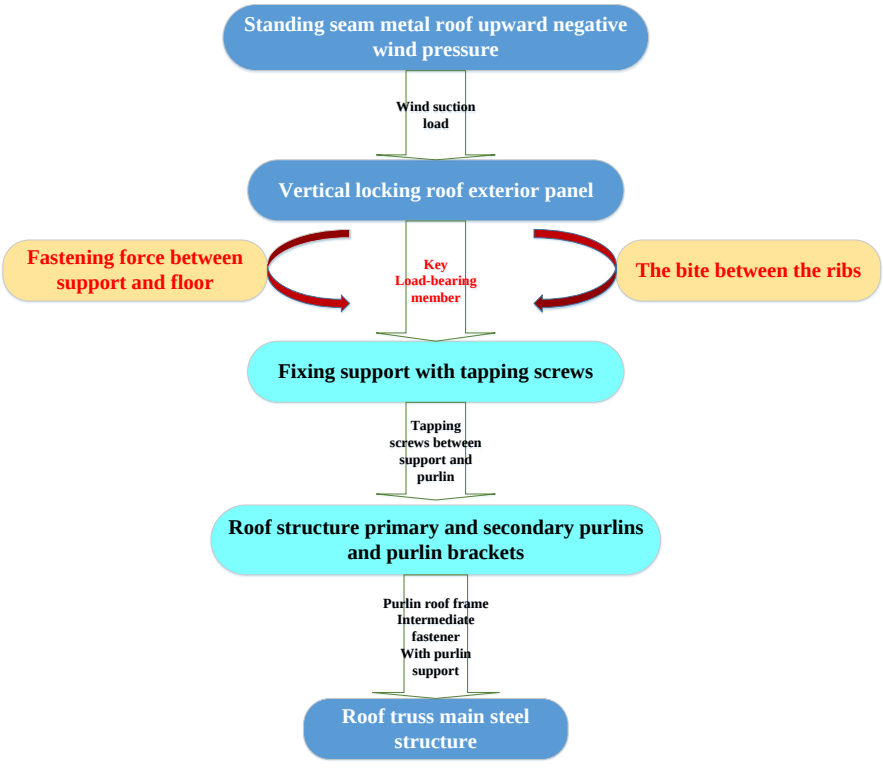

Fig. 18 Typical metal roofing wind resistance mechanism

i) Decreasing the roof load is the pivotal factor in improving the wind resistance of metal roofs. The main measures include optimizing the roof configuration, minimizing the roof weight, lowering roof height, and rationally implementing the roof drainage system.

ii) The improvement of wind resistance of metal roofing is inseparable from the strength and stability of the connection and support system. Specific measures include enhancing the connectivity of the connector, opting for the appropriate connection methods, and enhancing the support strength.

iii) It is very important to choose the appropriate material and construction to improve the wind resistance of metal roofs. Specific measures include the selection of metal materials with good quality and high performance and the design of reasonable support structures.

6.2.2. Windproof design and construction

The standing seam metal roof has also encountered wind-induced challenges in various settings such as airport terminals, large exhibition centers, and sports stadiums. For the prevailing standing seam metal roofing system, several researchers have proposed measures to improve and optimize wind resistance. It is appropriate to ensure key areas and take into account the general area; The strength of the roof plate and the actual strength of the biting part of the fixed support should be determined by the tests. Addressing engineering failure cases, checking calculations and the "short-plate effect" to enhance the strength of the occluding part of the metal roofing plate and the fixed support, as shown in Eq. (23) [52]. The extent of reinforcement between different areas of the roof slab and the occlusal parts of the fixed supports can be established by the experimental tests.

$$F = \min\{F_1, F_2, F_3, F_4\} \tag{23}$$

Where F is the bearing capacity of the weakest part of the roof system; F_1 is the ultimate strength of the lock joint at the support; F_2 is the ultimate bearing capacity of the lock joint without support. F_3 is the ultimate bearing capacity of the fixed support; F_4 is the ultimate bearing capacity of the connecting fasteners.

6.3. Wind resistance measures of this project

The wind tunnel tests are conducted by combining the basic wind pressure once in 100 years with the intricate roofing shape, obtaining the most unfavorable positive and negative wind pressure at each measuring joint in all wind direction angles. The distribution of wind pressure is analyzed, and the locations and areas of the edge region, corner region, and large area are divided. Calculations are performed for the main and secondary purlin sections, spacing, fastener connections, panels, fixtures, eaves, and ridges of each partition. Finally, a solid model is made based on detailed drawings, and dynamic wind resistance tests are carried out.

6.3.1. Structure design and material selection

Metal roofing is susceptible to wind damage in typhoon-prone areas, therefore, selecting high-strength metal roofing materials becomes imperative to ensure stability and load-bearing capacity during strong winds. Currently, the metal roofing plates mainly include: pressed steel plate, titanium zinc plate, aluminum magnesium manganese alloy, and copper plate. For the metal roofing project of XIEC, an aluminum-plated zinc steel plate is selected as the main external maintenance system for the roofing panel. Compared with other materials, aluminum-plated zinc roofing panels have unique advantages, as delineated in **Table 6**.

It is crucial to fully consider factors such as wind pressure, wind load, and wind resistance in the structural design of metal roofing. This project primarily adopted the double-layer metal roofing system, with the detailed structural layer presented in **Fig. 19**. There are reliable connections between the layers to ensure roofing safety under the wind load. To reinforce the connection between the metal roofing and its supports, fasteners, and connectors are strategically positioned on the supporting structure. The metal roofing panels are first connected to the lower fixed supports by bite lock, which in turn are connected between the tapping screws and purlins. Various joints in the roofing structure, including roof standard joints, main and secondary purlins, connection joints, ridge joints, drainage gutter joints, and fall prevention system joints, play a pivotal role. The design quality of these joints significantly contributes to determining the overall wind resistance of the roofing structure.

Table 6
Comparison of roofing panel materials

Roof panel type	Advantage	Limitation
Stainless steel plate roofing	It has excellent corrosion resistance, high strength, long service life, and unique architectural beauty.	Stainless steel plate prices are higher, so only important public construction will be used.
Aluminum magnesium manganese alloy plate	Form a dense oxide film, good anti-corrosion; Lightweight, strong plastic deformation ability, easy to bend molding.	The coefficient of thermal expansion is very high, so the roof plate must leave deformation space for the plate expansion, which also indirectly leads to the overall stiffness of the roof being low, and the wind resistance lacking.
Titanium zinc sheet roofing sheet	Natural passivation layer, no pollution; Corrosion resistance; With self-cleaning function, save operating costs; Good flexibility, convenient processing.	Titanium zinc plate is expensive, about 10-15 times that of aluminum magnesium manganese alloy roof plate. Although titanium zinc plate is favored by roof designers, it is not widely used in public buildings.
Copper roofing panel	With natural copper oxide passivation film, good protection ability; Good plasticity, easy to process; Flame retardant, and recycling advantages.	Due to the relatively high price of copper sheets, copper sheet roofing is rarely used in large public buildings in China.
Aluminized zinc roofing panel	Good flexibility and ductility; Strong corrosion resistance and heat resistance, and high thermal reflectivity, so it is widely used in China.	Once the aluminized zinc plate is cut, it will rust quickly when the cut edge is unprotected. Once cut, an anti-rust paint or zinc-rich paint is applied to protect the edge, which can extend the service life of the sheet.

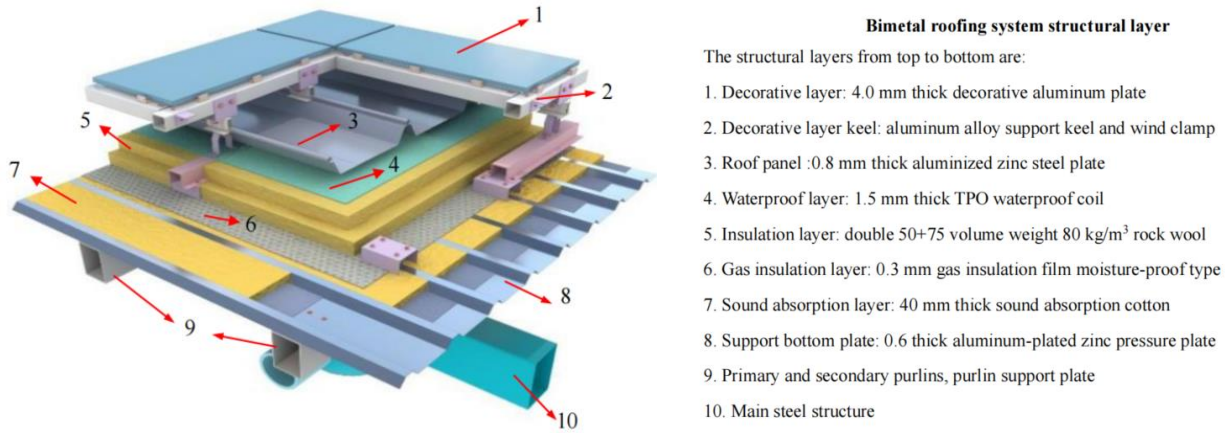

Fig. 19 Structural layers of bimetal roofing system

The wind resistance performance of metal roofs is an important measure to ensure the safety of roofing structures. The stainless steel continuous welding roof is preferred in areas with high wind-resistant requirements, and aluminum alloy standing seam metal roofing is avoided as far as possible. Structural strengthening measures should be taken in the special areas of the roof, such as the cornice and arch. This project has taken some strengthening measures to effectively address the aforementioned concerns. The laying of metal plates should pay attention to the perennial wind direction, and the lapping of plate ribs should be opposite to the wind direction. Securing the fixed support within the vulnerable wind-protected zone by aligning it along the longitudinal direction of the board. When installing galvanized steel fixed supports in the encrypted area, incorporate a hot-dip galvanized steel support to bolster the wind resistance of the eaves section. In the context of the aluminum-plated zinc standing seam metal roofing system, employ galvanized steel fixed supports for fixation. Subsequently, affix the roofing plate onto the support, and use an electric edge-locking machine to secure the plate rib onto the fixed seat. This method avoids penetrating the plate surface, averting stress concentration, and contributing to superior wind resistance.

6.3.2. Construction and transportation phase

This project encountered several challenges in the construction process, as shown in **Fig. 20**. An error in the spacing or angle of fixed seat installation, coupled with difficulties in operating the edge-locking machine on corner parts, led to incomplete roofing panels. These areas represent the most vulnerable zones against negative wind pressure, and once the wind is inserted, it is likely to be damaged by the wind. The structure is prone to overturning or being dislodged by wind load originating from the cornice. The substantial wind pressure at the eaves poses a risk during the installation of galvanized steel fixing seats. Insufficient strength in the screws may weaken the pulling force of the fixing seat, resulting in failure.

The structure configuration of the standing seam metal roof is inherently intricate, with the construction quality posing a substantial challenge. The overall quality of the construction process plays a pivotal role in determining the wind resistance and waterproof capacities of the roofing. During the construction phase of a metal roof, it is necessary to strictly control the angle and installation direction of its wind surface to avoid the phenomenon of opening and warping under the action of strong winds. The key technical processes integral to the construction phase encompass the following aspects.

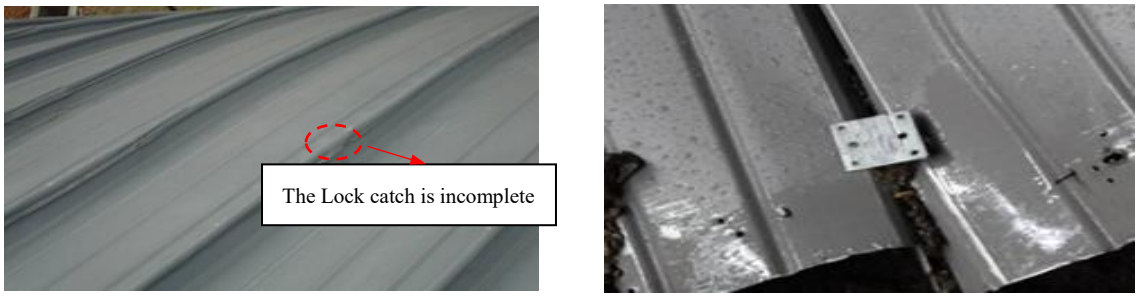

(a) The overlock is incomplete (b) The strength of the fixed seat is weakness

Fig. 20 The problems in the construction of roofing panels

6.3.2.1. Roofing plate processing and transportation

The transportation of metal roofing panels can be combined with ramps and tower cranes. The finished roof panels were transported to the middle of the roof along the upper ramp and installed from the midpoint towards both sides. Short roof plates, having undergone ground pressing and forming, are transferred to the roof using a welding square tube flatbed truck on the ground. The longer roof plates need to be transferred by two simultaneously to prevent excessive deflection and bending damage. After the roofing plate is transported to the roof, it is horizontally lifted to the installation site, as shown in **Fig. 21 (b)**.

(1) Due to the manual handling involved in the transportation of roof panels, considering that the roof panel is prone to deformation during the handling process. Therefore, the slope of the ramp for the upper board can't be too large, and it is controlled below 30 °. To further mitigate risks, roofing panels are strategically handled at intervals of 10 meters. Upon reaching the roof, the panels are uniformly arranged in the predetermined stacking location.

(2) Rigorous and effective protective measures are imperative throughout the production and vertical/horizontal transportation of the panels. This is crucial to guarantee the integrity of the roof panels, with any damaged panels strictly prohibited from being used in the project. The vertical transportation method involves a ropeway system and bench lifting, a combination chosen to safeguard the roofing panels from potential damage.

(3) Post-installation, the finished roofing panel must be protected. Walking on or subjecting it to impact from hard objects is strictly forbidden. The installed roof is not allowed to place heavy objects, especially metal materials.

(a) Roofing plate bending and arc processing (b) Roofing panel transport in place

Fig. 21 Schematic diagram of metal roofing plate processing and installation

6.3.2.2. Construction quality of purlin and support

The installation process for hot-dip galvanized steel purlins must adhere rigorously to the prevailing installation specifications for steel structures, ensuring that the welds of the purlins meet the Grade II standard. During the installation of purlins, utmost attention must be paid to prevent any secondary scratching of the hot-dip galvanized surface. Additionally, any purlins that incur scratches during installation must be meticulously addressed to prevent the installation of damaged purlins on the roof. Purlins are installed by the tower crane and car crane through a hook and multiple lifting, as shown in **Fig. 22 (a)**.

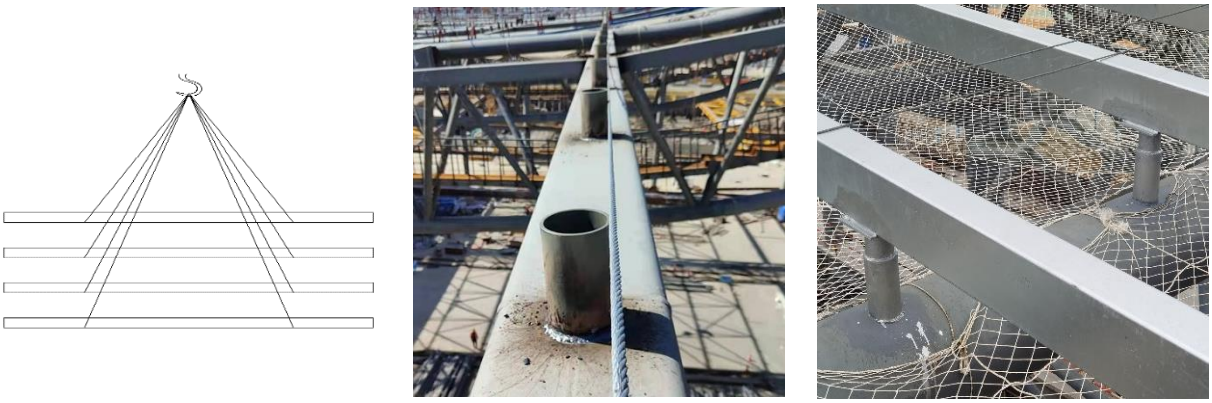

(a) Purlin hoisting (b) Support installation (c) Purlin installation

Fig. 22 Purlin and support installation diagram

Due to the upper purlin support is a second purlin, the second purlin is first used to pop out the control line on the main purlin along the slope of the roof according to the distance of the purlin. Subsequently, the support locations for the second purlin are marked on the main purlin using the positioning line. A hot-dip galvanized purlin steel plate support is welded onto the designated position. The primary purlin reinforcement zone is predominantly situated near the ridge and overhanging eaves, areas subjected to greater negative wind pressure. The primary purlins are distributed in the middle of the roof, which is bolted on the primary purlin bracket. The primary purlin in other positions is welded at one end and the other end is bolted, and the local area is welded at both ends. The overall arrangement direction of the main purlin is perpendicular to the direction of the steel structure truss, and the secondary purlin is filled during the arrangement. Whereas, the overall arrangement direction of the primary purlin in other positions is parallel.

6.3.2.3 Installation of pressed steel bottom plate

The bottom plate for the roofing is made of aluminum-zinc-plated perforated pressed steel, with a thickness of 0.6 mm and a galvanized surface. The yield strength is more than 250 MPa, tensile strength exceeds 330 MPa. Positioned above both the primary and secondary purlins, this steel bottom plate is affixed to the primary purlin using self-tapping nails at the installation trough. The orientation of the bottom plate is perpendicular to the direction of the secondary purlin, as illustrated in **Fig. 23**. The length of the bottom plate is determined by the spacing of the adjacent purlins, and the connection between the bottom plate is the lap joints fixed onto the primary purlin with special steel nail connections.

Fig. 23 Installation diagram of the base plate of metal roofing

The installation of the bottom plate starts from the edge line of the gable and spreads from one side to the other, the frame at the cornice of the gable is used as the reference line to determine the installation axis of the bottom plate. The installation of the roof bottom plate directly affects the performance of the whole roof. Therefore, it is imperative to conduct a thorough reassessment of the steel structure purlins and the elevations of key components already installed on the construction surface before installing the roofing plate. The bottom plate of the project is located under the secondary purlin, the additional primary purlin is placed on, which is reverse lifted construction through the hanging basket.

6.3.2.4. Mounting quality of the fixed support

The fixed support for aluminized zinc roof plates plays a pivotal role in transferring the wind load from the roof to the secondary purlin. The galvanized steel fixing base comprises both a galvanized steel base and galvanized steel stranding pieces, these components are integrated using M8 self-tapping and self-drilling screws to form a cohesive support structure. Due to the thermal expansion and contraction processes, the roof plate is allowed to freely slip, thus mitigating the risk of plate fracture resulting from improper installation. During the installation of the galvanized steel fixed base, it is imperative to first apply butyl tape and a modified asphalt gasket beneath the support. The installation of the support adopts two symmetrical self-tapping nails. A self-tapping screw is initially driven, followed by a corrective adjustment of the support to rectify any deviation. After the correction, insert the second screw and fix it, tighten the screws properly to avoid heavy or floating nails. **Table 7** lists the installation requirements for the support.

Table 7
Galvanized steel fixed base installation dimension deviation requirements

Description	Permissible error
Transverse angle	Deviation from roofing reference line <1°
longitudinal angel	Deviation from roofing reference line <1°
Longitudinal fixed seat height deviation	Less than 1/200 fixed seat spacing
Lateral fixed seat height deviation	≤3 mm
Longitudinal axis deviation	≤2 mm

(a) Drilling at fixed points (b) Roof panel locking

Fig. 24 Roofing panel fixing and locking edge process

6.3.2.5. The occlusal quality of the standing seam roofing plate

When securing the edges, the plates are arranged in the direction of the small lock edge line, with the larger lock edge overlapping the smaller one. Generally, the plate is installed from one end of the roof to the other end, as illustrated in **Fig. 24 (b)**. However, in certain unique circumstances, adjustments to the laying order of the plates may be necessary. A different panel installation sequence may be required when the roof pitch is perpendicular to the panel orientation.

After adjusting the position of the panel, install the foam seal under the end panel before locking the edge. It is essential that the side after locking remains uniformly continuous and smooth, devoid of any distortion or cracks. As the locking machine advances, particular attention must be given to ensuring that the lap edge joint within the 1-meter range at the front is tightly compressed. The crux of stitching quality lies in the forceful and tight joining of the overlapping edge during the stitching process.

6.3.2.6. Construction quality of key parts

An excessive error in the installation of the fixed seat, or difficulties in accessing corner parts where the locking machine cannot easily operate, can result in incomplete locking of the roof panel. These vulnerable sections are susceptible to negative wind pressure, leading to stress concentration when wind penetrates the roofing panel. Consequently, there is a heightened risk of the roofing panel being lifted during strong winds. To address this during roof construction, emphasis must be placed on enhancing wind resistance through the implementation of robust anti-typhoon emergency plans and temporary measures, including closing the side of the completed area in time, setting up three wind clips and wind rope in the eaves, trenches and so on.

To enhance the wind resistance of standing seam metal roofs, current reinforcement techniques mainly focus on the following aspects: Firstly, optimizing the joint between the roofing plate and support by utilizing locking angles with improved biting efficacy, with existing angles reaching up to 540°, thereby advancing wind resistance. Additionally, increasing the edge height is a widely employed method to improve wind resistance, which can increase the strength and stability of the edge. Augmenting the number of locking edges is another effective strategy, particularly for roofs with standing seam metal roofing. This approach enhances connection points between the metal roof and support structure, thereby boosting overall stability. The supporting structure at the locking edge is the key part of the wind resistance of metal roofing. By strengthening the supporting structure at the lock edge, the stability and strength of the lock edge can be enhanced. For example, the installation of transverse and longitudinal stiffeners at the locking edge can enhance the stability of the support structure. The use of high-strength bolts and reinforcing materials at the locking edge can increase the connection strength and stability of the locking edge, improving the wind resistance of the metal roof.

In the wind tunnel test of metal roofing, the findings of this study also have certain guiding significance for the development of design specifications and engineering practices, which are mainly reflected in the following aspects: Firstly, wind tunnel experiments can provide accurate wind pressure distribution and dynamic response data, which is crucial for evaluating the wind resistance performance of metal roofing under extreme weather conditions. These data can be used to revise existing design codes, ensuring they more closely align with actual wind loads and structural responses. Secondly, the experimental results contribute to optimizing the detailed design of the roof structure, such as strengthening the connecting parts of the roof panel, improving the drainage system, or adjusting the roof shape, to improve the stability and safety of the metal roofing structures. Finally, through comparison with theoretical models and practical engineering cases, the research results can provide a practical basis for the guidelines to ensure that the wind load design is more realistic and targeted.

7. Conclusions

In the current environment of frequent climate change and natural disasters, it is an important issue to improve the safety of large public buildings. Based on the metal roofing project of XIEC, this paper completed the wind tunnel test analyzed the experimental results, and obtained the standard wind load of the conference center envelope structure, the overall wind load of the roofing structure, and the contour line distribution results of the roofing systems under each wind direction angle under the action of maximum wind pressure. The analysis delved into the causes of wind-induced damage to metal roofs and explores common reinforcement methodologies. The following main conclusions can be drawn:

- A wind tunnel test platform was built to simulate the wind load conditions of large metal roofs under different wind speeds, which can simulate the airflow state under different wind speeds and the stress situation of metal roofs. For this wind tunnel test, the geomorphic index α=0.12, the physical height of the wind speed reference point H=132 m, and the basic wind pressure w_0 =0.95 kN/m^2 once in 100 years, the reference wind pressure can be obtained by calculation.
- The structure of the convention and exhibition center is complex, and the space shape is novel. Select typical joint 18953 for analysis, it is found that: i) the displacement of this joint is mainly in the z-direction, and the displacement in the x and y directions is almost zero; ii) In the z-direction displacement of this joint, all displacements are upward, and the displacements at 45° and 315° wind angles are the largest, indicating that the roofing structure under these two wind angles experiences greater wind suction near the position of this joint.
- Peak factor method and extreme value analysis were respectively used to calculate the standard wind load value of the roofing structure. In general, the results of the two methods are close to each other, and the extreme value analysis method can better predict the extreme value of negative wind pressure in the non-Gaussian region of wind pressure distribution. In this paper, the envelope of peak factor method and extreme value analysis method were used to give the standard value of the design wind load of the roofing structure.
- The average wind load and equivalent wind load of 2803 roofing upper joints in the z direction were obtained through FE calculation. It is found that the equivalent wind load and the average wind load in the z direction reach the positive maximum at 45° and 270°, and the overall wind vibration coefficient corresponding to the ultimate wind load is 1.65.
- The stress characteristics and failure modes of metal roofs in a strong wind environment were summarized, and the factors affecting the wind resistance of metal roofing were analyzed. Taking this project as an example, the reinforcement measures for the wind resistance design of metal roofing were proposed, including reducing the roof load, enhancing the wind connection and locking height, and reasonable selection of materials and structures. The possible measures to further improve the wind resistance performance of metal roofs were discussed.

The research on wind resistance performance of metal roofs has promoted the updating of roof structure design and wind protection standards to a certain extent, there are still some problems in the existing research, such as single experimental conditions and insufficient consideration factors. Therefore, future research should pay more attention to the comprehensive consideration of the interaction between wind load and roof system, strengthen the wind resistance performance test under multiple scenarios and conditions, and improve the

accuracy and practicability of wind resistance performance evaluation through field data feedback and model calibration.

Acknowledgements

The authors gratefully acknowledge the financial support provided by China Construction Fourth Engineering Division Corp., LTD, Xiamen 361000, China. Key Laboratory of New Technology for Construction of Cities in Mountain Area (Chongqing University) and Xiamen International Expo Center metal roofing innovation technology research team for the work reported in this paper.

References

[1] Lu Q.R, Li M.C, Zhang M.X, Min Q.L, Zhang Y.J, Liu X.D. Wind-resistance performance investigation of 360◦ vertical seam-locked roof system reinforced by sliding support and sandwich panel. Journal of Building Engineering, 2022; 45: 103689.

[2] Ou T, Wang D.Y, Xin Z.Y, Tan J, Wu C.Q, Guo Q.W, Zhang Y.S. Full-scale tests on the mechanical behaviour of a continuously welded stainless steel roof under wind excitation. Thin-Walled Structures, 2020; 150: 106680.

[3] Estephan J, Feng C.D, Chowdhury A.G, Chavez M, Baskaran A, Moravej M. Characterization of wind-induced pressure on membrane roofs based on full-scale wind tunnel testing. Engineering Structures, 2021; 235:112101.

[4] Ignatowicz R.L, Gierczak J. Increase in wind load during assembly causes collapse of the hall structure. Engineering Failure Analysis, 2020; 113: 104538.

[5] Baheru T, Development of test-based wind-driven rain intrusion model for hurricane-induced building interior and contents damage. FIU Electronic Theses and Dissertations, FIU, 2014.

[6] Baheru T, Chowdhury, A.G. Pinelli J.P. Estimation of wind-driven rain intrusion through building envelope defects and breaches during tropical cyclones. NatHazards Rev, 2014;16: 04014023.

[7] Darwish Y, ElGawady M. Finite element analysis of TPO membrane- retrofitted metal roof system subjected to wind loads. Structures, 2023; 50: 330-346.

[8] Tian M.L, Gao X.X, Zhang A.F, Han L.J, Xiao H.T. Study on the deformation failure mechanism and coupling support technology of soft rock roadways in strong wind oxidation zones. Engineering Failure Analysis, 2024;156: 107840.

[9] Tolera A.B, Estephan J, Chowdhury A.G, Zisis I, Sherman E, Kirby J. Wind loading on commercial roof edge metals: A full-scale experimental study. Journal of Building Engineering, 2023; 75:106910.

[10] Pieper L, Mahendran M. Numerical investigation and design of crest-fixed corrugated steel claddings under static wind uplift loading. Thin-Walled Structures, 2023; 182: 110270.

[11] Pawar S, Jugade H, Mukhopadhyay G. Investigation of corrosion of 55AlZn coated roof sheets in Al smelting plant. Engineering Failure Analysis, 2020;115:104691.

[12] Chen W.S, Hao H, Du H. Failure analysis of corrugated panel subjected to windborne debris impacts. Engineering Failure Analysis, 2014; 4: 229-249.

[13] Kopp G.A, Bank D. Use of the wind tunnel test method for obtaining design wind loads on roof-mounted solar arrays. Journal of Structural Engineering, 2012; 139: 284-287.

[14] Li R., Chowdhury A.G, Bitsuamlak G, Gurley K.R. Wind effects on roofs with high-profile tiles: experimental study. Journal of Architecture Engineering, 2014.

[15] Hadane A, Redford J.A, Gueguin M, Hafid F, Ghidaglia J.M. CFD wind tunnel investigation for wind loading on angle members in lattice tower structures. Journal of Wind Engineering & Industrial Aerodynamics, 2023; 236:105397.

[16] Wu B, Zhao H, Chen B, Yang Q.S. Comparison of wind-resistant capacities of standing seam roof systems under static uniform pressures and dynamic non-uniform wind pressures. Journal of Wind Engineering & Industrial Aerodynamics, 2023; 241:105552.

[17] Xia Y.C, Kopp G.A, Chen S.F. Failure mechanisms and load paths in a standing seam metal roof under extreme wind loads. Engineering Structures, 2023; 296: 116954.

[18] Baskaran B.A, Lei W. New design procedure for wind uplift resistance of architectural metal roofing systems. Journal of Architectural Engineering, 2006; 168-177.

[19] Schroter R.C. Air pressure testing of sheet metal roofing. NRCA Second International journal of Roofing Technology, 1985; 254-260.

[20] Xu Q.H, Wan T, Liu K. Optimal design of strengthening wind exposure resistance of vertical whipstitch mental roofing board. Engineering Mechanics, 2020;17-26. (in Chinese)

[21] Farquhar S, Kopp G.A, Surry D. Wind tunnel and uniform pressure tests of a standing seam metal roof model. Journal of Structural Engineering, 2005; 131: 650-659.

[22] Min Q.L, Li N, Zhang Y.J, Lu Q.R, Liu X.D. A novel wind resistance sliding support with large sliding displacement and high tensile strength for metal roof system. Engineering Structures, 2021; 243: 112670.

[23] Sinno R.R, Surry D, Fowler S, Ho T.C. Testing of metal roofing systems under simulated realistic wind loads. In: Proc 11th International Conference Wind Engineering, 2003;1065-1072.

[24] Li M, Yin X.Z, Zhang W, Fan F, Zhu Z.Q. Finite element analysis of wind-resistance performance of standing seam roof. Steel Structures, 2017; 72-76. (in Chinese)

[25] Liang Q.S, Yang Q.S, Liu M, Nie S.D, Wang Z, Liu R.L. An efficient method for evaluating the wind resistance performance of high-vertical standing seam metal cladding systems. Thin-Walled Structures, 2024; 205: 112433.

[26] Wang M.M, Ou T, Xin Z.Y, Wang D.Y, Zhang Y.S, Cui L. Experimental study on static temperature field effect on standing seam metal roof system. Structures, 2021; 31: 1-13.

[27] Simiu E, Miyata T. Design of buildings and bridges for wind: a practical guide for ASCE-7 standard users and designers of special structures. New Jersey: John Wiley & Sons, 2006.

[28] Peov A. Dynamic response and life prediction of steel structures under wind loading. Journal of Wind Engineering and Industrial Aerodynamics, 1998; 1057-1065.

[29] Suresh K. Prediction of wind-induced fatigue on claddings of low buildings. Computers and Structures, 2000;31-48.

[30] Myuran K, Mahendran M. New test and design methods for steel roof battens subject to fatigue pull-through failures. Thin-Walled Structures, 2017; 558-571.

[31] Myuran K, Mahendran M. Unified static-fatigue pull-through capacity equations for cold formed steel roof batten. Journal of Constructional Steel Research, 2017;135-148.

[32] Wu T, Sun Y, Cao Z.G, Zhang J. Wind vulnerability analysis of standing seam roof system considering fatigue damage. Thin-Walled Structures, 2023; 184: 110550.

[33] Sun Y, Wu T, Cao Z.G, Wind vulnerability analysis of standing seam roof system with consideration of multistage performance levels. Thin-Walled Structures, 2021;165(1):107942.

[34] Habte F, Mooneghi M.A, Chowdhury A.G. Full-scale testing to evaluate the performance of standing seam metal roofs under simulated wind loading. Engineering Structures, 2015;231-248.

[35] Holmes J.D. Wind Loading of Structures. CRCPress, Oakville, 2015.

[36] Luo Y.F, Xiao B.B, Liu S. Analysis of the load-bearing capacity of thin-walled steel roof panels and connections. Progress in Steel Building Structures, 2006; 1-4.

[37] Wijesooriya K, Mohotti D, Lee C.K, Mendis P. A technical review of computational fluid dynamics (CFD) applications on wind design of tall buildings and structures: Past, present and future. Journal of Building Engineering, 2023; 74:106828.

[38] Gaur N, Raj R. Aerodynamic mitigation by corner modification on square model under wind loads employing CFD and wind tunnel. Ain Shams Engineering Journal, 2022; 13: 101521.

[39] Shan X.F, Luo N, Sun K.Y, Hong T.Z, Lee Y.K, Lu W.Z. Coupling CFD and building energy modelling to optimize the operation of a large open office space for occupant comfort. Sustainable Cities and Society, 2020; 60:102257.

[40] BaskaranB.A, Ksk P. Optimizing the wind uplift resistance of mechanically attached roofing systems. Journal of Architectural Engineering, 2008; 65-75.

[41] Baskaran B.A, Molleti S, Booth R.J. Understanding air barriers in mechanically attached low slope roofing assemblies for wind uplift. Journal of ASTM International, 2006; 1-13.

[42] Azzi Z, Habte F, Vutukuru K.S, Chowdhury A.G, Moravej M. Effects of roof geometric details on aerodynamic performance of standing seam metal roofs. Engineering Structures, 2020; 225:111303.

[43] ASTM E1592. Standard test method for structural performance of sheet metal roof and siding systems by uniform static air pressure difference. West Conshohocken, PA: ASTM International, 2001.

[44] ANSI/FM Approvals 4474. Evaluating the simulated wind uplift resistance of roof assemblies using static positive and/or negative differential pressures. Norwood, MA: American National Standards Institute, 2004.

[45] UL 1897. Standard for uplift tests for roof covering systems. Cames, WA: Underwriters Laboratories, 2004.

[46] JGJ/T 338-2014, Standard for wind tunnel test of buildings and structures. China Architecture & Building Press, Beijing, 2014. (in Chinese)

[47] GB 50009-2012, Load code for the design of building structures. China Architecture & Building Press, Beijing, 2012. (in Chinese)

[48] Guan W.L. Study on wind-resistant capacity of typical metal roof panels. South China University of Technology, 2019. (In Chinese)

[49] Nan N. Research on the wind resistance performance of large-span metal roof and the bearing capacity of new connectors. Lanzhou University of Technology, 2021. (In Chinese).

[50] Mackiewicz M, Krentowski J.R, Knyziak P, Kowalski R. The influence of the fire temperature on the condition of steel roof structure. Engineering Failure Analysis, 2023;146:107080.

[51] Wang M.M, Ou T, Xin Z.Y, Wang D.Y, Zhang Y.S. Mechanical behavior and fatigue failure analysis of standing seam aluminum alloy roof system under temperature effect. Journal of Building Engineering, 2021; 44: 103001.

[52] Wang M.M, Xin Z.Y, Ge L.F, Wang D.Y, Zhang Y.S. Wind load design and test methods for standing seam metal roofing system. Building Structures, 2023; 1-8.

Advanced Steel Construction – Vol. 21 No. 1 (2025) 21–30
DOI:10.18057/IJASC.2025.21.1.2

INDUSTRIAL FLOOR CONSTRUCTION JOINT – EXPERIMENTAL AND NUMERICAL ANALYSIS

Isidora Jakovljević [1, *], Nina Gluhović [1], Milan Spremić [1] and Dušan Rajnović [2]

[1] *University of Belgrade, Faculty of Civil Engineering, Belgrade, Republic of Serbia*
[2] *Rinol d.o.o, Belgrade, Republic of Serbia*
** (Corresponding author: E-mail: isidora@imk.grf.bg.ac.rs)*

ABSTRACT

Transverse plane joints of concrete industrial ground floors are mostly constructed with various steel dowel geometry and arrangements to provide effective shear load transfer and prevent differential vertical movements. Several features of the construction joints can lead to the loss of the joint serviceability and resistance requirements, such as geometry misalignment, corrosion and joint lockup upon concrete casting. In addition, subsequent deterioration and damage of the exposed edges of the concrete surfaces have been indicated, influencing the serviceability of industrial floors and maintenance difficulties. Newly introduced construction joint geometry represents a functional solution of free-movement joints towards increasing construction efficiency and prevention of joint geometry misalignment and joint lockup upon concrete casting. The paper presents experimental tests and a comprehensive finite element analysis of the behaviour of the integral construction joint with steel dowels and embedded formwork. The experimental campaign covered testing of two orientations of the newly introduced construction joint to shear load. Numerical finite element analysis including the parametric study was performed to complement experimental results and reach a final stage of joint efficiency.

ARTICLE HISTORY

Received: 30 April 2024
Revised: 20 November 2024
Accepted: 30 November 2024

KEYWORDS

Steel dowel;
Free-movement joint;
Concrete ground floor;
Finite element method;
Shear resistance;
Dowel design analysis

1. Introduction

Transversal construction joints, designed to relieve longitudinal stresses due to volumetric changes in large concrete panels (surfaces), can be generally classified into two groups: construction joints for concrete pavements of highways and airports, and construction joints for concrete industrial ground floors and exterior pavements. Within these two main groups, various geometries of construction joints have been designed and examined, considering the differences in level and frequency of applied load and serviceability requirements or other structural issues that directly affect the safe and efficient use of concrete pavements and floors. Nevertheless, construction joints must fulfil the main requirements: to maintain horizontal movements of the concrete slab panels due to expansion and contraction and to transfer vertical loads between adjoining slabs [1]. The demand for construction joint application in large concrete panels originates also from interrupted construction activities during concrete casting [2].

Dowels are the most common form of construction joints which are used to provide smooth transition between adjoining concrete slab panels and to prevent cracking due to volumetric phenomena such as expansion and shrinkage, but also warping and curling caused by temperature and moisture gradients across the depth of the concrete slab [3]. Steel dowels (steel bars or plate dowels) are the most often used type of construction joints. Epoxy coatings for steel dowels are usually applied to prevent corrosion susceptibility. However, it has been reported that corrosion remains still a potential issue that affects the resistance and serviceability requirements [4] since the epoxy coating is susceptible to damage during the concrete casting and service life of the pavement [3]. Despite the reduction of dowel surface due to corrosion and its direct influence on joint resistance, corrosion also results in joint lockup. Construction joint lockup leads to the prevention of lateral movement of concrete slab and flexibility of construction joint, therefore mislaying the main function and consequently resulting in spalling, joint faulting and mid-span cracking [4].

Joint lockup and distress of the construction joint can also be influenced by misalignment of the joint geometry upon the concrete casting [4]. Misalignments of the steel dowel can be classified into two main groups: translation which represents movement of the constriction joint in horizontal, vertical or longitudinal direction and therefore offset from the concrete central plane and rotational misalignment of the joint which is the result of the joint tilting [1]. Zuzulova et al. [5] reported in their investigation that vertical tilt (rotational misalignment) of dowel bars results in high concrete tensile stresses around the dowel. Laboratory tests pointed to the higher tensile stresses for traditionally used 25 mm diameter dowels in comparison to the 30 and 40 mm dowels diameter and therefore suggest the increase of dowels diameter to 30 mm in highways. Experimental tests and finite element analysis of the steel and Glass Fibre Reinforced Polymer (GFRP) dowel bars' performance when they are installed with different geometry misalignments are in detail presented in the work of Al-Humeidawi and Mandal [1], [4]. Also, the aforementioned investigation highlights the influence of non-uniform misalignment of the dowels over the transverse joint length on the joint lockup and therefore achieved pull-out load for the joint opening during the tests. The same investigation also resulted in comparable characteristics of 38 mm GFRP dowel diameter with 25 mm epoxy-coated steel dower bar considering dowel looseness and relative deflection of the construction joint. Also, a substantial reduction in pull-out load for the joint opening during the investigation was achieved using GFRP dowel bars [4].

The GFRP and stainless steel dowel bars can be a suitable alternative to the mostly used epoxy-coated steel dowel bars considering corrosion susceptibility and were in detail investigated in the previous period. Dowels in construction joints often fail due to excessive bearing stress in the concrete surrounding the dowel resulting the cracks in concrete [6], since it is the principal mechanism in load transfer. Fasil et al. [3] found out that GFRP dowel bars fail due to the shear in the transverse direction considering the low shear capacity and high tensile strength of the embedded glass fibers. According to Vijay et al. [7] the stiffness mismatch between steel dowel and concrete localises the load transfer region at a higher level and results in concrete cracking near the steel dowel in comparison to the application of dowels with lower material stiffness. GFRP dowel bars have a lower elastic modulus in comparison to the steel ones and therefore should be applied with 20–30% larger diameter or in smaller distances across the transversal joint length to achieve comparable behaviour considering resistance, deflections and concrete bearing stresses in case of heavy loads [3]. However, for most of the concrete industrial ground floors, the application of GFRP dowel bars with smaller diameters is achievable for low frequency of heavy loads. Despite the higher costs of the GFRP dowels (approximately 50%), the long-term maintenance costs are less in comparison to the steel dowels [2].

According to ACI 302.1R-04 [8], concrete ground slabs continue to shrink for years, while the most significant volumetric change takes place within the first 60 to 90 days and continues through the first year till the fourth year upon concrete casting. Opening of the joint is a result of fulfilled service requirements of the construction joint but also can affect the serviceability requirements and safe and efficient use of the concrete pavements and floors. Maintenance of the construction joints represents a specific aspect of the overall inspection and maintenance of the concrete surfaces (floors). Available design guides for construction joints, ACI 302.1R-04 [8] and Technical Report 34 [9], propose an application of different types of joint sealants or low viscosity fillers, during the lifetime of the applied construction joint to balance between the ability to achieve joint opening, but also to prevent deterioration and damage of the exposed edges of the concrete surfaces.

However, 3D finite element analyses of steel and GFRP dowel bars give a wider insight into the behaviour of the construction joints and have been reported in many works [10], [11], [12], [13], [14]. Together with experimental tests or real environment monitoring of construction joints, numerical 3D analyses of the previous period resulted in findings which were implemented in

technical reports and design procedures. Certain directions for the design of construction joints including recommended dowel size and spacing, depending on the concrete slab depth, are provided in the American Concrete Institute Guide for Concrete Floor and Slab Construction ACI 302.1R-04 [8]. Technical Report 34 [9] published by The Concrete Society, UK, prescribes analytical expressions for obtaining design resistance of joints with round and plate dowels, and defines the classification of joints according to the movement they allow and the method by which they are formed. Therefore, construction joints are classified as free-movement joints, restrained-movement joints, tied joints and isolation joints. Free-movement joints, which are the main focus of the forthcoming investigation through experimental and numerical investigation, should be applied between the floor ground slab and adjoining such as external pavements and dock leveller or machine base. This type of joint has the potential to open wider than restrained-movement joints, without the application of reinforcement across the joint and therefore dowels or other mechanisms should provide load transfer. Construction joints should be designed to reduce vertical movement to the minimum.

Here presented previous works are mostly focused on the behaviour of various dowels as construction joint components. Limited laboratory testing on the resistance and response of the overall construction joints with embedded formworks as integral solutions for industrial floors is indicated. In the current study, experimental testing and 3D finite element analysis of the free-movement construction joint for concrete industrial ground floors are presented. The study took into account the aforementioned features of the construction joints which lead to loss of the joint serviceability and resistance requirements. Therefore, a new type of free-movement construction joint was investigated, through several aspects of higher construction accuracy of the joint geometry, lower misalignments of steel dowels and highly reduced potential in joint lockup considering well-integrated design and construction process. Towards more functional joint geometry, a numerical parametric study was performed to complement experimental results and reach a final stage of joint efficiency.

2. Experimental programme

2.1. Construction joint geometry

The geometry of the newly introduced construction joint is given in Fig. 1. Several parts of the free-movement construction joint were designed and assigned individually or simultaneously with other parts to improve the geometry during construction interruptions, prevent joint lockup, reduce vertical deformations and enable efficient load transfer. The presented construction joint, which is a subject of further experimental and numerical analysis, can be installed in industrial floors as an integral structural solution.

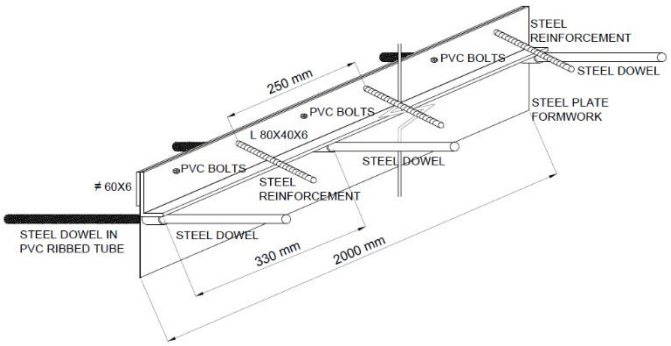

Fig. 1 Construction joint geometry

Three main constructive parts of the analysed construction joint, given in Fig. 1, are (i) steel plate of 60 mm height and 6 mm thickness, (ii) steel hot-rolled angle profile L 80 x 40 x 6 mm, and (iii) steel dowel of 22 mm diameter and overall length through construction joint of 500 mm. Among those three main constructive parts, additional parts of the construction joint are (a) PVC ribbed tube, (b) steel plate formwork of 1–2 mm thickness, (c) 10 mm diameter steel reinforcement bars welded to the 60 mm steel plate and angle profile, (d) steel tube leader of 26 mm outside diameter and 4 mm thickness, and (e) PVC bolts. Steel dowels are positioned on 330 mm spacing over the length of the construction joint, while reinforcement bars are welded at a 250 mm distance (Fig. 1). Steel dowels are placed in the middle of the height of the construction joint.

Described construction joint parts carrying a specific function should provide following: a) steel plate of dimensions of 60 x 6 mm together with steel plate of 1–2 mm thickness represent integral formwork for interrupted construction activities during concrete casting; b) steel angle profile enables sufficient stiffness of formwork to maintain initial geometry of the joint during concrete casting and therefore providing main free-movement characteristics of the joint; c) PVC ribbed tube wraps the steel dowel at the half length of the construction joint achieving in certain amount additional anti-corrosion protection, providing free movement of the steel dowel inside construction joint and preventing the joint lockup; d) PVC bolts supply the joint with integral geometry, preventing the separation of the steel plate and angle profile during installation and concrete casting, but also high longitudinal flexibility for undemanding opening of the construction joint due to volumetric changes, e) steel tube leader positioned on the side of the angle profile provides bearing surface to the steel dowels in order to minimize vertical and horizontal misalignments of the steel dowels; f) steel reinforcement prevents deterioration and damage of the exposed edges of the concrete surfaces and provides additional anchoring of steel formwork and angle profile in concrete slab on both sides.

2.2. Test set-up and loading protocol

The geometry of the specimens with the new construction joint is given in Fig. 2. Two orientations of the construction joint within test series R1 and R2 were investigated through experimental tests and 3D finite element analysis. Three specimens were tested for both test series, six specimens overall.

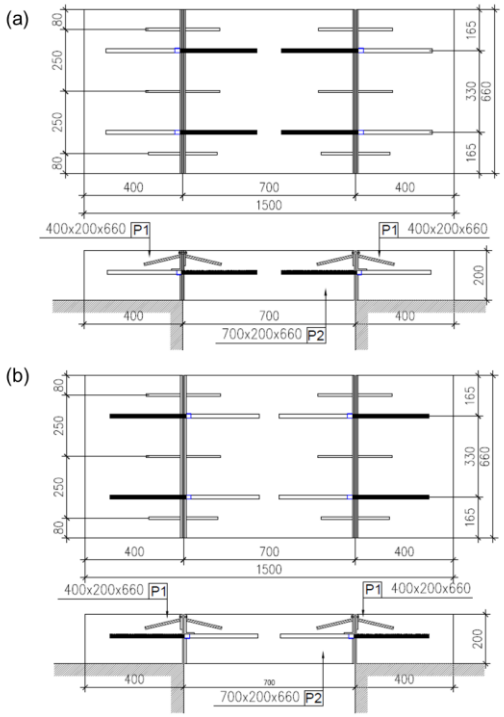

Fig. 2 Geometry of the specimens: (a) R1 series, (b) R2 series

Specimens were designed and constructed as double shear specimens with two side slabs and one middle (loaded) slab which were connected with construction joints. The overall dimensions of the specimens were 1500 x 660 mm, with 400 mm width of side slabs, 700 mm width of the middle slab and 200 mm depth of each slab. Construction joint within tests series R1 was installed with angle profile and steel dowel placed in the side slabs, i.e. steel dowel with PVC ribbed tube and 60 x 6 mm steel plate were positioned in the middle (loaded) slab (Fig. 2a). The opposite direction was adopted for test series R2, therefore angle profile and steel dowel were positioned in the middle (loaded) slab (Fig. 2b). The overall geometry of the specimens was in detail measured after the installation, showing the maximum misalignment of 3% in the vertical position of steel dowels in comparison to the middle plain of the concrete slab. Two layers of Q355 reinforcement mesh of 8 mm diameter were positioned at the bottom layer of the middle slab to prevent bending slab failure before the resistance of the construction joint is achieved. To analyse the resistance and overall behaviour of the construction joint in the most unfavourable conditions, when the joint has achieved the expected opening in industrial ground floors of approximately 10 mm, the polystyrene foam sheet was installed between 60 x 6 mm steel plate and angle profile.

Double shear tests were performed through the application of the linear vertical load in the middle width of the loaded slab through a stiff hot-rolled steel

profile with adequate flange width, not affecting the failure region of the concrete close to the construction joint, but accomplishing uniform and symmetrical loading of both joints. Stiff supports were provided at the end of the side slabs to prevent horizontal movement of the slabs or their rotation (Fig. 3). Vertical movement at the position of load application was monitored with LVDTs of the hydraulic testing machine, but also with two additional LVDTs, labelled as P1 and P2 in Fig. 3a. Relative vertical movement between two slabs at the position of the construction joints was measured with four LVDTs (V1–V4), symmetrically placed considering the load position and overall geometry of the specimens. Additionally, vertical movement was controlled at the position of the support of the side slabs with two LVDTs (O1 and O2) to monitor the efficiency of the support structure.

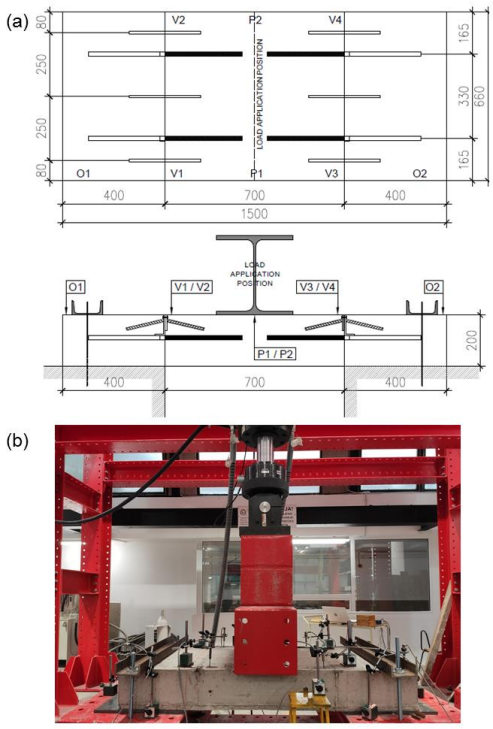

Fig. 3 Test set-up: (a) measuring positions, (b) specimen during testing

A hydraulic testing machine with a capacity of 300 kN was used for specimen testing. Specimens were tested through two phases. Within the first phase, cyclic loading was applied through three cycles with load in the range from 5 kN to 20 kN, with 0.2 kN/s. Upon reaching the 20 kN of vertical load, the loading of the specimen was maintained constant for 40 s and consequently unloaded with the same load rate of 0.2 kN/s until 5 kN. The first phase of the specimen testing was performed within 10 min, followed by the second phase of loading until failure. The load of the second testing phase was introduced as displacement controlled with a loading rate of 0.015 mm/s, therefore failure was not achieved within 15 min of the second loading phase [15]. The testing continued until the load dropped by 20% of the ultimate load.

2.3. Material properties

Alongside the main experimental testing, material properties of concrete and steel components of construction joints were obtained through standardised testing procedures. Concrete compressive strength was determined by conducting tests on concrete cubes 150 x 150 x 150 mm. Prisms 120 x 120 x 360 mm and cylinders Ø150 x 150 mm were used to obtain concrete flexural and splitting tensile strength, respectively. The mean and characteristic values of concrete strength on the day of the testing of specimens' series R1 and R2 are provided in Table 1.

Table 1
Material properties of concrete

	Compressive strength $f_{c,cube}$	Flexural strength $f_{ct,fl}$	Splitting tensile strength $f_{ct,sp}$
Mean value [MPa]	59.4	3.83	4.15
CoV [%]	3.01	1.39	10.23
Characteristic [MPa]	54.7	3.65	2.72

Mechanical properties of steel dowel, angle profile and 60 x 6 mm steel plate, as the main constructive elements of the construction joint, were determined from coupon tensile tests according to the ISO 6892-1 [16]. The values of steel yield and tensile strength, as well as strain at ultimate strength and fracture strain, are summarized in Table 2.

Table 2
Material properties of steel components of the construction joint

Steel component	Yield strength			Ultimate strength			Strain at ultimate strength	Strain at fracture
	Mean f_y [MPa]	CoV [%]	Charact. f_{yk} [MPa]	Mean f_u [MPa]	CoV [%]	Charact. f_{uk} [MPa]	Mean ε_u [%]	Mean ε_f [%]
Steel dowel	333.4	1.36	318.0	458.8	0.02	458.4	20.39	36.79
Angle profile L 80 x 40 x 6 mm	316.1	3.96	273.9	458.4	0.34	453.2	20.28	35.50
Steel plate 60 x 6 mm	343.9	/	/	482.1	/	/	19.08	34.30

Table 3
Evaluation of construction joint resistance and deformation

Specimen	Ultimate load F_{max} [kN]	Vertical displacement		Stiffness $k_{70\%}$ [kN/mm]*
		at 70% of the ultimate load $V_{70\%}$ [mm]	at the ultimate load V_{ULT} [mm]	
R1-1	168.8	2.59	3.58	10.17
R1-2	165.7	2.59	4.81	11.05
R1-3	199.4	2.78	3.19	12.55
Mean value, m_x	177.95	2.65	3.86	11.26
Characteristic fractile factor, k_n	3.37			
St. deviation, s	18.61			
Characteristic value, R_k	115.25			
R2-1	143.1	2.61	3.93	9.58
R2-2	121.1	1.21	2.28	17.52
R2-3	144.2	2.63	3.89	9.59
Mean value, m_x	136.15	2.15	3.37	12.23
Characteristic fractile factor, k_n	3.37			
St. deviation, s	13.07			
Characteristic value, R_k	92.11			

*obtained per one steel dowel at 70% of the ultimate load

2.4. Experimental results

Results of the experimental analysis are given in Fig. 4, for two analysed test series R1 and R2, respectively, as the applied load in function of the vertical displacement at the position of the construction joint measured with LVDTs with designation V1–V4. In addition, the results of the tests are given in Table 3 through the resistance of the construction joint, vertical displacement for load corresponding to 70% of ultimate load, vertical displacement for ultimate load and the stiffness of the construction joint, together with statistical evaluation of the results according to the EN 1990 – Annex D [17].

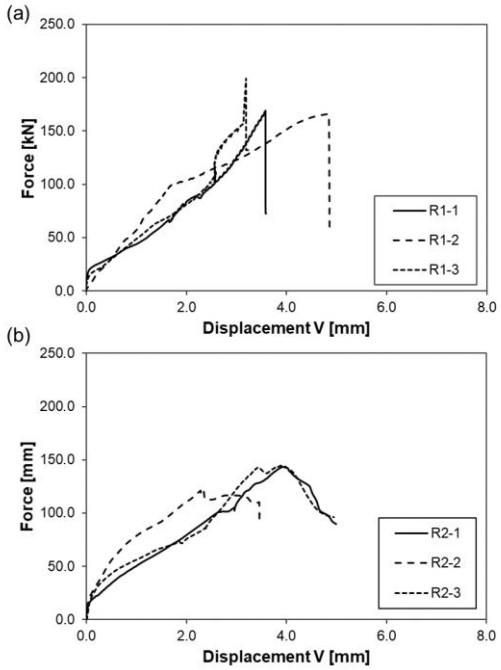

Fig. 4 Experimental test results – force-displacement at joint: (a) R1 series, (b) R2 series

According to the test results gained from two test series, approximately 31% higher resistance was obtained for test series R1 (177.95 kN) than for test series R2 (136.15 kN) when the resistance mean values of the two series are compared. The characteristic resistance of test series R1 determined according to the EN 1990 – Annex D [17] is approximately 25% higher in comparison to the test series R2.

Moreover, the different performance of the construction joint within the two test series is evident when comparing the construction joint post-ultimate response, described through force-displacement curves in Fig. 4. All specimens of test series R1 are characterized by a sudden decrease of the resistance upon the maximum force is reached, while a much slower decrease of the resistance is achieved for test series R2, indicating potentially different failure modes for the two test series.

Evaluation of the obtained deformation of the construction joint is analysed through measurements of the V1–V4 LVDTs, at the position of the construction joint. The mean value of the vertical displacement for the loading level corresponding to 70% of the ultimate load for test series R1 is 3.86 mm, which is to some extent increased in comparison to the 3.37 mm for test series R2. The mean value of the analysed stiffness for test series R1 and R2 are 11.26 kN/mm and 12.23 kN/mm, respectively, indicating relatively uniform behaviour of both test series considering the stiffness per one steel dowel obtained for 70% of the ultimate load. Larger vertical displacement at the ultimate load for test series R1 follows the results obtained for the load corresponding to 70% of the ultimate load. The mean value of vertical displacement for ultimate load is 2.65 mm for test series R1 and 2.15 mm for test series R2. This is approximately 23% higher vertical displacement for test series R1 in comparison to series R2, corresponding to approximately 31% higher resistance.

For all tested specimens within two test series, concrete failure close to the construction joint in the middle (loaded) slab is achieved. Fig. 5 represents the vertical surface of the middle slab when the maximum load is reached. Although diagonal cracks occurred in all tested specimens in both vertical surfaces of the middle slab, they do not represent the governing failure mode of the construction joint, which is in more detail described through numerical analysis.

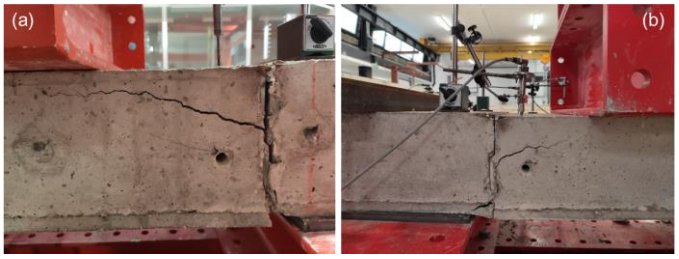

Fig. 5 Cracks on the middle slab – vertical surface of the test specimens: (a) R1 series, (b) R2 series

Upon the testing, construction joints were relatively simply disassembled (Fig. 6), highlighting the high-performance characteristics of the free-movement joint. Significant deformation of the construction joint upon the testing was not observed. Embedded steel formwork remained unaffected, while steel dowels were subjected to certain, but not distinct deformation during the testing procedure, according to Fig. 6.

Fig. 6 Construction joint upon the testing

The presented results demonstrate the straightforward influence of the construction joint orientation on the behaviour of the construction joint with particular emphasis on shear resistance and post-ultimate response. Specimens within test series R1, where the angle profile and steel dowels of the construction joint are placed in side slabs of double-shear tests, obtained higher resistance in comparison to the opposite orientation of the construction joint. Specimens within test series R2, where the angle profile and steel dowels of the construction joint are positioned in the middle (loaded) slab obtained more ductile behaviour in comparison to the test series R1.

3. Finite element numerical analysis

3.1. Development of finite element models

Numerical models were developed to simulate the experimental testing, evaluate specimen behaviour and failure modes, and perform further parametric analysis. 3D models were developed in finite element software Abaqus [18], performing the geometrical and material nonlinear analysis in the Dynamic Explicit solver.

3.1.1. Model geometry

According to the experimental programme, two 3D finite element models were created representing the test series R1 and R2, with the opposite orientations of the construction joint. Numerical models simulated the double shear test conditions, with two side concrete slabs connected to the middle concrete slab through the construction joint. The symmetry of tested specimens was exploited by modelling a quarter of the specimen and applying appropriate double vertical symmetry conditions, as illustrated in Fig. 7a. All relevant components of the construction joint were modelled, including round dowels, steel plate and angle profile, reinforcement bars for plate and angle anchoring, PVC ribbed tubes and steel plate 1–2 mm thickness with steel tube leader. Moreover, the base plate for bearing slabs was created, as well as the bottom reinforcement mesh in the middle slab. The components of the numerical model were solid parts, except for the reinforcement mesh and plate of 1–2 mm thickness, which were modelled as a truss and shell, respectively.

3.1.2. Boundary conditions, interactions and loading

Vertical loading was applied through the reference point RP1 on the middle slab top surface, whereas fully fixed boundary conditions were added to the reference point RP2 on the bottom surface of the base plate, as presented in Fig. 7a. Reference points were constrained to the nodes on the corresponding surface, accounting for the width of the loaded area. Welded connection between

components of the construction joint was simulated using the tie constraint. Reinforcement mesh was connected to the concrete slab by the embedded constraint. Contacts between other parts were simulated through "hard" contact in the normal direction and friction contact in the tangential direction. Values on friction coefficients were assigned as: 0.45 for contacts between concrete and steel or plastic parts embedded in concrete, as well as for the contact between the side slab and the supporting plate, 0.30 for the contact between dowel and plastic sleeve, and 0.20 for the contact between dowel and steel tube.

The vertical loading was applied through the smooth step function as a displacement-controlled. The total duration of the simulation was set to 1000 s with the mass scaling time increment of 0.005 s.

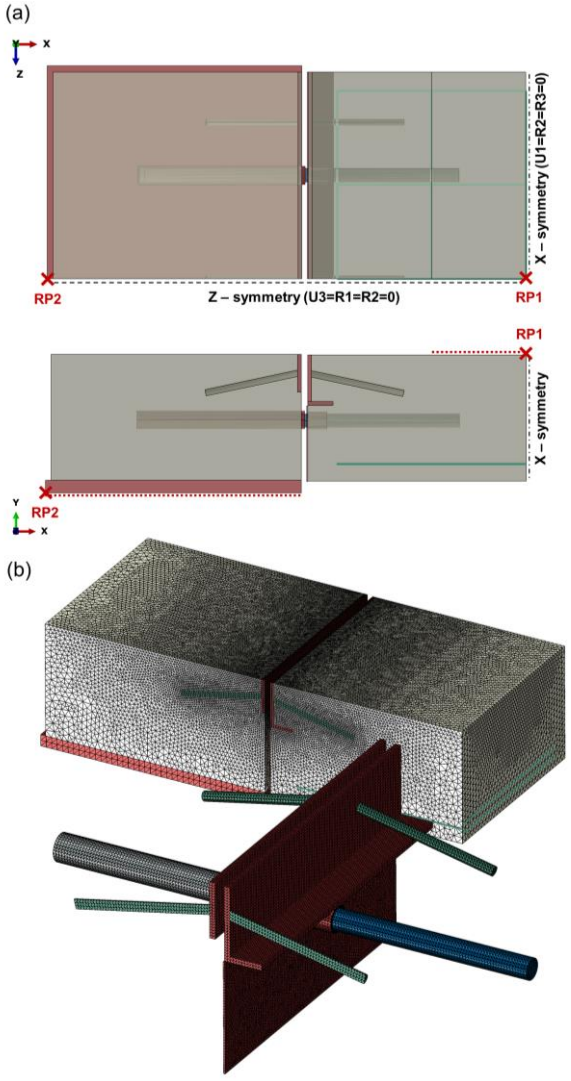

Fig. 7 Model R2: (a) Model geometry and boundary conditions, (b) Finite element mesh

3.1.3. Finite element mesh

Due to the complex geometry of the developed model, tetrahedral finite elements C3D10M were selected for meshing solid parts. Similarly, S3 elements were used for meshing shell parts and T3D2 elements were used for truss parts. The adopted mesh size resulted from the convergence analysis conducted to optimize the computing time while providing accurate model behaviour. Finite element size was varied throughout the model, applying the smallest size elements of 3 mm to steel dowels and other components of the construction joint. The mesh size was then gradually increased throughout the concrete slabs in the range from 3 mm at the construction joint to 10 mm at the opposite slab edges, according to Fig. 7b.

3.1.4. Material models

Material behaviour was assigned to the numerical model according to the performed testing of steel coupons and concrete cubes.

Elastic properties of steel were defined through the modulus of elasticity of 210 GPa and Poisson's ratio of 0.3. The plastic response of the steel dowel, angle profile and steel plate was modelled through the appropriate true stress-strain curves based on the conducted experimental tensile tests. As reinforcement bars were not experimentally tested, their response was modelled according to EN 1992-1 [19] as elastic-perfectly plastic with a yield strength of 500 MPa.

The behaviour of the plastic sleeve was simulated by assigning the modulus of elasticity of 1 GPa, Poisson's ratio of 0.2, and perfect plastic response with a yield strength of 50 MPa.

Concrete behaviour was described using the Concrete Damage Plasticity model. Concrete response in the elastic domain was defined through the modulus of elasticity of 35.11 MPa and Poisson's ratio of 0.2. The plasticity parameters were set following the recommended values in the Abaqus user manual [18]: flow potential eccentricity of 0.1, the ratio of equibiaxial-to-uniaxial compressive strength of 1.16, and a parameter K of 0.67. The dilation angle was set to the value of 30°, according to Lubliner et al. [20].

The stress-strain relation for describing concrete behaviour to uniaxial compression was adopted according to the model proposed by Pavlović et al. [21], which demonstrated good accuracy in simulating the steel-concrete shear connections accomplished with various types of steel connectors [22–26]. For strains up to ε_{cu1} (between points A and D in Fig. 8a), the stress-strain relation is described through the expression provided in EN 1992-1-1 [19]:

$$\sigma_c(\varepsilon_c) = f_{cm}\frac{k\cdot\eta - \eta^2}{1 + (k-2)\eta},\ \varepsilon_c \le \varepsilon_{cu1} \tag{1}$$

where:

$$\eta = \frac{\varepsilon_c}{\varepsilon_{c1}} \tag{2}$$

$$k = 1.05\,\varepsilon_{c1}\frac{E_{cm}}{f_{cm}} \tag{3}$$

ε_{c1} is a compressive strain in the concrete at the maximum stress fcm,
$\varepsilon_{cu1} = \varepsilon_{cuD}$ is the ultimate compressive strain of concrete.

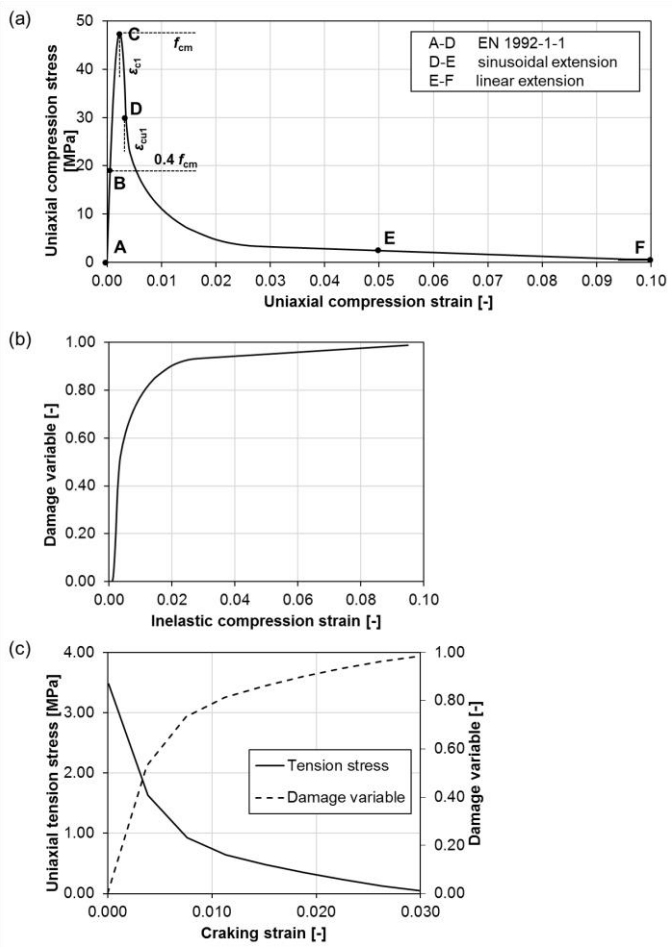

Fig. 8 (a) Concrete stress-strain relation for compression, (b) Concrete damage in compression, (c) Concrete behaviour in tension

For strains beyond ε_{cu1}, the stress-strain curve is based on the sinusoidal (for strains smaller than ε_{cuE}, between points D and E in Fig. 8a) and linear extension (for strains larger than ε_{cuE}, between points E and F in Fig. 8a):

$$\sigma_c(\varepsilon_c) = \begin{cases} f_{cm}\left[\frac{1}{\beta} - \frac{\sin(\mu^{\alpha_{tD}}\cdot\alpha_{tE}\,\pi/2)}{\beta\cdot\sin(\alpha_{tE}\,\pi/2)} + \frac{\mu}{\alpha}\right], \varepsilon_{cuD} < \varepsilon_c \le \varepsilon_{cuE} \\ \left[f_{cuE}(\varepsilon_{cuF} - \varepsilon_c) + f_{cuF}(\varepsilon_c - \varepsilon_{cuE})\right]/(\varepsilon_{cuF} - \varepsilon_{cuE}), \varepsilon_c > \varepsilon_{cuE} \end{cases} \quad (4)$$

where:

$$\mu = \frac{\varepsilon_c - \varepsilon_{cuD}}{\varepsilon_{cuE} - \varepsilon_{cuD}} \quad (5)$$

$$\beta = \frac{f_{cm}}{f_{cuD}} \quad (6)$$

$$\alpha = \frac{f_{cm}}{f_{cuE}} = 15 \quad (7)$$

$\alpha_{tD} = 0.50$ and $\alpha_{tE} = 0.60$ are parameters of the sinusoidal function shape,
$f_{cuE} = f_{cm}/\alpha$ and $f_{cuF} = 0.40$ MPa are compressive stresses at the points E and F, presented in Fig. 8a,
ε_{cuD}, ε_{cuE} =0.05 and ε_{cuF} = 0.20 are compressive strains at points D, E and F, respectively, presented in Fig. 8a.

Damage evolution for compression was defined through damage variable D_c, presented in Eq. (8) and illustrated in Fig. 8b:

$$D_c = 1 - \frac{f_{cm}}{\sigma_c} \quad (8)$$

The stress-strain relation for concrete subjected to uniaxial tension was derived from the following relation between the stress and crack opening w [27,28]:

$$\sigma_t(w) = f_{ctm}\left[g(w) - \left(\frac{w}{w_c}\right)g(w_c)\right] \quad (9)$$

where:
f_{ctm} is the mean value of the concrete tensile strength,

$$g(w) = \left[1 + \left(\frac{3w}{w_c}\right)^3\right]e^{-\frac{6.93w}{w_c}} \quad (10)$$

w_c is the critical value of the crack opening at which tensile stress cannot be transferred;

$$w_c = 5.14\frac{G_F}{f_{ctm}} \quad (11)$$

G_F is the fracture energy, which was adopted as the function of the concrete compressive strength and nominal aggregate size according to Model Code 1990 [29].

The relation between the crack opening and strain is dependent on the finite element characteristic length, l_{eq}, according to Eq. (11):

$$\varepsilon_t = \varepsilon_{t1} + w\cdot l_{eq} \quad (12)$$

where ε_{t1} is a tensile strain at the peak stress f_{ctm}.

As the size of finite elements inside the concrete slab varies in the range from 3 mm to 10 mm, the characteristic element length had to be obtained by model calibration. The best match between model and specimen response was accomplished with l_{eq} = 5 mm. The adopted stress-cracking strain relation is illustrated in Fig. 8c.

Similarly to compression, damage evolution for tension was defined through variable D_t [21,28]:

$$D_t = 1 - \frac{f_{ctm}}{\sigma_t} \quad (13)$$

3.2. Validation of finite element models

Developed finite element models were validated by comparing their behaviour to the response of experimental specimens. Load-vertical displacement curves for models R1 and R2, obtained through numerical simulations, are compared with experimental curves of corresponding specimens in Fig. 9. Developed models successfully replicate the double shear test, clearly distinguishing the difference in the construction joint response for two analysed orientations. Model R1 features brittle failure with a sudden drop in force after reaching the ultimate load, which was also present in all of the three tested specimens of series R1. On the opposite, the failure of model R2 is more ductile, but the ultimate load and vertical displacement at that load are smaller than for model R1, which is in agreement with the experimental findings. Values on the maximum load for test series R1 and R2 obtained through numerical simulations and experimental testing are compared in Table 4. The maximum relative difference between the numerical and mean experimental ultimate load is 4%, confirming the satisfying accuracy of the developed numerical models.

Table 4
Comparison between experimental and numerical ultimate loads

Series	Ultimate load		Ratio
	EXP	FEA	FEA/EXP
	$P_{ult,exp}$ [kN]	$P_{ult,fea}$ [kN]	$P_{ult,fea}/P_{ult,exp}$
R1	177.95	170.25	0.96
R2	136.15	138.04	1.01

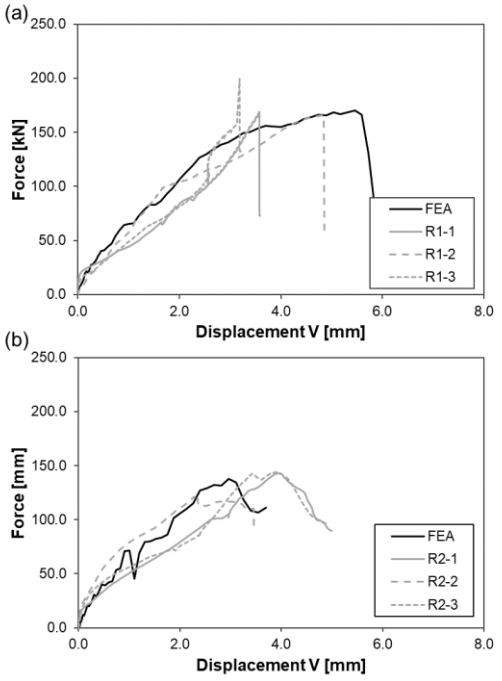

Fig. 9 Comparison between experimental and numerical force-displacement curves: (a) model R1, (b) model R2

3.3. Results of numerical analysis

Validated numerical models enabled further evaluation of the construction joint behaviour and investigation of the effect of the joint orientation on its shear performance. Comparison between force-displacement curves of models R1 and R2 presented in Fig. 10 illustrates the difference in joint response depending on whether the load is applied to the slab with the angle profile installed on its edge or to the slab with the steel plate on the edge. Up to the load of approximately 130 kN, the force-displacement relation for models R1 and R2 is almost identical, indicating that the joint orientation has no impact on the initial stiffness of the construction joint. Stiffness per steel dowel of approximately 13.0 kN/mm is almost identical for the two models. After reaching 138 kN, the load in model R2 drops, whereas the load in model R1 continues to increase until 170 kN. The construction joint with an installed steel plate in the middle (loaded) slab features postponed failure and non-negligibly increased ultimate resistance in comparison to the joint with an angle profile positioned in the middle slab, confirming the experimental findings.

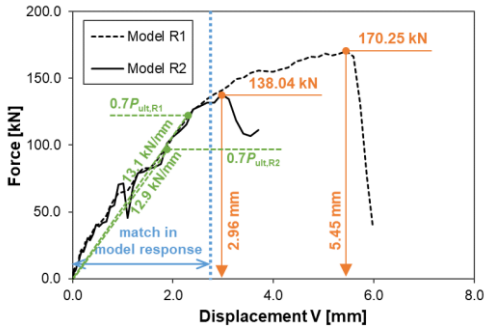

Fig. 10 Comparison between force-displacement curves for models R1 and R2

Deformed shapes of steel dowels in numerical models presenting two types of experimentally tested specimens, shown in Fig. 11, indicate larger dowel deformation in model R1 than in model R2 at the corresponding ultimate load of each model. This is in agreement with structural join vertical displacement at failure presented in Fig. 10, which is also larger for model R1. Stress distribution in steel dowels indicates the development of two plastic hinges along the dowel length. The position of plastic hinges slightly differs in the case of the two analysed joint orientations but in both cases, plastic hinges are significantly distant from the dowel ends. Accordingly, the possible reduction of dowel length should be considered, as later analysed through parametric analysis.

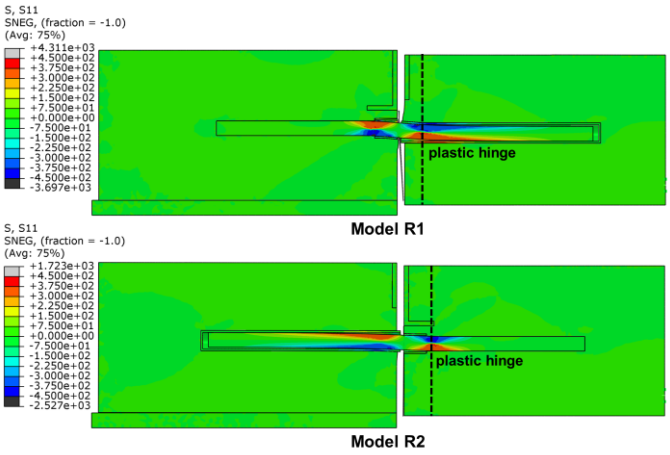

Fig. 11 Normal stress in steel dowels at the ultimate load

The levels of concrete tension and compression damage in models R1 and R2 at the point when the corresponding ultimate load is reached are compared in Fig. 12. In model R1, the concrete above the steel dowel is significantly damaged due to high compressive stresses on the contact between the dowel and surrounding concrete at the construction joint. As a result, concrete bearing causes failure of the middle slab of model R1. Unlike model R1, diagonal cracks in the concrete slab of model R2 propagate all along the construction joint from the horizontal angle leg towards the top surface of the middle slab. Their cause is associated with the presence of steel angles. The horizontal leg of the angle profile, continuous along the construction joint, disrupts the continuity of the concrete slab. It is positioned close to the steel dowel, reducing the zone of the concrete above the dowel subjected to bearing pressure and having a negative influence on the construction joint shear resistance, inducing premature failure of model R2.

To prove that the difference in shear behaviour of models R1 and R2 is solely influenced by the presence of an angle profile on the slab edge which is subjected to shear load, an additional numerical model was developed. The model R2 was modified by cutting the horizontal leg of the angle and comparing the response of such joint to the models R1 and R2. The results presented in Fig. 13 show the equivalent force-displacement responses of model R1 and modified model R2. Diagonal cracks observed in model R2 are not present in the modified model. Analogues to model R1, the governing failure mode of the modified model was concrete bearing.

It is concluded that the absence of an angle profile enhances the construction joint resistance and therefore its elimination would be favourable from the load-bearing perspective. However, the angle profile has an essential role during the construction joint execution, providing lateral stiffness and preventing formwork deformation before and during the installation process. Therefore, the consideration of the potential removal of the angle profile should be carefully approached.

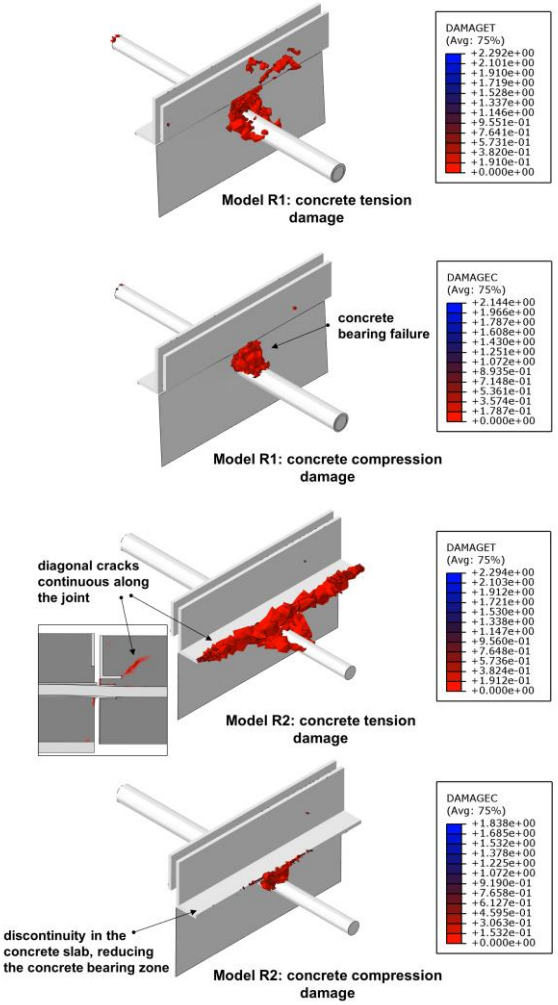

Fig. 12 Concrete damage at the ultimate load

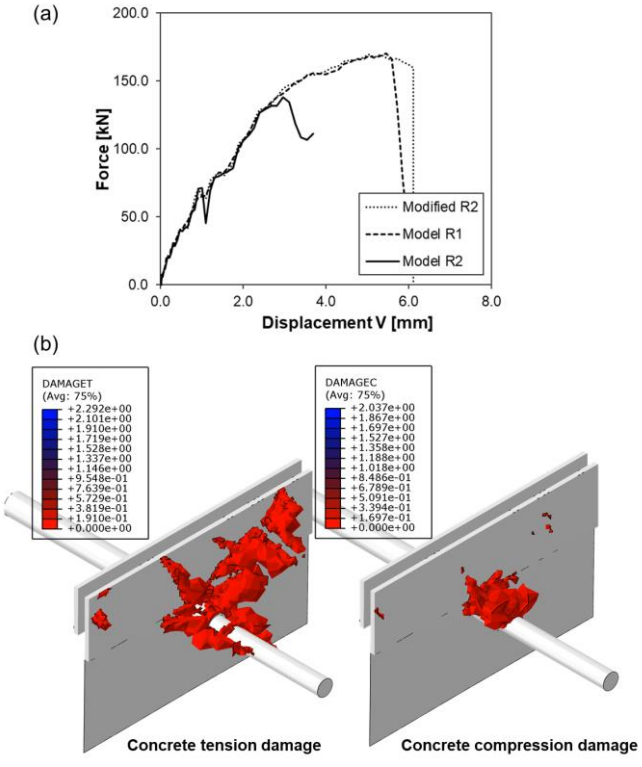

Fig. 13 Response of modified R2 model without horizontal angle leg:
(a) Force-displacement curves, (b) Concrete damage at the ultimate load

4. Parametric analysis

Validated numerical models were used for studying the effects of key material and geometric parameters on the construction joint response, including the joint opening, concrete strength, slab depth, steel dowel diameter and length. The parametric analysis was carried out for the joint orientation corresponding to model R2 since this orientation was shown to be relevant for determining joint resistance to derive safe-sided results. The primary model had the following geometrical and material properties, corresponding to the experimentally tested specimens: construction joint opening of 10 mm, concrete class C40/50, steel dowel diameter of 22 mm and length of 500 mm, and concrete slab depth of 200 mm. Through parametric analysis, each of these parameters was varied while the other parameters remained constant as in the primary model.

4.1. Effect of the construction joint opening

The experimental campaign was conducted with adjoining slabs spaced at a distance of 10 mm, replicating the construction joint opening of 10 mm caused by concrete slab shrinkage. Two additional numerical models were developed with opening sizes of 5 mm and 15 mm to observe the effect of the construction joint opening on its shear response.

Results presented in Fig. 14 show that the distribution of stress in steel dowels does not considerably change with the variation of the joint opening, but the increased deformation of steel dowels for the wider opening is evident. With the increase of opening, the joint is subjected to larger deformations and the joint stiffness is decreased. The displacement at the ultimate load rises, whereas the joint resistance decreases. Each 5 mm increase in joint opening reduces the ultimate load by around 5% and stiffness by 12–16%.

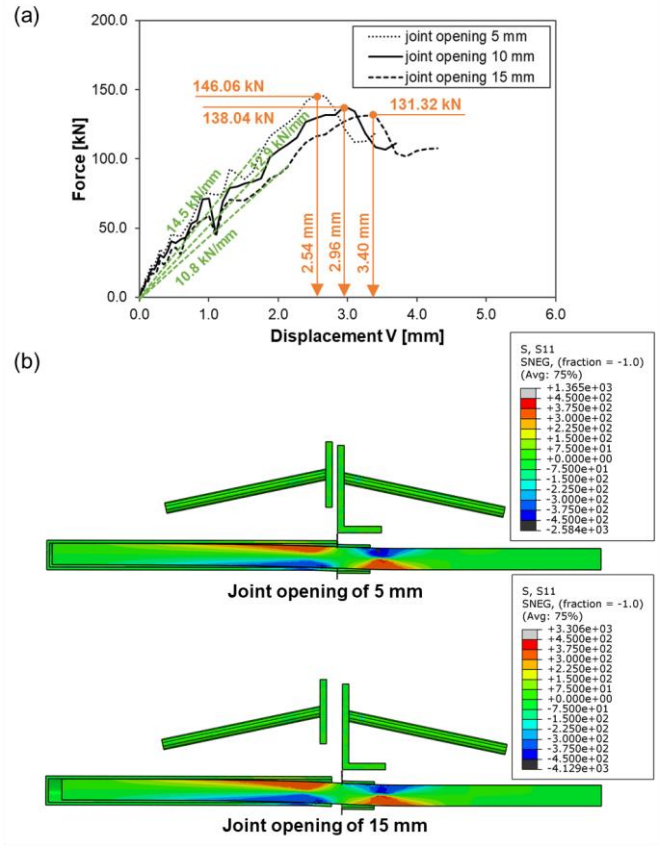

Fig. 14 Effect of the joint opening: (a) Force-displacement curves, (b) Stress in steel dowels at the failure

4.2. Effect of the concrete strength

As the governing failure mode of the analysed construction joint is the failure of concrete, the concrete strength is expected to have a major influence on the construction joint resistance. A set of numerical models with concrete classes in the range from C20/25 to C50/60 was made.

The increase in concrete strength does not significantly affect the joint stiffness according to Fig. 15a, but the increase in the resistance is considerable. For models with higher concrete strengths, the failure is postponed and ultimate loads are larger, followed by a certain increase in relative vertical displacement between the adjoining slabs. The difference in resistance between models with concrete C20/25 and C50/60 is over 30%. Ultimate loads of the analysed models presented in Fig. 15b in the function of the square root of the mean concrete strength f_{cm}, demonstrate that the resistance of the construction joint is a linear function of the $f_{cm}^{0.5}$.

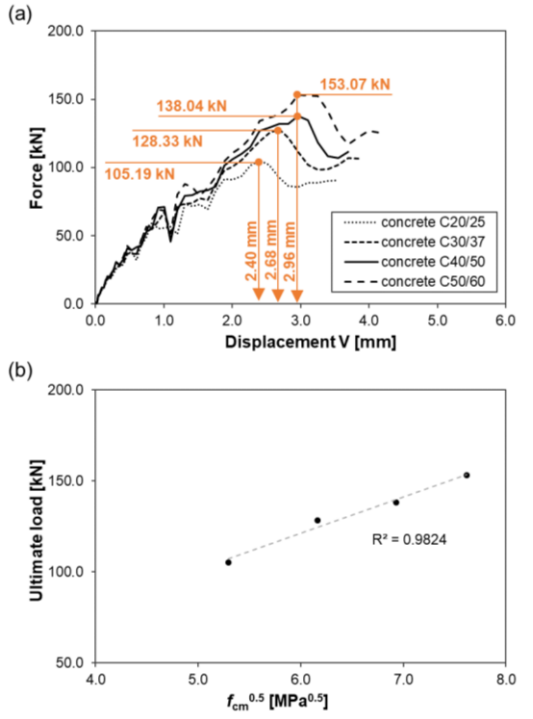

Fig. 15 Effect of the concrete strength: (a) Force-displacement curves, (b) Relation between the ultimate load and square root of the mean concrete strength

4.3. Effect of the steel dowel diameter

As the investigated construction joint with round dowels may be fabricated with varied steel dowel sizes, numerical models with dowels of diameters of 20 mm, 22 mm and 24 mm were developed and their behaviour was compared.

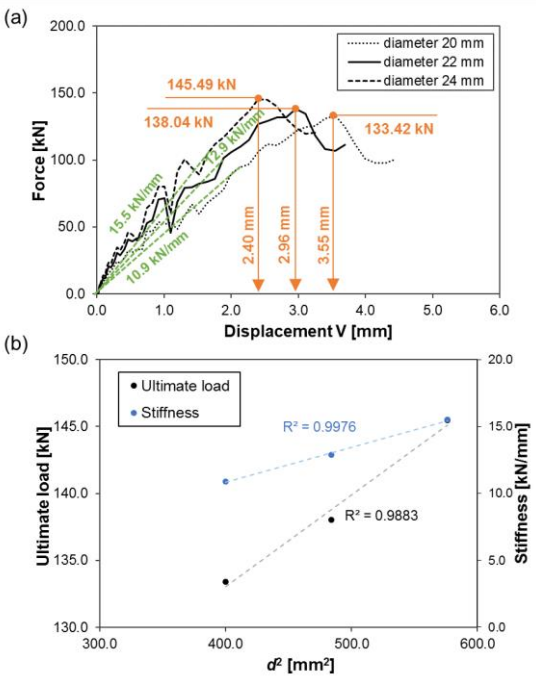

Fig. 16 Effect of the steel dowel diameter: (a) Force-displacement curves, (b) Relation between the ultimate load/stiffness and square of the dowel diameter

According to Fig. 16a, the dowel diameter affects the joint resistance, i.e.

when the diameter is increased from 20 mm to 22 mm, the rise in resistance is 3.5%, whereas, for the increase from 22 mm to 24 mm, the resistance is raised by 5.4%. Although the diameter of the steel dowel appears to have a lower effect on joint resistance than the concrete class, dowel size non-negligibly affects construction joint stiffness which varies in the range of 10.9–15.5 kN/mm for the analysed models. Fig. 16b illustrates the linear dependency between the square of the dowel diameter and the joint resistance, as well as the joint stiffness.

4.4. Effect of the steel dowel length

ACI 302.1R-04 [8] specifies dowel length depending on the floor slab depth: 400 mm for round dowels in slabs of a depth of 175–200 mm, and 450 mm for round dowels in slabs of a depth of 225–275 mm. According to this recommendation, the dowels of the analysed construction joint may be shortened. For calculating the construction joint resistance to shear according to Technical Report 34 [9], the loaded length of a steel round dowel should not be taken as greater than 8*d*, where *d* is the dowel diameter. In other words, the total effective length of a dowel could be approximated by 16*d*, accounting for both sides of the construction joint. In the particular case of the investigated construction joint, the effective steel dowel length would be around 350 mm according to this recommendation. Three additional numerical models were created with steel dowel lengths of 300 mm, 200 mm and 150 mm, to study the influence of dowel length on the joint response, and the possibility of reducing this length to optimise the construction joint.

Numerical results show little difference in the force-displacement response of construction joints with steel dowels of a length of 300 mm and 500 mm, leading to the conclusion that a reduction of the dowel length by 40% would not affect the structural performance of the construction joint. According to Fig. 17, the model with a dowel length of 200 mm also has comparable shear resistance, although force-displacement curves do not completely overlap in the pre-ultimate domain with the ones presented for longer dowels. However, when the dowel length is reduced to 150 mm, a reduction in joint resistance exceeds 20%, followed by a decrease in joint stiffness. Stress distribution in the construction joint presented in Fig. 18 shows that in the 150 mm long dowel, the plastic hinge is only developed in the right half of the dowel. This length of steel dowel is insufficient to transfer shear force between adjoining slabs in comparison to longer dowels. According to the presented results, the dowel length may be kept at 14*d* (14 · 22 mm = 308 mm ≈ 300 mm) while retaining the same construction joint response in terms of deformation and load capacity as when longer dowels are applied.

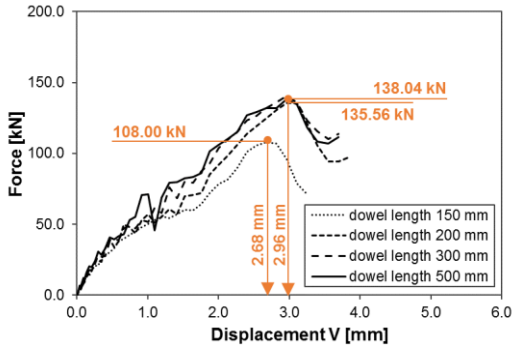

Fig. 17 Effect of the steel dowel length: Force-displacement curves

4.5. Effect of the concrete slab depth

The effect of concrete slab depth was investigated through the set of numerical models covering floor slabs with depths in the range of 180 mm to 240 mm. Steel dowels were positioned in the slab mid-depth in each of the developed models. The size of the steel plate and angle profile remained unchanged, while their position was linked to the upper surface of the concrete slab, meaning the distance between the angle profile and steel dowel was increased with the increase of the slab depth.

The increase in slab depth significantly increased the construction joint resistance, although the stiffness remained unchanged, as presented in Fig. 19a. The decrease in slab depth to 180 mm from the original 200 mm, caused a drop in ultimate load of 4%, while the increase to 220 mm led to the rise of almost 12%. All three of these models featured similar shape force-displacement curves without a sudden decline of force in the post-ultimate domain. The additional increase of the slab depth to 240 mm, improved the shear resistance by 30% in comparison to the model with a slab depth of 200 mm. However, a model with a 240 mm deep slab showed a different force-displacement response with brittle failure and rapid force drop after reaching its maximum, similar to the one observed in model R1 with the opposite joint orientation.

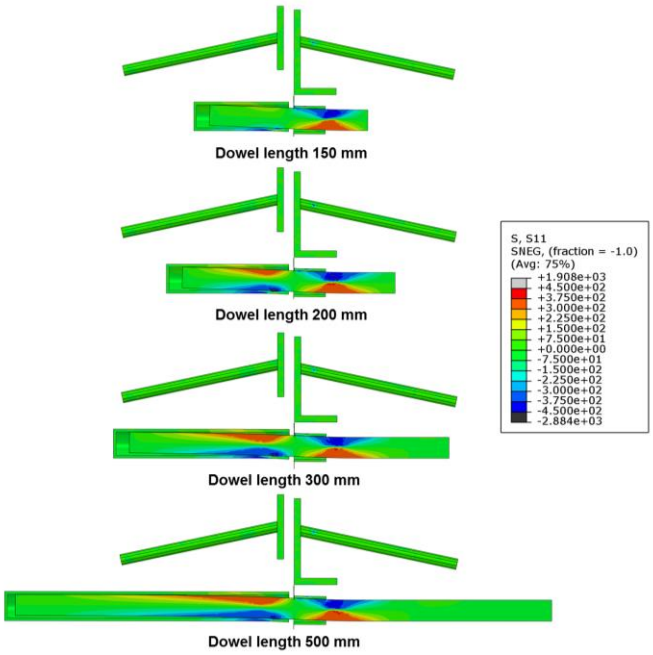

Fig. 18 Effect of the steel dowel length: Stress in steel dowels at the failure

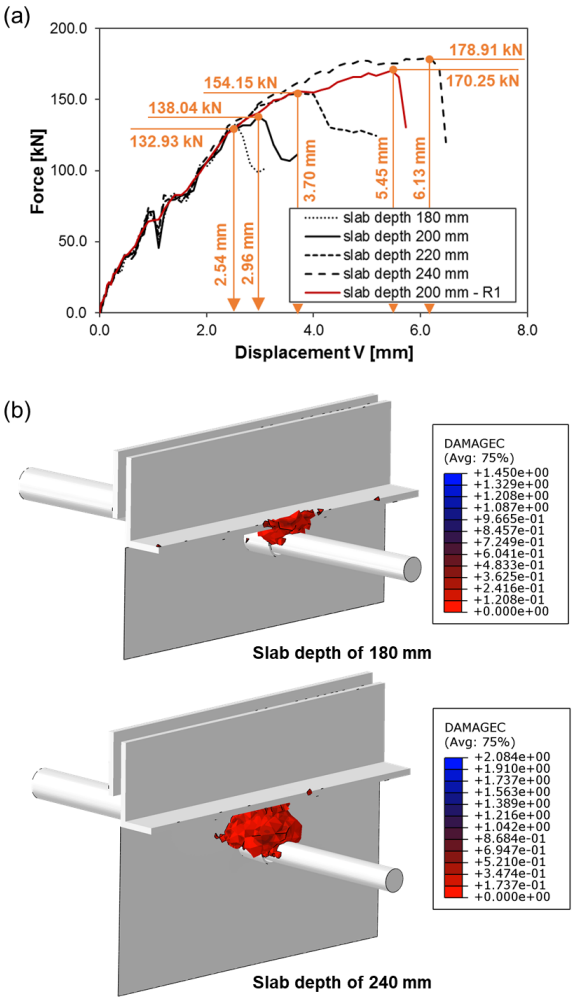

Fig. 19 Effect of the concrete slab depth: (a) Force-displacement curves, (b) Concrete compression damage at the failure

Concrete damage in slabs of a depth of 180 mm and 240 mm, presented in Fig. 19b, illustrates the differences in the response of construction joints in those two cases. When the slab depth is larger, the distance between the angle profile and steel dowel is also greater, causing the distribution of bearing stresses in concrete similar to the one in the construction joint with a 60 x 6 mm steel plate in the slab subjected to failure (model R1). On the opposite, with a decrease in the slab depth and spacing between the angle profile and steel dowel, the construction join resistance is reduced due to the discontinuity in the bearing concrete influenced by the horizontal angle leg. Therefore, the slab thickness is an important factor affecting the shear behaviour of the investigated construction joint including the angle profile that is continuous along the slab edge.

5. Conclusions

The integral solution of the free-movement construction joint developed for application in concrete industrial ground floors was experimentally and numerically investigated. The construction joint shear behaviour was studied considering two joint orientations through the experimental campaign, and covering five additional influential parameters through finite element simulations. According to the obtained results, the following conclusions could be drawn:

(1) Construction joint orientation does not affect stiffness, but it influences joint resistance and post-ultimate behaviour. When failure occurs in the concrete slab with an angle profile installed on the slab edge, construction joint resistance is decreased by more than 20% in comparison to the opposite case when the slab with a steel plate is subjected to failure. Joint failure in the concrete slab with steel plate is highly brittle, unlike the joint failure in the slab with angle profile, which is more ductile.

(2) Differences in construction joint response for opposite joint orientations are attributed to different steel components on the slab edges in those two cases: steel plate and angle profile. The horizontal leg of the angle profile cuts through the slab, causing discontinuity in the concrete and resulting in the development of diagonal cracks along the construction joint. If steel dowels are positioned directly below the angle profile, the concrete zone above the dowel is insufficient to bear compression stresses, inducing the earlier failure of the joint.

(3) Construction joint opening caused by concrete slab dry shrinkage affects the bending deformation of steel dowels, as well as the construction joint stiffness and resistance. For the analysed construction joint, the 5 mm increase in the joint opening results in approximately 5% lower joint resistance and 12–16% lower joint stiffness.

(4) The increase in concrete strength improves the construction joint resistance. This increase is proportional to the square root of the concrete compressive strength. Moreover, the diameter of the steel dowel affects the construction joint stiffness and resistance. The increases in resistance and stiffness are both proportional to the square of the dowel diameter.

(5) The construction join response remains the same when the dowel length is varied between 300 mm and 500 mm, meaning that for the analysed dowel, the reduction of dowel length to 14*d* does not affect the joint deformation and load capacity. However, a further decrease in length below 200 mm induces a considerable drop in the stiffness and resistance.

(6) Concrete slab depth significantly affects the construction joint resistance. As the slab depth increases, the vertical distance between the steel dowel and the angle profile gets larger, reducing the negative impact of the angle profile and influencing the higher resistance of the joint. As a result, increasing the slab depth from 200 mm to 240 mm can increase joint resistance by 30%.

Funding

This investigation was supported by the Innovation Fund of the Republic of Serbia, through the Innovation voucher programme (Voucher No. 1397, 2023).

Acknowledgements

The authors are grateful to the company Rinol d.o.o, Belgrade, for their support.

References

[1] Al-Humeidawi BH, Mandal P. Experimental investigation on the combined effect of dowel misalignment and cyclic wheel loading on dowel bar performance in JPCP. Engineering Structures 2018;174:256–66. https://doi.org/10.1016/j.engstruct.2018.07.052.
[2] Al-Humeidawi BH, Mandal P. Evaluation of performance and design of GFRP dowels in jointed plain concrete pavement – part 1: experimental investigation. International Journal of Pavement Engineering 2014;15:449–59. https://doi.org/10.1080/10298436.2013.824081.
[3] Fasil M, Rahman MK, Al-Zahrani MM, Nanni A, Najamuddin SK. Load transfer of small-diameter GFRP and stainless steel doweled-joints in slabs-on-ground. Engineering Structures 2024;302:117241. https://doi.org/10.1016/j.engstruct.2023.117241.
[4] Al-Humeidawi BH, Mandal P. Numerical evaluation of the combined effect of dowel misalignment and wheel load on dowel bars performance in JPCP. Engineering Structures 2022;252:113655. https://doi.org/10.1016/j.engstruct.2021.113655.
[5] Zuzulova A, Grosek J, Janku M. Experimental Laboratory Testing on Behavior of Dowels in Concrete Pavements. Materials 2020;13:2343. https://doi.org/10.3390/ma13102343.
[6] Shalaby A. Using fiber-reinforced polymer load transfer devices in jointed concrete pavements, Orlando, Florida, USA: 2001.
[7] Vijay PV, Li H, GangaRao VH. Laboratory testing, field construction, and decade long performance evaluation of jointed plain concrete pavement with FRP dowels. International Journal of Pavement Engineering 2020;21:713–24. https://doi.org/10.1080/10298436.2018.1508841.
[8] ACI Committee 302. ACI 302.1R-04 Guide for Concrete Floor and Slab Construction. Farmington Hills: American Concrete Institute; 2004.
[9] Concrete Society Project Steering Committee and Design sub-group. Technical Report 34 Concrete industrial ground floors - a guide to their design and construction. Camberley: The Concrete Society; 2013.
[10] Li YL, Li LK, Tan YQ, Xue ZJ. Performance Properties of GFRP Dowels in Concrete Pavement Joints. Applied Mechanics and Materials 2012;178–181:1147–51. https://doi.org/10.4028/www.scientific.net/AMM.178-181.1147.
[11] Al-Humeidawi BH, Mandal P. Evaluation of performance and design of GFRP dowels in jointed plain concrete pavement – part 2: numerical simulation and design considerations. International Journal of Pavement Engineering 2014;15:752–65. https://doi.org/10.1080/10298436.2014.893314.
[12] Mackiewicz P. Analysis of stresses in concrete pavement under a dowel according to its diameter and load transfer efficiency. Can J Civ Eng 2015;42:845–53. https://doi.org/10.1139/cjce-2014-0110.
[13] Sadeghi V, Hesami S. Investigation of load transfer efficiency in jointed plain concrete pavements (JPCP) using FEM. International Journal of Pavement Research and Technology 2018;11:245–52. https://doi.org/10.1016/j.ijprt.2017.10.001.
[14] Grosek J, Zuzulova A, Brezina I. Effectiveness of Dowels in Concrete Pavement. Materials 2019;12:1669. https://doi.org/10.3390/ma12101669.
[15] EN1994-1-1. Eurocode 4: Design of composite steel and concrete structures. Part 1-1: General rules and rules for buildings. Brussels: CEN; 2004.
[16] ISO6892-1:2009. Metallic materials - Tensile testing - Part 1: Method of test at room temperature. Brussels: CEN; 2009.
[17] EN1990:2010. Eurocode - Basis of structural design. Brussels: CEN; 2010.
[18] Abaqus/CAE. User's Guide. Providence: DS SIMULIA Corp.; 2009.
[19] EN1992-1-1. Eurocode 2: Design of Concrete Structures. Part 1-1: General rules and rules for buildings. Brussels: CEN; 2004.
[20] Lubliner J, Oliver J, Oller S, Oñate E. A plastic-damage model for concrete. International Journal of Solids and Structures 1989;25:299–326. https://doi.org/10.1016/0020-7683(89)90050-4.
[21] Pavlović M, Marković Z, Veljković M, Buđevac D. Bolted shear connectors vs. headed studs behaviour in push-out tests. Journal of Constructional Steel Research 2013;88:134–49. https://doi.org/10.1016/j.jcsr.2013.05.003.
[22] Spremic M, Pavlovic M, Markovic Z, Veljkovic M, Budjevac D. FE validation of the equivalent diameter calculation model for grouped headed studs. Steel and Composite Structures 2018;26:375–86. https://doi.org/10.12989/scs.2018.26.3.375.
[23] Gluhović N. Behaviour of shear connections realised by connectors fastened with cartridge fired pins. University of Belgrade, 2019.
[24] Žuvelek V, Ćurković I, Lukačević I, Rajić A. Finite Element Analyses of Demountable Shear Connection in Cold-Formed Steel-Concrete Composite Beam Based on Experimental Data. Ce/Papers 2023;6:213–9. https://doi.org/10.1002/cepa.2629.
[25] Jakovljević I, Spremić M, Marković Z. Shear behaviour of demountable connections with bolts and headed studs. Advanced Steel Construction 2023;19:341–52. https://doi.org/10.18057/IJASC.2023.19.4.3.
[26] Jakovljević I, Spremić M, Marković Z. Effect of rib-to-beam angle on the shear resistance of headed studs in composite slab. Engineering Structures 2024;303:117574. https://doi.org/10.1016/j.engstruct.2024.117574.
[27] Birtel V, Mark P. Parameterised Finite Element Modelling of RC Beam Shear Failure. ABAQUS Users' Conference, 2006, p. 95–108.
[28] Vigneri V, Odenbreit C, Lam D. Different load bearing mechanisms in headed stud shear connectors for composite beams with profiled steel sheeting. Steel Construction 2019;12:184–90. https://doi.org/10.1002/stco.201900019.
[29] CEB-FIP. Model Code 1990. London: Thomas Telford Services Ltd; 1993.

Advanced Steel Construction – Vol. 21 No. 1 (2025) 31–41
DOI:10.18057/IJASC.2025.21.1.3

STUDY ON BENDING PERFORMANCE AND LOAD-CARRYING CAPACITY OF SINGLE-LAYER CYLINDRICAL RETICULATED SHELL WITH NEW SPRAYER JOINT

Ren Li, Jun-Ji Jin, Zhi-Cheng Xiao, Shou-Fang Jiang and Hui-Jun Li *

College of Water Resources and Architectural Engineering, Northwest A&F University, Shaanxi Yangling, 712100
** (Corresponding author: E-mail: lihuijun2893118@163.com)*

ABSTRACT

The bending stiffness of joints is a critical factor that impacts the bearing capacity of large-span spatial reticulated shell structures. To address the issue of relatively low bending stiffness of traditional socket joints, a novel type of sprayer joint is introduced in this study. Initially, the bending performance of the socket joint is validated, leading to the proposal of the sprayer joint. Then, a refined finite element model is established to investigate the bending performance of the sprayer joints with varying surrounding bolt radii under axial tension and compression loads. Subsequently, an improved bilinear model is developed to effectively determine the bending performance with precise yield position. Finally, the comparative performance of the new sprayer joint and the traditional socket joint in single-layer cylindrical reticulated shells is studied in detail. The findings indicate that the bending performance of the new sprayer joint surpasses that of the traditional socket joint, and the ultimate load of the new sprayer joint reticulated shell has significantly increased compared to the traditional socket joint, highlighting the efficiency and success of the new sprayer joint design. Moreover, it is observed that axial compression and the radius of surrounding bolts can enhance the bending performance, while axial tension exhibits opposite effect. The failure mode of the new sprayer joint is elucidated, and the improved bilinear model accurately describes the yield position and bending process of the joint. These conclusions offer valuable insights for the structural design and application of the sprayer joint.

ARTICLE HISTORY

Received: 28 February 2024
Revised: 12 November 2024
Accepted: 30 November 2024

KEYWORDS

Bending stiffness;
Spatial reticulated shell structures;
New sprayer joint;
Improved bilinear model

1. Introduction

Joint stiffness, particularly bending stiffness, is a critical factor that impacts the stability, bearing capacity, and failure mode of reticulated shells [1-3]. Recent researches have primarily focused on bending stiffness, bearing capacity, and failure mode of semi-rigid joints [4-26]. Research has been conducted, including extensive experimental, numerical, and theoretical studies. Fan *et al*. [27] conducted experiments on bolted-ball joints under combined compression and bending loads. The refined numerical analysis model has been developed for semi-rigid joints that considers axial pressure and bolt preload, and determined the rotational stiffness and ultimate bearing capacity of joints under compression and bending. Zhang *et al*. [28] delved into the bending performance of embedded hub joints, utilizing a power function model to analyze the bending moment-rotation relationship and its impact on the bearing capacity of single-layer spherical reticulated shells. Guo *et al*. [29] performed experimental investigations on plate joints, examining the failure modes under varying plate thicknesses and noting an increase in joint stiffness with thicker plates.

The traditional socket joint (shown in Fig.1) is commonly utilized in large-span spatial reticulated shell structures due to its simple assembly, convenient construction, and aesthetic appeal [30, 31]. However, for spatial reticulated shell structures with larger spans, the bending stiffness of the traditional bowl joint is insufficient, measuring only about 20% of the Temcor joint [30, 32]. Therefore, enhancing the bending stiffness of traditional socket joint to accommodate larger spans is crucial. The bending moment-rotation curve of semi-rigid joints serves as a key index of their mechanical properties. To simplify calculations, scholars have proposed various mathematical models. Current moment-rotation curve models include linear, bilinear, polynomial, B-spline, power function, exponential function, and trilinear models [33-37]. The bilinear and trilinear models are commonly used in calculating reticulated shell structures, although issues regarding accuracy still exist, particularly in accurately describing the bearing capacity at nonlinear stage and the yield point of the bending moment-rotation curve.

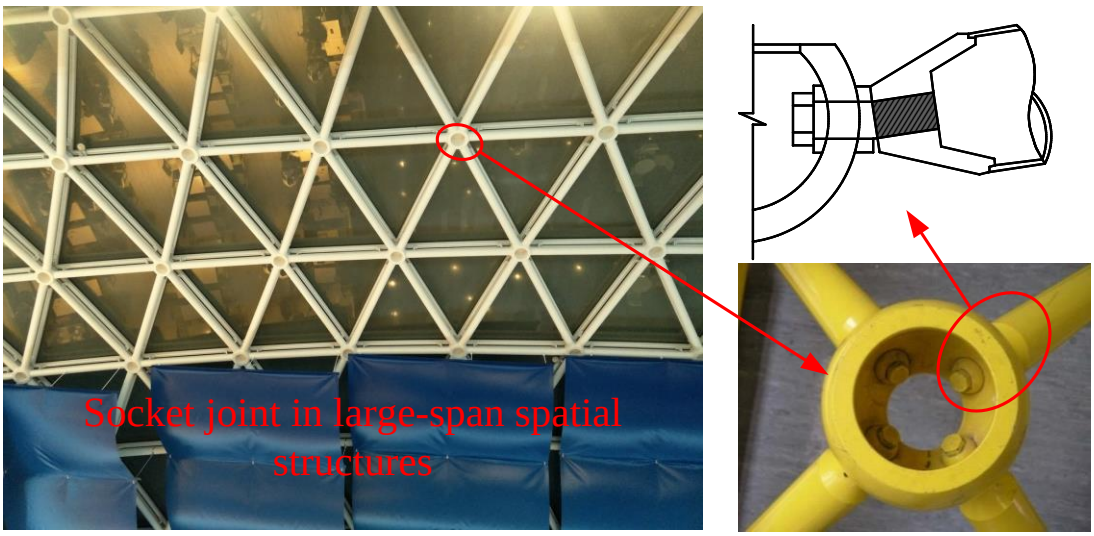

Fig. 1 Socket joint in large-span spatial structures

To address the aforementioned challenges, this study initially validates the bending performance of the socket joint and introduces a new sprayer joint. To evaluate the bending performance of the joint, a refined finite element model was developed to analyze the bending performance of sprayer joints with varying surrounding bolt radii under axial tension and compression loads. Subsequently, an improved bilinear model is proposed which can effectively depicts the bearing capacity at nonlinear stage and the yield point of the bending moment-rotation curve. Finally, the comparative performance of the new sprayer joint and the traditional socket joint in single-layer cylindrical reticulated shells is studied in detail.

2. Establishment of FE model of the new sprayer joint and comparison with socket joint

Traditional socket joint exhibits relatively weak bending stiffness due to its less bending moment resistance [30], a new type of spray joint is proposed to improve the bending stiffness of the conventional joint [38]. The sprayer joint introduced in this study is composed of a bowl-shaped steel hollow ball with a welded cylinder (sprayer body), washers, a central bolt, four surrounding bolts, and a sprayer cone. The assembly and configuration of the sprayer joint are depicted in Fig. 2.

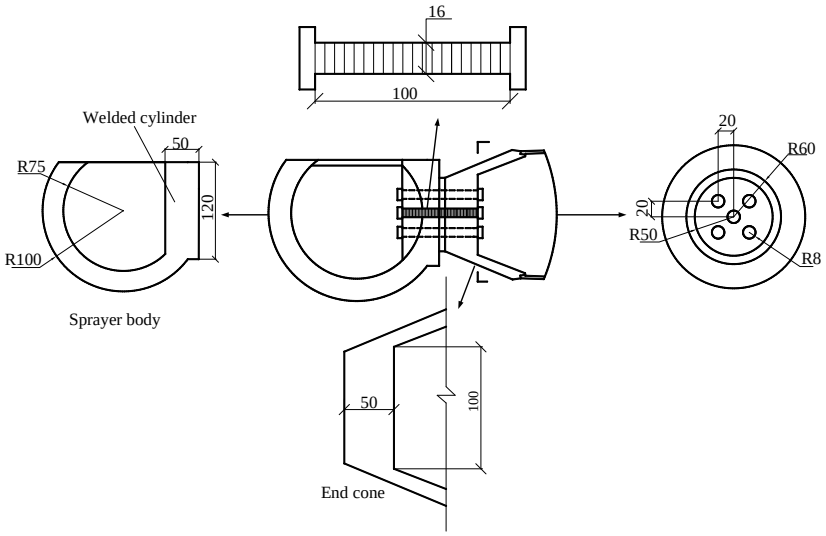

Fig. 2 Assembly and configuration of the sprayer joint (unit: mm)

In order to investigate the bending performance of the novel sprayer joint, refined FE model was constructed for both the traditional socket joint and the new sprayer one in ABAQUS package. Each joint component was simulated using the secondary reduced integration solid element (C3D8R). The meshed joint model is depicted in Fig. 3, with a total of 42472 elements and 65104 nodes. To accurately capture the stress distribution of the joint, 17 contact pairs are established, as shown in Table 1. The material property parameters for each joint component are outlined in Table 2, and the bilinear constitutive relation was used in the FE model. To reduce the computational effort, half of the finite element model (left side) was applied fixed constraints due to the symmetry of the new sprayer node. A bolt preload of 100kN was applied to both the traditional socket joint and the new sprayer-type one, with the joint achieving its ultimate bearing capacity under pure bending (a specific bending moment applied to the cone section).

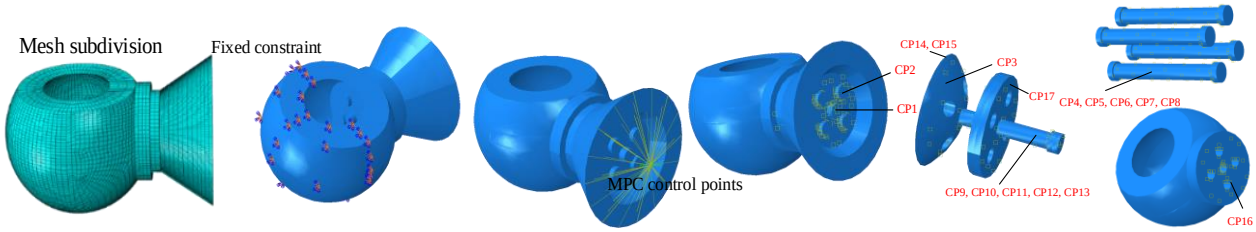

Fig. 3 Refined finite element model of sprayer joint

Table 1
Contact pair settings

Contact pairs	Master surface	Slave surface
CP1	End cone-down	Central bolt-down
CP2	End cone-down	Surrounding bolt-down
CP3	Sprayer body-inside	Washer 1
CP4	Washer 1-hole	Central bolt-side
CP5	Washer 2-hole	Central bolt-side
CP6	End cone-hole	Central bolt-side
CP7	Welded cylinder-hole	Central bolt-side
CP8	Sprayer body-hole	Central bolt-side
CP9	Washer 1-hole	Surrounding bolt-side
CP10	Washer 2-hole	Surrounding bolt-side
CP11	End cone-hole	Surrounding bolt-side
CP12	Welded cylinder-hole	Surrounding bolt-side
CP13	Sprayer body-hole	Surrounding bolt-side
CP14	Washer 1	Central bolt-up
CP15	Washer 1	Surrounding bolt-up
CP16	Welded cylinder	Washer 1
CP17	End cone	Washer 2

Table 2
Material property parameters [31,38]

Assembly part	E	v	$f_{0.2}$	ρ
Sprayer body of sprayer joint	2.06×10^5 MPa	0.3	328MPa	7850kg/m^3
Bowl-joint ball of socket			328MPa	
Bolts of sprayer joint			684MPa	
Bolt of socket			684MPa	
End cone of sprayer joint			405MPa	
End cone of socket			405MPa	

The numerical simulation results of the traditional socket joint were obtained and compared with the experimental results to validate the model used in this study [31]. Fig. 4 displays the moment-rotation curve, showing a satisfactory agreement between the finite element results and the experimental results of traditional socket joints. This alignment serves to validate the accuracy of the finite element model. Fig. 4 presents a comparative diagram of the bending moment-rotation curve for both the new sprayer joint and the traditional socket joint. It is evident that the bending performance of the new sprayer joint exhibits significant enhancement as compared to the traditional socket joint.

According to the moment-rotation curve (Fig. 4), it is evident that the bending performance of the novel sprayer joint surpasses that of the socket joint. The failure mode of the joint is illustrated in Fig. 5, revealing that, prior to joint failure, the lower part of the surrounding bolt experiences initial tension and yielding, which increases the resistance moment of the joint. The ductility of the joint is inferior to that of the traditional socket joint. To delve into its failure mechanism and bending performance, the bending performance of the sprayer joint with varying bolt radii is further examined in the next section.

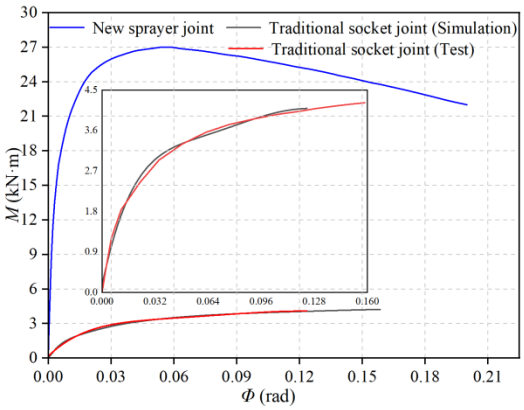

Fig. 4 Verification of numerical model and comparison on bending moment-rotation curve with socket joint

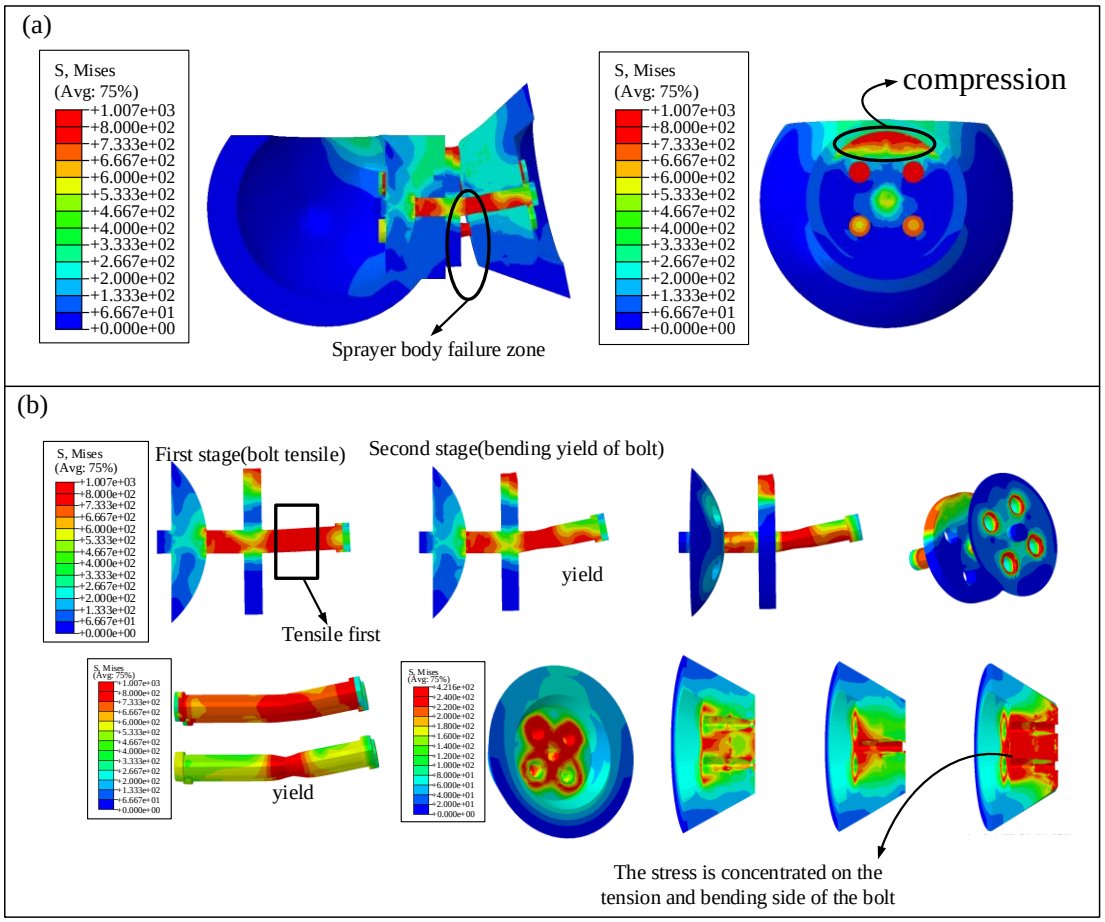

Fig. 5 Mises stress contour and failure mode of the new sprayer joint

3. Bending performance of the new sprayer joint with different diameters of surrounding bolts under axial compression and tension

3.1. Bending properties

From Fig. 6 it can be seen that as the diameter of the surrounding bolts increases, the stress value in the yield region gradually decreases in the ultimate failure state. Additionally, the yield point of the surrounding bolts moves from positions *A* to *B*. When the diameter of the surrounding bolts exceeds 9mm, the bolts no longer neck in the ultimate state. Instead, the surrounding bolts of lower side and the joints bend and yield simultaneously. When the joint is subjected to a bending moment, the tension side bolt and the cylinder compression area form a resistance bending moment. If applied bending moment is less than the rotational capacity, the joint will not experience significant rotation. At this point,

the smaller diameter bolt of the tension side will reach ultimate strength. The analysis above demonstrates that the cylinder and surrounding bolts of the new sprayer joint can enhance the bending stiffness of the joint. Table 3 shows that compared to the socket joint with an 8mm surrounding bolt, the new joint, with the same size surrounding bolt, has an increased initial stiffness by 21.71 times and an increased ultimate bearing capacity by 5.42 times, with only a 15% increase in steel consumption. Consequently, the surrounding bolts with larger diameters provide greater resistance to bending moment and significantly improve the ultimate bearing capacity of the joint.

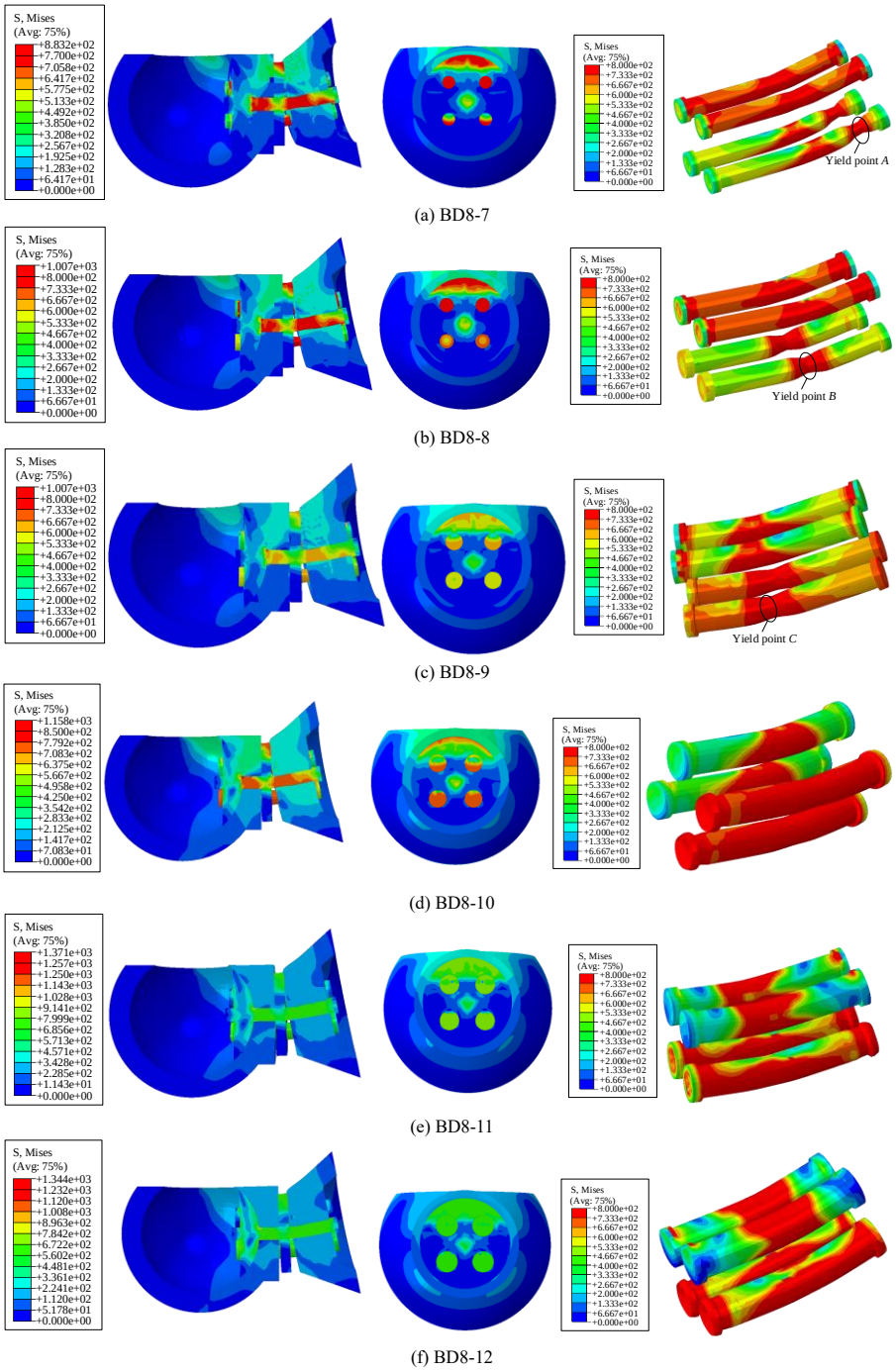

Fig. 6 Mises stress contour diagrams of the sprayer joint with different diameters of the surrounding bolts

Table 3
Main characteristics of bending moment-rotation curves

Specimen ID	N_p (kN)	N_t (kN)	K_i (kN·m/rad)	M_u (kN·m)	θ_u (rad)	Specimen ID	N_p (kN)	N_t (kN)	K_i (kN·m/rad)	M_u (kN·m)	θ_u(rad)
Socket	0	0	227	4.22	0.158	——	——	——	——	——	——
BD8-7	0	0	4921	22.89	0.043	BD8-10	0	0	5037	35.99	0.158
BD8-7AP	100	0	5215	25.46	0.043	BD8-10AP	100	0	5283	37.22	0.148
BD8-7BP	200	0	5470	27.76	0.046	BD8-10BP	200	0	5503	38.38	0.121
BD8-7CP	300	0	5687	29.82	0.047	BD8-10CP	300	0	5693	39.53	0.101
BD8-7DP	400	0	5868	31.66	0.042	BD8-10DP	400	0	5856	40.42	0.089
BD8-7EP	500	0	6017	33.22	0.045	BD8-10EP	500	0	5990	40.99	0.078

BD8-7AT	0	100	4579	20.09	0.047	BD8-10AT	0	100	4761	34.74	0.170
BD8-7BT	0	200	4198	16.98	0.045	BD8-10BT	0	200	4453	33.47	0.176
BD8-7CT	0	300	3777	13.58	0.039	BD8-10CT	0	300	4114	32.07	0.180
BD8-7DT	0	400	3307	9.87	0.042	BD8-10DT	0	400	3747	30.64	0.187
BD8-7ET	0	500	2782	7.22	0.013	BD8-10ET	0	500	3352	29.24	0.202
BD8-8	0	0	4928	26.98	0.056	BD8-11	0	0	5041	40.02	0.235
BD8-8AP	100	0	5200	29.19	0.057	BD8-11AP	100	0	5262	40.92	0.176
BD8-8BP	200	0	5436	31.18	0.059	BD8-11BP	200	0	5467	41.83	0.145
BD8-8CP	300	0	5637	32.95	0.060	BD8-11CP	300	0	5649	42.47	0.119
BD8-8DP	400	0	5804	34.45	0.061	BD8-11DP	400	0	5803	42.79	0.092
BD8-8EP	500	0	6275	35.70	0.061	BD8-11EP	500	0	5929	42.78	0.081
BD8-8AT	0	100	4615	24.59	0.057	BD8-11AT	0	100	4774	39.04	0.203
BD8-8BT	0	200	4262	21.99	0.058	BD8-11BT	0	200	4489	37.93	0.211
BD8-8CT	0	300	3872	19.41	0.072	BD8-11CT	0	300	4174	36.77	0.216
BD8-8DT	0	400	3447	16.23	0.075	BD8-11DT	0	400	3836	35.29	0.223
BD8-8ET	0	500	3026	12.79	0.087	BD8-11ET	0	500	3472	33.95	0.227
BD8-9	0	0	4997	31.60	0.097	BD8-12	0	0	5100	44.27	0.244
BD8-9AP	100	0	5249	33.35	0.097	BD8-12AP	100	0	5329	45.09	0.201
BD8-9BP	200	0	5468	34.96	0.089	BD8-12BP	200	0	5534	45.40	0.181
8-9CP	300	0	5659	36.43	0.080	BD8-12CP	300	0	5716	45.34	0.132
BD8-9DP	400	0	5822	37.65	0.067	BD8-12DP	400	0	5873	45.21	0.099
BD8-9EP	500	0	5956	38.56	0.067	BD8-12EP	500	0	6002	44.71	0.084
BD8-9AT	0	100	4709	29.69	0.097	BD8-12AT	0	100	5919	43.35	0.231
BD8-9BT	0	200	4387	27.62	0.097	BD8-12BT	0	200	4578	42.38	0.237
BD8-9CT	0	300	4026	25.35	0.097	BD8-12CT	0	300	4055	41.27	0.239
BD8-9DT	0	400	3396	22.86	0.098	BD8-12DT	0	400	3954	40.05	0.243
BD8-9ET	0	500	3268	20.15	0.105	BD8-12ET	0	500	3606	38.68	0.250

Notes: N_p denotes the axial pressure, N_t denotes the axial tension, K_i denotes the initial stiffness, M_u denotes the ultimate bending moment, θ_u denotes the ultimate rotation angle, where the bolt radius of the socket joint is 12mm.

Table 3 provides the initial stiffness, stiffness during bolt yield, bending moment during bolt yield, ultimate rotation angle, and ultimate bending moment of the sprayer joint under different load scenarios. It demonstrates that compared to the 100kN axial compression, the yield stiffness of the 500kN axial compression at the surrounding bolt radii of 7mm, 8mm, 9mm, 10mm, 11mm, and 12mm increased by 31.49%, 27.14%, 23.62%, 21.32%, 18.51%, and 16.72%, respectively, and the bending moment of the bolt yield increased by 31.45%, 27.28%, 23.62%, 21.32%, 18.51%, and 16.69%, respectively. On the other hand, compared to the 100kN axial tension, the yield stiffness of the 500kN axial tension at the surrounding bolt radii of 7mm, 8mm, 9mm, 10mm, 11mm, and 12mm decreased by 95.05%, 81.38%, 70.23%, 62.23%, 55.14%, and 51.59%, respectively, and the bending moment of the bolt decreased by 95.04%, 81.41%, 70.22%, 62.21%, 55.11%, and 51.63%, respectively.

The axial compression and axial tension exert a significant influence on the ultimate bending moment and rotation angle of the sprayer joint. Table 3 demonstrates that, compared to the 100kN axial compression, the ultimate bending moment of the sprayer joints with surrounding bolt radii of 7mm, 8mm, 9mm, 10mm, and 11mm increased by 30.48%, 22.31%, 15.62%, 10.13%, and 4.54%, respectively, under the 500kN axial compression. Additionally, the ultimate rotation angle of the joints with a bolt radius of 12mm approximately increased by 0.84%. Moreover, the ultimate rotation angle of the joints with bolt radii 7mm and 8mm increased by 4.05% and 7.07%, respectively, while the ultimate bending moment of the joints with bolt radii around 9mm, 10mm, 11mm, and 12mm decreased by 30.93%, 47.29%, 53.97%, and 58.21%, respectively. Furthermore, when compared to the 100kN axial tension, the yield stiffness of the 500kN axial tension decreased by 64.06%, 47.98%, 32.13%, 15.83%, 13.04%, and 10.77% for surrounding bolt radii of 7mm, 8mm, 9mm, 10mm, 11mm, and 12mm. The ultimate rotation angle of the bolt radius 7mm decreased by 72.34%, while the ultimate bending moment of the bolt radius joints around 8mm, 9mm, 10mm, 11mm, and 12mm increased by 52.63%, 8.25%, 18.82%, 11.82%, and 8.23%, respectively. The above phenomena demonstrate that the sprayer joint exhibits satisfactory ductility. Enhancing the radius of the surrounding bolt and increasing the axial pressure will augment the ductility of the specimen. However, applying axial tension will diminish the ductility of the specimen. This is attributed to the alteration in the initial stress state of the specimen caused by the initial external load.

3.2. Failure mode

From the analysis in the previous section, it is evident that there is a significant necking phenomenon in the lower part of the surrounding bolt when the radius of the new sprayer joint is less than 10mm. Fig. 7 illustrates Mises stress contour of different groups of sprayer joints under various load schemas. As the bolt radius decreases, the yield point of the surrounding bolt shifts from points *C* to *B*, and eventually to point *A* when the radius is 7mm. The influence of load schemas on the bending stiffness and bearing capacity of the sprayer joints has been previously illustrated. It is worthy to note that load conditions not only affect bending properties previous mentioned but also have a substantial impact on the failure mode of the joints. Fig. 7(b) reveals that when the axial tension exceeds 300kN, the surrounding bolts yield prematurely, and the yield point occurs at *A*. For other loading conditions, the failure mode remains the yield of the surrounding bolts at point *B*. This suggests that the axial tension weakens the bearing capacity of the joint, thereby influencing its failure mode. Furthermore, in the limit state, the stress value at the failure point gradually increases as the axial force increases.

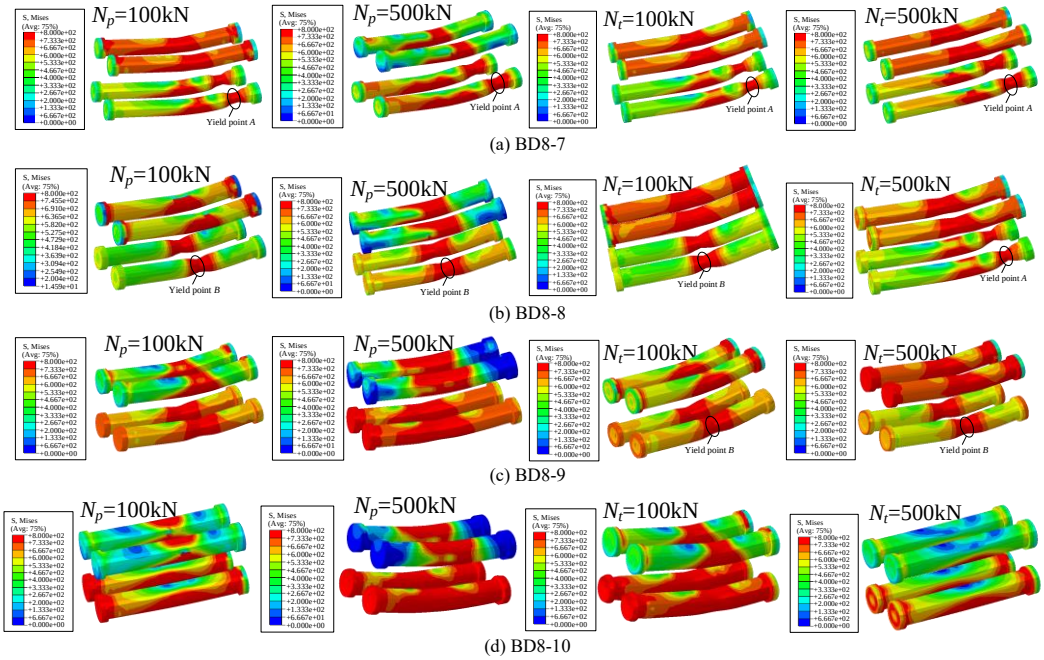

(a) BD8-7

(b) BD8-8

(c) BD8-9

(d) BD8-10

Fig. 7 Mises stress contour of the sprayer joint under different load schemas

4. The establishment of the improved bending moment-rotation bilinear model of the joint and the derivation of the equation

4.1. Initial stiffness of the joint

The sixth-order polynomial fitting method is utilized to determine the initial stiffness of the joint by calculating the first-order derivative of the bending moment-rotation curve at the origin. The fitting result can be observed in Fig. 8 and satisfactory results are obtained.

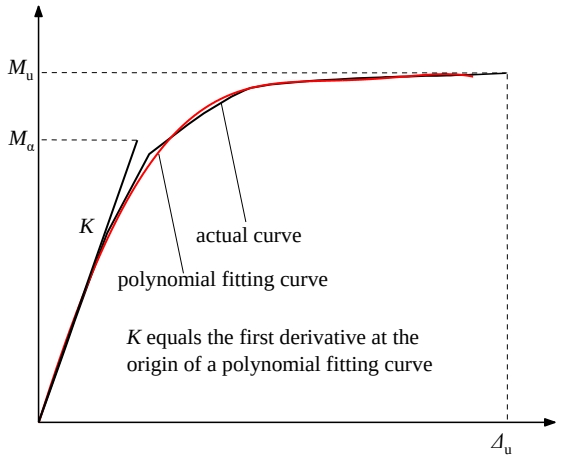

Fig. 8 Determination of initial stiffness

4.2. Modified yield coefficient

In the traditional model, parameters yield coefficient a and stiffness coefficient b are determined using the energy equivalent method where the area enclosed by the actual bending moment-rotation curve is made equal to the area enclosed by the simplified bilinear model. This method ensures energy conservation in seismic analysis by maintaining the same area through the geometric energy method. However, in static analysis, the bearing capacity of the reticulated shell is influenced by the initial stiffness and yield bending moment of the joints. The simplified bilinear model in the traditional method may encounter inaccuracy in basic static parameters such as initial stiffness and yield bending moment. Therefore, this paper proposes an improvement to the traditional method by obtaining the second derivative using the function relation of the bending moment-rotation angle curve. The yield point, which represents the minimum value of the second derivative, provides the real value of the yield bending moment M_α. The bilinear model is then modified by directly replacing the yield moment M_S obtained by the energy method with M_α.

The Fig. 9 depicts the modified bilinear model. In this model, the initial stiffness is denoted as K and the yield coefficient is represented as A (where the true value of the yield bending moment corresponds to the ultimate bearing capacity under bending moment). Additionally, the second stage in bilinear model is characterized by the stiffness coefficient B, then

$$A = M_\alpha / M_u \tag{1}$$

$$B = \left(M_u - M_\alpha\right) / \left(\Delta_u - M_\alpha / K\right) / K \tag{2}$$

where, A is the corrected yield coefficient, B is the corrected stiffness coefficient, M_u is the ultimate bending moment, M_α is the corrected yield bending moment, Δ_u is the rotation angle corresponding to the ultimate bending moment, and K is the initial stiffness.

The method described above is utilized to obtain the actual values of the yield bending moment M_α for the joints under varying surrounding bolt radii and loading schemas, as presented in Table 4. Subsequently, an improved bilinear model is developed for the sprayer joints with different surrounding bolt radii and loading schemas.

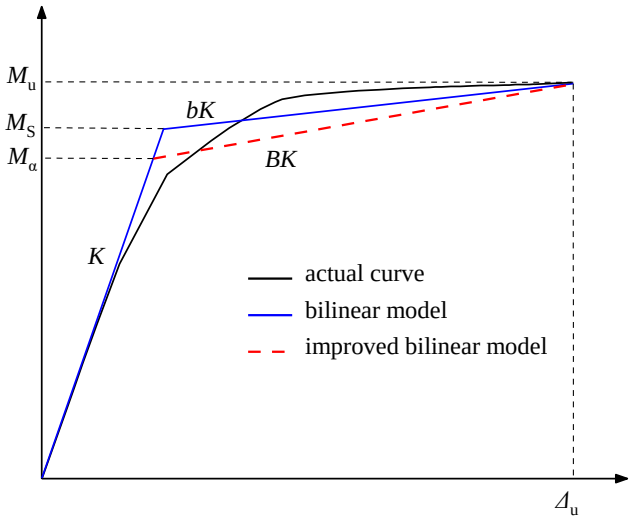

Fig. 9 Comparison between the improved bilinear model and the traditional one

4.3. Establishment of bilinear model

This section focuses on establishing a bilinear model using the radius of the surrounding bolt and the load conditions as parameter variables. The radius of the surrounding bolt is normalized by the maximal bolt radius, denoted as the

dimensionless index m. Similarly, the load condition (measured in kN) is normalized by 500kN and recorded as the dimensionless index n. It is important that a positive value of n indicates the joint under compression, while a negative value indicates tension. The bilinear model is constructed following the method described in the previous section. The yield bending moment, the yield coefficient A and the stiffness coefficient B of the bilinear model is listed in Table 4.

Table 4
The value of yield bending moment, the yield coefficient A and the stiffness coefficient B of the bilinear model

SI	m	n	M_α	A	B	SN	m	M_α	A	B	SI	m	M_α	A	B
BD8-7	0.58	0	20.28	0.886	0.014	BD8-8	0.67	22.08	0.818	0.019	BD8-9	0.75	27.53	0.871	0.009
BD8-7	0.58	0.2	21.29	0.836	0.021	BD8-8	0.67	25.19	0.863	0.015	BD8-9	0.75	29.44	0.883	0.008
BD8-7	0.58	0.4	24.18	0.871	0.016	BD8-8	0.67	27.20	0.872	0.014	BD8-9	0.75	31.53	0.902	0.008
BD8-7	0.58	0.6	27.26	0.914	0.011	BD8-8	0.67	29.21	0.886	0.012	BD8-9	0.75	32.89	0.903	0.008
BD8-7	0.58	0.8	30.05	0.949	0.007	BD8-8	0.67	32.72	0.950	0.005	BD8-9	0.75	34.37	0.913	0.009
BD8-7	0.58	1	30.78	0.927	0.010	BD8-8	0.67	33.00	0.924	0.008	BD8-9	0.75	34.10	0.884	0.012
BD8-7	0.58	-1	16.91	0.842	0.016	BD8-8	0.67	20.41	0.830	0.017	BD8-9	0.75	25.07	0.844	0.011
BD8-7	0.58	-2	14.49	0.853	0.014	BD8-8	0.67	17.51	0.796	0.020	BD8-9	0.75	22.56	0.817	0.013
BD8-7	0.58	-3	11.15	0.821	0.018	BD8-8	0.67	15.16	0.781	0.016	BD8-9	0.75	19.95	0.787	0.015
BD8-7	0.58	-4	7.58	0.768	0.017	BD8-8	0.67	13.05	0.804	0.013	BD8-9	0.75	16.37	0.716	0.021
BD8-7	0.58	-5	4.09	0.566	0.098	BD8-8	0.67	9.28	0.726	0.014	BD8-9	0.75	13.45	0.667	0.020
BD8-10	0.83	0	31.76	0.882	0.006	BD8-11	0.92	34.94	0.873	0.004	BD8-12	1	37.88	0.856	0.005
BD8-10	0.83	0.2	33.63	0.904	0.005	BD8-11	0.92	37.02	0.905	0.004	BD8-12	1	39.47	0.875	0.005
BD8-10	0.83	0.4	34.96	0.911	0.005	BD8-11	0.92	38.00	0.908	0.005	BD8-12	1	41.12	0.906	0.004
BD8-10	0.83	0.6	36.16	0.915	0.006	BD8-11	0.92	37.96	0.894	0.007	BD8-12	1	40.88	0.902	0.006
BD8-10	0.83	0.8	36.60	0.905	0.008	BD8-11	0.92	37.79	0.883	0.010	BD8-12	1	40.30	0.891	0.009
BD8-10	0.83	1	36.11	0.881	0.011	BD8-11	0.92	37.11	0.867	0.013	BD8-12	1	39.06	0.874	0.012
BD8-10	0.83	-1	29.53	0.850	0.007	BD8-11	0.92	32.99	0.845	0.006	BD8-12	1	35.99	0.830	0.006
BD8-10	0.83	-2	27.05	0.808	0.008	BD8-11	0.92	30.54	0.805	0.008	BD8-12	1	33.62	0.793	0.008
BD8-10	0.83	-3	24.36	0.760	0.011	BD8-11	0.92	28.08	0.764	0.010	BD8-12	1	31.13	0.754	0.011
BD8-10	0.83	-4	22.29	0.727	0.012	BD8-11	0.92	25.22	0.715	0.012	BD8-12	1	28.50	0.712	0.012
BD8-10	0.83	-5	19.00	0.650	0.016	BD8-11	0.92	22.46	0.662	0.015	BD8-12	1	25.51	0.660	0.015

Notes: SI and M_α stands for Specimen ID and yielding bending moment (kN·m), respectively.

Yield coefficient A, stiffness coefficient B, initial bending stiffness K_i and yield bending moment M_α are nonlinearly fitted respectively using Eq. (3). The independent variables are surrounding bolt radius index m and load condition index n. The specific values of fitting coefficients are shown in Table 5.

$$T = a_{20}m^2 + a_{02}n^2 + a_{11}mn + a_{10}m + a_{01}n + a_{00} \quad (3)$$

where T represents the fitting functions, and a_{20}, a_{02}, a_{11}, a_{10}, a_{01}, a_{00} represent the corresponding fitting coefficients. Table 5 shows the relevant parameters of nonlinear fitting of bilinear model, and Fig. 10 shows the corresponding fitting surface.

Table 5
Corresponding fitting coefficients of bilinear model

T	a_{20}	a_{02}	a_{11}	a_{10}	a_{01}	a_{00}
A	-0.047	-0.004	0.003	0.034	0.021	0.880
B	0.101	3.9E-4	0.008	-0.186	-0.008	0.090
K_i	1980.6	-17.55	-531.7	-3486.3	742.2	6680.8
M_α	-5.552	-0.174	-4.979	41.98	6.239	0.961

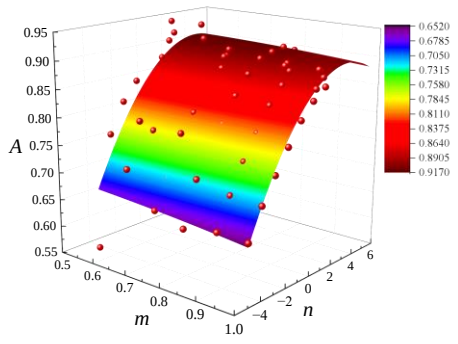

(a) A

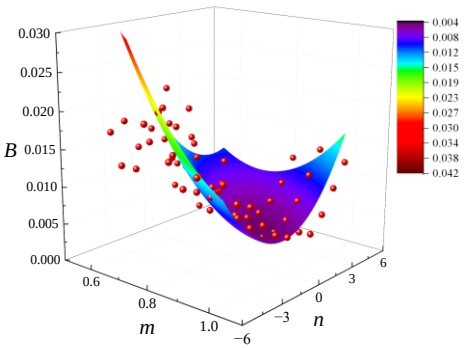

(b) B

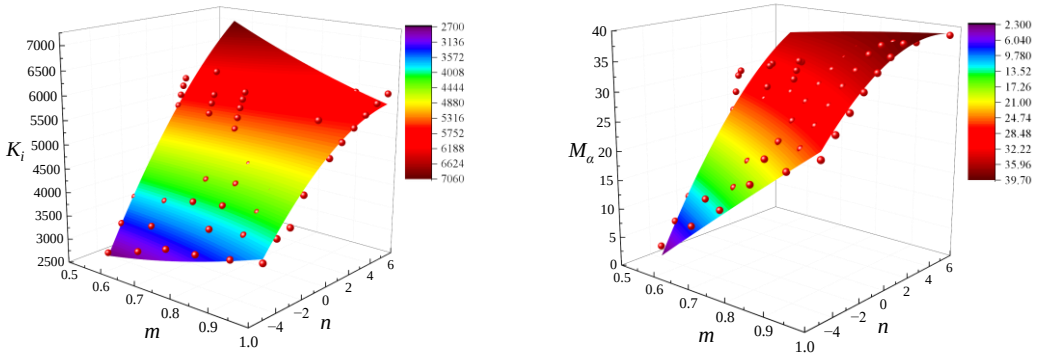

(c) K_i (d) M_α

Fig. 10 Bilinear model fitting surface diagram

4.4. Evaluation of Bilinear Models

In summary, the bending moment-rotation curve of the sprayer joint can be determined using Eq. (3) and Table 4 when the surrounding bolt diameter radius and loading schemas of the joint are known. This section evaluates the bilinear model. First, consistency between the original bending moment-rotation curve and the bilinear model is compared shown in Fig. 11, and it is evident that the *A*, *B*, bending stiffness, and yield moment provided by the bilinear model align well with the numerical results. Hence, it can be concluded that the estimation of the bilinear model can serve as a reference for a preliminary prediction of the bending moment-rotation curve of the sprayer joint.

Then, the prediction model is tested. The predicted values are obtained using the fitted formula and then plotted on a scatter diagram (shown in Fig. 12) with the true value as the *T*-axis and the predicted value as the T_{fit}-axis, which is normalized. The *R*-square values for *A*, *B*, bending stiffness, and yield bending moment are 0.884, 0.824, 0.935, and 0.958, respectively. The points on the scatter diagram predominantly fall along the ideal fitting line, indicating that the fitted formula can accurately calculate the main parameters of the bilinear model.

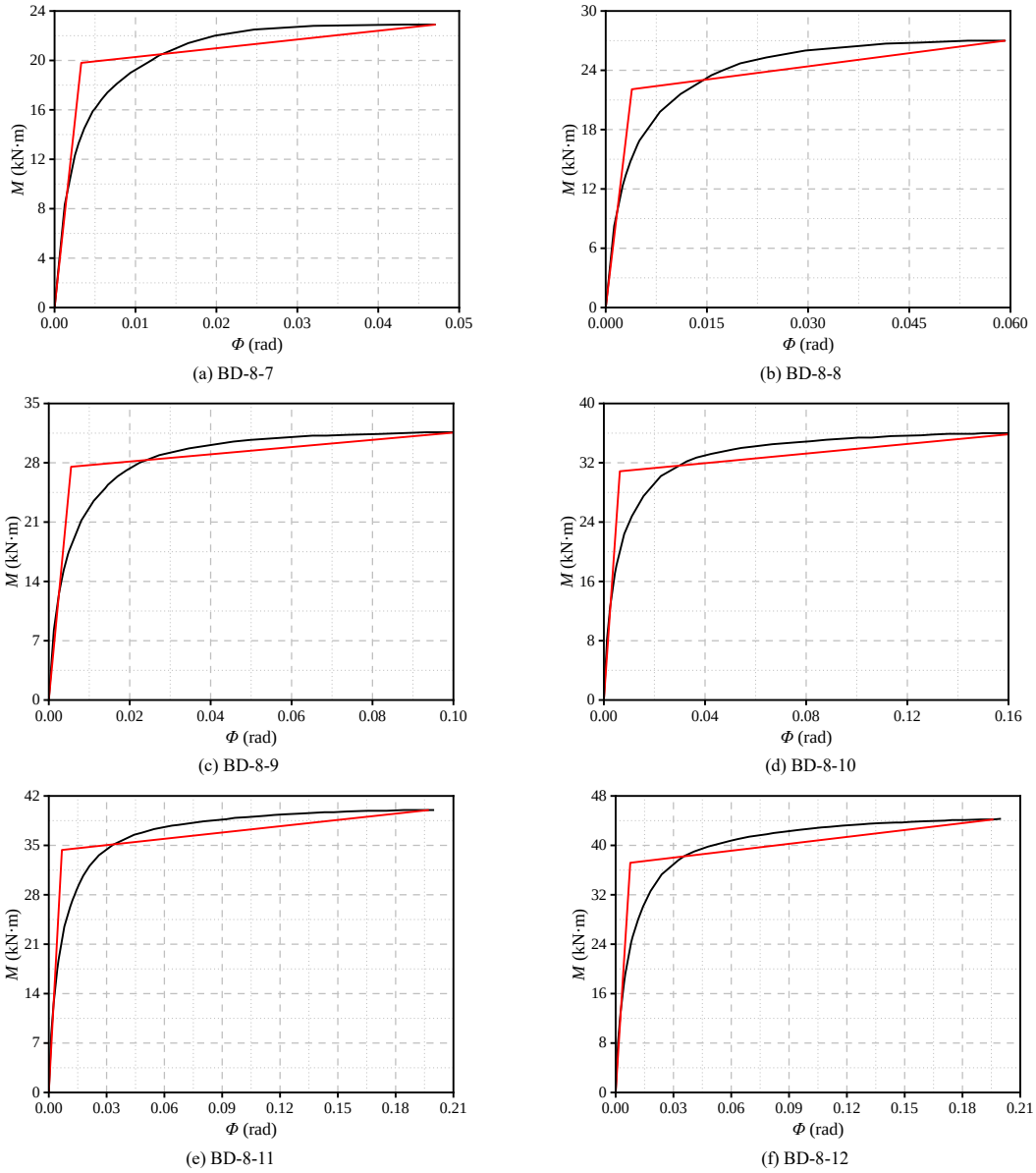

(a) BD-8-7 (b) BD-8-8

(c) BD-8-9 (d) BD-8-10

(e) BD-8-11 (f) BD-8-12

Fig. 11 Comparison of the bending moment-rotation curves between improved bilinear model and actual curve.

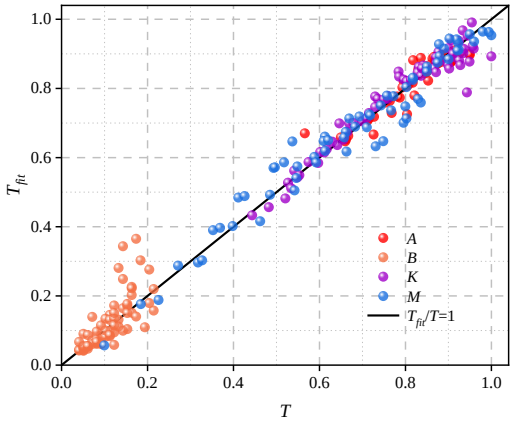

Fig. 12 Scatter diagram between actual values and predicted values

5. Semi-rigid reticulated shell with new sprayer joint

5.1. Modeling of semi-rigidly reticulated shell

The single-layer cylindrical reticulated shell, shown in Fig. 13, is selected to further investigate the bending performance of the new sprayer joint under a vertically uniform load. The joints located along the longitudinal side at the bottom of the reticulated shell are subjected to three-way constraints (i.e. hinged), while the joints at both ends experience vertical constraints. The shell members are made of circular tubes, denoted as C-100×5 (with a diameter of 100 mm and a thickness of 5 mm). The material is Q235 steel, and an isotropic, strain-hardening von Mises elastic-plastic model is used, while the elastic modulus is 2.1×10^{11} Pa, Poisson's ratio is 0.3, and the density is 7850 kg/m³. In this FE model, both geometric and material nonlinearities are considered, with the ultimate load of the reticulated shell determined using the arc-length method [39].

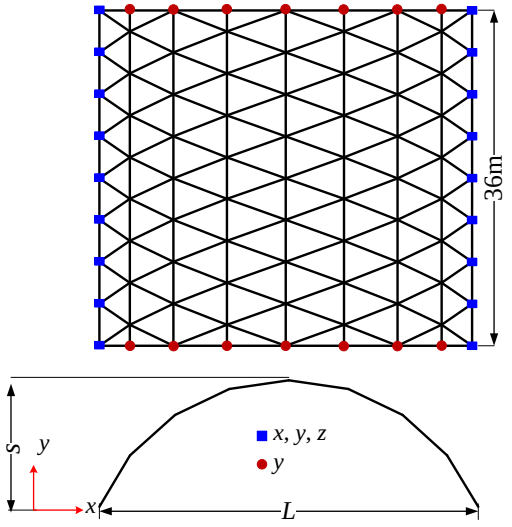

Fig. 13 Single-layer cylindrical reticulated shell model

To investigate the effect of joint stiffness on the load-carrying capacity of single-layer reticulated shells, this study employs a semi-rigid joint model, as shown in Fig. 14 [40]. Each member of the reticulated shell is modeled using 10 beam elements, as illustrated in Fig. 14(a). The distance between the centers of two joints *i*' and *j*', denoted as *l*, is considered. To account for joint size, two rigid beams are attached at both ends of each member, with a length equal to the diameter of the joint, denoted as $2\lambda l$. The actual length of the member is $(1\text{-}2\lambda)l$, where λ represents the joint size and is much smaller than 0.5. In this study, 2λ is set to 0.06. To simulate the semi-rigidity of the joint, two types of spring elements (the linear Combin14 and nonlinear Combin39 elements in the ANSYS package) are used to connect the ordinary and rigid beams, as shown in Fig. 14(a). In the ANSYS package, both the ordinary and rigid beams are modeled using the Beam188 element, which is suitable for analyzing slender to moderately stubby/thick beam structures and accounts for shear deformation effects, based on Timoshenko beam theory. The elastic modulus of the ordinary beam is assigned the actual value corresponding to the steel material used, while the elastic modulus of the rigid beam is increased by a factor of 1000 to represent infinite joint stiffness.

Fig. 14(b) illustrates a joint connecting six members, while the semi-rigid joint is simulated using both the linear spring element Combin14 and the nonlinear Combin39. At the junction of the ordinary and rigid beams, there are two coincident nodes. One node belongs to the ordinary beam, while the other one belongs to the rigid beam. These two nodes have the same coordinates, indicating that they coincide and the length of the spring element is zero. For each junction between the ordinary and rigid beams, a total of six springs are used. Three of springs are used to simulate translational stiffness (specifically, one axial stiffness K_{ax} and two shear stiffness K_{sy} and K_{sz}, as shown in Fig.14(b)), while the remaining three springs are used to simulate rotational stiffness (namely, two bending stiffness K_{by} and K_{bz}, and one torsional stiffness K_{tx}). In the typical joint area shown in Fig. 14(b), a total of 36 springs are present in the system, effectively simulating a semi-rigid joint. K_{bz} is simulated by nonlinear Combin39 element, while other stiffness are simulated by linear Combin14 element. According to the existing researches [40, 41], the bending stiffness K_{bz} of the strong axis of the joint has a significant effect on the bearing capacity of the reticulated shell, while other stiffness (axial, shear, torsion, weak axis bending stiffness) has slight effect. Therefore, the bending stiffness K_{bz} (Combin39) of the strong axis is taken from the bending moment-rotation angle curve obtained in Section 3 when carry out numerical calculation of the semi-rigid reticulated shell, while the stiffness of the other five types of stiffness (Combin14) is taken as a large value 10^{15} representing infinite stiffness.

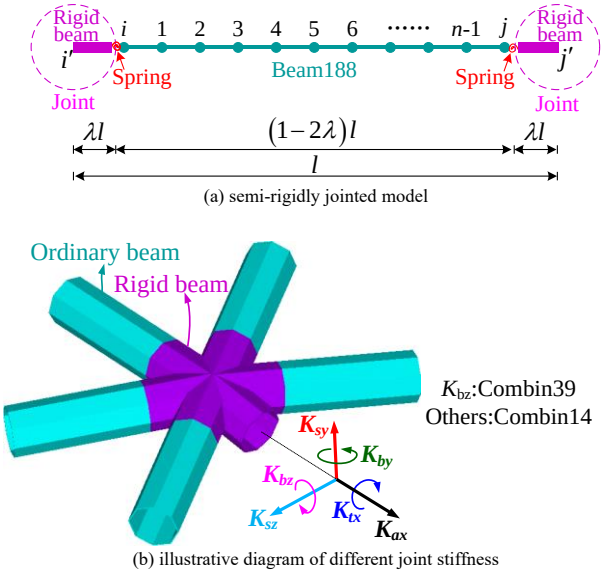

Fig. 14 Mechanical model considering joint size and joint semi-rigid stiffness

5.2. Stability analysis of reticulated shell with new sprayer joint

To systematically investigate the comparative performance of the new sprayer joint (i.e. BD-8-8) and the traditional socket joint in single-layer cylindrical reticulated shells, this section presents a comprehensive parametric study considering 100 spans of the reticulated shell. Table 6 summarizes the geometric parameters of the reticulated shell considered in the present parametric study. The bending moment-rotation curves obtained in Section 3 are imported into the ANSYS package (i.e. the semi-rigidly modeled reticulated shell described in Section 5.1), where the comparative performance of the new sprayer joint and the traditional socket joint in single-layer cylindrical reticulated shells is analyzed in detail.

Table 6
Parametric study of cylindrical reticulated shell with new sprayer joint

Joint	Span *L*/m	Rise-to-span ratio *s*/*L*	No.
New sprayer joint	30–70	1/3	100
Socket joint	30–70	1/3	100
Summary			200

The ultimate load of reticulated shells with different spans was obtained using the arc-length method, considering both material and geometric nonlinearity. The ultimate load of reticulated shells with sprayer joints was normalized by the ultimate load of rigid reticulated shells and plotted against the parameter of the reticulated shells (i.e. span), as shown in Fig. 15. The results

revealed that (i) the ultimate load of the new sprayer joint reticulated shell has significantly increased compared to the traditional socket joint, indicating an efficient and successful design approach for the new sprayer joint, and (ii) the bending stiffness of the new sprayer joint reticulated shell with a large span has a greater influence on the bearing capacity of the reticulated shell. The typical failure mode of the new sprayer joint reticulated shell is shown in Fig. 16. The single-layer cylindrical reticulated shell is observed to fail due to local joint failure combined with flexural buckling of the members, as depicted in Fig. 16.

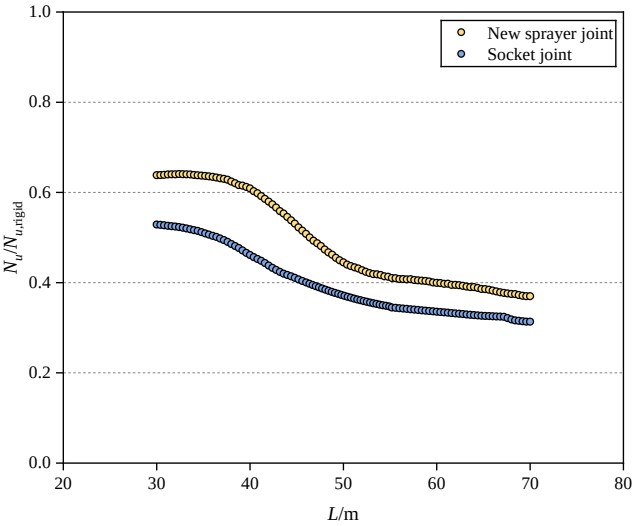

Fig. 15 Ultimate load of reticulated shells with sprayer joints and socket joint normalized by that of the rigid shell

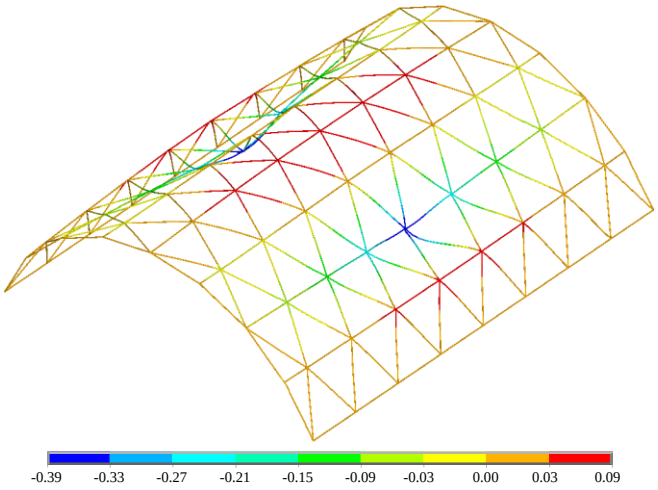

(a) L=30m, s/L=1/3

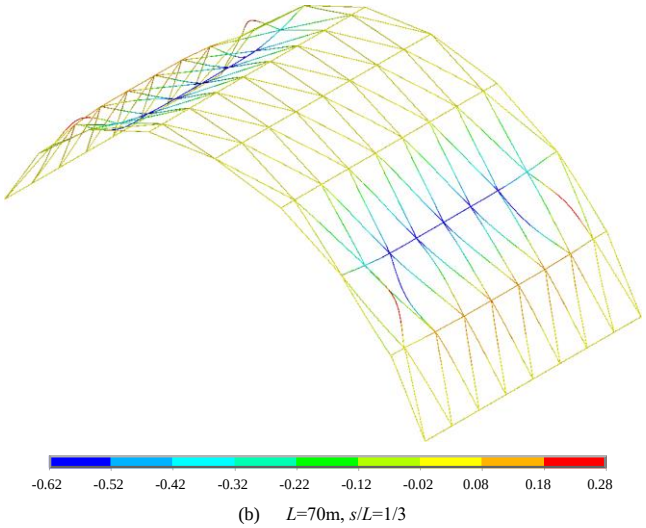

(b) L=70m, s/L=1/3

Fig. 16 Typical failure mode of reticulated shell with sprayer joint

6. Conclusion

This paper develops a novel sprayer joint that features a more rational force transmission mechanism. Initially, the joint is designed, followed by finite element simulation and mechanical analysis. Subsequently, the bending performance of the new sprayer joints under various surrounding bolt radii and load schemas is investigated. The improved bilinear model is established to depict the bending moment-rotation curve by parametric study. Finally, the comparative performance of the new sprayer joint and the traditional socket joint in single-layer cylindrical reticulated shells is studied in detail. The main research contents and conclusions of this study are summarized as follows:

(1) The new sprayer joint exhibits a considerable enhancement in bending stiffness and ultimate bending moment compared with the socket joint, with a slight increase in material cost.

(2) The surrounding bolt radius and load conditions have a substantial effect on the bending performance of the new sprayer joints. As the bolt radius increases, the initial stiffness remains relatively constant, while the ultimate bending moment significantly increases, resulting in a shift in failure mode. Moreover, axial compression boosts the initial stiffness and ultimate bearing capacity, postponing bolt necking, whereas axial tension diminishes these characteristics and triggers premature yielding of surrounding bolts under particular circumstances.

(3) The improved bilinear mode is proposed, and the bending moment-rotation curve of the sprayer joint can be determined by developed equation when the surrounding bolt diameter radius and loading schemas of the joint are known. Bending stiffness and yield moment provided by the bilinear model align well with the numerical results. The proposed bending moment-rotation curve effectively characterizes the bending performance of the joint, thereby offering valuable insights for joint design and application.

(4) The comparative performance of the new sprayer joint and the traditional socket joint in single-layer cylindrical reticulated shells is analyzed in detail. The results revealed that (i) the ultimate load of the new sprayer joint reticulated shell has significantly increased compared to the traditional socket joint, indicating an efficient and successful design approach for the new sprayer joint, and (ii) the bending stiffness of the new sprayer joint reticulated shell with a large span has a greater influence on the bearing capacity of the reticulated shell.

Acknowledgements

This work was supported by National Natural Science Foundation of China (No.51408490), Natural Science Basic Research Program of Shaanxi (2022JM-234), Training Programs of Innovation and Entrepreneurship for Undergraduates (202310712067, 202410712019), are gratefully appreciated.

Declarations

Conflict of interest: No potential conflict of interest was reported by the authors.

Reference

[1] Fan F., Ma H., Chen G. and Shen S., “Experimental study of semi-rigid joint systems subjected to bending with and without axial force”, Journal of Constructional Steel Research, 2012, 68(1), pp.126-137.
[2] Fan F., Ma H., Cao Z. and Shen S., “Direct estimation of critical load for single-layer reticulated domes with semi-rigid joints”, International Journal Space Structure, 2010, 25(1), pp.15-24.
[3] Zhang X., Li H., Yu X. and Han J., “Research on stiffness and bilinear model of hub-shape inlay joints”, Spatial Structures, 2022, 28(2), pp.56-62.
[4] Xiao Z., Li R., Li H., Bi S. and Li B., “Effect of joint stiffness on the load- carrying capacity of single-layer cylindrical reticulated shell with improved bolt-column (IBC) joint”, Thin-Walled Structures, 2024, 198, pp.111691.
[5] Elhout E., “Effect of beam-column connection types on the response modification factors of steel frames”, International Journal of Steel Structures, 2024, 24(1), pp.132-143.
[6] Fan J., Wu Z., Liu J., Wang, Y., Zheng, H. and Tee, K., “Damage and failure of semi-rigid steel joints during progressive collapse”, Structures, 2023, 58, pp.05632.
[7] Gou B., Wang X., Wu C. and Wang R., “Experimental investigation of aluminium alloy gusset joints' dynamic response to lateral impact loads: Evaluating the influence of gusset plate bending stiffness”, Structures, 2024, 62, pp.106288.
[8] Qi L., Yuan Z. and Xue J., “Experimental and numerical study on seismic performance of steel semi-rigid joints equipped with SMA bars and friction dampers”, Engineering Structures, 2024, 301, pp.117320.
[9] Xiao Z., Li R., Li H., Yan G., Fan R. and Jiang S., “Effect of joint behaviors on the load-carrying capacity of single-layer reticulated dome”, Structures, 2024, 68, pp.107124.
[10] Reinosa J., Loureiro A., Gutierrez R. and Lopez, M., “Artificial neural network prediction of the initial stiffness of semi-rigid beam-to-column connections”, Structures, 2023, 56, pp.104904.
[11] Tan Y., Zhang Y., Zhang Q. and Fan F., “Structural performance of a novel combined nested bolted joint for aluminum alloy mega-latticed structures”, Structures, 2023, 57, pp.105246.
[12] Wang X., Lu G., Liu Y., Chen Z., An Q. and Wang X., “Lateral stiffness of modular steel joint

with semi-rigid bolted intra-module connection", Journal of Building Engineering, 2024, 97, pp.110668.
[13] Wu Z., Lu X., Bao H., Li L. and Lu Z., "Experimental response of semi-rigid reinforced concrete beam-column joints with bolted angle dissipating connections", Journal of Building Engineering, 2024, 90, pp.109345.
[14] Yao H. Huang Y., Ma W., Liang L. and Zhao Y., "Dynamic analysis of a large deployable space truss structure considering semi-rigid joints", Aerospace, 2023, 10(9), pp.821.
[15] Xiao Z., Li R., Li H., Luo G. and Li B., "Research on bending performance and bilinear model of an improved bolt-column (BC) joint", Advanced Steel Construction, 2024, 20, pp.3-10.
[16] Dong S., Yu Y., Ge H. and Luo Y., "Nonlinear dynamic collapse analysis of space semi-rigid frames using finite particle method", Journal of Constructional Steel Research, 2024, 216, pp.108607.
[17] Jiao Z., Cui L., Liu H., Wei J., Xu D. and Bao Y., "Design and numerical analysis of new earthquake-resilient semi-rigid joints", Journal of Constructional Steel Research, 2024, 213, pp.108393.
[18] Lemes I., Silveira R., Teles L. Barros R. and Silva A., "Numerical formulation for advanced non-linear static analysis of semi-rigid planar steel frames", Journal of the Brazilian Society of Mechanical Sciences and Engineering, 2023, 45(7), pp.358.
[19] Liu D., Zheng Y., Wang Z., Pan J., Hu, S. and Yin T., "Boundary-oriented optimization of semi-rigid connections in steel frames using BNSGA", Journal of Constructional Steel Research, 2024, 214, pp.108471.
[20] Lu S., Wang M., Han X. and Yin T., "Seismic performance analysis of semi-rigid steel frame based on panel zone mechanical characteristics of the joint experiment study", Ksce Journal of Civil Engineering, 2024, 28(5), pp.60-79.
[21] Ma H., Zhao C., Jiang Y., Zhou J. and Wang Y., Rotational resistance test of a new aluminum alloy penetrating (AAP) joint system", Advanced Steel Construction, 2023, 19(2), pp.121-129.
[22] Li R., Su A., Wang Y. and Zhao O., "Geometric analysis and local buckling behavior of wire arc additively manufactured ER110S cruciform section stub columns", Engineering Structure, 2025, 322, pp.118819.
[23] Petrovic M., Pavicevic D., Ilic I., Terzovic J. and Sekularac N., "Elements of a timber lamella structure: analysis and systematization of joints", Buildings, 2023, 13(4), pp.885.
[24] Wang G., Zhuo X., Zhang S. and Wu J., "Study on the mechanical properties and design method of frame-unit bamboo culm members based on semi-rigid joints", Buildings, 2024, 14(4), pp.991.
[25] Xiao S., He Y., Golea T., Denoël V. and Demonceau J., "Simplified methods to predict the robustness of steel parking-structure joints", Journal of Constructional Steel Research, 2024, 213, pp.108355.
[26] Yu J., Zhao C., Zhong W., "Seismic behavior of partially encased composite columns-steel plate shear wall structure with different semi-rigid joints", Journal of Building Engineering, 2024, 82, pp.108177.
[27] Feng F., Ma H. and Shen S., "Numerical simulation and experimental study on mechanical characters of bolt-ball joint system", Engineering Mechanics, 2009, 26(12), pp.92-99.
[28] Zhang X., Li H., Chen X., Zhu Z. and Yu X., "Research on stiffness of hub-shape inlay joint and bearing capacity of single-layer spherical reticulated shell", Engineering Mechanics, 2022, 39(9), pp.179-190.
[29] Guo X., Zhu S., Xiong Z. and Luo Y., "Design method for buckling capacity of K6 single-layer reticulated shells with aluminum alloy gusset joints", Journal of Building Structures, 2017, 38(7), pp.16-24.
[30] Fan F., Ma H., Chen G. and Shen S., "Experimental study of semi-rigid joint systems subjected to bending with and without axial force", Journal of Constructional Steel Research, 2012, 68(1), pp.126-137.
[31] Ma H., Fan F., Chen G., Chao Z. and Shen S., "Numerical analyses of semi-rigid joints subjected to bending with and without axial force", Journal of Constructional Steel Research, 2013, 90, pp.13-28.
[32] Shi M., Xiang P. and Wu M., "Experimental investigation on bending and shear performance of two-way aluminum alloy gusset joints", Thin-Walled Structures, 2018, 122, pp.124-136.
[33] Wu F. and Chen W., "A design model for semi-rigid connections", Engineering Structures, 1990, 12(2), pp.88-97.
[34] Ma H., Ren S. and Fan F., "Parametric study and analytical characterization of the bolt-column (BC) joint for single-layer reticulated structures", Engineering Structures, 2016, 123, pp.108-123.
[35] Frye M. and Morris G., "Analysis of flexibly connected steel frames", Canadian Journal of Civil Engineering, 1975, 2(3), pp.280-291.
[36] Mohammad R., Hoshyar N. and John E., "Proposed mathematical model for semi-rigid joint behaviour (M-θ) in space structures", International Journal of Space Structures, 2014, 29(2), pp.71-80.
[37] Chen W. and Kishi N., "Semi-rigid steel beam-to-column connections: data base and modeling", Journal of Structural Engineering, 1989, 115(1), pp.105-119.
[38] Li R., Xiao Z., Li, H. and Li B., "Research on bending stiffness of the new sprayer joint", International Journal Steel Structure, 2024, 24, pp.256-263.
[39] Zhao C., Zhou Y., Wang G., Li H. and Wang Y. "Calculation method of the bearing capacity of a novel modular joint of an aluminium alloy lattice shell structure", Structures, 2021, 34, pp.3268-3282.
[40] Li H. and Taniguchi Y., "Effect of joint stiffness and size on stability of three-way single-layer cylindrical reticular shell", International Journal of Space Structures, 2020, 35(3), pp.90-107.
[41] Li H. and He S., "Stability of semi-rigid jointed space truss considering member instability", Spatial Structures, 2019, 25(04), pp.18-26.

Advanced Steel Construction – Vol. 21 No. 1 (2025) 42–53
DOI:10.18057/IJASC.2025.21.1.4

SECOND-ORDER INELASTIC ANALYSIS OF STEEL FRAME STRUCTURES USING IMPROVED FIBER PLASTIC HINGE METHOD

Fan Xu [1, 2], Yi-Qun Tang [1, 2, *], Xiao-Meng Ding [1, 2], De-Hong Huang [3, 4] and Yao-Peng Liu [3, 4]

[1] *School of Civil Engineering, Southeast University, Nanjing, China;*
[2] *Jiangsu Key Laboratory of Mechanical Analysis for Infrastructure and Advanced Equipment, Nanjing, China*
[3] *School of Civil Engineering and Transportation, South China University of Technology, Guangzhou 510641, China;*
[4] *State Key Laboratory of Subtropical Building and Urban Science, South China University of Technology, Guangzhou 510641, China*
** (Corresponding author: E-mail: yi-qun.tang@seu.edu.cn)*

ABSTRACT

In the realm of inelastic analysis for steel structures, the plastic hinge method is recognized for its computational efficiency but is often criticized for its lower accuracy than the plastic zone method. The present study aims to improve the accuracy of the plastic hinge method by discretizing the cross-section of the plastic hinges located at the element ends. Besides, the proposed fiber plastic hinge method is more efficient than the plastic zone method where each cross-section at the integration points of the element should be discretized. This study utilizes the improved fiber plastic hinge method to compute the initial and full yield surfaces of the cross-section, determine the section spring stiffness, and integrate this method into the second-order inelastic analysis of steel frame structures. Several classic benchmark problems are solved by the present method and the obtained results are compared with results generated by the plastic zone method as implemented in finite element software. The comparison reveals that the proposed fiber plastic hinge method matches the plastic zone method in terms of high accuracy for predicting the inelastic behavior of steel structures, with the added advantage of greater efficiency.

ARTICLE HISTORY

Received: 10 September 2024
Revised: 10 September 2024
Accepted: 9 October 2024

KEYWORDS

Steel structures;
Second-order inelastic analysis;
Fiber plastic hinge;
Beam-column element;
Transverse shear deformation

1. Introduction

Over the past several decades, technological advancements have significantly accelerated the evolution of the second-order analysis method for steel frame structures. The second-order analysis can fully account for the geometric nonlinearities of the P-Δ and P-δ effects. Thus, it eliminates the need to consider the effective length of each component during the stability design process, and the classification of the frame in the analysis process is not required. In light of this, it has been fully integrated into the steel structure design codes of numerous countries [1]. To predict more accurately the actual response of the steel structure, the influence of material nonlinearity should be taken into account in the analysis [2]. However, considering both geometric and material nonlinearities in analysis consumes a considerable amount of time. Therefore, improving both the accuracy and efficiency of second-order inelastic analysis for steel frame structures is a pivotal research topic.

The second-order plastic hinge analysis method based on the concept of one element per member has been verified as efficient and suitable for practical engineering design [5,6]. It enables the simulation of steel structures with fewer nodes and elements, thereby markedly reducing computational costs [7-9]. To ensure the accuracy of the local second-order effect in the displacement-based beam-column element, high-order interpolation should be adopted in the derivation of element formulations. For instance, Lu et al. [10] utilized a fourth-order polynomial function to simulate the vertical displacement of the beam-column element, deriving a fourth-order element and conducting the nonlinear analysis of steel structures. Chan et al. [11][12] introduced the pointwise equilibrating polynomial (PEP) element, which adopts a fifth-order polynomial function to model the vertical displacement of the beam-column element, achieving significantly higher computational accuracy than other elements. Based on the PEP element, Tang et al. [13] proposed a new second-order beam-column element based on Timoshenko beam theory. Both transverse shear deformation and local second-order effect are taken into account simultaneously in the element formulations, enabling accurate results to be obtained using only one element per member in structural analysis. Doan-Ngoc et al. [14] further improved the accuracy of the calculation by using an approximate seventh-order polynomial function to simulate the vertical displacement of the element.

The plastic zone method and the plastic hinge method are the mainstream approaches for the inelastic analysis of steel frame structures. The former approach discretizes the cross-section and length of the element, so it requires significant computational resources and can provide nearly exact solutions. The latter approach considers the inelastic behavior of the steel member only at the element ends and the discretization of cross-section is commonly not required in the analysis. Thus, the derived elastic second-order beam-column elements can be integrated with the plastic hinge method to realize the second-order inelastic analysis of steel frame structures with relatively low effort. However, the accuracy of the plastic hinge method is not as good as the plastic zone method. To enhance it, many researchers have contributed great efforts in the last three decades.

In early research about the second-order plastic hinge analysis of steel frame structures, Kassimal et al. [15] proposed a simple plastic hinge model and integrated it with the stability functions which are closed-form solutions of the second-order beam-column element based on Euler-Bernoulli beam theory. In this model, the hinges at element ends are assumed to be ideally elastoplastic and overlook the gradual yielding process of the hinge cross-section, resulting in reduced precision in modeling the elastoplastic behavior of the element. To solve this issue, Liew et al. [16] introduced a refined plastic hinge method that considers a gradual reduction in the inelastic stiffness of the element. Nguyen et al. [17] considered the gradual yield of plastic hinges by introducing a stiffness degradation formula for springs at both ends of beam-column elements. Zhou et al. [18] proposed an improved refined plastic hinge model using an approximate sixth-order polynomial function to simulate transverse displacements in beam-column elements, incorporating second-order effects between axial loads and bending moments into the element formulation. Liu et al. [19][20] proposed a new type of beam-column element, in which a plastic hinge can be formed at any position on the element. For nonlinear materials with obvious hardening effects, such as stainless steel, Fieber et al.[21][22], Gardner et al.[23], Walport et al.[24], and Quan et al. [25] proposed a new approach for second-order inelastic analysis of steel frame structures.

Although many researchers have endeavored to improve the accuracy of the plastic hinge model, the differences in precision between the plastic hinge model and the plastic zone model are still apparent. Thus, this paper aims to further improve the precision of the plastic hinge model in the second-order inelastic analysis of steel frame structures. The present study proposes modifications to the classic end-spring-type plastic hinge model through the incorporation of the fiber plastic hinge concept. The classic model comprises a second-order beam-column element and two zero-length spring elements positioned at both ends, assuming that the beam-column element is in an elastic state throughout and elastoplastic behavior is only confined to the spring elements [3][4]. The accuracy of this model depends primarily on determining the initial and full yield surfaces of the cross-section, as well as the spring stiffness, which is typically empirical and approximate. Thus, the present study discretizes the sections of the spring elements and computes more accurate initial and full yield surfaces of the cross-section, as well as the moment-curvature relationship. Then, the length of the plastic hinge and the spring stiffness are determined according to numerical tests. Furthermore, to ensure the accuracy of the structural analysis using one element per member, this study adopts a second-order beam-column element based on the Timoshenko beam theory [13]. The element takes into

account both local second-order effects and transverse shear deformation. In addition, the present study integrates an advanced incremental-iterative force recovery method [26]. Finally, several benchmark problems are solved by the present study, and the results are compared with those from previous literature and the plastic zone method in ANSYS. The comparison verifies the accuracy, efficiency, and robustness of the proposed methodology and computational program for the second-order inelastic analysis of steel frame structures using only one element per member.

2. Element model and assumptions

Assumptions for the planar element model in this study are given as follows: 1. The applied loads are nodal and conservative; 2. The cross-section of the member is doubly symmetric and remains planar after deformation, neglecting warping and torsion; 3. The element exhibits small-strain and large-displacement characteristics; 4. The transverse shear deformation of the members is considered based on Timoshenko beam theory, while the local second-order effects (bowing effects) in the element are permitted; 5. The interior beam-column element is prismatic and elastic throughout the inelastic analysis, situated between the two spring elements; 6. The elastoplastic behavior of the element is confined to its ends where plastic hinges are simulated using zero-length springs; 7. The material is assumed to be elastic-perfectly plastic, ignoring strain-hardening effects.

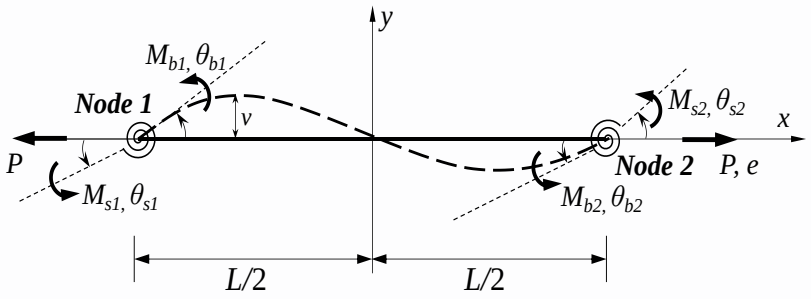

Fig. 1. Beam-column element model with plastic hinges

Fig. 1 depicts a beam-column element with two spring elements at both ends, where L represents the length of the beam-column element; E and I denote Young's modulus and moment of inertia, respectively. M_{si} (i=1,2) are the bending moments acting on the external nodes i, with θ_{si} (i=1,2) being the corresponding rotations. M_{bi} (i=1,2) signifies the bending moments acting on internal node i, located at the interface between the spring elements and the beam-column element, with θ_{bi} (i=1,2) as their respective rotations. P and e represent the axial force and axial displacement of the element, respectively. $v(x)$ denotes the transverse displacement function of the element.

3. Improved fiber plastic hinge method

In the traditional end-spring-type plastic hinge model, the full yield surface of the cross-section and the spring stiffness are determined commonly using a simplified and empirical method, therefore it is difficult to obtain accurate results as good as those by the plastic zone model. To fill this gap, the present study utilizes the fiber hinge concept to improve the accuracy of the end-spring-type plastic hinge model. This section presents how to utilize the improved fiber plastic hinge method for calculating the initial and full yield surfaces, the moment-curvature curve of the cross-section, as well as the stiffness of the fiber section spring element.

3.1. Discretion of wide flange section

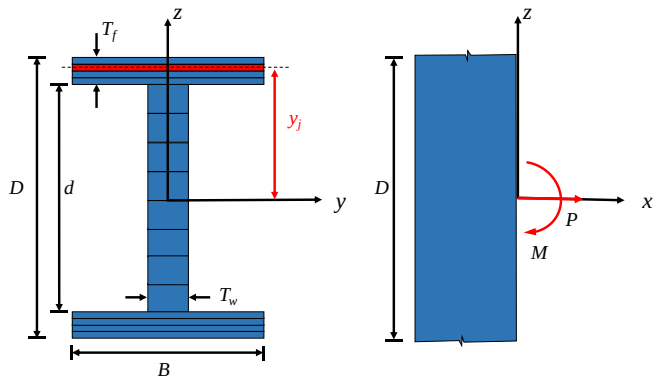

Fig. 2. Discretization of cross-section

Fig. 2 depicts the discretization of the wide flange section under the axial force P and the major-axis bending M. Assume that the stress at the j-th fiber σ_j is uniform, so the axial force P and the major-axis bending M can be given by,

$$P = \sum_{j=1}^{N} \sigma_j A_j \tag{1}$$

$$M = \sum_{j=1}^{N} \sigma_j A_j y_j \tag{2}$$

in which, A_j represents the area of the j-th fiber; y_j denotes the distance from the centroid of the j-th fiber to the center of the wide flange section. Besides, this paper denotes the width and height of the j-th fiber as b_j and Δh_j, respectively; N is the total number of fibers in the section.

3.2. Initial and full yield surfaces of fiber section

When the wide flange section is subjected to a combined action of axial force and bending moment, for a given axial force P, the ultimate elastic moment capacity of the section can be easily given as follows

$$M_{er} = (\sigma_y - \frac{P}{A}) \frac{I}{y_{j\max}} \tag{3}$$

where A is the total section area, σ_y represents the yield stress and I is the moment of inertia of the cross-section about the major axis z; y_{jmax} denotes the distance from the centroid of a layer of fibers farthest from the neutral axis.

When the wide flange section reaches the ultimate limit state of bearing capacity, stresses at all fibers are equal to the yield stress, as shown in Fig. 3. Furthermore, the offset of the neutral axis from the center of the cross-section β should be considered in the determination of the ultimate plastic moment capacity of the discrete wide flange section.

Residual stresses are not considered herein, so the offset of the neutral axis from the center of the cross-section β can be calculated in the following,

$$p = \frac{P}{P_y} \tag{4}$$

$$\beta = \frac{p \cdot A}{2T_w} \qquad for \quad p < \frac{A_w}{A} \tag{5}$$

$$\beta = \frac{p \cdot A - A_F - A_w}{2B} + \frac{D}{4} + \frac{d}{4} \qquad for \quad p \geq \frac{A_w}{A} \,\&\&\, p \leq 1 \tag{6}$$

where P_y is the axial force capacity of the cross-section; A_w represents the area of the web, and A_F is the area of the flange.

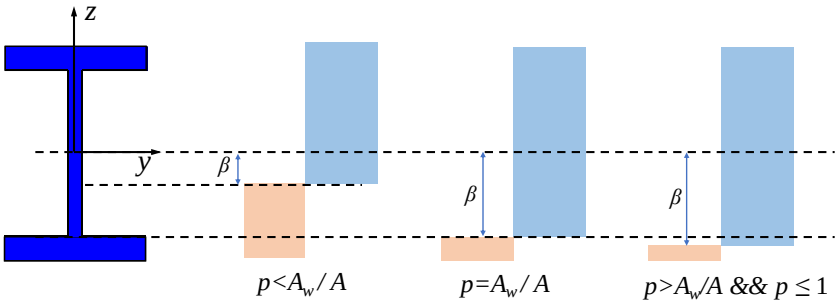

Fig. 3. Diagram of the complete yield stress under different axial forces

After the calculation of β, the ultimate plastic moment capacity M_{pr}, which the axial force may reduce, can be defined as the sum of three parts,

$$M_{pr} = M_{p1} + M_{p2} + M_{p3} \tag{7}$$

$$M_{p1} = -\sum b_j \cdot \Delta h_j \cdot y_j \cdot \sigma_y \qquad for\ y_j + \frac{\Delta h_j}{2} \le -\beta \tag{8}$$

$$M_{p2} = \sum b_j \cdot \Delta h_j \cdot y_j \cdot \sigma_y \qquad for\ y_j - \frac{\Delta h_j}{2} \ge -\beta \tag{9}$$

$$M_{p3} = \sum \left(\frac{\sigma_y b_j (y_j + \frac{\Delta h_j}{2} + \beta)(y_j + \frac{\Delta h_j}{2} - \beta)}{2} - \frac{\sigma_y b_j (-\beta - (y_j - \frac{\Delta h_j}{2}))(y_j - \frac{\Delta h_j}{2} - \beta)}{2} \right) \quad for \quad y_j + \frac{\Delta h_j}{2} > -\beta \ \&\& \ y_j - \frac{\Delta h_j}{2} < -\beta \tag{10}$$

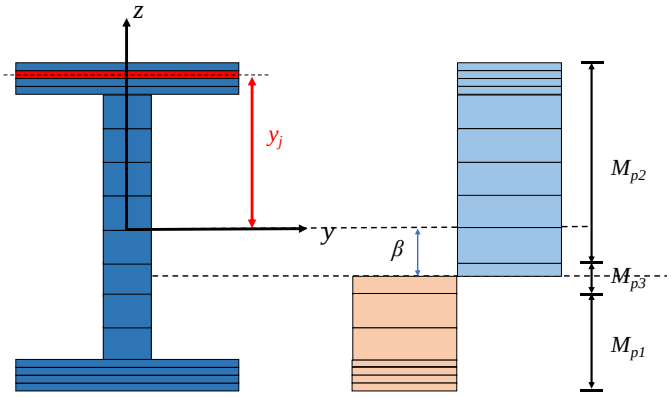

Fig. 4. The calculation of the ultimate moment capacity

Fig. 4 shows the definitions of the three parts contributing to the ultimate plastic moment capacity. When the j-th fiber is completely located below the neutral axis, its contribution to the cross-section's moment capacity is M_{p1} in Eq. (8). When the j-th fiber is completely located above the neutral axis, its contribution to the cross-section's moment capacity is M_{p2} given by Eq. (9). M_{p3} is calculated by artificially dividing the layer of fiber into two parts when the neutral axis of the cross-section intersects during the layer, resulting in Eq. (10). When P is equal to zero, M_{pr} is equal to the ultimate plastic moment capacity of the cross-section only under pure bending, M_p.

The ultimate elastic moment capacity M_{er} and the ultimate plastic moment capacity M_{pr} of the cross-section can be computed by Eq. (3) and Eqs. (7-10), respectively. The initial and full yield surfaces are depicted in Fig. 5 according to the calculation of M_{er} and M_{pr} for a given axial force P. Fig. 6 shows the cross-section's stress distributions during the gradual yielding process under a fixed axial force P, where the stress distributions of Points 1, 2, and 3 correspond to the points in Fig. 5. Note that the derivation of the initial yield surface and the full yield surface is calculated based on the wide flange section of W21×50.

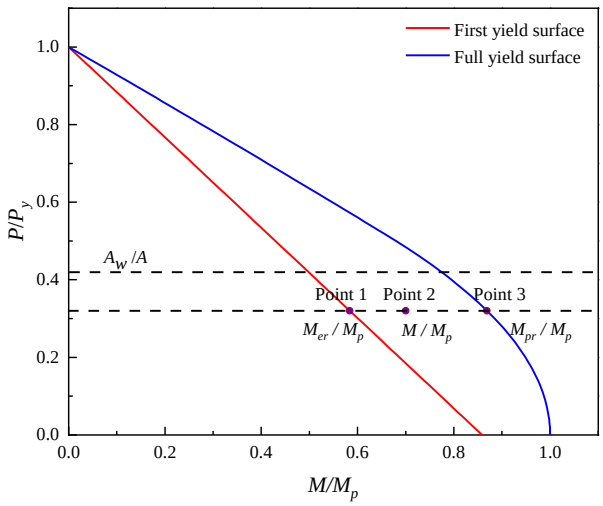

Fig. 5. First and full yield surfaces of section

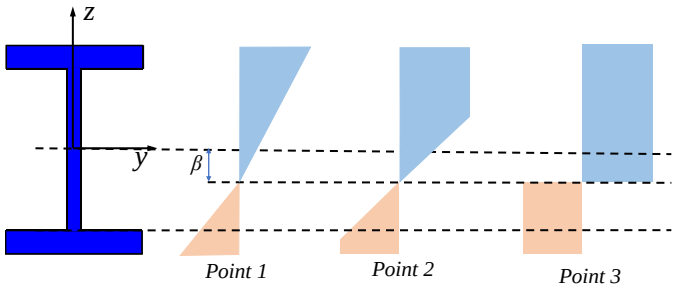

Fig. 6. Stress distribution

As shown in Fig. 5 and Fig. 6, the section is within the elastic range when the axial force and bending moment are within the initial yield surface. The section partially yields when the load coordinates between the initial and full yield surfaces. As the bending moment M increases, the extent of section yielding progressively intensifies, ultimately culminating in the full yield surface.

3.3. Moment-curvature curve for wide flange section

During an incremental-iterative load step of the end-spring-type plastic hinge analysis, the stiffness of the spring element is determined by the current forces applied to the spring element. Thus, this study employs the axial force and the bending moment applied to the fiber plastic hinge to calculate its curvature and the offset of the neutral axis.

According to the assumption of the elastic-perfectly plastic material model, the stress at the j-th layer of the cross-section is

$$\sigma_j = \begin{cases} E\varepsilon_j & for \quad \varepsilon_j < \sigma_y / E \\ \sigma_y & for \quad \varepsilon_j \geq \sigma_y / E \end{cases} \tag{11}$$

in which E is Young's modulus; ε_j is the strain at the j-th layer of the cross-section. It can be given as follows,

$$\varepsilon_j = \varepsilon_0 + \kappa(y_j + \beta) \tag{12}$$

where ε_0 is the strain due to the axial force P and it equals P/EA; κ and β are the curvature and the offset of the neutral axis of the cross-section, respectively.

The tangent modulus of the j-th layer of the cross-section can be easily given as follows,

$$E_{tj} = \begin{cases} E & for \quad \varepsilon_j < \sigma_y / E \\ 0 & for \quad \varepsilon_j \geq \sigma_y / E \end{cases} \tag{13}$$

To determine the curvature κ and the offset of the neutral axis β of the cross-section based on the known axial force F^n and the bending moment M^n at the current load step n, the *Newton-Raphson* iteration procedure should be constructed in the following,

$$\begin{bmatrix} \beta_{k+1} \\ \kappa_{k+1} \end{bmatrix} = \begin{bmatrix} \beta_k \\ \kappa_k \end{bmatrix} - \begin{bmatrix} \frac{\partial M_k}{\partial \beta} & \frac{\partial M_k}{\partial \kappa} \\ \frac{\partial P_k}{\partial \beta} & \frac{\partial P_k}{\partial \kappa} \end{bmatrix}^{-1} \begin{bmatrix} M^n - M_k \\ P^n - P_k \end{bmatrix} \tag{14}$$

$$\frac{\partial M_k}{\partial \beta} = E_{tj} \cdot \kappa \cdot b_j \cdot \Delta h_j \cdot y_j \tag{15}$$

$$\frac{\partial M_k}{\partial \kappa} = E_{tj} \cdot (y_j + \beta) \cdot b_j \cdot \Delta h_j \cdot y_j \tag{16}$$

$$\frac{\partial P_k}{\partial \beta} = E_{tj} \cdot \kappa \cdot b_j \cdot \Delta h_j \tag{17}$$

$$\frac{\partial P_k}{\partial \kappa} = E_{tj} \cdot (y_j + \beta) \cdot b_j \cdot \Delta h_j \tag{18}$$

in which the axial force P_k and the moment M_k are computed by substituting the curvature κ_k and the offset of the neutral axis β_k at the k-th iteration into Eqs. (12), (11), (1), and (2) in sequence.

The iteration procedure in Eq. (14) terminates when the following convergence criteria are satisfied,

$$\left| \frac{M^n - M_k}{M^n} \right| \leq Tolerance \tag{19}$$

$$\left| \frac{P^n - P_k}{P^n} \right| \leq Tolerance \tag{20}$$

in which *Tolerance* is set to 10^{-6} in the present study.

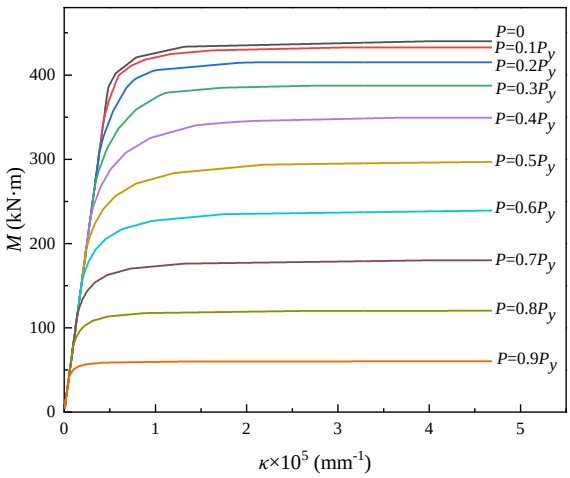

Fig. 7. Moment-curvature curves at different axial forces

Based on the algorithm presented before, Fig. 7 shows moment-curvature curves at different axial forces, taking the wide flange section of W21×50 for example.

3.4. Stiffness of fiber section spring element

In the end-spring-type plastic hinge model, the stiffness of the section spring element is infinite when it is elastic, which means that the difference in rotation between the spring element and the interior beam-column element is zero. The stiffness varies from infinity to zero as the moment transitions from initial yielding to full yielding. Thus, in the computational procedure, the spring stiffness is set to a large value, $10^{10}\,EI/L$, instead of infinity when the spring element is elastic, while the spring stiffness is set to zero when the spring element is fully plastic. The key point of the end-spring-type plastic hinge model lies in the definition of the spring stiffness during partial yielding which controls the gradual yielding progress of the member. Therefore, this section introduces how to determine the spring stiffness during partial yielding based on the improved fiber plastic hinge method.

Fig. 8 presents the moment-curvature curve for the section of W21×50 under pure major-axis bending moment. Where M_{pr} is calculated by Eq. (7) and M_{er} is calculated by Eq. (3). It can be seen from Fig. 8 that the total curvature κ can be divided into two parts when the section partially yields, including the elastic curvature κ_e and the plastic curvature κ_p.

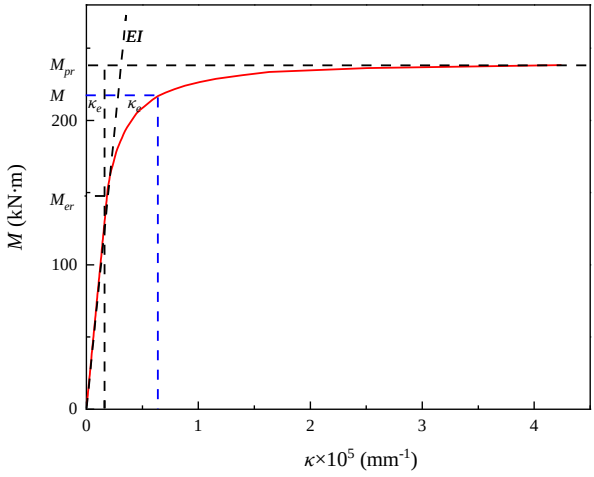

Fig. 8. Moment-curvature curve

Note that the difference in nodal rotation between the spring element and the interior beam-column element during the partial yielding state is due to the plastic deformation of the spring element. Thus, the spring stiffness during partial yielding is related to the relationship between moment and plastic curvature. Fig. 9 presents the moment-plastic curvature curve, from which the differential relationship between moment and plastic curvature can be derived as follows

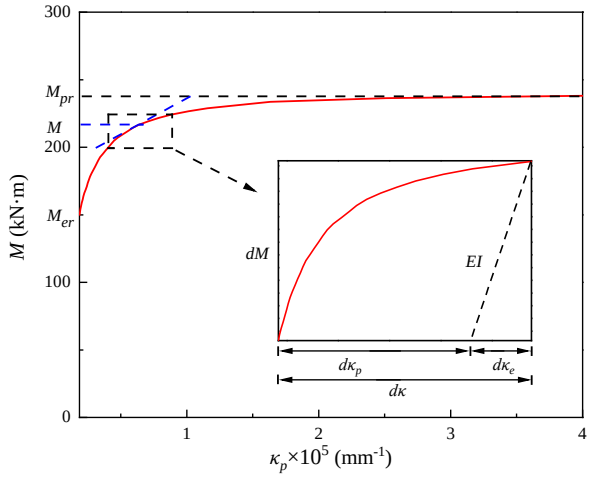

Fig. 9. Moment-plastic curvature curve

$$\frac{\mathrm{d}M}{\mathrm{d}\kappa_{\mathrm{p}}}=\frac{\dfrac{\mathrm{d}M}{\mathrm{d}\kappa}\dfrac{\mathrm{d}M}{\mathrm{d}\kappa_{\mathrm{e}}}}{\dfrac{\mathrm{d}M}{\mathrm{d}\kappa_{\mathrm{e}}}-\dfrac{\mathrm{d}M}{\mathrm{d}\kappa}} \tag{21}$$

$$\frac{\mathrm{d}M}{\mathrm{d}\kappa_{\mathrm{e}}}=EI_{\mathrm{z}} \tag{22}$$

$$\frac{\mathrm{d}M}{\mathrm{d}\kappa}=-\sum Et_j\cdot\left(-y_j+\beta\right)\cdot b_j\cdot\Delta h_j\cdot y_j \tag{23}$$

In the end-spring-type plastic hinge model, the spring stiffness is defined as the relationship between moment and rotation. Thus, to transfer the differential relationship between moment and plastic curvature into the spring stiffness, a parameter named the length of the plastic hinge L_p is assumed, and the spring stiffness S_s can be given by,

$$S_s=\frac{\mathrm{d}M}{\mathrm{d}\theta_{\mathrm{p}}}=\frac{1}{L_{\mathrm{p}}}\frac{\mathrm{d}M}{\mathrm{dk}_{\mathrm{p}}} \tag{24}$$

This study performed a large number of numerical tests of several wide flange sections under various loading combinations. The comparison between the present plastic hinge model and the plastic zone model shows that the length of the plastic hinge is mainly affected by the bending moments at member ends and the member's axial force level. The plastic hinge length L_p of the spring

element during partial yielding is fitted according to the results from the simulation by the BEAM188 element in ANSYS in the following,

$$L_p = (0.02388e^{0.6789\xi} + 0.0003397e^{7.394\xi})\,(8.282e^{0.9745p} - 7.376e^{-7.109p})\,L \quad (25)$$

$$\xi = -\frac{\min\{|M_1|,|M_2|\}}{\max\{|M_1|,|M_2|\}} \qquad for\ \ M_1M_2 > 0 \quad (26)$$

$$\xi = \frac{\min\{|M_1|,|M_2|\}}{\max\{|M_1|,|M_2|\}} \qquad for\ \ M_1M_2 \le 0 \quad (27)$$

where M_1 is the bending moment at the member end associated with the current plastic hinge, M_2 is the bending moment at the other end of the member; and the abscissa ξ is the ratio of the two end moments. Fig. 10 shows the bending moment diagram of the member at different ratios of two end moments.

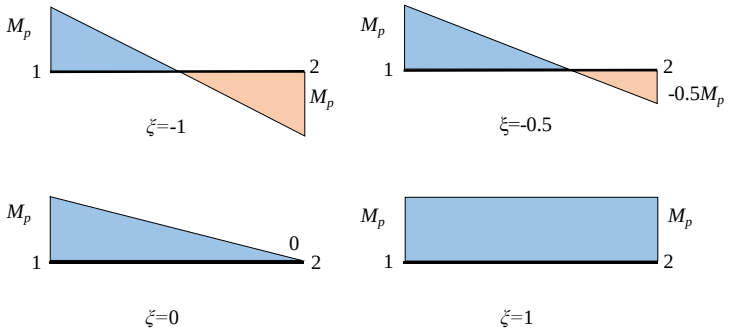

Fig. 10. Bending moment diagram of a member

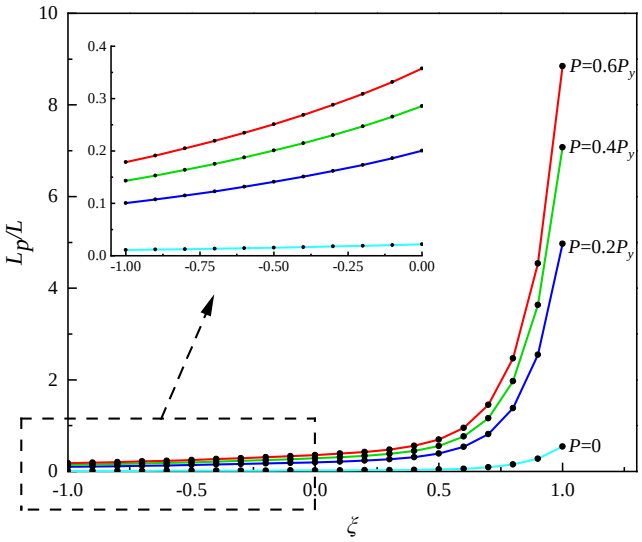

Fig. 11. Normalized L_p at different loadings

The length of plastic hinge L_p under different loadings is plotted in Fig. 11. It is observed that the length of the plastic hinge in a member tends to increase with the magnitude of the axial load and the ratio of the bending moments at the two ends of the member. However, the increase in plastic hinge length is less significant when the ratio of the end moments is negative, and it becomes more pronounced when this ratio exceeds 0.5.

4. Second-order inelastic analysis of steel frame structures

The improved fiber plastic hinge method is integrated into the second-order inelastic analysis of steel frame structures using one element per member. Additionally, this study employs a second-order beam-column element that accounts for both transverse shear deformation and bowing effects. It also utilizes a rigorous incremental-iterative recovery force method to further enhance the analysis's accuracy.

The integrated element model shown in Fig. 1 comprises an elastic second-order beam-column element and two spring elements. The two key factors in the nonlinear analysis are the tangent stiffness and the internal forces of the integrated element. Here the displacement and force vectors of the integrated element are denoted as $\boldsymbol{d}_s=\{\theta_{s1}, \theta_{s2}, e\}^{\mathrm{T}}$ and $\boldsymbol{f}_s=\{M_{s1}, M_{s2}, P\}^{\mathrm{T}}$, respectively.

4.1. Second-order beam-column element

The interior beam-column element adopted herein is proposed by Tang et al. [13]. It is derived from the Timoshenko beam theory, which incorporates both the bowing effect and the transverse shear deformation. As shown in Fig. 12, the element uses a fifth-order polynomial to assume transverse displacements, ensuring high accuracy using just one element per member in the analysis.

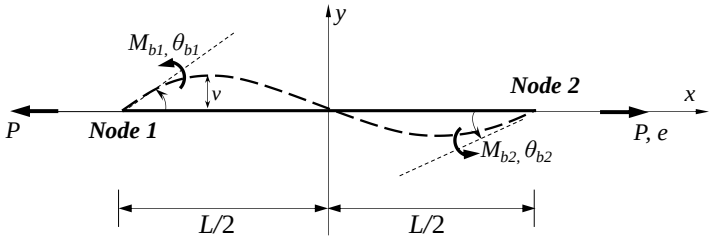

Fig. 12. Beam-column element

In the basic coordinate system, the presented beam-column element has three degrees of freedom, see Fig. 12. Its nodal displacement vector is $\boldsymbol{d}_b=\{\theta_{b1}, \theta_{b2}, e\}^{\mathrm{T}}$, while the corresponding nodal load vector is $\boldsymbol{f}_b=\{M_{b1}, M_{b2}, P\}^{\mathrm{T}}$. The secant relationships between the forces and the displacements of the element are given as follows:

$$M_{b1}=\frac{EI}{L}(S_1\theta_{b1}+S_2\theta_{b2}) \tag{28}$$

$$M_{b2}=\frac{EI}{L}(S_2\theta_{b1}+S_1\theta_{b2}) \tag{29}$$

$$P=EA(\frac{e}{L}+c_{\mathrm{b}}) \tag{30}$$

and

$$c_{\mathrm{b}}=b_1(\theta_{b1}+\theta_{b2})^2+b_2(\theta_{b1}-\theta_{b2})^2 \tag{31}$$

where S_i (i=1, 2) and b_i (i=1, 2) represent the stability functions considering the bowing effect and bow functions in the beam-column element, respectively. c_b is the length correction factor due to the bowing effect. For the sake of simplification, these functions are not detailed in this paper and can be found in Reference [26].

4.2. Tangent stiffness of the integrated element

In the incremental-iterative process of nonlinear structural analysis, the tangent stiffness of the integrated element is crucial, significantly influencing the convergence rate of the analysis. It is assembled by the tangent stiffness matrices of the interior beam-column element and the two spring elements.

The tangent stiffness matrix of the beam-column element is derived by variational operations on Eqs. (28-30). The resulting matrix is presented as follows,

$$[\boldsymbol{k}_e]=\frac{\partial \boldsymbol{f}}{\partial \boldsymbol{d}^T} \tag{32}$$

$$[\boldsymbol{k}_e]=\frac{EI}{L}\begin{bmatrix}\frac{1}{L^2H} & \frac{G_1}{LH} & \frac{G_2}{LH}\\ & c_1+c_2+\frac{G_1^2}{H} & c_1-c_2+\frac{G_1G_2}{H}\\ \text{sym.} & & c_1+c_2+\frac{G_2^2}{H}\end{bmatrix} \tag{33}$$

where the parameters H, G_1, G_2, c_1 and c_2 in Eq. (33) can be found in Reference [13].

After the determination of the spring stiffness, the differential moment-rotation relationship of the spring element located at node i of the element model can be easily given as follows,

$$\begin{Bmatrix}dM_{si}\\ dM_{bi}\end{Bmatrix}=\begin{bmatrix}S_{si} & -S_{si}\\ -S_{si} & S_{si}\end{bmatrix}\begin{Bmatrix}d\theta_{si}\\ d\theta_{bi}\end{Bmatrix} \quad (i=1, 2) \tag{34}$$

The tangent stiffness matrix of the end spring calculated in Eq. (34) and the tangent stiffness matrix of the beam-column elements calculated in Eq. (33) are assembled to form the overall tangent stiffness matrix of the integrated element. Note that the assembled moments, M_{b1} and M_{b2}, acting on the inner degrees of freedom, θ_{b1} and θ_{b2}, are zeros. Thus, the inner degrees of freedom, θ_{b1} and θ_{b2}, can be condensed in the assembled tangent stiffness matrix, leading to a 3×3 tangent stiffness matrix of the integrated element. This process is a classical finite element procedure and will not be described in detail herein.

After the determination of the tangent stiffness of the integrated element in the basic coordinate system, it can be transferred into the global system through the co-rotational technique and assembled into the tangent stiffness matrix of the whole structure.

4.3. Incremental iterative force recovery method

In the incremental-iterative process of nonlinear structural analysis, the force recovery method is pivotal to the accuracy of the results. Consequently, this study adopts a rigorous incremental-iterative force recovery method, as proposed by Tang et al. [26], to ensure a high level of precision in the analysis. This force recovery method adopts the incremental secant relationship between forces and displacements for the second-order beam-column element, offering greater precision than traditional methods that rely on the incremental tangent relationship of the element.

After an iteration of nonlinear structural analysis, the incremental pure deformations of the integrated element $\Delta\boldsymbol{d}_s=\{\Delta\theta_{s1}, \Delta\theta_{s2}, \Delta e\}^{\mathrm{T}}$ can be extracted from the incremental global displacements of the structure based on the co-rotational technique. Then, the internal forces of the integrated element at the current load step n+1 can be computed according to the incremental pure deformations of the integrated element and the known quantities of the element at the last load step n.

For the interior beam-column element, the incremental secant relationship between forces and displacements for the second-order beam-column element are,

$$\Delta M_{b1}=\frac{EI}{L}\left(S_1^{n+1}\Delta\theta_{b1}+S_2^{n+1}\Delta\theta_{b2}+\Delta S_1\theta_{b1}^n+\Delta S_2\theta_{b2}^n\right) \tag{35}$$

$$\Delta M_{b2}=\frac{EI}{L}\left(S_2^{n+1}\Delta\theta_{b1}+S_1^{n+1}\Delta\theta_{b2}+\Delta S_2\theta_{b1}^n+\Delta S_1\theta_{b2}^n\right) \tag{36}$$

$$\Delta P=EA\left(\frac{\Delta e}{L}+\Delta c_b\right) \tag{37}$$

and

$$\Delta M_{bi}=M_{bi}^{n+1}-M_{bi}^n \quad (i=1, 2) \tag{38}$$

$$\Delta S_i=S_i^{n+1}-S_i^n \quad (i=1, 2) \tag{39}$$

$$\Delta c_b=c_b^{n+1}-c_b^n \tag{40}$$

For the spring element at node i of the integrated element, the differential moment-rotation relationship depicted in Equation (34) from the last load step n is utilized to approximate its incremental relationship during both the elastic and partial yielding states. It can be given as follows,

$$\Delta M_{si}=S_{si}^n\left(\Delta\theta_{si}-\Delta\theta_{bi}\right) \quad (i=1, 2) \tag{41}$$

$$\Delta M_{bi}=S_{si}^n\left(\Delta\theta_{bi}-\Delta\theta_{si}\right) \quad (i=1, 2) \tag{42}$$

Once the spring element is fully plastic, its applied moment will stay on the full yield surface in the subsequent analysis process, and the incremental moment is the difference in the plastic moment capacity ΔM_{pr} which will be reduced due to the increase of the axial load. Therefore, when the spring element reaches a fully plastic state, Equations (41) and (42) should be superseded by the following equations

$$\Delta M_{si}=\Delta M_{pr,i} \quad (i=1, 2) \tag{43}$$

$$\Delta M_{bi}=\Delta M_{pr,i} \quad (i=1, 2) \tag{44}$$

It is noted that the bending moment M_{bi} at the inner degrees of freedom of the integrated element, θ_{b1} and θ_{b2}, must be zero (M_{bi}=0), implying that the increment of the bending moment ΔM_{bi} is also zero. Consequently, the following relationship can be established.

$$\frac{EI}{L}\left(S_1^{n+1}\Delta\theta_{b1}+S_2^{n+1}\Delta\theta_{b2}+\Delta S_1\theta_{b1}^n+\Delta S_2\theta_{b2}^n\right)+\Delta M_{b1}=0 \tag{45}$$

$$\frac{EI}{L}\left(S_2^{n+1}\Delta\theta_{b1}+S_1^{n+1}\Delta\theta_{b2}+\Delta S_2\theta_{b1}^n+\Delta S_1\theta_{b2}^n\right)+\Delta M_{b2}=0 \tag{46}$$

Depending on the state of the spring elements, $\Delta\theta_{bi}$ has different expressions. Specifically, when the spring element at both ends of the element is in either an elastic or elastoplastic state, the formulas for $\Delta\theta_{bi}$ are shown below,

$$\Delta\theta_{b1}=\left(\left(S_1^{n+1}+S_{s2}^{n}\right)\left(S_{s1}^{n}\Delta\theta_{s1}-\Delta S_1\theta_{b1}^{n}-\Delta S_2\theta_{b2}^{n}\right)-S_2^{n+1}\left(S_{s2}^{n}\Delta\theta_{s2}-\Delta S_2\theta_{b1}^{n}-\Delta S_1\theta_{b2}^{n}\right)\right)/\beta_1 \tag{47}$$

$$\Delta\theta_{b2}=\left(\left(S_1^{n+1}+S_{s1}^{n}\right)\left(S_{s2}^{n}\Delta\theta_{s2}-\Delta S_2\theta_{b1}^{n}-\Delta S_1\theta_{b2}^{n}\right)-S_2^{n+1}\left(S_{s1}^{n}\Delta\theta_{s1}-\Delta S_1\theta_{b1}^{n}-\Delta S_2\theta_{b2}^{n}\right)\right)/\beta_1 \tag{48}$$

and

$$\beta_1=\left(S_1^{n+1}+S_{s1}^{n}\right)\left(S_1^{n+1}+S_{s2}^{n}\right)-\left(S_2^{n+1}\right)^2 \tag{49}$$

If a fully plastic hinge is formed at node 1 of the element,

$$\Delta\theta_{b1}=\left(\left(S_1^{n+1}+S_{s2}^{n}\right)\left(\Delta M_{pr,1}-\Delta S_1\theta_{b1}^{n}-\Delta S_2\theta_{b2}^{n}\right)-S_2^{n+1}\left(S_{s2}^{n}\Delta\theta_{s2}-\Delta S_2\theta_{b1}^{n}-\Delta S_1\theta_{b2}^{n}\right)\right)/\beta_2 \tag{50}$$

$$\Delta\theta_{b2}=\left(\left(S_1^{n+1}+S_{s1}^{n}\right)\left(S_{s2}^{n}\Delta\theta_{s2}-\Delta S_2\theta_{b1}^{n}-\Delta S_1\theta_{b2}^{n}\right)-S_2^{n+1}\left(\Delta M_{pr,1}-\Delta S_1\theta_{b1}^{n}-\Delta S_2\theta_{b2}^{n}\right)\right)/\beta_2 \tag{51}$$

and

$$\beta_2=S_1^{n+1}\left(S_1^{n+1}+S_{s2}^{n}\right)-\left(S_2^{n+1}\right)^2 \tag{52}$$

If a fully plastic hinge is formed at node 2 of the element,

$$\Delta\theta_{b1}=\left(S_1^{n+1}\left(S_{s1}^{n}\Delta\theta_{s1}-\Delta S_1\theta_{b1}^{n}-\Delta S_2\theta_{b2}^{n}\right)-S_2^{n+1}\left(\Delta M_{pr,2}-\Delta S_2\theta_{b1}^{n}-\Delta S_1\theta_{b2}^{n}\right)\right)/\beta_3 \tag{53}$$

$$\Delta\theta_{b2}=\left(\left(S_1^{n+1}+S_{s1}^{n}\right)\left(\Delta M_{pr,2}-\Delta S_2\theta_{b1}^{n}-\Delta S_1\theta_{b2}^{n}\right)-S_2^{n+1}\left(S_{s1}^{n}\Delta\theta_{s1}-\Delta S_1\theta_{b1}^{n}-\Delta S_2\theta_{b2}^{n}\right)\right)/\beta_3 \tag{54}$$

and

$$\beta_3=S_1^{n+1}\left(S_1^{n+1}+S_{s1}^{n}\right)-\left(S_2^{n+1}\right)^2 \tag{55}$$

When the element forms fully plastic hinges at both ends,

$$\Delta\theta_{b1}=\left(S_1^{n+1}\left(\Delta M_{pr}-\Delta S_1\theta_{b1}^{n}-\Delta S_2\theta_{b2}^{n}\right)-S_2^{n+1}\left(\Delta M_{pr}-\Delta S_2\theta_{b1}^{n}-\Delta S_1\theta_{b2}^{n}\right)\right)/\beta_4 \tag{56}$$

$$\Delta\theta_{b2}=\left(S_1^{n+1}\left(\Delta M_{pr}-\Delta S_2\theta_{b1}^{n}-\Delta S_1\theta_{b2}^{n}\right)-S_2^{n+1}\left(\Delta M_{pr}-\Delta S_1\theta_{b1}^{n}-\Delta S_2\theta_{b2}^{n}\right)\right)/\beta_4 \tag{57}$$

and

$$\beta_4=\left(S_1^{n+1}\right)^2-\left(S_2^{n+1}\right)^2 \tag{58}$$

Once $\Delta\theta_{bi}$ is computed, the incremental forces of the integrated element can be obtained readily through Eqs. (35-42). Subsequently, the internal forces of the element for the current load step are updated. The co-rotational method is then applied to transform these forces into the global coordinate system. Finally, these forces are assembled to achieve force recovery for the entire structure.

5. Numerical examples

The present study adopts the load control Newton-Raphson method to conduct the second-order inelastic analysis of steel frame structures. In this section, the accuracy and efficacy of the proposed methodology are verified through several benchmark problems. The results from the BEAM188 element within the commercial software ANSYS, utilizing the plastic zone model, serve as the benchmark for precise solutions in these numerical examples. It is noted that the spring sections at both ends of the beam-column elements need to be discretized before the calculation begins. For all present examples, the wide flange section features a precise division into 16 layers, with uniform thickness across the 8 layers for each web and the 4 layers allocated for the flange.

5.1. Cantilever beam under vertical end point load

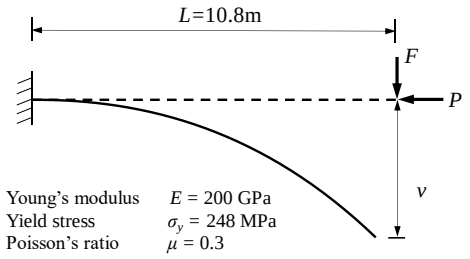

Fig. 13. Cantilever beam under vertical end point load

The cantilever beam depicted in Fig. 13 is subjected to the combined action of shear and axial forces at its free end. The cantilever beam, constructed from a wide flange section of W21×50, measures 10.8 meters in length. The Young's modulus E and yield stress σ_y of the material are 200 GPa and 248 MPa, respectively. The Poisson's ratio μ is 0.3. The shear force F is defined as M_p/L, and the axial forces are taken as 0, $0.2P_y$, $0.4P_y$, and $0.6P_y$, respectively. In this example, the cantilever member is simulated by only one proposed integrated element, and the applied loads are increased proportionally until the cantilever beam fails. Fig. 14 compares the vertical displacements at the free end of the cantilever beam, as determined by this study, with the results obtained from a simulation using 100 BEAM188 elements in ANSYS.

It can be seen from Fig. 14 that the results given by the present study and the BEAM188 element in ANSYS have good agreement. The present second-order inelastic analysis of steel frame structures only needs one proposed element to achieve accurate results in this example. Therefore, the present improved fiber plastic hinge model matches the accuracy of the plastic zone model, yet it offers superior efficiency in computational performance.

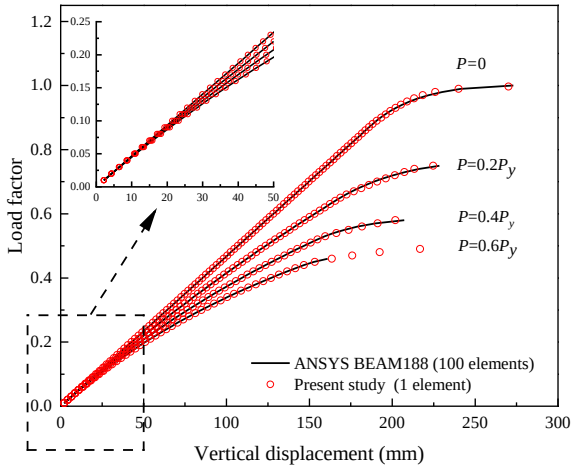

Fig. 14. Load-displacement curve of cantilever beam

5.2. Fixed-end Beam

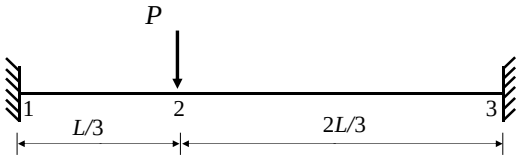

Fig. 15. Fixed-end beam subjected to shear force at $L/3$

Fig. 15 shows a beam with fixed supports at both ends and subjected to a vertical force P=8000 kN at one-third the distance from the left support. This example was first investigated by Liew et al. [27] to verify their proposed refined plastic hinge method. The beam measures 6 meters in length and features a W8×48 cross-sectional profile. The Young's modulus E and yield stress σ_y of the material are 205 GPa and 235 MPa, respectively. In the present analysis, the beam is simulated by two proposed elements, with the loading point coinciding with a node. For comparative analysis, this benchmark problem was also examined using a mesh of 100 BEAM188 elements within the ANSYS software. In both analytical approaches, the vertical point force P is incrementally applied until the analysis fails to converge.

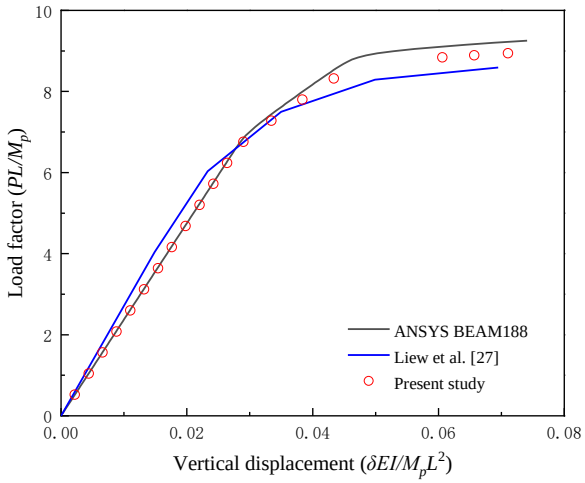

Fig. 16. Bending load-displacement curve of a major axis of fixed-end beam

Fig. 16 illustrates a comparative analysis of vertical displacements δ at the load application point, showcasing results from the current study, simulations using BEAM188 elements in ANSYS, and the refined plastic hinge method proposed by Liew et al. [27]. It can be seen that the present results are very close to those of 100 BEAM188 elements in ANSYS with only two elements in this example. Moreover, the accuracy of the proposed improved fiber plastic hinge

method surpasses that of the conventional plastic hinge method, as it achieves a level of precision comparable to the plastic zone method.

5.3. Single-layer Portal Frame

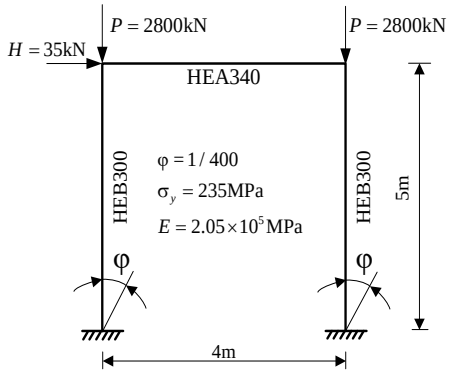

Fig. 17. Single-layer portal frame

Fig. 17 illustrates a single-layer portal frame, a classic structural problem initially introduced by Vogel et al. [28] in 1985. Many researchers have used this example to verify their analysis methods for steel frame structures. The portal frame comprises two 5-meter-high columns, each featuring a HEB300 cross-section, and a 4-meter-long beam with a HEA340 cross-section. The single-layer portal frame is rigidly fixed at its base, with both columns exhibiting an initial inclination angle of φ=1/400 relative to the column height. The yield stress for all members of the portal frame σ_y is 235 MPa, and the Young's modulus E is 205 GPa. A horizontal force H=35 kN and two vertical forces P=2800 kN are applied on the top of the frame. Consequently, the frame is expected to experience sway, and the columns will exhibit second-order effects under these loads.

In this example, the portal frame is modeled by one proposed element per member, and the loads are applied proportionally in the analysis until the frame reaches its failure point. Fig. 18 displays the lateral displacement outcomes for the left top of the frame, compared with those given by the BEAM188 element in ANSYS and the traditional plastic hinge method proposed by Vogel et al. [28]. In the ANSYS simulation, each member of the portal frame is modeled using 100 BEAM188 elements, which allows the obtained solutions to be considered precise. It can be seen from Fig. 18 that the results given by the present study and the BEAM188 element are very close to each other, therefore the proposed improved fiber plastic hinge method is more accurate than the traditional plastic hinge method and has the same precise as the plastic zone method. Furthermore, the present study can achieve accurate results with a simulation employing just one element per member, offering significantly greater efficiency than the plastic zone method.

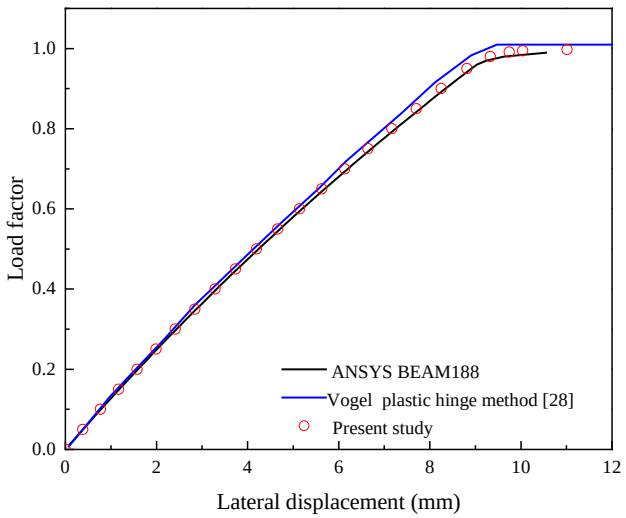

Fig. 18. Load-displacement curve of single-layer portal frame

5.4. Two-span four-layer frame

Fig. 19 shows a two-span four-story frame which was investigated by Yang et al. [29] to verify their present elastoplastic analysis of steel frames based on the traditional plastic hinge method. The geometry, boundary conditions, and loading of the frame are depicted in Fig. 19. In this analysis, each column was simulated by a single proposed beam-column element, while each beam was modeled using two proposed elements, with the loading point coinciding with the node. The present research employs the Newton-Raphson method for the incremental-iterative analysis of this example, gradually increasing the applied loads in proportion until the steel frame reaches its failure threshold. Fig. 20 plots the lateral displacements (Δ) of the frame from the present study, alongside a comparison with the outcomes from the BEAM188 element in ANSYS and the analytical approach suggested by Yang et al. [29]. Specifically, each beam and column of the frame are simulated by 20 BEAM188 elements in ANSYS, employing the Newton-Raphson method to iterate until the frame experiences failure. The analysis method proposed by Yang et al. [29] which is based on the traditional plastic hinge method, adopted the same mesh of the frame as the present study. However, it utilized the generalized displacement control method which can get the solutions after the structural failure occurs.

Through the comparison presented in Fig. 20, it is evident that the proposed analysis method based on the improved fiber plastic hinge approach, exhibits a strikingly similar level of accuracy compared to the simulations conducted using 20 BEAM188 elements per member in ANSYS. Also, the difference between the traditional plastic hinge method [29] and the plastic zone method (the BEAM188 element in ANSYS) is obvious in this example. The proposed plastic hinge method improved by the discretization of the hinge section, offers a high degree of precision that closely matches the plastic zone method, and provides greater efficiency.

6. Conclusions

This paper introduces an innovative plastic hinge method, termed the "improved fiber plastic hinge method," which is predicated on the discretization of the hinge section, offering a refined approach to structural analysis. The improved fiber plastic hinge method is capable of accurately calculating the ultimate elastic and plastic moment capacities, as well as the moment-curvature relationship. Thus, it is more accurate than the traditional plastic hinge method which commonly depends on an empirical and simplified formula.

The present second-order inelastic analysis of steel frame structures, which employs the improved fiber plastic hinge method, has been rigorously validated through several benchmark numerical examples. The present results for these examples were compared with the plastic zone method which is the BEAM188 element in ANSYS and conventional plastic hinge methods. The findings indicate that the accuracy of the present study not only outperforms conventional plastic hinge methodologies but also achieves a comparable level of accuracy to the plastic zone method. However, the present study is more efficient than the plastic zone method, as it requires merely one or two elements per member to achieve precise outcomes. Moreover, the improved fiber plastic hinge method holds significant promise over traditional approaches, as it is capable of accurately accounting for the impacts of residual and transverse shear stresses. These aspects are slated for exploration in our forthcoming research endeavors.

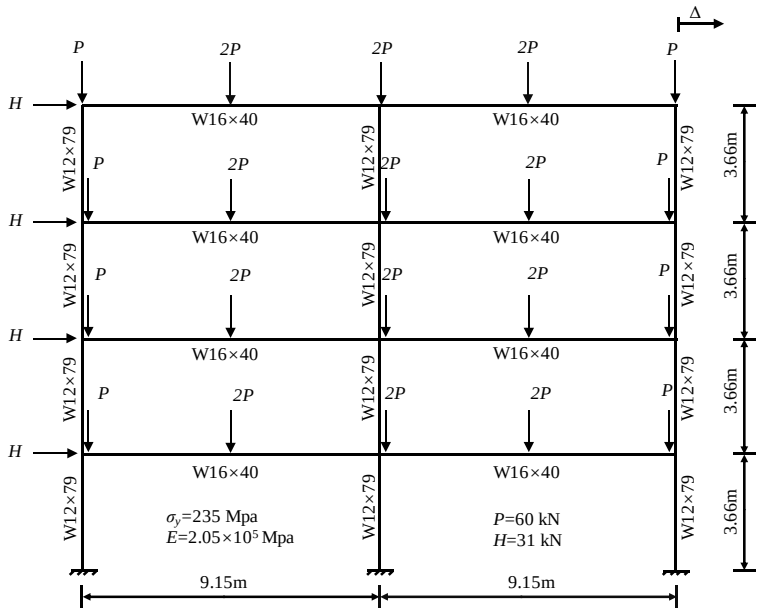

Fig. 19. Two-span four-story frame structure and calculation information

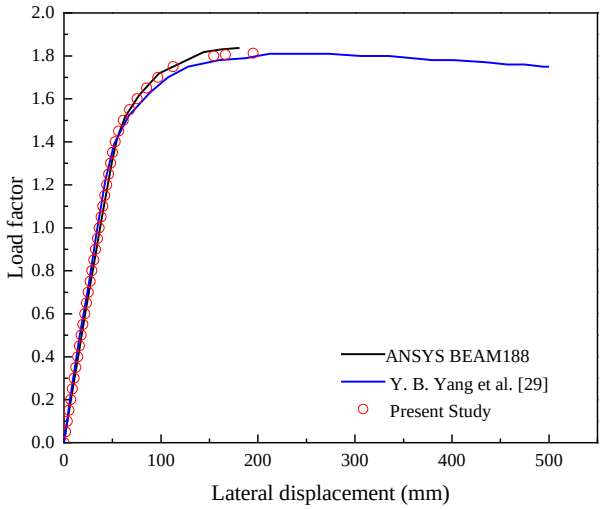

Fig. 20. Load-displacement curve of two-span four-story frame

Acknowledgments

The research described in this paper was financially supported by the National Natural Science Foundation of China (52108120), the Natural Science Foundation of Jiangsu Province (BK20210258), and the Fundamental Research Funds for the Central Universities (2242024k30065).

References

[1] Trahair, N. S., "Trends in the code design of steel framed structures", Advanced Steel Construction, WOS, 2018, 14(1): 37–56.
[2] Kim, S. E., Park, M. H. and Choi, S. H., "Direct design of three-dimensional frames using practical advanced analysis", Engineering Structures, Elsevier, 2001, 23(11): 1491-1502.
[3] Iu, C. K. and Bradford, M. A., "Higher-order non-linear analysis of steel structures. Part II: Refined Plastic Hinge Formulation", Advanced Steel Construction, WOS, 2011, 8(2): 183-198.
[4] Iu, C. K. and Bradford, M. A., "Higher-order non-linear analysis of steel structures. Part I: Elastic Second-Order Formulation", Advanced Steel Construction, WOS, 2011, 8(2): 168-183.
[5] Zhou, Z. H. and Chan, S. L., "Elastoplastic and large deflection analysis of steel frames by one element per member. I: One Hinge along Member", Journal of Structural Engineering, ASCE, 2004, 130(4): 538-544.
[6] Zhou, Z. H. and Chan, S. L., "Elastoplastic and large deflection analysis of steel frames by one element per member. II: Three Hinges along Member", Journal of Structural Engineering, ASCE, 2004, 130(4): 545-553.
[7] Wen, R. K. and Lange, J., "Curved beam element for arch buckling analysis", Journal of the Structural Division, ASCE, 1981, 107(11): 2053-2069.
[8] Van, L. H. and Dang, H. N., "Second-order plastic-hinge analysis of 3-D steel frames including strain hardening effects", Engineering Structures, Elsevier, 2008, 30(12): 3505-3512.
[9] Thai, H. T. and Kim, S. E., "Second-order inelastic dynamic analysis of steel frames using fiber hinge method", Journal of Constructional Steel Research, Elsevier, 2011, 67(10): 1485-1494.
[10] Lu, C. K. and Bradford, M. A., "Second-order elastic finite element analysis of steel structures using a single element per member", Engineering Structures, Elsevier, 2010, 32(9): 2606–2616.
[11] Chan, S. L. and Zhou, Z. H., "Pointwise equilibrating polynomial element for nonlinear analysis of frames", Journal of Structural Engineering, ASCE, 1994, 120(6): 1703–1717.
[12] Chan, S. L. and Zhou, Z. H., "Second-order elastic analysis of frames using single imperfect element per member", Journal of Structural Engineering, ASCE, 1995,121(6): 939–945.
[13] Tang, Y. Q., Liu, Y. P. and Chan, S. L., "An innovative co-rotational pointwise equilibrating polynomial element based on Timoshenko beam theory for second-order analysis", Thin-Walled Structures, Elsevier, 2019, 141: 15-27.
[14] Doan-Ngoc, T. N., Dang, X. L. and Ngo-Huu, C., "Second-order plastic-hinge analysis of planar steel frames using corotational beam-column element", Journal of Constructional Steel Research, Elsevier, 2016, 121: 413–426.
[15] Kassimali, A., "Large deformation analysis of elastic-plastic frames", Journal of Structural Engineering, ASCE, 1983, 109(8): 1869–1886.
[16] Liew, J. Y. R., White, D. W. and Chen, W. F., "Second-order refined-plastic hinge analysis for frame design. Part I", Journal of Structural Engineering, ASCE, 1993, 119 (11): 3196–3216.
[17] Nguyen, P. C. and Kim, S. E., "Nonlinear inelastic time-history analysis of three-dimensional semi-rigid steel frames", Journal of Constructional Steel Research, Elsevier, 2014, 101: 192-206.
[18] Zhou, Y., Hu, B., Gong, Y., Tang, L. and Li, Y., "Second-order improved refined plastic hinge method with implementation of continuous strength method", Journal of Constructional Steel Research, [19] Elsevier, 2023, 211: 108169.
[19] Liu, S. W., Liu, Y. P. and Chan, S. L., "Direct analysis by an arbitrarily-located-plastic-hinge element - part 1: planar analysis", Journal of Constructional Steel Research, Elsevier, 2014, 103: 303–315.
[20] Liu, S. W., Liu, Y. P. and Chan, S. L., "Direct analysis by an arbitrarily-located-plastic-hinge element - part 2: spatial analysis", Journal of Constructional Steel Research, Elsevier, 2014, 103: 316–326.

[21] Fieber, A., Gardner, L. and Macorini, L., "Structural steel design using second-order inelastic analysis with strain limits", Journal of Constructional Steel Research, Elsevier, 2020, 168: 105980.
[22] Fieber, A., Gardner, L. and Macorini, L., "Design of structural steel members by advanced inelastic analysis with strain limits", Engineering Structures, Elsevier, 2019, 199: 109624.
[23] Gardner, L., Yun, X., Fieber, A. and Macorini, L., "Steel design by advanced analysis: material modeling and strain limits", Engineering, Elsevier, 2019, 5 (2): 243–249.
[24] Walport, F., Gardner, L. and Nethercot, D. A., "Design of structural stainless steel members by second order inelastic analysis with CSM strain limits", Thin-Walled Structures, Elsevier, 2020, 159: 107267.
[25] Quan, C. Y., Kucukler, M. and Gardner, L., "Design of web-tapered steel I-section members by second-order inelastic analysis with strain limits", Engineering Structures, Elsevier, 2020, 224: 111242.
[26] Tang, Y. Q., Zhu, H. and Du, E F., "A novel incremental iterative force recovery method for second-order beam-column elements in plastic hinge analysis of steel frames", International Journal of Structural Stability and Dynamics, WOS, 2022, 22(02): 2250027.
[27] Liew, J. Y. R., White, D. W., Chen, W. F., "Second-order refined plastic hinge analysis of Frames", Journal of Structural Engineering, ASCE, 1992, 119:11.
[28] Vogel, U., "Calibrating frames", Stahlbau, 1986, 10(55): 295-301.
[29] Yang, Y. B., Chen, Z. H. and Tao, Y. C., "Elastoplastic analysis of steel framed structures based on rigid body rule and plastic-hinge concept", International Journal of Structural Stability and Dynamics, WOS, 2019, 19(09): 1950104.

Advanced Steel Construction – Vol. 21 No. 1 (2025) 54–63
DOI:10.18057/IJASC.2025.21.1.5

BENDING CAPACITY OF COLD-FORMED THIN-WALLED STEEL TUBES INFILLED WITH GYPSUM

Bo Su [1,*], Yi-Wen Liu [1] and Jiao Zhang [2]

[1] *Department of Civil Engineering, Jiangsu University, Zhenjiang, 212000, China*
[2] *School of Building Engineering, Changzhou Vocational Institute of Engineering, Changzhou, 213161, China*
** (Corresponding author: E-mail: subo@ujs.edu.cn)*

ABSTRACT

Cold-formed thin-walled steel tubes (CTSP) find common use in light steel structures and solar panel brackets, yet they are prone to collapse due to local instability and bending failure. To enhance the bending capacity of CTSP, this paper introduces a new composite structure known as gypsum-reinforced cold-formed thin-walled steel tubes (GCTSP), aiming to preserve high stiffness, stability, and lightweight characteristics. The study proceeds in two main phases: Three types of GCTSP (Section sizes of 80mm×40mm, 80m×60mm, 80mm×80mm) undergo four-point bending experiments to determine components' ultimate bending capacity. Finite element (FE) models are established to investigate the influence of different aspect ratios (1.00, 1.14, 1.33, 1.60, 2.00) on the bending capacity of GCTSP. Gypsum has been shown to significantly improve the bending capacity of CTSP. This study emphasizes considerable impact of changes in aspect ratio on GCTSP, leading to an increase in bearing capacity between 22% and 90%. Additionally, a proposed calculation formula, accounting for both gypsum reinforcement and aspect ratio effects, demonstrates excellent alignment with experimental data, yielding an error rate below 4%. This study provides valuable insights for enhancing the flexural bearing capacity of GCTSP through gypsum reinforcement, considering different aspect ratios.

ARTICLE HISTORY

Received: 4 March 2024
Revised: 6 December 2024
Accepted: 7 December 2024

KEYWORDS

CTSP;
Gypsum;
Four-point bending;
Composite structure;
Finite Element

1. Introduction

CTSP provide benefits including light weight, high strength, ease of prefabrication, fast assembly, and recyclability. Their widespread use in steel structure housing, factory buildings, sunrooms, and various engineering projects and auxiliary structures has significantly contributed to the development of lightweight assembled green buildings, showcasing broad application prospects [1]. However, the inherent challenge of these tubes lies in their thin wall with small thickness (1.5 mm-3.0 mm), resulting in issues such as low stiffness and poor stability. These limitations restrict their spanning and bearing capacities. In the face of strong wind loads, earthquakes, or snowstorms, these structures may be susceptible to collapse due to local instability and bending failure of components, leading to substantial property losses and potential casualties [2-4].

Researchers have thoroughly studied the mechanical properties of CTSP. For instance, Yongbo Shao et al. [7] carried out a finite element analysis to investigate the axial behavior of square steel tubes. Their calculations revealed that the buckling coefficient closely resembles that of a simply supported thin plate under axial compression, providing a valuable reference for the stability calculation of square steel tubes. Paola Pannuzzo et al. [8] explored the bending behavior of square and rectangular hollow CTSP after heat treatment through three-point bending tests and numerical simulation studies. Noteworthy references, such as the European standard [9] and AISC 360-16 [10], have categorized cold-formed steel into different cross-sections and provided calculation methods for the flexural ultimate of CTSP. More recently, Melina Bosco et al. [11] have developed and studied formulas that consider parameters such as slenderness ratio, shear length, and axial load. CTSP clearly show limitations in both overall and local stability, as well as bending capacity, which undermine structural reliability.

To enhance the bearing capacity of rectangular steel tubes, various studies have explored the use of CFSTs and their mechanical capabilities. Lin Xiao et al. [12] conducted a comprehensive review of the current research on concrete-filled steel tubes in bridge structures. They highlighted potential areas for future research, including bending capacity, spatial stress characteristics, dynamic response, and local stress characteristics. Zijian Chen et al. [13] concentrated on the axial compression capacity of steel-reinforced concrete short columns, consolidating design formulas, material constitutive models, and experimental research conclusions from various countries. This work provides a valuable reference for further investigations into the axial compression capacity of steel-reinforced concrete. Saifeng Wu et al. [14] developed CFSTs that inherit the advantages of traditional reinforced concrete columns and have been utilized in several super high-rise buildings. However, it is worth noting that current scholarly attention is predominantly focused on the research of CFSTs, with limited studies on the flexural capacity of steel tubes.

In addition to concrete, researchers have explored the use of lighter materials, such as gypsum, to form composite thin-walled steel components. For instance, Yifeng Xu [15] proposed and studied phosphogypsum-filled thin-walled square steel short columns. Filling phosphogypsum into thin-walled square steel tubes not only enhances their compressive capacity but also preserves their "lightweight" characteristics. Yuan et al. [16] introduced a composite steel tube filled with gypsum slurry and waste concrete blocks. This tube exhibits early strength, fast hardening, and high bearing capacity, making it suitable for use as temporary components in the construction of emergency rescue and disaster relief houses. However, while the mentioned contributions focus on the compressive capacities of gypsum-filled columns, there is still a gap in research regarding the bending capacity of gypsum-filled beams.

This study aims to analyze the bending capacity of GCTSP. Section 2 outlines the experimental programs, including material preparation, test cases, and device installation. Section 3 provides an in-depth analysis of the test results. Section 4, numerical models are established for simulation, and the analysis of the aspect ratio effect on mechanical capacity is presented. Section 5 introduces a practical theoretical formula for calculating the flexural capacity, taking into account the plastic development coefficient. While scholars have started to recognize the lightweight and high-strength characteristics of steel tubes filled with gypsum, research on gypsum-filled steel tubes remains limited, particularly in terms of their bending capacity.

2. Experimental program

2.1. Materials preparation: steel tubes and gypsum

The gypsum manufacturer is produced by Shandong Taiyuan Gypsum Technology Co., Ltd. As the setting final setting time of pure gypsum is too short for specimen preparation, a 0.12 % dosage of retarder is added to prong its final setting time (135 minutes). The retarder is wheat protein hydrolysate provided by Beijing Longtengda Chemical Co., Ltd. Table 1 presents properties of gypsum.

Table 1
Physical properties of gypsum

Name	Initial setting time/min	Final setting time/min	Break off strength/MPa	Compressive strength/MPa	Measurement of powders/%	Whiteness/%
Gypsum	5	10	3.5	16	0.01	50

The hollow galvanized square steel tubes are manufactured by Tianjin Steel Co., Ltd. It is made of Q235 grade steel mechanical properties illustrates in Table 2.

Table 2
Material properties of Q235

Name	Density g/cm^3	Tensile strength/Mpa	Yield strength/ MPa	Elongation	Impact ductility /J	Welding property
Q235 steel tube	7.85	370-500	235	> 25%	27-30	better

2.2. Test cases

As depicted in Table 3, each cross-sectional steel tube undergoes two working conditions (hollow or fully filled by gypsum), and each working condition includes two similar members to obtain average test results. In total, 12 members are tested in this study. Q235, being a commonly used model in engineering, was chosen for its combination of lightweight and high strength. As a result of this property, the CTSP with a smaller cross-sectional size was selected to investigate its bending characteristics. The dimensions of three types of Q235 CTSP are illustrated in Fig. 1.

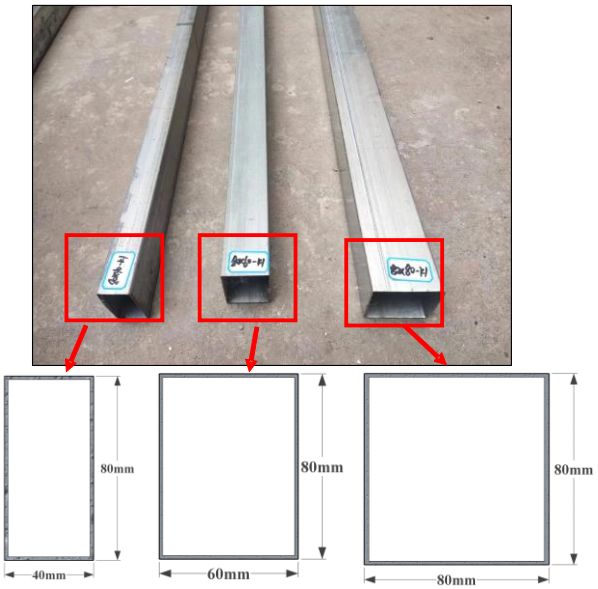

Fig. 1 Cold-formed thin-walled steel tubes and their section size

Table 3
Test cases

No.	Test condition	Cross section	Aspect ratio	Gypsum filling
1	80×40-k	80mm×40mm	2	Yes
2	80×40-s			No
3	80×60-k	80mm×60mm	1.33	No
4	80×60-s			yes
5	80×80-k	80mm×80mm	1	No
6	80×80-s			yes

Note: k indicates that the steel tube is hollow, and s indicates that the steel tube is full filled with gypsum.

2.3. Test procedures

2.3.1. Preparation of GCTSP specimens

The CTSP has a length of 1500 mm and a thickness of 1.5 mm. To examine the impact of aspect ratio on the filling effect, three cross-sectional types are selected (80 mm × 40 mm, 80 mm × 60 mm, and 80 mm × 80 mm). After weighing a certain quantity of gypsum, water, and retarder, mix them into a uniform slurry, as shown in Fig. 2(a). Finally, pour the mixed gypsum slurry into the empty tube using a funnel until the compactness is 100%, as depicted in Fig. 2(b). A one-week maintenance period is required for the gypsum to achieve the maximum strength standard when poured into the three types of steel tubes, as illustrated in Fig. 2 (c), for the three types of GCTSP sections with a filling rate of 100%.

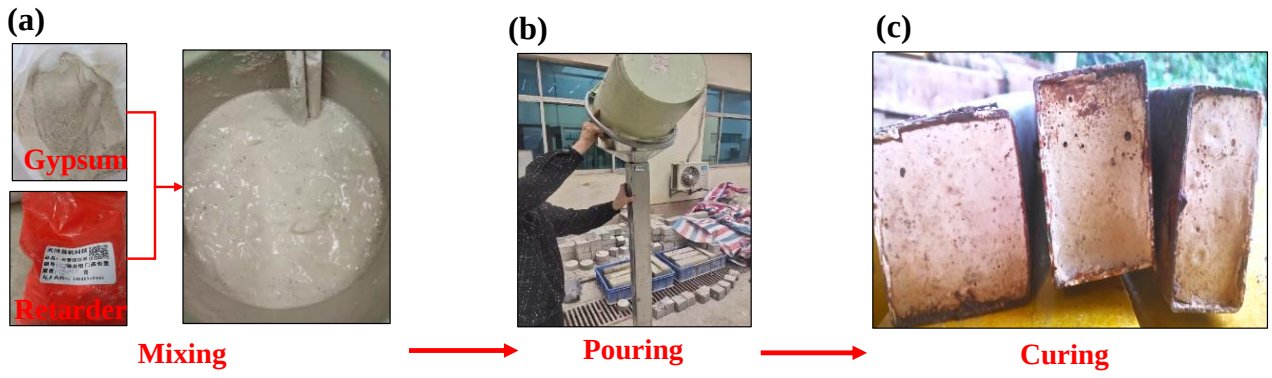

Fig. 2 The preparation process of GCTSP: (a) Mixing gypsum and retarder; (b) Pouring gypsum slurry; (b) Curing specimens

2.3.2. Strain gauges

In Fig. 3, To monitor strain distribution, seven sensors are placed at the central section of the specimen, with five (No. 1 to No. 5) arranged vertically along its height. Additionally, two strain gauges (No.6 and No.7) are positioned at the middle points of the top and bottom surfaces to measure tensile and compressive strains on the surface.

2.3.3. Test loading

The four-point bending tests are conducted in the Civil Engineering Laboratory of Jiangsu University. As illustrated in Fig. 4, the test system comprises a 50T self-balanced structure vertical loading reaction system with a separated hydraulic jack, simple supports at both ends, a universal compression hinge, a pressure sensor, and strain and displacement gauges. Prior to the four-point bending test, adjustments are made to the distribution beam, loading hinge point distance, and bearing position in the vertical loading reaction system of the self-balanced structure.

After installing both the hollow and gypsum-reinforced cold-formed thin-walled steel tubes, three displacement meters (dial indicators) are set up using magnetic supports to record the specimen's displacement at midspan and two ends [18]. The vertical force of the hydraulic jacks is distributed by the distribution beam to two concentrated loads at the steel rollers with a distance of 400 mm. Before the formal loading, a preload force with a value of 0.5kN is applied to ensure that the loading rollers are in full contact with the specimen. Subsequently, the load is unloaded to zero, and then continuously increased with a step of 0.5kN until the tube is destroyed.

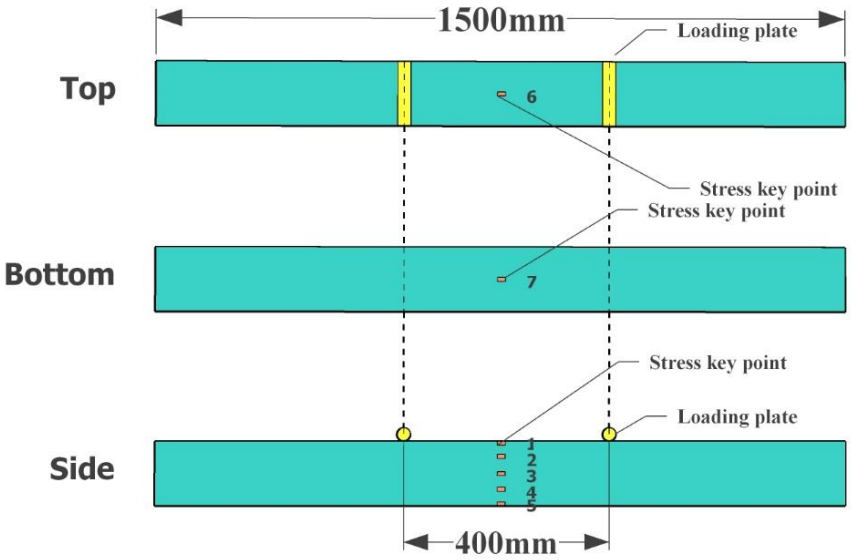

Fig. 3 Arrangement of strain gauges at midspan section

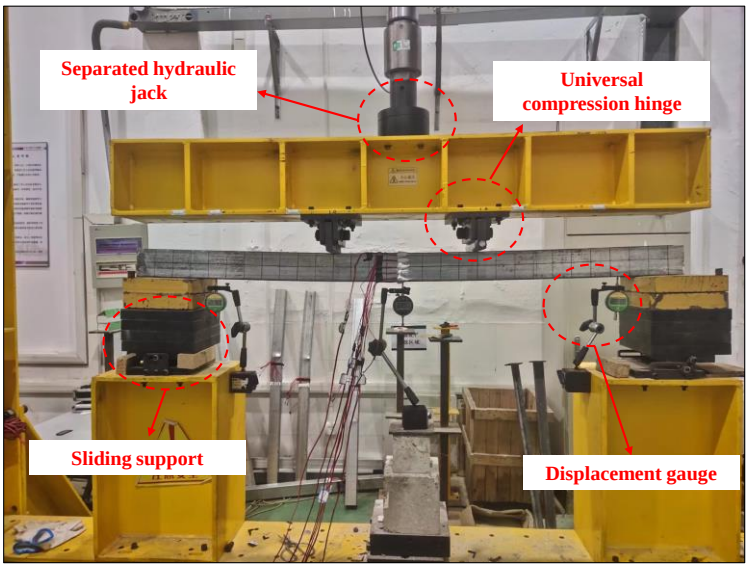

Fig. 4 50T self-balancing vertical loading reaction system

3. Test results and discussion

3.1. Load–deflection behavior

At the beginning of the four-point bending tests, the entire component undergoes slight bending deformation without any significant local changes. Nevertheless, with the increase in loading value, the steel plate at loading point slowly depresses, resulting in noticeable bulging protrusions on the front and back sides of the steel tube. Finally, complete buckling failure occurs around the loading points, leading to the component reaching its ultimate load capacity. However, the failure patterns exhibit variations with changes in aspect ratios. As illustrated in Fig. 5(a), local buckling in the 80×40-k tube is more pronounced and localized, effectively highlighting the stress concentration phenomenon. The degree of local failure of the 80×60-k and 80×80-k tubes is less than that of the 80×40-k tube; however, it appears that local buckling expands along the horizontal direction to a larger area (Fig. 5(b)-Fig. 5(c)).

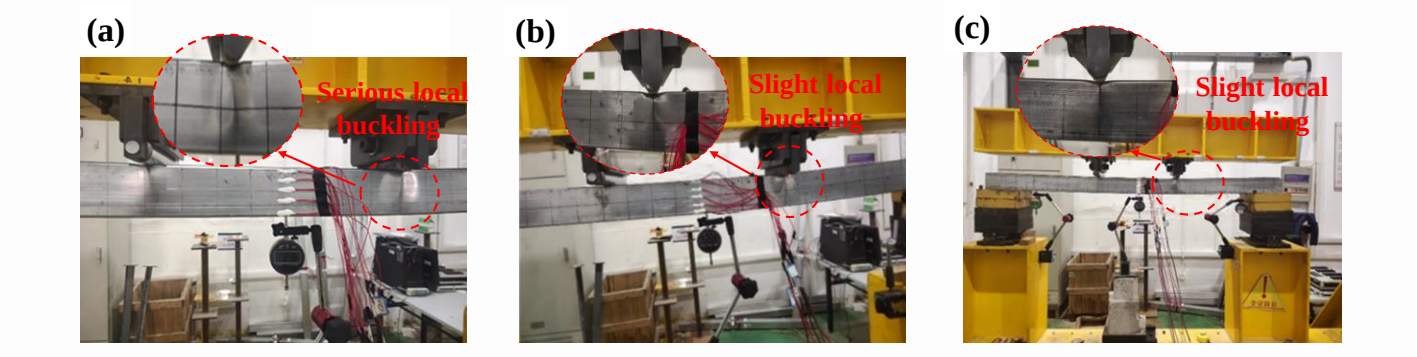

Fig. 5 Failure mode of the hollow steel tubes. (a) 80×40-k; (b) 80×60-k; (c) 80×80-k

During the four-point bending tests on GCTSP, none of the three types of specimens (80×40-s, 80×60-s, 80×80-s) produced noticeable sounds and maintained load-bearing capacity until local buckling occurred at the midspan. However, when compared with the corresponding hollow tubes, GCTSP exhibited smaller localized deformation areas and reduced the crushing degree of the upper surface at the loading points. Evidently, the infilled gypsum provides support to the steel tubes, alleviating stress concentration and enhancing overall bending capacity (Fig. 6(a)-Fig. 6(c)). However, due to the smallest aspect ratio (1.0) of the 80×80-s steel tube, the constraint effect between gypsum and steel panels is less than that of the 80×40-s and 80×60-s tubes. As seen in Fig. 6(c), two local buckling zones occur symmetrically along 45° angles below the loading points, indicating the shearing failure of the inner gypsum.

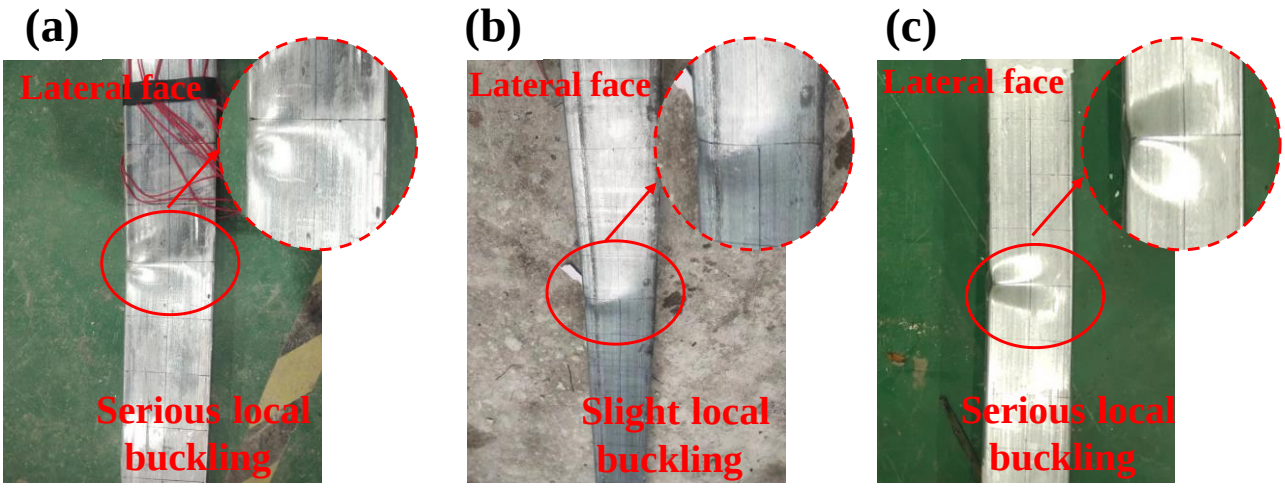

Fig. 6 local failure of different GCTSP. (a) 80×40-s; (b) 80×60-s; (c) 80×80-s

3.2. Flexural Capacity of Gypsum-Reinforced Steel Tubes

3.2.1. The improvement of bending bearing capacity

The load-deflection curves of both the hollow and gypsum-infused steel tubes are illustrated in Fig. 7. In Fig. 7(a), for the steel tubes with a section size of 80mm×40mm, the curves for both hollow and infused tubes are initially linear and nearly coincident. However, as the loading process progresses, the slope of the curve (representing bending stiffness) for the hollow tubes decreases abruptly, reaching its ultimate load value quickly. In contrast, the infused tubes exhibit significantly larger plastic deformation and better load-bearing capacity.

Moving to Fig. 7(b), which represents steel tubes with a section size of 80 mm × 60 mm, the slope of the curve for the infused tubes is consistently larger than that of the hollow tubes throughout the loading process, indicating superior load-bearing capacity. Finally, in Fig. 7(c) for steel tubes with a section size of 80 mm × 80 mm, the stiffness and load-bearing capacity of the infused tubes surpass those of the hollow tubes during the entire loading process. The larger aspect ratio (1.33) of the 80×60-s specimen enhances the constraint effect between the gypsum and steel panels, leading to an improved overall bending capacity.

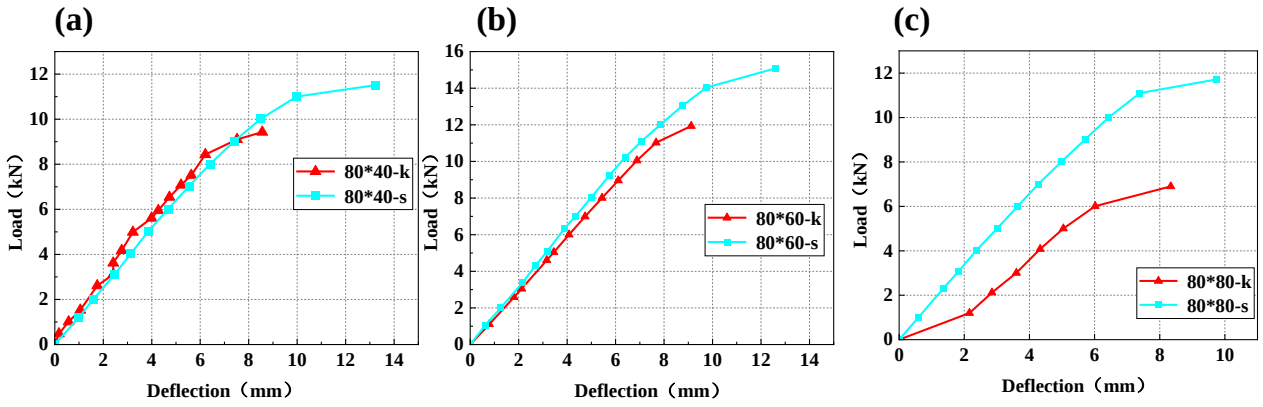

Fig. 7 Load-deflection cures of hollow and gypsum infilled steel tubes

Table 4
Bending capacity of hollow steel tubes

Number	Ultimate bearing capacity /kN	Average value/kN	Number	Ultimate bearing capacity /kN	Average value/ kN	Increased proportion/%
80×40-k1	9.4	9.5	80×40-s1	11.5	11.5	22
80×40-k2	9.5		80×40-s2	11.6		
80×60-k1	11.0	11.5	80×60-s1	15.0	15.1	36
80×60-k2	11.9		80×60-s2	15.1		
80×80-k1	6.9	6.9	80×80-s1	11.1	11.4	90
80×80-k2	6.9		80×80-s2	11.7		

The experimental results, presented in Table 4, show the ultimate bending capacity of both hollow and infilled steel tubes. The ultimate bending capacity of GCTSP for the 80 mm × 40 mm, 80 mm × 60 mm, and 80 mm × 80 mm sections are 11.5 kN, 15.1 kN, and 11.4 kN, respectively, representing increases of 22%, 36%, and 90% compared to the corresponding hollow tubes. It is clear that the aspect ratio plays a crucial role in determining the ultimate load-bearing capacity and plastic deformation characteristics of GCTSP.

3.2.2. Stress-strain at mid span

Fig. 8 shows the variations in load and strain at the mid-section of square steel tubes with different cross-sections. The y-axis shows the applied load, while the x-axis depicts the corresponding axial strain.. Fig. 8(a) illustrates the variation curve for the 80×40-k configuration, and Fig. 8(b) depicts the curve for the 80×40-s configuration. Both configurations demonstrate compliance with the assumption of a flat cross-section. The interaction with gypsum enhances the ductility of the steel tube, thereby increasing its restraint capacity, leading to significant improvements in both maximum load and strain. (Fig. 8(c) and Fig. 8(d)) The variation curves for the 80×60-k and 80×60-s configurations are presented. Here, the influence of aspect ratio is apparent, with the GCTSP performance optimal at this size, exhibiting the best flexural capacity among the three sizes. Local strains of up to 2500με are observed. Lastly, Fig. 8(e) and Fig. 8(f) demonstrate the variation curves for the 80×80-k and 80×80-s configurations, respectively. As the aspect ratio decreases, the steel tube's constraint on the gypsum weakens, reducing the GCTSP's ductility and resulting in smaller maximum strains at the tube's bottom, reaching only 1600 με.

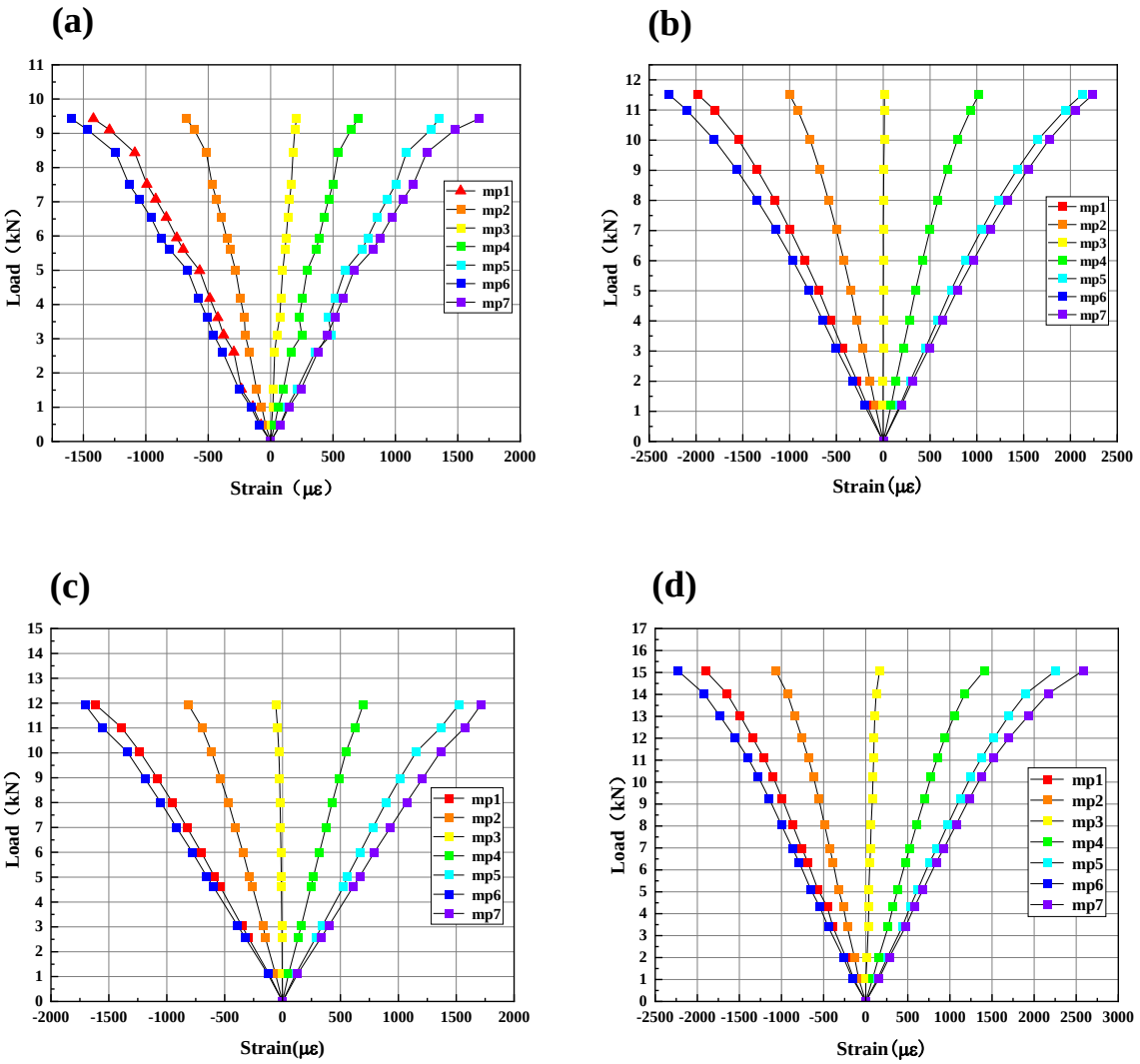

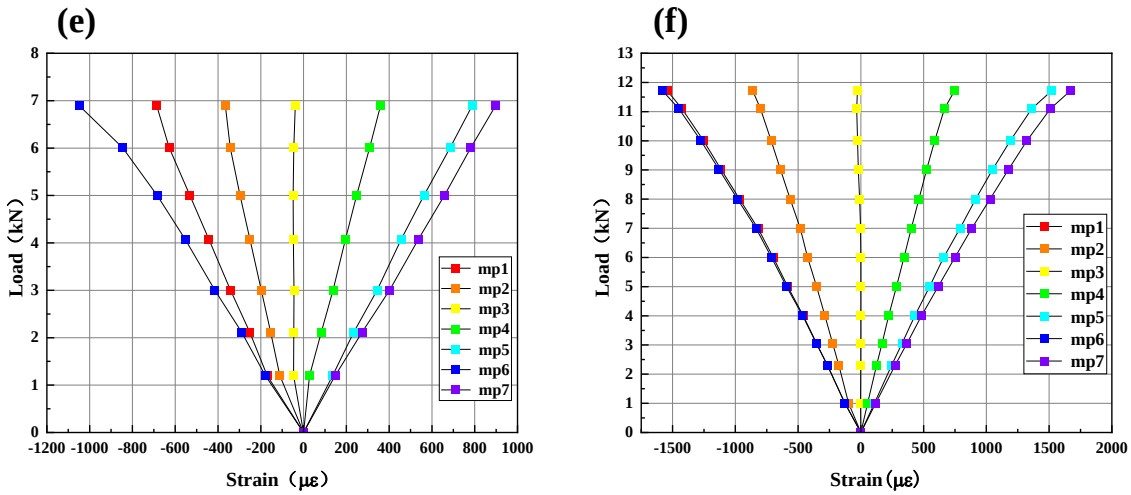

Fig. 8 Stress-strain curves of components with different sizes. (a) 80×40-k; (b)80×40-s; (c) 80×60-k; (d) 80×60-s; (e) 80×80-k; (f) 80×80-s

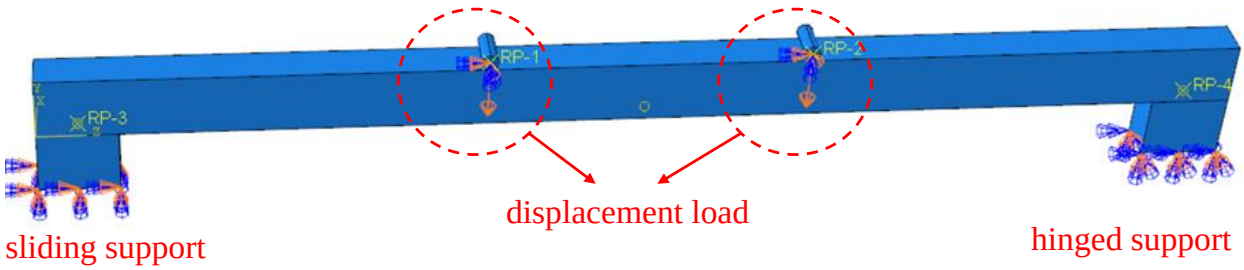

Fig. 9 Boundary conditions of GCTSP

4. Numerical simulation

4.1. FE model

4.1.1. Boundary conditions and grid division

In the experiment, one end of the GCTSP is a hinged support and the other end is a sliding support. The two ends of the component are not limited by the device to limit the displacement on both sides, so the degrees of freedom on both sides are not limited in the simulation. We simplify the 50T self-balancing vertical reaction loading system into two circular loading columns. One loading point has only the degree of freedom of rotation, and the other is completely constrained Fig. 9. The degree of freedom is set as a rigid body, including the pad at the bottom.

GCTSP is modeled using C3D8R linear hexahedral elements and S4R linear quadrilateral elements. This meshing approach reduces computation time while enhancing calculation accuracy. To guarantee the calculation's accuracy [20], it is recommended that the aspect ratio of the element is below 2.0. The model contains a total of 42563 nodes and 36496 elements.

The ' general static ' solver in Abaqus is used to solve the problem of GCTSP material nonlinearity. The loading method is realized by displacement loading. The advantage of this loading method is that the displacement control is used instead of the load application to limit the degree of freedom to eliminate the rigid body displacement to achieve a stable contact relationship.

4.1.2. Materials property

The CTSP in GCTSP adopts the double broken line model Fig. 10, and the standard von mises yield surface and related fluidity laws and anisotropy are used to define the properties of CTSP. The corresponding stress and plastic strain are input in Abaqus. Gypsum [19] is an isotropic material, so the ideal elastic-plastic model Fig. 11 can be used for numerical simulation.

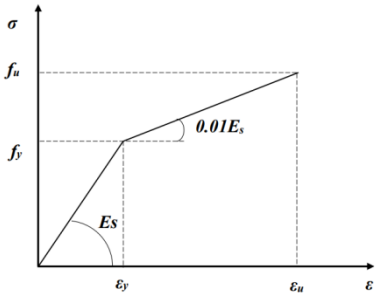

Fig. 10 Steel double broken line model

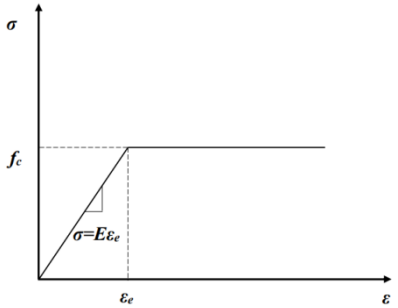

Fig. 11 Ideal elastic-plastic model of gypsum

$$\sigma_s = \begin{cases} E_s\varepsilon_s & ,(\varepsilon \le \varepsilon_y) \\ f_y + \alpha E_s(\varepsilon_s - \varepsilon_y), & (\varepsilon > \varepsilon_y) \end{cases}, \quad (1)$$

where αE_s is the elastic modulus of steel in the strengthening stage, α is 0.01.

$$\sigma_s = \begin{cases} E\varepsilon_e, & (\varepsilon \le \varepsilon_y) \\ f_c & ,(\varepsilon > \varepsilon_y) \end{cases}, \quad (2)$$

where f_c is ultimate compressive strength, ε_e is compressive strain.

4.1.3. Contact interaction

Because there is no device to limit slip in the test, It is essential to account for the effect on bond slip in the numerical simulation. The contact between CTSP and gypsum is defined as surface to surface, and the tangential contact needs to be defined as fiction formulation [20,21]. Penalty, friction coefficient is 0.1, and normal contact is hard contact. The master-slave surface selection assigns the stiffer surface as the master. Thus, the steel tube's internal surface is the master, the gypsum-steel tube contact surface is the slave, and the steel tube is modeled with shell elements. Thus, the steel tube thickness must be considered during setup, with the shell thickness defined to extend 1.5 mm from the bottom to prevent surface penetration.

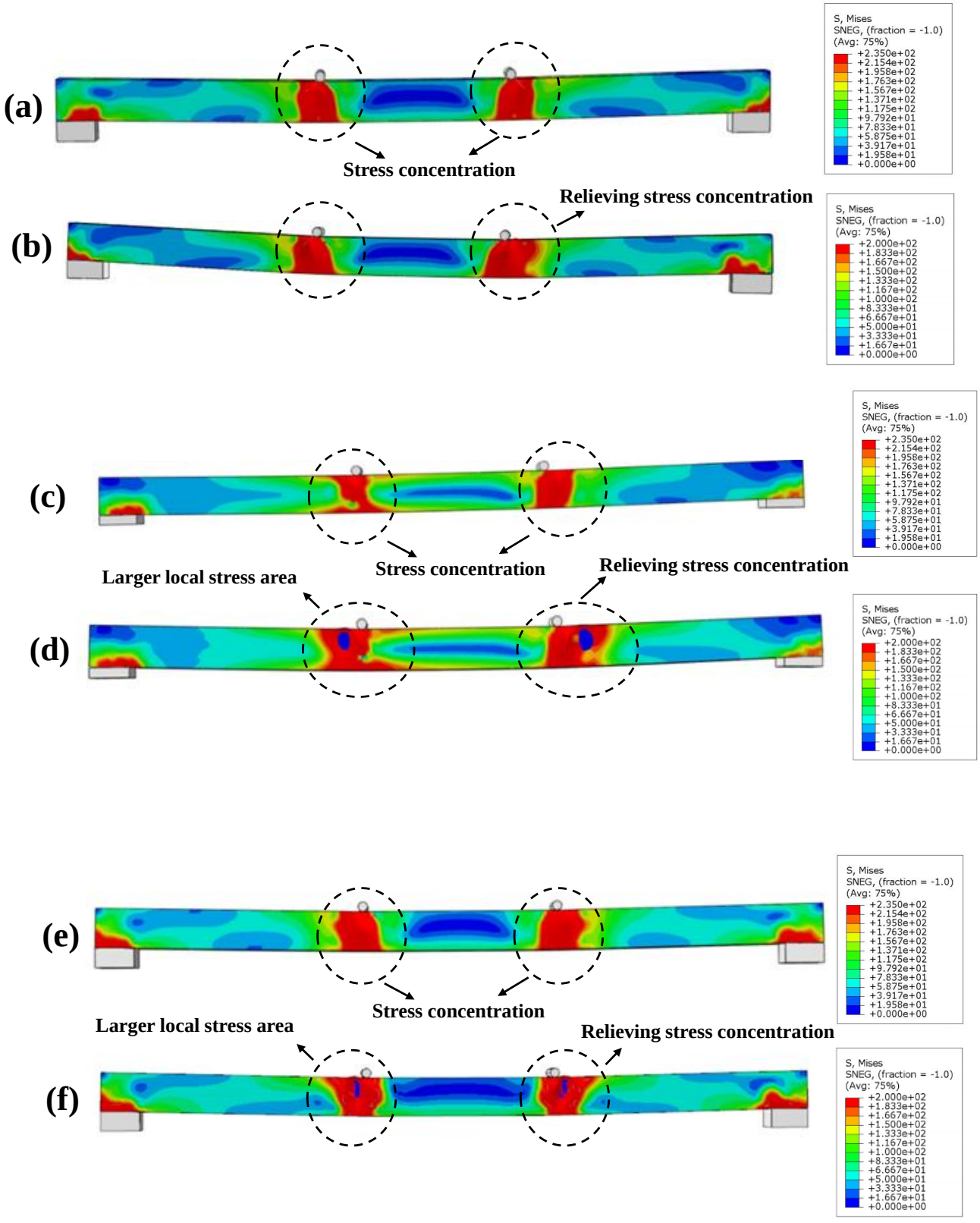

Fig. 12 The stress cloud diagram of different size components. (a) 80×40-k; (b) 80×40-s;(c) 80×60-k; (d) 80×60-s; (e) 80×80-k; (f) 80×80-s

4.2. Result and analysis

4.2.1. Stress cloud

In Fig. 12(a)-(f), the stress-strain diagrams of the gypsum-reinforced cold-formed thin-walled steel tubes with dimensions 80×40-s, 80×60-s, and 80×80-s align with the experimental results. From the stress contour plots in Fig. 12 (a)-(f), it can be observed that the stress distribution aligns with the experimental failure patterns. However, for the hollow steel tube, the stress concentration area at the loading point is relatively small and accompanied by local instability and failure. The corresponding maximum stress reaches 235 MPa, which is equivalent to the ultimate strength of the selected steel material. In practice, the steel in gypsum-filled steel tubes (GCTSP) near the loading point reaches its ultimate stress of 235 MPa before the ultimate load is attained. After localized failure occurs, the presence of gypsum facilitates stress redistribution in the composite beam, decreases the stress level in the steel. The ultimate load of GCTSP exceeds that of conventional steel tubes (CTSP) due to the interaction between the two materials (steel-gypsum) which maintains the overall load-bearing capacity.As a result, the GCTSP beam lose its bearing capacity due to collapse of infilled gypsum, and the ultimate stress in the steel reaches 200 MPa according to simulation results.

Simulation of the experiment further demonstrates the enhancement effect of GCTSP. Gypsum has weaker bending resistance but possesses certain compressive strength, which synergizes well with CTSP. The steel tubes provide confinement to the internal gypsum, thereby improving the overall bending capacity of the components. Fig. 13(a) to Fig. 13(c) compare the displacement-load curves of the experiment and simulation. From the figures, it can be analyzed that the error is within 10%.

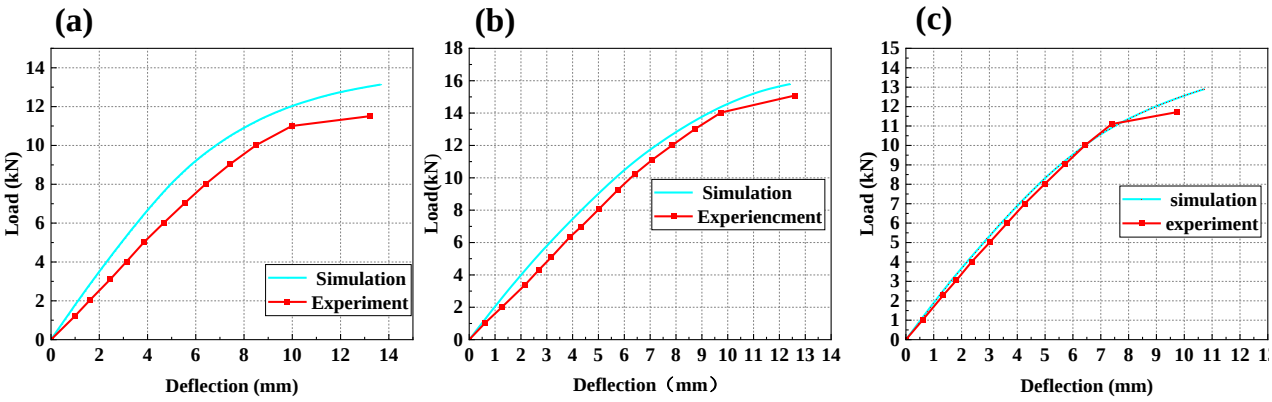

Fig. 13 Comparison between experiment and numerical simulation. (a) 80×40; (b) 80×60; (c) 80×80

4.2.2. The influence of aspect ratio

Fig. 14(a) presents the numerical simulation results for five cases with cross-sectional widths ranging from 40 to 80. The strength of each cross-section is closely related to its height-to-width ratio. This observation highlights the significant influence of the aspect ratio of the section [17]. This trend aligns with the findings in this paper on GCTSP. Specifically, the aspect ratio of 80mm×40mm is 2.0, 80mm×50mm is 1.6, 80mm×60mm is 1.33, 80mm×70mm is 1.14, and 80mm×80mm is 1.0. In Fig. 14(b), as the width decreases from 80 mm (1.0) to 50 mm (1.6), the bearing capacity gradually increases. However, when the width is reduced to 40 mm (2.0), the bearing capacity decreases. The aspect ratio exerts a pronounced constraint effect on the gypsum filling material within a specific range. In gypsum-reinforced steel tubes, the aspect ratio influences the constraint effect of the steel tube on the internal gypsum, subjecting the gypsum to three-dimensional compression and improving its compressive strength. The gypsum inside the steel tube effectively prevents local buckling, while the optimal aspect ratio enables both materials to utilize their respective properties, thereby improving the overall bending capacity of the component .

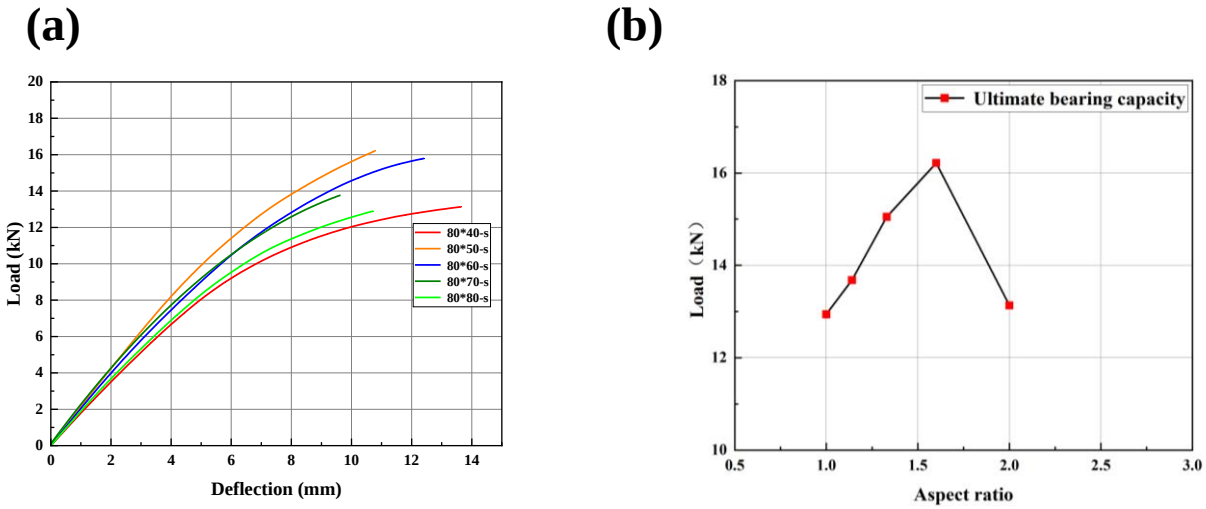

Fig. 14 (a) The ultimate bearing capacity of different size components; (b) Height-width ratio and bearing capacity curve

5. Bearing capacity calculation formula

5.1. Bending capacity calculation

Presently, composite members involving steel tube filling materials primarily focus on concrete-filled steel tubes, with theoretical calculations often considering the compressive capacity of the filled concrete. Building upon the principles of concrete-filled members, this paper incorporates considerations for the steel tube's yield capacity, local damage, gypsum compressive strength, and aspect ratio.

Han et al. [22] has proposed a semi-empirical theoretical formula for calculating the ultimate bending bending capacity of the CSTS, as shown in Eq.3.

$$M_u = \gamma_m W_s f_y, \tag{3}$$

where W_s is the sectional bending modulus, γ_m is the calculation coefficient, and f_y is the axial compression yield limit $\gamma_m = -0.2428\xi + 1.4103\sqrt{\xi}$, $\xi = (f_y A_s)/(f_{ck} A_c)$ is the constraint effect coefficient, A_s and A_s are the cross-sectional area of steel tube and concrete respectively, f_{ck} is the standard value of concrete compressive strength. Further, Li Liming et al. [23,24] introduced the plastic development coefficient of steel on the basis of considering the constraint effect.

$$M_u = (1 + \alpha) W_s f_y, \tag{4}$$

where $\alpha = A_s/A_c$ is the steel ratio of concrete filled steel tube section, (1+α) is the plastic development coefficient of steel.

Due to the calculation theories of Eq.3 and Eq.4 both designed for concrete-filled steel tubes, significant discrepancies are observed when applied to GCTSP. The errors in the calculations by Eq.3 range from a minimum of 100% to a maximum of 338%, while those by Eq.4 exhibit errors ranging from 158% to 432%. These results highlight the incompatibility of concrete-filled steel tube theories with GCTSP calculations, necessitating the introduction of new coefficients and theories for more accurate optimization.

As concrete and gypsum are both cementitious materials, they have similar characteristics in some mechanical properties. However, concrete has higher compressive strength and forms a stronger bond with CTSP. In contrast, the bond between gypsum and CTSP is weaker compared to concrete. Therefore, the constraint effect of the steel tube will be weakened, and the plastic development of the steel tube and the influence of the aspect ratio should also be considered. The following assumptions are made for GCTSP: (i) Considering the influence of aspect ratio β.(ii) Considering the constraint effect and the plastic development of steel, the correction is made by using β.

Under the above assumptions, formulas (5) and (6) are proposed to calculate the bending capacity of GCTSP.

$$M = \xi \beta W_s f_y, \tag{5}$$

$$\beta = 2.15x - 0.68x^2 - 1.2, \tag{6}$$

in the formula: M for the bending bearing capacity of the component; W_s is the section bending modulus of the rectangular steel tube; f_y for the yield strength of the steel material; β is the plastic development coefficient of steel considering the influence of aspect ratio; x is aspect ratio. $\xi = (f_y A_s)/(f_{gk} A_g)$, A_s and A_g are the cross-sectional area of steel tube and gypsum respectively, f_{gk} indicates is the standard value of gypsum compressive strength.

The analysis of the aspect ratio's influence on bending capacity reveals a direct relationship between the aspect ratio and the ultimate bending capacity. Additionally, when inversely calculating the plastic development coefficient, the obtained value of " β " aligns with the trend of the bearing capacity. Therefore, the plastic development coefficient is determined through curve fitting. The fitting curve is illustrated in Fig. 15. Utilizing the formulas (5) and (6), the corresponding findings are provided in Table 5.

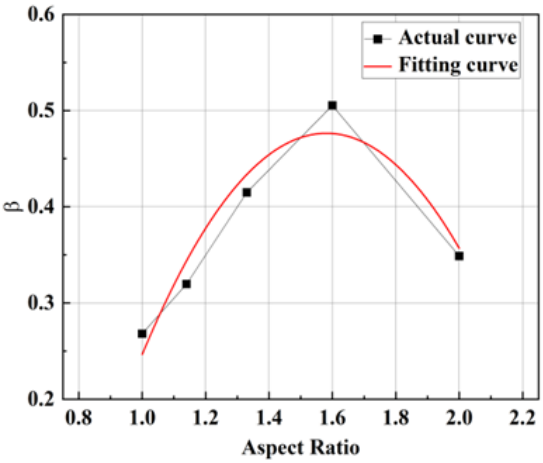

Fig. 15 Fitting curve of aspect ratio and coefficient β

Table 5
Theory and experimental results

Number	Specimens Number	M_u/kN	M_{u2}/kN	$\lvert M_u - M_{u2} \rvert / M_u$
1	80×40-s	11.5	11.1	3%
2	80×50-s	16.0	16.6	4%
3	80×60-s	15.1	15.4	2%
4	80×70-s	12.8	12.3	4%
5	80×80-s	11.4	11.3	1%

From the calculated results and experimental results, it can be observed that they are in good agreement, with an error of approximately 4%. The reason for the lower theoretical value is that it does not consider the enhanced effect of the lateral confinement of the steel tube during the actual loading process. Although this semi-empirical formula has certain practical value, its accuracy and scope of application have certain limitations, so careful evaluation and proper correction are needed in practical engineering.

6. Conclusion

This study comprehensively investigated the bending capacity of GCTSP through a combination of experimental, numerical simulation, and theoretical analyses. The key findings are summarized as follows:

- Flexural Behavior of Hollow Steel Tubes: Four-point bending experiments were performed on CTSP with 3 different cross-sectional dimensions (80mm×40mm, 80mm×60mm, 80mm×80mm). The results indicated that these tubes experienced local compression failure or warping at the loading point, leading to an ultimate flexural bearing capacity of 9.5kN, 11.5kN, and 6.9kN, respectively.
- Effect of Gypsum Infusion on Bending Capacity: Four-point bending tests were performed on GCTSP with the same three different section sizes after filling them with building gypsum. Gypsum filling effectively delayed local failure and significantly enhanced the ultimate bending capacity, resulting in capacities of 11.5kN, 15.1kN, and 11.4kN for the respective cross-sections. Compared to hollow tubes, the ultimate bending capacity increased by 22%, 36%, and 90%.
- Aspect Ratio Influence on Gypsum Effect: The effect of gypsum on flexural capacity was found to be related to the aspect ratio of the beam section. The aspect ratios of the tested sections were 2.0, 1.33, and 1, respectively, and additional aspect ratios of 1.6 and 1.14 were considered. The study revealed that, with a constant height of the steel tube (80mm), the flexural bearing capacity gradually increased with the aspect ratio. It reached a maximum at an aspect ratio of 1.6 and then decreased when the aspect ratio was reduced to 2.0. This is attributed to the dimensions of the height-to-width ratio enhancing the gypsum's constraining ability, thereby achieving the optimal coordination between the two materials.
- Numerical Simulation Validity: A 3D numerical model for the four-point bending test was created using Abaqus. Numerical simulation results closely matched experimental findings, with an agreement of about 10%.
- Semi-Empirical Formula and Correction Factor: A semi-empirical formula was developed for calculating the maximum bending capacity of GCTSP. A new correction factor (β) was introduced to consider the influence of the aspect ratio on the constraint effect. The proposed formulas demonstrated good reliability, with errors between theoretical and experimental results for ultimate load below 4%.

Overall, the study offers valuable insights into the flexural behavior of GCTSP, providing a thorough understanding through experimental, numerical, and theoretical methods.

Credit authorship contribution statement

Bo Su: Conceptualization, Methodology, Formal analysis, Writing – original draft, Writing – Review & Editing; **Yiwen Liu:** Formal analysis, Visualization, Writing – original draft, Writing – Review & Editing; **Jiao Zhang**: Writing - review & editing Investigation Validation.

Declaration of competing interest

The authors declare that they have no known competing financial interests or personal relationships that could have appeared to influence the work reported in this paper.

Acknowledgments

The research in this paper was supported by three foundations: (i) National Natural Science Foundation of China (grant number 51108210), (ii) Youth support foundation of Jiangsu University (grant number 5621480001), (iii) Zhenjiang Key Research and Development Project (Grant No. GY2021006).

Reference

[1] H. Dong, Y. Jin, W. Cao, X. Liang, S. Liu, Seismic performance of wooden straight-tenon joints reinforced with lightweight steel members, Engineering Structures. 282 (2023) 115825.
[2] Z. Fırat Alemdar, F. Alemdar, Progressive collapse of a steel structure under expected snow loads, Engineering Failure Analysis. 125 (2021) 105378.
[3] H. Peng, S. Song, H. Liu, S. Dai, F. Zhang, Investigation of wind loading characteristics of roof-mounted solar panels on tall buildings, Sustainable Energy Technologies and Assessments. 54 (2022) 102800.
[4] C. Tao Y. Zheng, Deng B. "Study on Seismic Behavior of Double Leg C-Type Cold-Formed Thin-Walled Steel Frame." Journal of Constructional Steel Research, vol. 209, Oct. 2023, p. 108035.
[5] 'Sudden! A viaduct under construction collapsed, and a car was hit and buried. _ Accident _ Fujian _ case. ' www.sohu.com/a/587887907_162758. Accessed 21 July 2023.
[6] 'Typhoon area photovoltaic bracket ' flip belly ' Gust coefficient and wind vibration coefficient of 1.0? Big mistake! 'Kandra, 12 Aug. 2019,_www.cd-class.com/a369e594f6/. Accessed 21 July 2023.
[7] Y Shao, L Peng. Finite element analysis of local buckling instability of thin-walled square steel tubes under axial compression. Journal of Yantai University (Natural Science and Engineering Edition). Apr. 2008, 304-309.
[8] P. Pannuzzo, C Ming, Flexural behaviour of cold-formed steel square and rectangular hollow sections with moderate heat-treatment, 197 (2022) 107454–107454.
[9] Eurocode 4: Design of Composite Steel and Concrete Structures[S]. Part 2: Bridge ENV, 1994-2,2001.
[10] American Institute of Steel Construction. Steel Construction Manual. American Institute of Steel Construction, 2015.
[11] M. Bosco, E. Mangiameli, P.P. Rossi, Influence of uncertainties on the seismic performance of steel moment resisting frames, Journal of Constructional Steel Research. 205 (2023) 107811.
[12] L. Xiao. "Research progress of steel-concrete composite bridge in 2019." Journal of Civil and Environmental Engineering 42 (2020) 168-182.
[13] Z. Chen, H. Ban, and Y. Wang. Research progress on the application of high-capacity steel in concrete-filled steel tubular structures. Collection of papers of the 17th (ISSF-2021) Academic Exchange and Teaching Seminar of Structural Stability and Fatigue Branch of China Steel Structure Association.
[14] S. Wu, W. Liu, J. Zhang, W. He, Y. Guo, Experimental and analytical investigation of square-shaped concrete-filled steel tube columns, Journal of Constructional Steel Research. 201 (2023) 107737.
[15] Y. Xu. Experimental study on axial compression capacity of thin-walled square steel tubular short columns filled with phosphogypsum. Steel structure 38 (2023) 21-28.
[16] Y. Lv. Experimental study on axial compression capacity of circular steel tube-gypsum-waste concrete block composite columns. New building materials 46 (2019) 19-21.
[17] L. Guo, and S. Zhang. The effect of section length-width ratio on the mechanical properties of high strength concrete filled rectangular steel tube. Journal of Harbin Institute of Technology. 2007: 530-535.
[18] Standard Test Method for Flexural Strength of Concrete (Using Simple Beam with Third-Point Loading): [C78/C78M-21]
[19] Y. Cao, and Y. Yin. Research on practical analysis method of concrete dense column gypsum composite wallboard. Proceedings of the 12 th National Symposium on Modern Structural Engineering and the 2 nd National Symposium on Technical Exchange of Cable Structures. Ed. Industrial Architecture Journal, (2012), 1163-1167.
[20] B.W. Schafer, Cold-Formed Steel Behavior and Design: Analytical and Numerical Modeling of Elements and Members with Longitudinal Stiffeners (Ph.D. thesis), Cornell University, 1997.
[21] Jiang, Ao, et al. Experimental Investigation and Design of Thin-Walled Concrete-Filled Steel Tubes Subject to Bending.Thin-Walled Structures, 63 (2013) 44–50.
[22] L. Han, Y. Yang. Modern Concrete Filled Steel Tubular Structure Technology [M]. Beijing: China National Building Industry Press, (2004).
[23] L. Li, X. Jiang, Z. Chen. Numerical analysis and simplified calculation of flexural behavior of concrete-filled rectangular steel tube. Journal of Tianjin University. (2007) 990-994.
[24] L. Li, X. Jiang, Z. Chen et al. Comparison of Computational Theory of Concrete Filled Rectangular Steel Tubes. Proceedings of the 6th National Symposium on Modern Structural Engineering. Ed. Industrial Architecture Magazine. Industrial Architecture Magazine, (2006) 1499-1507.
[25] M.-T. Chen, T. Zhang, B. Young, Behavior of concrete-filled cold-formed steel built-up section stub columns, Thin-Walled Structures. 187 (2023) 110692.
[26] Z. Zhu, F. Hai, H Shi, C. Yang et al. Flexural Property Study of Multiaxial Fiber Reinforced Polymer Sandwich Panels with Pultruded Profile Cores, Thin-Walled Structures. 189 (2023) 110910.
[27] F. Meza, and B. Jurgen. Numerical Modelling of Cold-Formed Steel Built-up Columns. Thin-Walled Structures, 188 (2023) 110781.
[28] L. Han, Y. Yang. Modern Concrete Filled Steel Tubular Structure Technology [M]. Beijing: China Construction Industry Press, (2004)
[29] A. Bello, M. Su. An Assessment of Different Direct Strength Methods for Cold-Formed Thin-Walled Steel Beam-Columns under Compression and Major Axis Bending. Structures, 34 (2021) 4788–802.
[30] K Dubey, H. Byadgi, N. Raykar. Enhancing Bending Buckling Strength of Hollow Tubes Using Concrete Filling. Materials Today: Proceedings, 72 (2023) 636–42.
[31] H. Song, L. Zhou, Y. Huang, et al. Experimental Investigation on the Seismic Capacity of Phosphogypsum-Filled Cold-Formed Thin-Walled Steel Composite Walls. Thin-Walled Structures, 186 (2023) 110664.
[32] Z. Lai, Y. Jie, Xiaohui Liu, et al. "High-Strength Rectangular Concrete-Filled Steel Tube Long Columns: Parametric Studies and Design." Journal of Building Engineering, 75 (2023), p. 107012.
[33] X. Li, S Zhang, W Lu, et al. Axial Compressive Behavior of Steel-Tube-Confined Concrete-Filled-Steel-Tubes. Thin-Walled Structures, 181 (2022) 110138.
[34] P. Kuan, Q. Wang, Y. Shao, et al. Test on Shearing Capacity of Concrete Filled Square CFRP-Steel Tube. Ocean Engineering, 274 (2023) 114065.
[35] H. Tang, L. Hou, Z. Yuan, et al. Eccentric Compressive Behavior of Square Concrete-Filled StainlessSteel Tube (CFSST) Stub Columns. Structures, 55 (2023) 1920–35.
[36] F. Wang, W. Xie, Bo Li, et al. "Experimental Study and Design of Bond Behavior in Concrete-Filled Steel Tubes (CFST)." Engineering Structures, 268 (2022) 114750.
[37] H. Wu, S. Chao, T. Zhou, et al. Cold-Formed Steel Framing Walls with Infilled Lightweight FGD Gypsum Part I: Cyclic Loading Tests. Thin-Walled Structures, 132 (2018) 759–70.
[38] L. Zhong, L. Guo, C. Jia, et al. Axial Compression Behavior of Stub Square Concrete-Filled Steel Tubes with Regional Defect. Engineering Structures, 278 (2023) 115510.
[39] Z. Zhu, F. Hai, H. Shi, et al. Flexural Property Study of Multiaxial Fiber Reinforced Polymer Sandwich Panels with Pultruded Profile Cores. Thin-Walled Structures, 189 (2023) 110910.
[40] S. Zong, Y. Lu, W. Ma, et al. Research on Eccentric-Compressive Behaviour of Steel-Fiber-Reinforced Recycled Concrete-Filled Square Steel Tube Short Columns. Journal of Constructional Steel Research, 206 (2023) 107910

Advanced Steel Construction – Vol. 21 No. 1 (2025) 64–72
DOI:10.18057/IJASC.2025.21.1.6

METHOD OF IMPERFECTION RANDOM FIELD CONSTRUCTION FOR WELDED CYLINDRICAL SHELL BASED ON SMALL SAMPLE

Hong-Fei Fu [1], Yu-Hong Shi [1,*], Wei-Xiu Xv [1], Fan Yang [1], Hao Yang [2] and Liang-Liang Jiang [1]

[1] *Beijing Institute of Astronautical Systems Engineering, Beijing 100076, China*
[2] *State Key Laboratory of Structural Analysis, Optimization and CAE Software for Industrial Equipment, Dalian University of Technology, Dalian 116023, China*
** (Corresponding author: E-mail: 19217049700@163.com)*

ABSTRACT

The initial geometrical imperfections of thin-walled cylindrical shell structures are important factors that cause the actual bearing capacity of such products to deviate from the theoretical value. In recent years, with the development of digital image measurement technology, it is possible to obtain geometric imperfections(GIs) through the measurement of the real geometric shape of the product, and it is possible to accurately predict the structural load-bearing capacity by considering the imperfections. On this basis, the initial GIs random field can then be considered to carry out thin-walled cylindrical shell load carrying capacity simulation targeting to obtain the strength distribution, and the lower limit of structural strength can be determined scientifically through a probabilistic approach..In this paper, based on Fourier series method, a modeling method of imperfection random field considering geometrical imperfection features is proposed for welded plates of carrier rocket tank. In the first stage, in order to solve the problem of large GIs characterization parameters, a GIs characterization method based on simplified Fourier coefficients is proposed, and an evaluation criterion based on determination coefficient (R^2) and characterization accuracy (RP) is established. In the second stage, according to the simplified GIs, a dual construction method based on the waveform and amplitude of the distribution of sample GIs is innovatively proposed. And according to the structural characteristics, a single panel is used as a sample to achieve sample expansion. It solves the problem of uncertain random field construction of such structure morphology under the condition of small sample. Finally, the method is applied to the actual engineering structure, and the accuracy of the method is verified by the bearing capacity test data.

ARTICLE HISTORY

Received: 14 July 2024
Revised: 15 December 2024
Accepted: 16 December 2024

KEYWORDS

Plate welding;
Thin-walled cylindrical shell;
Geometric imperfections;
Random field;
Small sample

1. Introduction

Thin-walled structures are widely used in space vehicles due to light weight and high load-bearing efficiency [1,2]. There are many failure modes for thin-walled structure while compressive buckling is the main one. Basically, the theoretical buckling load depends on the structural dimensions and mechanical properties of material [3,4]. There exists certain random geometrical imperfections in dimension, surface quality etc., which could cause bearing capability deviation in thin-walled structures with the same design scheme. This uncertainty from geometric imperfections attracted NASA's attention since 1960s. The engineers in NASA introduced the reduction coefficient into buckling bearing evaluation for thin-walled structures, and provided the envelope on the buckling bearing capacity with sufficient engineering data subsequently [5]. With the development of product processing and quality control technology, structural products based on this envelope design have become so conservative to the improvement of structural bearing efficiency [6,7].

In order to predict more reasonable load response of thin-walled structures, many researchers have studied the effect of GIs on the bearing capacity. Based on the random field signatures of the GIs distribution of thin-walled structures, it mainly focuses on the imperfections distribution form and amplitude.In the early stage, due to the limitation of measurement means, the imperfection form was mainly based on the assumption when the real geometry of the structure was unknown. The influence trend of different imperfection amplitudes on carrying capacity was analyzed. Huhne [8] proposed a Single Perturbation Load Approach(SPLA), which uses radial concentrated force in the structure to cause a single dimple imperfection. On this basis, Wang et al.[9] developed it into the the worst multiple perturbation load approach to obtain the lower limit of structural bearing capacity.In order to study the influence of the most unfavorable imperfections, Schmidt et al.[10] introduced the structural buckling waveform, the most serious imperfection form, into the finite element model as the initial GIs.Based on this, the influence trend of different amplitude values on the bearing capacity was analyzed, and the lower limit of the structural bearing capacity was obtained.With the development of digital measurement technology, the real geometric shape deviation of products can be obtained by scanning measurement, and it can be introduced into the ideal finite element model to achieve fine analysis of carrying capacity.Many scholars such as Arbocz and Elishakoff [11-13] obtained the product GIs based on the measured geometric morphology data, and studied the GIs characterization method by Fourier series fitting. The GIs were introduced into the ideal finite element model to achieve the accurate calculation of the structure bearing capacity considering the measured morphology.

Based on the measured geometric deviation samples of the product, the study of the distribution characteristics of the total geometric deviation random field is the key to realize the uncertainty analysis of the thin-walled structure bearing [14,15]. Describing the distribution information of product imperfection field requires a large amount of data, and how to reasonably reduce the variable dimension and efficiently construct the imperfection random field model has become the key to study the uncertainty of morphology [16,17].With the well-known Karhunen-Loeve (KL) transform [18], the processing method of generating random variables through orthogonal transformation and greatly reducing the dimension of data set has been widely used in random field models.On this basis, Ghanem and Spanos [19] proposed a piecewise basis function to describe random fields. Li and Kiureghian et al. [20] proposed the Optimal linear estimation method (OLE) and the improved expension OLE method (EOLE). Random fields are described in terms of random variables and shape functions.This idea gradually developed into the mainstream method of structural imperfection random fields [21-23].

The geometrical imperfection random field of thin-walled structures is often assumed to be a two-dimensional Gaussian random process, and the relevant parameters need to be determined during characterization. Yang Hao [24] et al. proposed a two-stage random field parameter estimation method by quantifying the imperfection uncertainty, so as to achieve accurate prediction of random field characterization parameters. M. Fina and P. Weber et al. [25] extended the probabilistic method into a fuzzy process, fully considering the uncertainty of samples. However, this method introduces more variables and emphasizes the sensitivity analysis between variables, which undoubtedly increases the calculation cost. Limited by high cost, the samples and test data of thin-walled structures under the same conditions are limited. Under the condition of finite samples, Schenk and Christian et al. [26] used the KL expansion theory and Gaussian random process to give the second-order moment characteristics of the limit load through direct Monte Carlo simulation. Li et al. [27] proposed using maximum entropy distribution to estimate the probability density function of random variables, avoiding the introduction of Gaussian distribution hypothesis, and extending the equality constraint to an interval form to adapt to small sample conditions.

Some existing random field models do not give too much consideration to the sample structure and processing mode. In order to obtain as many test samples as possible, products with similar conditions are used as training samples to establish a unified random field model.However, in engineering, the imperfection features of products under some processing and forming processes have typical specificity. For example, the tank body of a large-diameter launch vehicle is generally welded by several wall plates after processing. The welding residual stress and the changes of bending stiffness at the welding position lead

to obvious mutation of GIs field at the welding position, which affects the overall imperfection features [11]. At the same time, due to high manufacturing and testing costs, the number of samples of the same product is limited. In this paper, a Fourier series geometric imperfection random field construction method is innovatively proposed for welded structures of panels, using a structural single-wall panel as a research sub-sample. The structure GIs distribution features and deviation amplitude law are studied, and the random field model suitable for the geometric uncertainty of small sample products is constructed, which has more practical engineering application value.

The content of each part of the article is summarized as follows. In section 2, the principle of Fourier series characterizing imperfections and its simplification method are introduced; Section 3 establishes the novel dual modelling method of imperfection random field proposed in this paper; Section 4 establishes a Fourier random field model with measured geometric imperfections of cylindrical shells, and verifies the validity of the model by combining with the results of the structural physical tests, and the characteristics of the sample imperfections, the effect of each feature on the load bearing are analysed; Finally, conclusions are drawn and the value of the study is illustrated in Section 5.

2. Fourier series-based geometric imperfections characterization method of thin-walled cylindrical shells

2.1. Extraction of geometric imperfections of thin-walled cylindrical shells

The radial deviation referenced to the ideal surface of the thin-walled structure can induce buckling failure[28]. Therefore, it is necessary to define and reconstruct the surface of imperfection. In this work, the morphological data of the thin-walled cylindrical structure was obtained by employing three-dimensional laser scanning technology. The radial deviation of point cloud data is expressed as the off-surface deviation value.

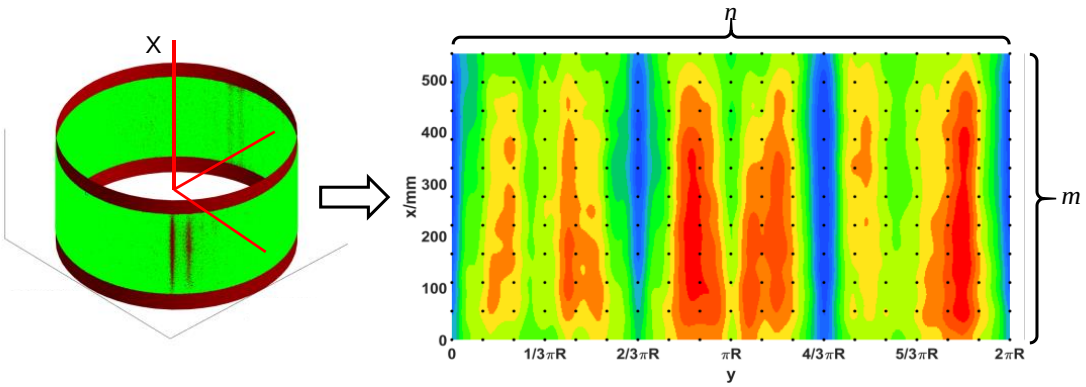

Fig. 1 Off-surface deviation contour of the outer surface

For the convenience to analyze the imperfection information, the radial deviation data was plotted as contour in Fig. 1. Based on the observation position of each measuring point, the structural imperfection was described by *m* off-surface deviation values in the axial direction and *n* off-surface deviation values in circumferential direction, respectively. The original off-surface deviation field was eventually expressed as two-dimensional matrix **w(x,y)** (as Eq. (1)).

$$\mathbf{w(x,y)}=\begin{bmatrix} w(x_1,y_1) & w(x_1,y_2) & \cdots & w(x_1,y_n) \\ w(x_2,y_1) & w(x_2,y_2) & \cdots & w(x_2,y_n) \\ \vdots & \vdots & \ddots & \vdots \\ w(x_m,y_1) & w(x_m,y_2) & \cdots & w(x_m,y_n) \end{bmatrix} \tag{1}$$

2.2. Fourier series-based representation method on imperfection field

Fourier series method is widely used to describe the initial GIs of cylindrical shells [29]. To efficiently represent imperfection field, the Fourier series method was employed in this work. Circumferential imperfection can be represented by the superposition of trigonometric functions with different periods and amplitudes at a fixed axial coordinate. The axial principle is similar, traversing through the coordinates of each point cloud to complete the representation of the imperfection field. Therefore, double Fourier series was employed to fit the off-surface deviation values of each scatter point as:

$$\begin{aligned} w(x_p,y_q) &= t\cdot\sum_{k=0}^{n_1}\sum_{l=0}^{n_2}\cos\frac{k\pi x_p}{L}\left(A_{kl}\cos\frac{ly_q}{R}+B_{kl}\sin\frac{ly_q}{R}\right) \\ &= t\cdot\sum_{k=0}^{n_1}\sum_{l=0}^{n_2}\gamma_{kl}\cos\frac{k\pi x_p}{L}\sin\left(\frac{ly_q}{R}+\theta_{kl}\right) \end{aligned} \tag{2}$$

Where A_{kl} and B_{kl} are the coefficients of Fourier series; *k* and *l* are the axial half-wave number and circumferential full wave number under the Fourier order respectively; By means of series fitting, the GIs information of the structure is retained in each order coefficient. For ease of analysis, the double series is expressed as wave peak value $\gamma_{kl}=\sqrt{A_{kl}^2+B_{kl}^2}$ and phase angle θ_{kl}. Fourier series method superimposes multi-order axial and circumferential waves. Respectively represent the imperfection information in the corresponding direction. The detailed principle is shown in Fig. 2.

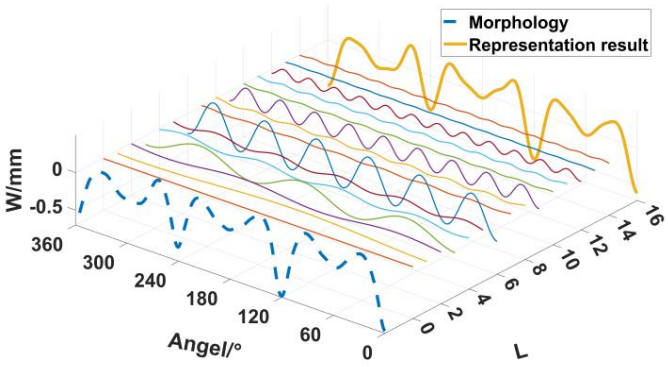

Fig. 2 Schematic diagram of imperfection expressed by Fourier series

The trigonometric function values **s(k, l)** for different *k* and *l* values were calculated and combined with the off-surface deviation matrix **w(x, y)**. Through singular value decomposition of the augmented matrix [**w(x, y) s(k, l)**], simple wave of Fourier periodic signals are obtained, and the Fourier series characterization of GI field is realized by extracting the coefficients of each term.

Affected by the production and processing methods, the surface imperfection signature of similar structural products have certain regularity. Fourier series method decouples the product axial and circumferential signature. The complex structural imperfections field is described by a relatively clear superposition of simple wave of each period.

2.3. Simplification on Fourier series of GIs field

According to the method mentioned above, there will be more than thousand coefficients used in the Fourier series. The Fourier coefficients A_{kl} and B_{kl} in Eq. (2) are a set of constants, reflecting the contribution from different periodic trigonometric functions to the overall GIs. In this work, the dominant coefficients which contribute the main trend of the GIs will be kept in order to reduce the complexity of calculation. If the integral values of the sine and cosine functions are equal in the whole period, the corresponding coefficients from the sine and cosine parts contribute equally to the imperfection field. Therefore, there are three methods to simplify the Fourier series as following:

1. Use the peak value of the wave γ_{kl} as the simplification factor;
2. Use the A_{kl} and B_{kl} as the simplification factor;
3. Use the group of coefficients [A_{kl} B_{kl}] as the simplification factor.

Since there are limited structures to collect the imperfection data, it should be reasonable to choose the simplification method according to the actual situation. First of all, the deviation measures were calculated for each simplification method. Then, the coefficients A_{kl} and B_{kl} of larger absolute deviation values were saved to represent the contribution from the corresponding series. Finally, the imperfection result from the simplified Fourier series was compared with the original one to ensure the accuracy of simplification.

Define μ_w as the mean of the off-surface deviation matrix, which is expressed as Eq. (3). A determination factor R^2 is defined subsequently as Eq. (4), which is used as the evaluation criterion of the fitting accuracy about Fourier series.

$$\mu_w = \frac{1}{m \times n} \sum_{p=1}^{m} \sum_{q=1}^{n} w(x_p, y_q) \tag{3}$$

$$R^2 = 1 - \frac{\sum_{p=1}^{m} \sum_{q=1}^{n} \left(\tilde{w}(x_p, y_q) - w(x_p, y_q)\right)^2}{\sum_{p=1}^{m} \sum_{q=1}^{n} \left(\tilde{w}(x_p, y_q) - \mu_w\right)^2} \tag{4}$$

Where $\tilde{w}$ is the deviation value from the simplified Fourier series; w is the true value from the structure.

The overall fitting accuracy is defined as the minimum value in limited samples, which indicates $R^2 = \min R_i^2$ .The calculation efficiency of three methods is compared to determine the optimal method at the same accuracy although the numbers of dominant coefficients are different. Eventually, the off-surface deviation after simplification is expressed as:

$$w(x_p, y_q) \approx t \cdot \sum_{k=0}^{n_1'} \sum_{l=0}^{n_2'} \cos\frac{k\pi x_p}{L} \left(A'_{kl} \cos\frac{ly_q}{R} + B'_{kl} \sin\frac{ly_q}{R} \right) \tag{5}$$

Where n_1' and n_2' are the numbers of retained parts after simplification; A'_{kl} and B'_{kl} represent the coefficients after simplification.

An criterion on structural bearing capacity is defined in order to ensure the accuracy of simplification which is:

$$RP = \frac{|P_{cr} - P_{cs}|}{P_{cr}} \le \zeta \tag{6}$$

Where P_{cr} is the critical load before simplification, and P_{cs} is the critical load after simplification. ζ is critical value to evaluate the accuracy on the simplification, which was 1% in this work.

The during the procedure in the following context, the value of R^2 will be increased until the *RP* criterion is met.

3. Construction method of Fourier series-based imperfection random field

Since there are extremely limited structures as samples in actual engineering (only three in this work). Some literature [30-32] shows that the structure welded by plates shows a trend of convex outside the welding area and concave inside the weld, and the imperfection signature have obvious rules. Taking Fourier coefficient as the control variable of imperfection random field, Fourier coefficient can reflect the imperfection signature of a class of structures [33]. Therefore, an imperfection random field model was proposed to describe the uncertainty from the imperfections in this work. The flowchart is shown as Fig. 3.

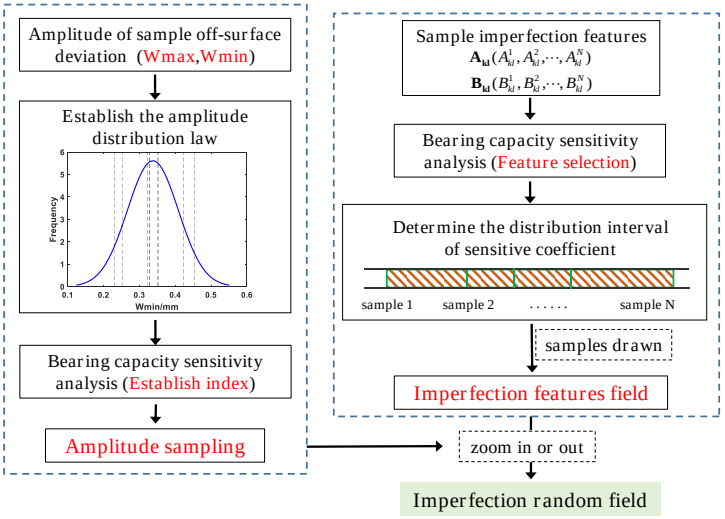

Fig. 3 Imperfection random field modeling method

First of all, the statistic distribution about Fourier series coefficients of same order in all samples are calculated according to the features of the imperfection wave. The random uniform sampling is carried out within the coefficient distribution interval to determine the imperfection features of the random field.

Then, the amplitude distribution of the imperfections random field is established based on the imperfections amplitude rule of the existing samples. Amplitude sampling was carried out within a certain confidence interval. Avoid situations where random field results deviate from the sample range due to adequate sampling.

According to the analysis about Fourier series, the trigonometric functions of each order represent independent imperfection features. The corresponding coefficients represent the proportion of imperfection features. The GIs of the sample is represented in the form of simplified series with different weights according to the specific weight ratio. Before sampling, the variable range was determined with the minimum value and maximum value in three samples for each coefficient. Then, uniform sampling was performed randomly in the range for all coefficients to construct the Fourier series-based imperfection,as Eq. (7).

$$\hat{A}_{kl} \in \left[\min A_{kl}^i, \max A_{kl}^i\right]$$

$$\hat{B}_{kl} \in \left[\min B_{kl}^i, \max B_{kl}^i\right]$$

$$\hat{w}(x_p, y_q) = t \cdot \sum_{k=0}^{n_1'} \sum_{l=0}^{n_2'} \cos\frac{k\pi x_p}{L} \left(\hat{A}_{kl} \cos\frac{ly_q}{R} + \hat{B}_{kl} \sin\frac{ly_q}{R} \right) \tag{7}$$

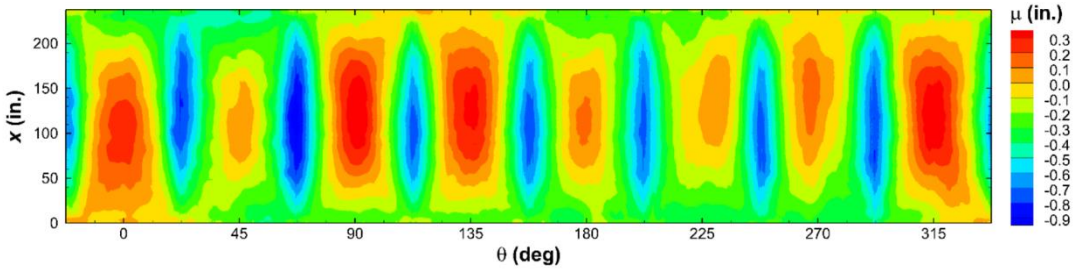

Fig. 4 Off-surface deviation field of welded plate structure [30]

In order to ensure that the amplitude of the imperfection field does not deviate from the statistical result of the sample, the amplitude of the off-surface deviation of the sample is measured under certain confidence requirements.According to the statistical results, the sampled off-surface deviation field is enlarged or reduced to realize the amplitude rule control of the imperfection random field.

For instance, Fig.4. shows the surface imperfections of the welded structure of eight plates measured by NASA [34]. It is obvious that it shows concave at weld line and convex in the middle of the shell between neighbored weld lines. In order to reflect the detail features about sample amplitude, the amplitude of the off-surface deviation in a single plate was taken as an independent statistical sample. The distributions about the minimum off-surface deviation values

$\min \hat{w}(x_p, y_q)$ and maximum off-surface deviation values $\max \hat{w}(x_p, y_q)$ of the single plate were tested respectively. The probability distribution model of the amplitude was established. According to its distribution features, random field amplitude sampling is carried out within the confidence interval [μ-3σ, μ+3σ] of the amplitude statistics results with 99.7 per cent confidence level, and the preliminary constructed defective feature field was deflated. The imperfection feature field constructed initially is scaled.

Taking the minimum off-surface deviation as an example, the scaled imperfection random field is expressed as:

$$\mathbf{w}_L(\mathbf{x},\mathbf{y}) = \frac{\tau}{\min \hat{w}(x_p, y_q)} \hat{\mathbf{w}}(\mathbf{x},\mathbf{y}) \tag{8}$$

Where, τ is the concave amplitude of the sample within the statistical range of the sample.The sensitivity analysis about the scaled maximum and minimum deviations were performed respectively. In order to ensure computational efficiency, global sampling was employed according to the features of the probability distribution model of $\min \hat{w}(x_p, y_q)$ and $\max \hat{w}(x_p, y_q)$. The corresponding sample of amplitude $\boldsymbol{\tau} = (\tau_1, \tau_2, \cdots, \tau_L)$ was obtained. Each bearing capacity $P(\tau_j)$ of the structure was calculated accordingly. The essential effect size of sample *i* is defined as:

$$EE_i = \frac{1}{q} \sum_{j}^{q} \left| \frac{P(\tau_j) - P_{cl}}{(\tau_j - \min \hat{w}(x_p, y_q)) / \min \hat{w}(x_p, y_q)} \right| \tag{9}$$

According to the mean value of the essential effect values of each sample, the sensitivities of two types of amplitudes on the bearing capacity were compared. The index with higher sensitivity was selected as the scaled standard. After amplitude sampling is introduced, the sampling results of the imperfection random field model include the basic features of the sample imperfections, and ensure that the imperfection amplitude falls within the confidence range of the sample. By Eq. (2), the values of random field off-surface deviation are expressed in Fourier series.The scatter field is fitted to the form of space surface to represent the imperfection, and the imperfection feature field is constructed based on Fourier series method.The operation process of this method is relatively simple,has clear the physical features, and it is suitable for all kinds of sample conditions.Especially for products with the same structural form and process, the random field model can fully include the imperfection features of such products.

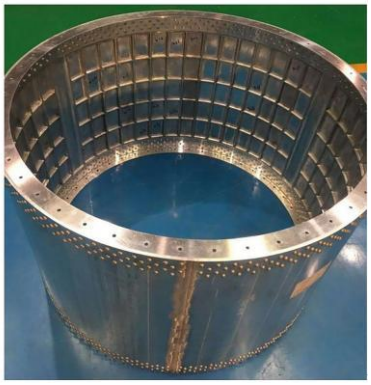

Fig. 5 Plate welded thin-walled cylinders

4. Results and discussions

As shown in Fig. 5, there are there structures used to verify the method in the following context. All of them are orthogrid-stiffened aluminum cylinders of 1m in diameter. The structure is divided into three aluminum shell parts which are welded together, and steel end rings which connect to the outer surface both ends of the cylinder. The overall height of the cylinder and the orthogrid-stiffened part are 710mm and 550mm, respectively. The thickness of the stringer is 2mm. A total of 3 products were produced, and the material properties, structural dimensions and GIs of each product were measured.

4.1. Measured product geometric imperfections and their bearing capacity

Abaqus was used to model and analyze the bearing capacity of the structure. As comparison, the bearing capacity of the ideal structure with smoothing surface was 3109.2 kN from simulation. Three weld lines failed first which caused the overall failure subsequently. The relative error of the bearing capacity was 9.10% between the ideal structure and the average of three samples from experiments.

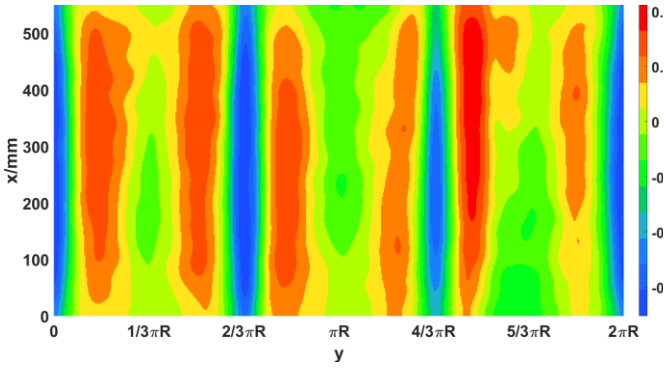

(a) Structure1

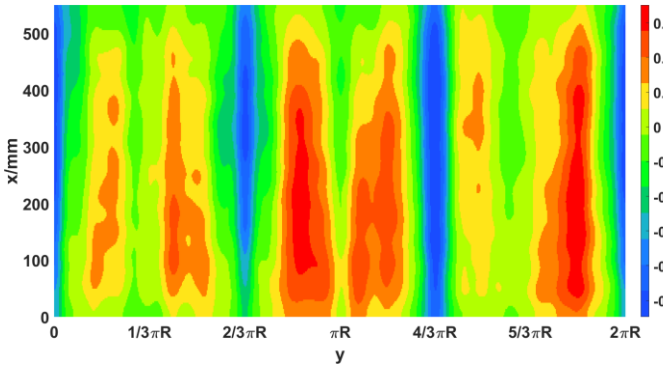

(b) Structure2

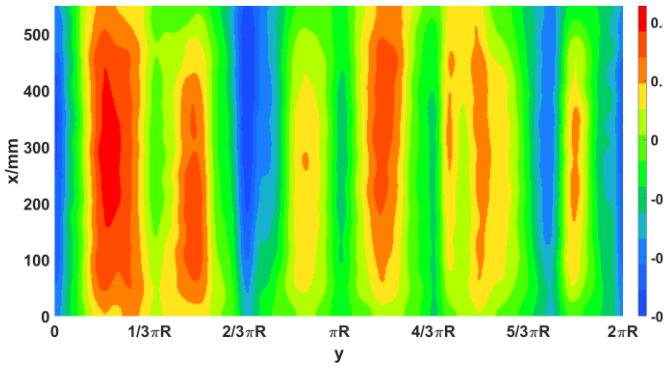

(c) Structure3

Fig. 6 Measured GIs of the product

Three-dimensional laser scanning technology was used to obtain the GIs information of each physical structure. The GIs were expressed as off-surface deviation normalized by thickness $^*t = 2$ of the structure , as shown in Fig.6. When the fitting accuracy of the determination coefficient R^2 is greater than 99.9, the structural bearing capacity of the measured GIs is considered in the calculation. The international KDF [34] is used to describe the influence of GIs on bearing capacity. Table 1 shows the relative deviation of the calculated results from the experiments and the corresponding GIs knockdown factor.

Table 1

Comparison between simulation and experiment

ID	Simulation (kN)	Experiment (kN)	Relative deviation (%)	KDF (%)	Buckling position
1	2737.3	2843.7	-3.74	88.04	$4\pi/3$
2	2898.7	2888.8	0.34	93.23	$2\pi/3$ and $4\pi/3$
3	2885.8	2817.4	2.43	92.81	0 and $2\pi/3$

The comparison shows two phenomena. One is that there is small deviation between the simulation and the experiment when the imperfection is taken into consideration. It indicates that considering the GIst method in this work can provide more accurate result. The other is that the positions of failure in all structures are different. Since the imperfection filed shows certain stochastic characterization, it introduces uncertainty in terms of the failure position and the magnitude of the critical load. It is worth to note that the failure happened in the weld line for all structures although the positions were not the same. The reason is that there is larger variation in term of the off-surface deviation.

Table 2

Statistics of peak off-surface deviation of single plate

	Convex amplitude	Concave amplitude
Sample data(mm)	0.33	-0.70
	0.33	-0.69
	0.42	-0.70
	0.23	-0.53
	0.32	-0.55
	0.35	-0.54
	0.45	-0.56
	0.35	-0.60
	0.25	-0.53
Mean value	0.338	-0.600
Standard deviation	0.071	0.077
Sensitivity $\overline{EE}$ (KN)	1530.97	1592.54

The maximum values of the outer protrusion and inner concave of each plate in the existing samples were counted.Based on the information of 9 plate samples, the general situation is estimated, and the peak deviation distribution of single plate is established.And the bearing capacity sensitivity of the two types of amplitudes is analyzed. Table 2 shows the analysis results and the statistical results of the peak off-surface deviation of the sample single plate.Under the condition of small sample, the Lilliefors test is applied, and when the significance level is greater than 0.05, the peak value distribution follows the normal distribution.The concave amplitude, that is, the minimum off-surface deviation, is more sensitive to load.It is used as the amplitude simplification standard for this group of samples.

4.2. Feature analysis and simplification of Fourier coefficients

There are thousands coefficients above which takes much simulation cost. The Fourier series is simplified reasonably according to the imperfection features to improve the efficiency. As discussed before, each amplitude of Fourier coefficients reflects the influence level of the order in the imperfection field. Fig.7 shows the amplitude of Fourier coefficients of each sample.

It is obvious that the value of γ_{kl} is relatively larger for smaller wave number and order than the larger wave number and order in Fig.7. It indicates that these parts dominantly contribute to the random field of imperfection.

Circumferential shapes under typical periods (l=2, 3, 6 and 9) are illustrated as Fig. 8 by ignoring the axial imperfection. The order of a wave represents the circular frequency of the wave. Fig. 8(a) shows the roundness deviation of the overall cylindrical structure; Fig. 8(b) shows the imperfection features with a single plate as a symmetric period, such as the imperfection at the weld. The other waveform reflect the periodic features of symmetry within a single plate, and the symmetric period is an integral multiple of the plate.

As shown in Fig.7, the periodic properties of axial waveform have no obvious rules. The coefficients with less axial wave number and relatively clear features account for a larger amplitude. Since the 0-order waveform reflects the radial deviation of the structure and has little effect on the axial bearing capacity, it is not discussed here. The corresponding imperfection features with larger coefficients are shown in Fig. 9. It is notable that the axial imperfection is obvious if the axial waveform is half wave or multiple entire waves. The superposition of half wave and multiple entire waves have less contribution to the structural imperfections.

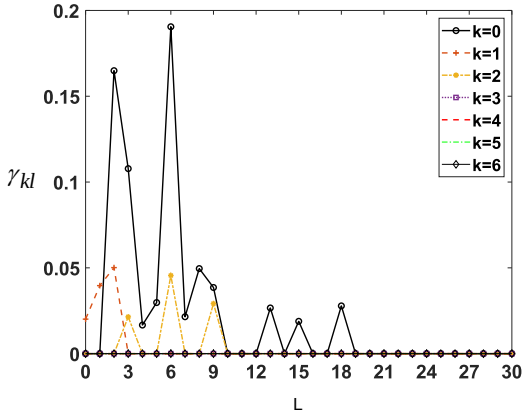

(a) Structure 1

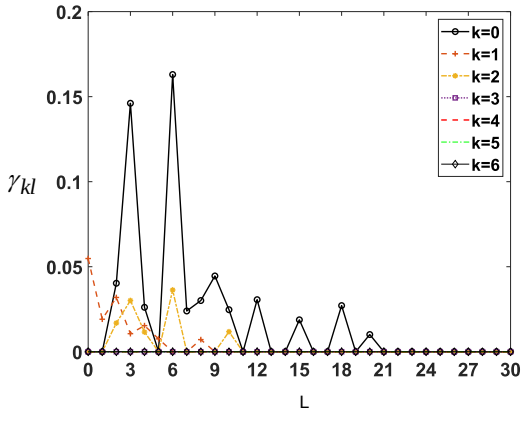

(b) Structure 2

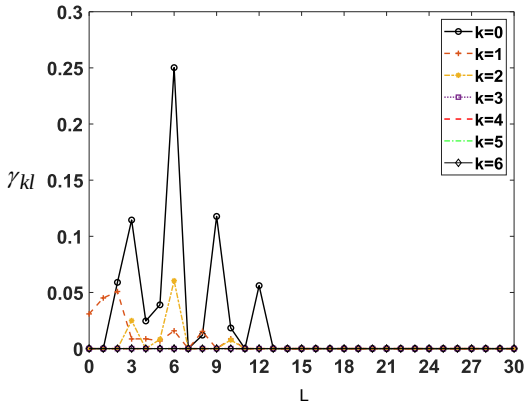

(c) Structure 3

Fig. 7 Fourier series amplitude of the sample shells

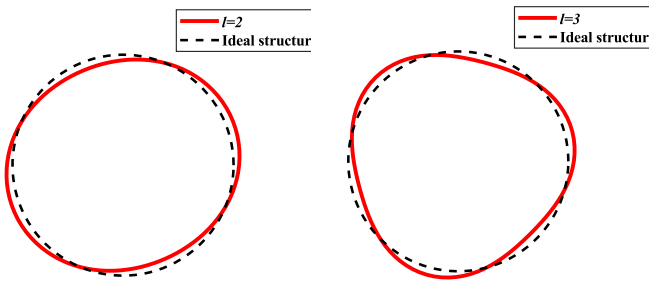

(a) $l=2$ (b) $l=3$

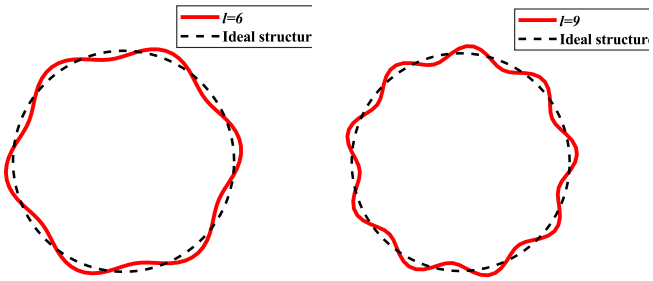

(c) $l=6$ (d) $l=9$

Fig. 8 Imperfection features of circumferential significant waveform

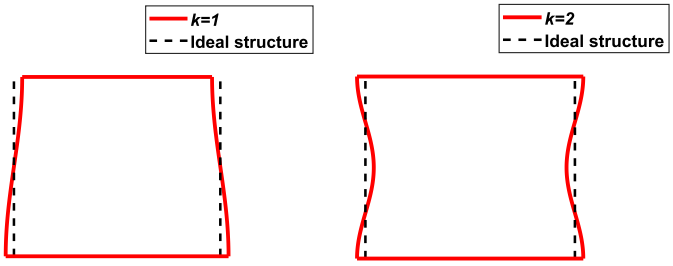

(a) $k=1$ (b) $k=2$

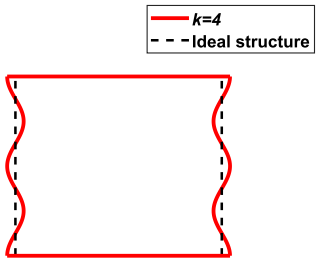

(c) $k=4$

Fig. 9 Imperfection features of axial significant waveform

The above features respectively construct the circumferential and axial imperfection bodies of welded plate structures, and reflect the overall law of imperfection features of such structures. The amplitude corresponding to each waveform reflects the difference of each product.The dominant Fourier coefficients are employed to reconstruct the structure. The reduction of the axial critical load of the structure under different waves is summarized. The results are shown in Table 3.

Table 3
The critical load characterized by single order coefficient

Order	Bearing load (kN)			Contribution of bearing capacity reduction(%)
	Shell 1	Shell 2	Shell 3	
$k=1$	3088.87	3100.47	3095.80	5.20
$k=2$	2823.00	2969.61	2971.57	68.29
$k=4$	3170.42	3156.34	3116.15	-13.99
$l=2$	3102.74	3089.46	3100.17	5.05
$l=3$	3100.63	3102.56	3098.49	3.42
$l=6$	2957.28	3029.39	2996.84	43.02
$l=9$	3155.28	3144.29	3140.09	-14.30

The results revealed that the off-surface deviation amplitude and period of the imperfection field are larger at lower order, which leads to larger reduction of the bearing load. As the order increases, it provides a smaller amplitude and period of the imperfection field. Among them, the two-order waveform of k=2 and l=6 contribute significantly to structural load reduction.The waveform signature of the structure during buckling are shown in Fig.10, which is manifested as 6 circumferential waves and 2 axial waves, consistent with the two-order waveform of k=2 and l=6. These two order imperfection signature are close to the buckling form of the structure, and can easily induce the structure to buckle under axial load.

The Fourier coefficients required to construct 1-m-diameter shell imperfections are more than 1000 terms.under $R^2 \geq 99.9\%$. The efficiencies about three simplification methods were analyzed and shown in Fig.11.

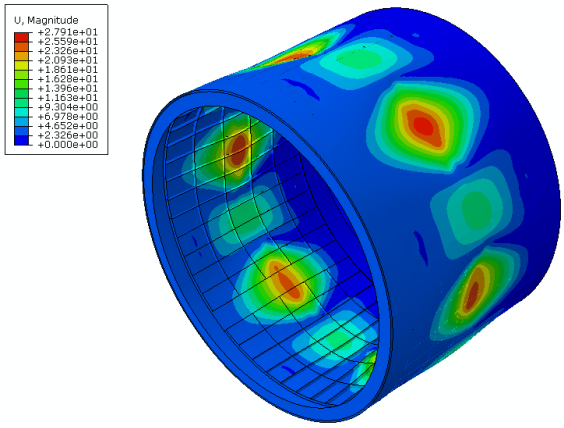

Fig. 10 Structural buckling waveform features

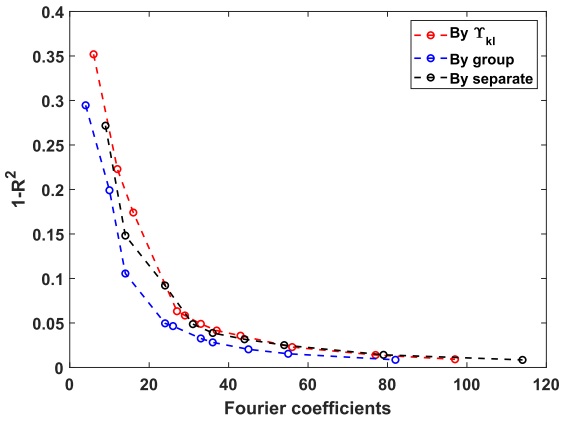

Fig. 11 Comparison of simplification efficiency

The number of Fourier coefficients required by the group set simplification method is lower than other two methods. Because the coefficients of each order A_{kl} and B_{kl} are different, some global small quantities will be retained in the simplified processing, resulting in low efficiency. Although γ_{kl} represents the amplitude of the two types of coefficients, the two types of coefficients of the same order are retained in the simplification process, so that part of the global small quantity is retained and the efficiency is reduced.However, set simplification method is more efficient because it selects from a global perspective and does not introduce global small quantity.

The coefficients of Fourier series are simplified considering the accuracy of the determination coefficient greater than 96%. The retained coefficients constitute the simplified GIs, and the comparison before and after is shown in Fig.12. The simplified imperfections ignore the items which influence the bearing capacity and keep the dominant items which can reduce the bearing capacity apparently.

In order to further test the rationality of simplification, the bearing capacity and buckling deformation of the structure were obtained which are tabulated in Table.4. The calculation deviation of structural bearing capacity compared with the full case is less than 1%, which meets the accuracy requirements. Moreover, the buckling mode and buckling position of the structure are highly coincident with the simulation results of real imperfections.

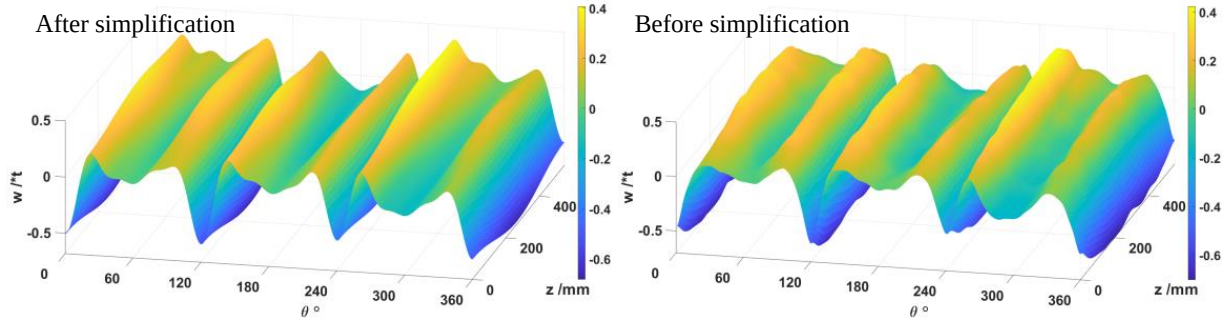

(a) Sample 1

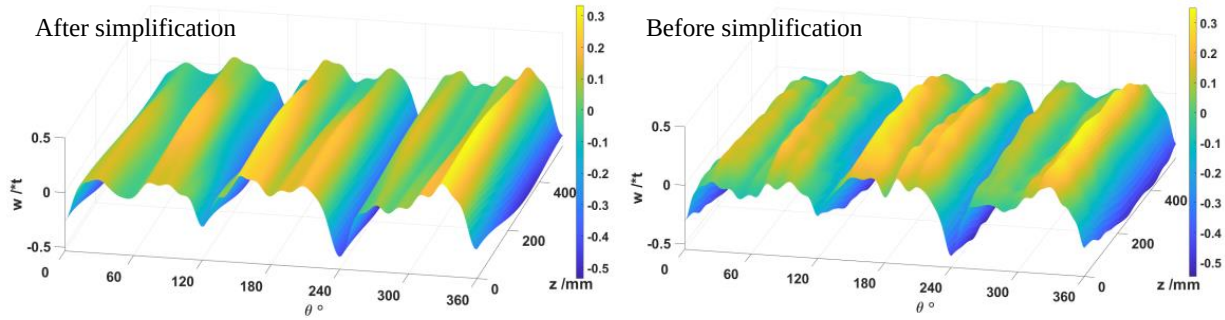

(b) Sample 2

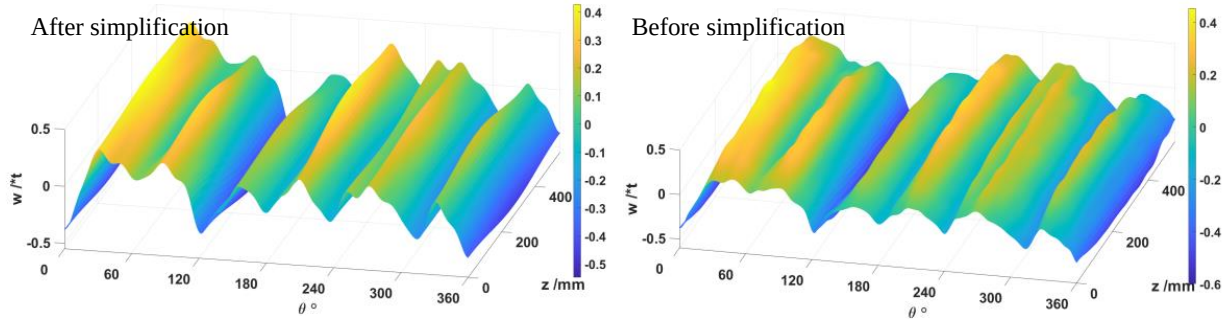

(c) Sample 3

Fig. 12 Comparison of simplification efficiency

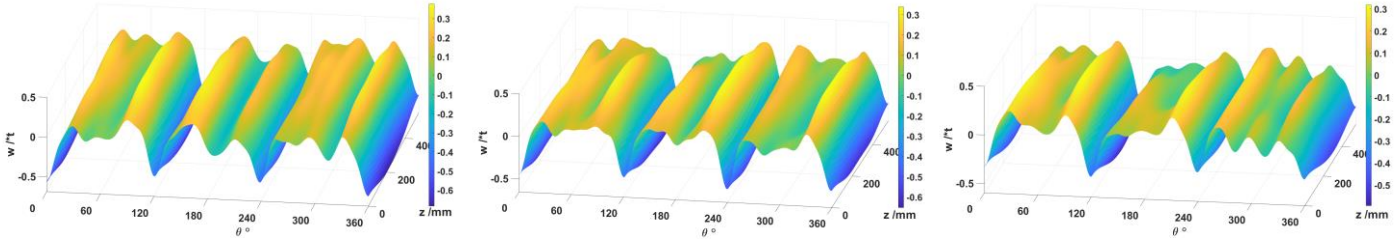

(a) (b) (c)

Fig. 13 Random field imperfection feature

Table 4
The bearing capacity of the structure after imperfection simplification

ID	Total Fourier coefficients	Coefficient of determination R^2	Bearing capacity(kN)	RP(%)	Buckling position
1	30	0.964	2783.1	0.3	$4\pi/3$
2	33	0.967	2874.8	0.8	$2\pi/3$ and $4\pi/3$
3	24	0.966	2906.8	0.7	0 and $2\pi/3$

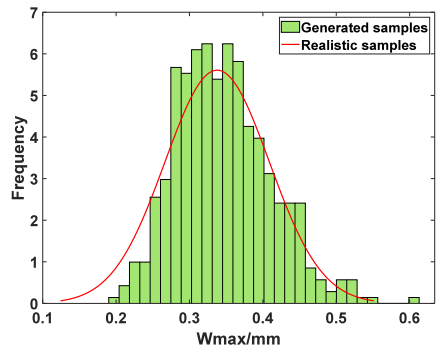

（a）Maximum statistics

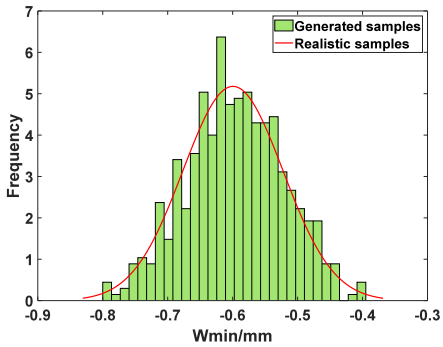

（b）Minimum statistics

Fig. 14 Distribution on the maximum off-surface deviation of random field

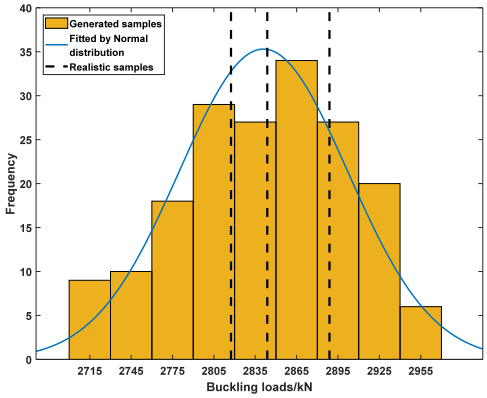

Fig. 15 Distribution on the bearing load

4.3. Imperfection random field-based bearing load prediction

Uniform sampling for imperfection field was carried out to reconstruct the structure for buckling analysis. The minimum off-surface deviation constraint is introduced in the imperfection feature field during sampling. 200 groups of imperfection characteristic fields were generated within 2 hours and the structures were reconstructed according to the sampling results.

According to the discussion above, the influence of imperfections on the bearing capacity is related to the features of imperfections and the amplitude of off-surface deviation. Three cases in the sample set were contoured to investigate the feature of the random field as shown in Fig.13. It presents the typical “M” shape for each part of the shell which is highly consistent with the actual samples.

The distribution about the maximum off-surface deviation of all random samples were shown in Fig.14. The results show that the minimum value is basically consistent with the sample distribution form, and the maximum value is slightly deviated from the decreasing direction of the deviation value under the sample distribution form. The majority of the results falls within the envelope of the sample probability density curve. The statistics of the maximum off-surface deviation of the test set are close to the sample state.

As shown in Fig.15, the results from the experiments all fall within the distribution range of the loading capacity of random fields.And it coincides with the high probability distribution. Using the Anderson-Darling test, when the significance level is greater than 0.05, the results are considered to follow normally distribution. According to the physical test results on the bearing capacity of the real sample, the mean and variance of the bearing capacity of the structure are predicted. Structural design orientated, the envelope of the structural load is realised by considering the confidence level of meeting the requirements based on the prediction of the load uncertainty. Under the normal distribution hypothesis of small sample, the mean and variance of the population are unknown. The confidence interval estimation on the mean and standard deviation can be expressed as:

$$\begin{aligned}\hat{\mu}&:\left(\overline{X}\pm\frac{S}{\sqrt{n}}t_{\alpha/2}(n-1)\right)\\ \hat{\sigma}&:\left(\frac{S\sqrt{n-1}}{\sqrt{\chi^2_{\alpha/2}(n-1)}},\frac{S\sqrt{n-1}}{\sqrt{\chi^2_{1-\alpha/2}(n-1)}}\right)\end{aligned}\tag{9}$$

Where $\overline{X}$ and S are the mean and standard deviation of the sample respectively. With the significance level $\alpha=1$, the confidence intervals for estimating the population mean and standard deviation are $\hat{\mu}\in[2760.32,2939.62]$ and $\hat{\sigma}\in[13.29,159.78]$, respectively. Under the imperfection random field, the mean μ=2839.3 and standard deviation σ=60.6 fall within the above confidence interval. The results clarify that the imperfection random field model proposed in this work can accurately reflect the influence of the surface detail on the bearing capacity.

5. Conclusion

In this paper, for the problem of uncertainty in the shape of welded thin-walled cylindrical shell structure of the panel, we innovatively put forward a small sub-sample-based Fourier series geometric imperfection random field construction method, and combined with the results of the strength test to carry out the load-bearing capacity of the target verification. Based on the typical surface imperfection characteristics of thin-walled cylindrical shells welded by panels in relation to the process, the sample expansion is realised using a single panel as a sample. From a completely new perspective, a dual defect imperfection uncertainty random field construction method based on the waveform and amplitude of the sample imperfection distribution is used, which ensures the adequacy of the sampling process and imposes constraints on the deviation of the results from the sample. The sampling test results match the experiments, verifying the accuracy of the method, and the following conclusions are drawn:

(1)The characterization of GIs by Fourier series in the traditional method requires a large number of coefficients, which is not conducive to random field modeling. The coefficient set reduction method proposed in this paper is applied, and the contribution degree of each order coefficient to the whole imperfection is taken as the reduction criterion. Under the premise of ensuring 99% accuracy of bearing capacity and consistent failure mode, more than 1,000 coefficients can be reduced to about 30, which greatly improves the characterization efficiency.

(2)According to the test results of the geometrical imperfections of welded cylindrical shell structures and the imperfection field data published in literature, the imperfection rules of each panel are consistent. By taking the smallest independent unit of the structure, the single wall panel, as the statistical sample of imperfection amplitude, a imperfection random field model is established to achieve sample expansion to a certain extent.

(3)Geometric imperfection feature sampling is carried out with Fourier series statistics of product samples, and imperfection magnitude constraints are carried out with statistics of panel samples to establish a geometric imperfection random field construction method. Tested by 200 sets of sampling data, the structural bearing capacity distribution under the random field model reasonably envelops the physical test results.

With the increase of the number of samples, the method has a tendency to grow in construction accuracy. The proposed method is a technical prerequisite for the simulation of thin-walled cylindrical shells' load-carrying capacity targeting in consideration of geometric imperfection random fields, and provides technical support for the realisation of scientific determination of the lower limit of structural strength and deviation based on the probabilistic method.

Acknowledgments

This work was supported by the National Natural Science Foundation of

China (Grant Nos. U2141217), and the Chinese pre-research project on Civil Aerospace Technologies (Grant Nos.305060504) .

References

[1] Chan S.L. and Chui P.T., Non-Linear Static and Cyclic Analysis of Steel Frames with Semi-Rigid Connections, Elsevier, New York, 2000.

[2] Liu S.W., Chan T.M., Chan S.L. and So. D.K.L., "Direct analysis of high-strength concrete-filled-tubular columns with circular & octagonal sections", Journal of Constructional Steel Research, 129, 301-314, 2017.

[1] Shi, Y.H., Fu, H.F., Xv, W.X. and Yang, F., "Research status and prospects on the strength variation coefficient of large diameter thin-walled structures" , Structure and Environment Engineering, 51, 1-12, 2024. (in Chinese)

[2] Jiao, P., Chen, Z., Tang, X., Su, W., and Wu, J., "Design of axially loaded isotropic cylindrical shells using multiple perturbation load approach–Simulation and validation", Thin-Walled Structures, 133, 1-16, 2018.

[3] Naraykin, O., Sorokin, F., and Kozubnyak, S., "Numerical Determination of the Splitting of Natural Frequencies of a Thin-Walled Shell with Small Nonaxisymmetric Imperfections of the Middle Surface", Mathematical Models and Computer Simulations, 15(5), 850-862, 2023.

[4] Teter, A., and Kolakowski, Z., "Interactive buckling of wide plates made of Functionally Graded Materials with rectangular stiffeners", Thin-Walled Structures, 171, 108750, 2022.

[5] Weingarten, V. I., Seide, P., and Peterson, J. P., "Buckling of thin-walled circular cylinders", No. NASA-SP-8007, 1968.

[6] Hilburger, M. W., Nemeth, M. P., and Starnes Jr, J. H., "Shell buckling design criteria based on manufacturing imperfection signatures", AIAA journal, 44(3), 654-663, 1968.

[7] Wang, B., Zhu, S., Hao, P., Bi, X., Du, K., Chen, B., Ma, X.,and Chao, Y. J., "Buckling of quasi-perfect cylindrical shell under axial compression: a combined experimental and numerical investigation", International Journal of Solids and Structures, 130, 232-247, 1968.

[8] Hühne, C., Rolfes, R., Breitbach, E., and Teßmer, J., "Robust design of composite cylindrical shells under axial compression—simulation and validation", Thin-walled structures, 46(7-9), 947-962, 2008.

[9] Wang, B., Hao, P., Li, G., Fang, Y., Wang, X., and Zhang, X., "Determination of realistic worst imperfection for cylindrical shells using surrogate model", Structural and Multidisciplinary Optimization, 48, 777-794, 2013.

[10] Schmidt, H., "Stability of steel shell structures: General Report", Journal of Constructional Steel Research, 55(1-3), 159-181, 2000.

[11] Arbocz, J., and Williams, J. G., "Imperfection surveys on a 10-ft-diameter shell structure", AIAA Journal, 15(7), 949-956, 1977.

[12] Elishakoff, I., and Arbocz, J. [1982] "Reliability of axially compressed cylindrical shells with random axisymmetric imperfections", International Journal of Solids and Structures, 18(7), 563-585.

[13] Wagner, H. N. R., Hühne, C., and Elishakoff, I., "Probabilistic and deterministic lower-bound design benchmarks for cylindrical shells under axial compression", Thin-Walled Structures, 146, 106451, 2020.

[14] Kepple, J., Herath, M. T., Pearce, G., Prusty, B. G., Thomson, R., and Degenhardt, R., "Stochastic analysis of imperfection sensitive unstiffened composite cylinders using realistic imperfection models", Composite Structures, 126, 159-173, 2015.

[15] Zhang, D., Chen, Z., Li, Y., Jiao, P., Ma, H., Ge, P., and Gu, Y., "Lower-bound axial buckling load prediction for isotropic cylindrical shells using probabilistic random perturbation load approach", Thin-Walled Structures, 155, 106925, 2020.

[16] Arbocz, J., and Hol, J. M. A. M., "Collapse of axially compressed cylindrical shells with random imperfections", AIAA journal, 29(12), 2247-2256, 1991.

[17] Gray, A., Wimbush, A., de Angelis, M., Hristov, P. O., Calleja, D., Miralles-Dolz, E., and Rocchetta, R., "From inference to design: A comprehensive framework for uncertainty quantification in engineering with limited information", Mechanical Systems and Signal Processing, 165, 108210, 2022.

[18] Hotelling, H. "Analysis of a complex of statistical variables into principal components", Journal of educational psychology, 24(6), 417, 1933.

[19] Ghanem, R. G., and Spanos, P. D., "Spectral stochastic finite-element formulation for reliability analysis", Journal of Engineering Mechanics, 117(10), 2351-2372, 1991.

[20] Li, C. C., and Der Kiureghian, A., "Optimal discretization of random fields", Journal of engineering mechanics, 119(6), 1136-1154, 1993.

[21] Lauterbach, S., Fina, M., and Wagner, W., "Influence of stochastic geometric imperfections on the load-carrying behaviour of thin-walled structures using constrained random fields", Computational Mechanics, 62, 1107-1125, 2018.

[22] Luo, Y., Zhan, J., Xing, J., and Kang, Z., "Non-probabilistic uncertainty quantification and response analysis of structures with a bounded field model", Computer Methods in Applied Mechanics and Engineering, 347, 663-678, 2019.

[23] Li, Z., Pasternak, H., and Geißler, K., "Buckling Analysis of Cylindrical Shells using Stochastic Finite Element Method with Random Geometric Imperfections", ce/papers, 5(4), 653-658, 2022.

[24] Yang, H., Feng, S., Hao, P., Ma, X., Wang, B., Xu, W., and Gao, Q., "Uncertainty quantification for initial geometric imperfections of cylindrical shells: A novel bi-stage random field parameter estimation method", Aerospace Science and Technology, 124, 107554, 2022.

[25] Fina, M., Weber, P., and Wagner, W., "Polymorphic uncertainty modeling for the simulation of geometric imperfections in probabilistic design of cylindrical shells", Structural Safety, 82, 101894, 2020.

[26] Schenk, C. A., and Schuëller, G. I., "Buckling analysis of cylindrical shells with random geometric imperfections", International journal of non-linear mechanics, 38(7), 1119-1132, 2003.

[27] Jianyu, L., Kun, Y., Bo, W., and Lili, Z., "A maximum entropy approach for uncertainty quantification of initial geometric imperfections of thin-walled cylindrical shells with limited data", Chinese Journal of Theoretical and Applied Mechanics, 55(4), 1028-1038, 2023.

[28] Wu, J., Luo, Y. F., and Wang, L., "Inversion algorithm for the geometric imperfection distribution of existing reticulated structures", Journal of Zhejiang University, 52(5), 864-872, 2018.

[29] Arbocz, J., and Hilburger, M. W., "Toward a probabilistic preliminary design criterion for buckling critical composite shells", AIAA journal, 43(8), 1823-1827, 2005.

[30] Hilburger, M. W. [2018] "On the development of shell buckling knockdown factors for stiffened metallic launch vehicle cylinders," In 2018 AIAA/ASCE/AHS/ASC structures, structural dynamics, and materials conference , pp. 1990.

[31] Lovejoy, A. E., Hilburger, M. W., and Gardner, N. W., "Test and analysis of full-scale 27.5-foot-diameter stiffened metallic launch vehicle cylinders", In 2018 AIAA/ASCE/AHS/ASC Structures, Structural Dynamics, and Materials Conference, 2018.

[32] Hilburger, M., Haynie, W., Lovejoy, A., Roberts, M., Norris, J., Waters, W., and Herring, H., "Sub-scale and full-scale testing of buckling-critical launch vehicle shell structures," In 53rd AIAA/ASME/ASCE/AHS/ASC Structures, Structural Dynamics and Materials Conference 20th AIAA/ASME/AHS Adaptive Structures Conference 14th AIAA, 2012.

[33] Hilburger, M., Lovejoy, A., Thornburgh, R., and Rankin, C., "Design and analysis of subscale and full-scale buckling-critical cylinders for launch vehicle technology development", In 53rd AIAA/ASME/ASCE/AHS/ASC Structures, Structural Dynamics and Materials Conference 20th AIAA/ASME/AHS Adaptive Structures Conference 14th AIAA , 2012.

[34] Hilburger, M. W., "Buckling of thin-walled circular cylinders", No. NASA/SP-8007-2020/REV 2, 2020.

Advanced Steel Construction – Vol. 21 No. 1 (2025) 73–82
DOI:10.18057/IJASC.2025.21.1.7

REPAIRING EFFECT OF DOUBLE-SIDED ARRAY STEEL-RODS REINFORCEMENT METHOD FOR U-RIB CRACKS

Cheng Meng, Zhi-Yuan Yuanzhou *, Bo-Hai Ji, Zhuang-Zhuang Chen and Jun-Yuan Xia

College of Civil and Transportation Engineering, Hohai University, Nanjing, Jiangsu, 210098, China
**(Corresponding author. Email: yz-zhiyuan@hhu.edu.cn)*

ABSTRACT

U-rib cracks are one of the typical fatigue cracking modes in steel box girders. To address this issue, a double-sided reinforcement technique, incorporating microstructural damage by using steel rods and steel plates, was proposed. The mechanical performance of steel-rod reinforcement (SRR) and steel-rod plate reinforcement (SRPR) was evaluated using a series of compact tension-shear (CTS) specimens under varying loading angles. Subsequently, finite element models were employed to simulate and compare the maintenance effects of the two configurations. Finally, field application and monitoring were conducted on a U-rid long fatigue crack in a real bridge. The results indicated that both SRR and SRPR significantly improved the tensile strength, effectively reducing the KI at the crack tip, with SRPR exhibiting stronger shear resistance. Monitoring data collected before and after maintenance demonstrated that the proposed new methods reduced stress concentration at the crack tip, inhibiting fatigue crack propagation.

ARTICLE HISTORY

Received: 21 March 2024
Revised: 16 December 2024
Accepted: 16 December 2024

KEYWORDS

Steel-rod and steel plate;
Structural damage;
Fatigue crack;
Effect evaluation;
Field maintenance

1. Introduction

Fatigue cracking is one of the main failure modes in steel box girders, and it is becoming an increasing concern for engineers [1][2]. Under cyclic traffic loading, components of steel box girder are prone to fatigue cracking because of their complex structure and numerous weld details, as demonstrated by previous studies [3][4]. The propagation of these cracks has the potential to significantly compromise the safety and performance of steel box girders, leading to secondary diseases such as corrosion failure and pavement damage. As a result, there is a growing demand for effective repair methods to mitigate crack propagation and extend the lifespan of the structure.

Given the time and cost associated with component replacement, various temporary repair techniques have been developed and extensively studied by researchers to impede fatigue crack growth and enhance local capacity A cost-effective and efficient approach is to drill a smooth stop-hole at the crack tip, which eliminates eliminate plastic region and relieve the stress concentration thereat [5][6][7]. Although drilling stop-holes is simple and cost-effective, its effectiveness can be compromised by challenges such as accurately locating the crack tip and the potential for secondary crack propagation. Impact crack-closure retrofit treatment has been proposed and found to be effective by closing the crack surface in experiments and field maintenance [8][9]. The stress intensity factor reduced and the crack propagation was retarded, as the crack surface remains closed after this treatment, but the effect of impact crack-closure retrofit treatment on long cracks still needs further research [10]. Rewelding, following the removal of original cracks, is a common repair method but is constrained by specific operational environment requirements. In addition, the effects of rewelding are uncontrollable and influenced by complex factors [11][12], this leads to frequent secondary cracking, which complicates future maintenance. Bonding or bolting metal or composite plates and angles onto the crack surface can bear the load together with component and restrain long fatigue crack propagation effectively, but result in irreparable structural damage [13][14].

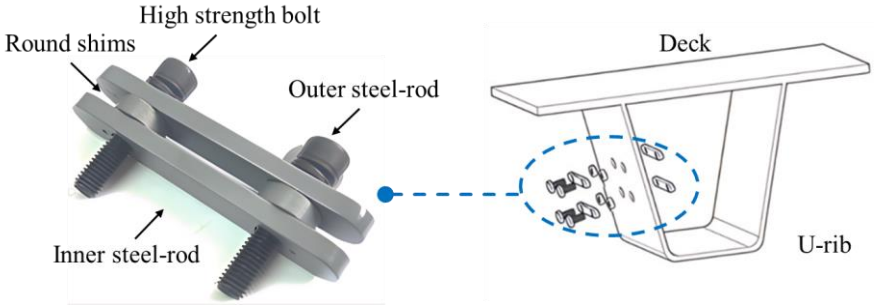

(a) Steel-rod reinforcement (SRR)

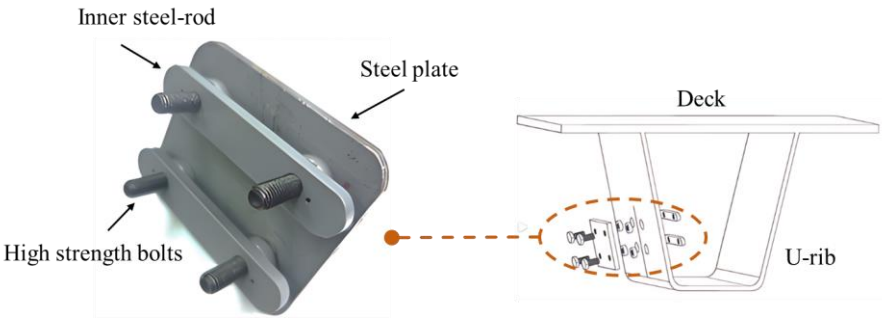

(b) Steel-rod-plate reinforcement (SRPR)

Fig. 1 Configurations of array steel-rod reinforcement

A significant challenge arises from the closure behaviour of U-ribs, which reduces the applicability of existing reinforcement methods for fatigue cracks in the U-rib. To minimize structural damage and prevent the introduction of new fatigue sources, a new array steel-rod reinforcement structure called SRR method was proposed for the U-rib web fatigue cracks [15]. This structure entailed the insertion of steel-rods into prefabricated holes within the U-rib, and connection either with steel-rods or steel plates on the outer side of the U-rib, thereby implementing double-sided reinforcement with micro structural damage, illustrated in Fig. 1a. However, real bridge structures usually experience complicated loads, where the crack direction is not vertical to the applied loads. On this basis, another configuration employing steel-rods on the inner side and steel plates on the outer side is proposed in this work, which is termed steel-rod-plate reinforcement (short for SRPR), seen in Fig.1b. Further research is needed to evaluate the effectiveness of SRR and SRPR in practical bridge crack repair scenarios.

In this work, compact tension-shear (short for CTS) specimens were designed for conducting tension-shear mixed load tests [16]. The mechanical performance of SRR and SRPR was compared. Then, a segmental finite element model was simulated to evaluate the maintenance effects of these two reinforcement configurations. In addition, field maintenance and monitoring on a real steel bridge were carried out, the strain data near the crack tip before and after maintenance was recorded and the stress distribution was analyzed. The research results provide a reference for the repair of fatigue cracks subjected to mixed loads in real bridge applications.

2. Experimental investigations

2.1. Specimen

The CTS specimen was fabricated from Q345qD steel, which is widely used in the real bridge construction. The specific geometric details of the CTS specimen are given in Fig. 2, and the size of specimens was 200 ×160 ×6 mm. Pre-existing edge cracks in the CTS specimens were introduced using wire electrical discharge machining, with a crack length of 80 mm and a width of 0.2 mm. For SRR, two pairs of steel rods were used, while SRPR adopted a combination of steel plate and inner steel-rods. The distance between steel-rods was 40 mm, and the steel plate with a size of 80×80 ×6 mm covered the crack.

The CTS fixtures, shown in Fig. 2, were made from Q420 steel to apply a tension-shear mixed load at different angles (α). α = 0° corresponds to pure tension load, while α = 90° represents pure shear load. The application of pure tension load, pure shear load, as well as mixed-mode load was allowed to the CTS specimens simply by change α. The test conditions with different angles, loads and schemes are detailed in Table 1.

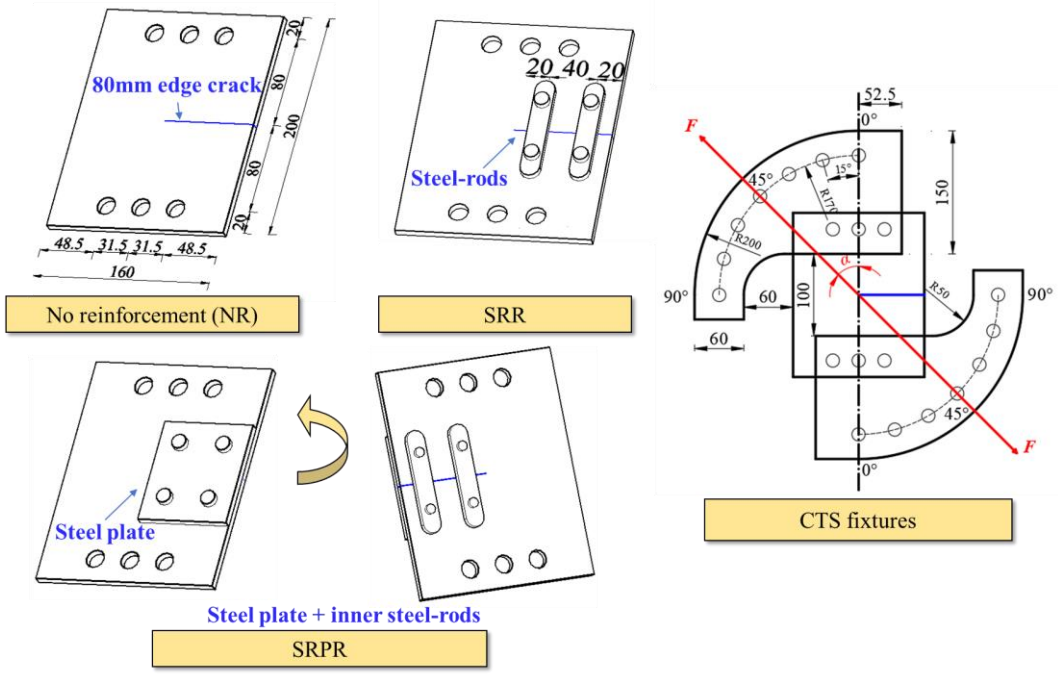

Fig. 2 Specimen details (Unit: mm)

Table 1
Test conditions

Specimen number	Angle α/°	Load /kN	Reinforcement scheme
SJ1	0	100	NR
SJ2			SRR
SJ3			SRPR
SJ4	45	70	NR
SJ5			SRR
SJ6			SRPR
SJ7	90	50	NR
SJ8			SRR
SJ9			SRPR

2.2. Experimental procedure

The test device is illustrated in Fig. 3. Static tests were conducted using an electric universal testing machine with a maximum test force of 200 kN and an accuracy of ±0.5%. Steel-rods and steel plates were implemented on SRR and SRPR specimens. The high-strength bolts were pre-tightened to about 35N·m. Throughout the entire experimental procedure, the loading speed of the machine was stringently controlled at a steady loading rate of 2.0mm/min.

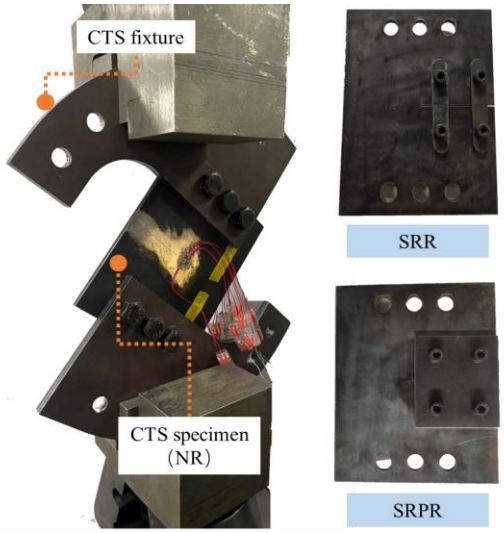

Fig. 3 Test device

To evaluate the effect of maintenance, strain gauges were strategically placed near the crack to analyze changes in the stress intensity factors. Rittel [17] proposed that the strains at any point located at (r, θ) can be expressed in a cartesian coordinate system (Fig. 4a), donating by K_{I} and K_{II} the two stress intensity factors. Zhou et al. [18]investigated the influence of strain gauge position on the stress intensity factors and suggested a reasonable strain gauge arrangement for calculating the stress intensity factors. Fig. 4b illustrates the arrangement of strain gauges on the specimen.

Where ε_{11} and ε_{22} are the strain measurements of the two strain gauges, E is the Young's modulus, here is 2.10×10^5 MPa. v is the Poisson's ratio, here is 0.3.

$$\varepsilon_{11}=\frac{1}{E\sqrt{2\pi r_1}}\cos\frac{\theta_1}{2}\left[(1-\nu)-(1+\nu)\sin\frac{\theta_1}{2}\sin\frac{3\theta_1}{2}\right]K_{\mathrm{I}}-\frac{1}{E\sqrt{2\pi r_1}}\sin\frac{\theta_1}{2}\left[2+(1+\nu)\cos\frac{\theta_1}{2}\cos\frac{3\theta_1}{2}\right]K_{\mathrm{II}}$$
$$\varepsilon_{22}=\frac{1}{E\sqrt{2\pi r_2}}\cos\frac{\theta_2}{2}\left[(1-\nu)-(1+\nu)\sin\frac{\theta_2}{2}\sin\frac{3\theta_2}{2}\right]K_{\mathrm{I}}+\frac{1}{E\sqrt{2\pi r_2}}\sin\frac{\theta_2}{2}\left[2\nu+(1+\nu)\cos\frac{\theta_2}{2}\cos\frac{3\theta_2}{2}\right]K_{\mathrm{II}} \quad (1)$$

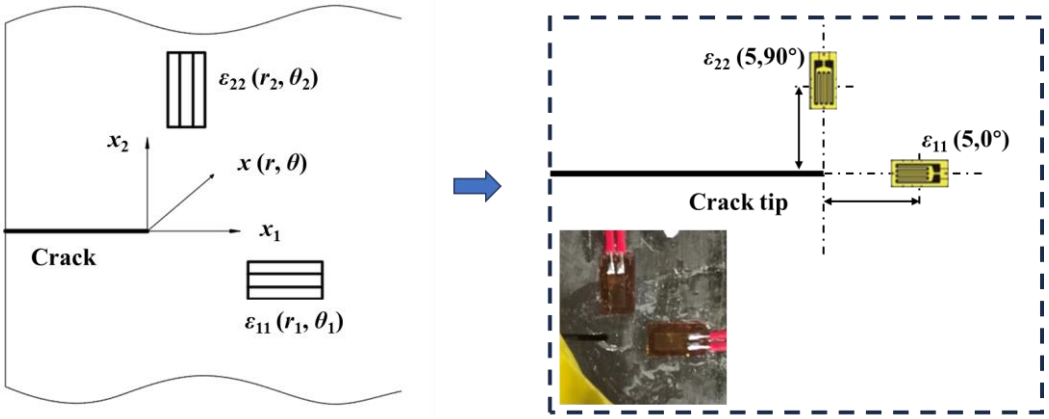

(a) Coordinate system (b) Strain gauge positions

Fig. 4 Measurement points layout

2.3. Experimental results

2.3.1. Pure tension load

The stress intensity factors versus forces under pure tension load are presented in Fig. 5. As the fracture toughness of Q345qD is 2 096 MPa·mm$^{1/2}$, the data exceeding 2 000 MPa·mm$^{1/2}$ have been omitted from the figure [19]. K_{I} exhibited a rapid increase as the applied load increased, while K_{II} remained consistently low and could be considered negligible. This behavior indicated that the specimens experienced a relatively uniform distribution of force, with the crack tip being subjected to approximately pure tension. The experimental load mode was close to the ideal uniaxial tension load. Both SRR and SRPR led to a reduction in the values of K_{I}. Notably, the presence of the steel plate resulted in a larger contact area, covering a greater portion of the effective crack length and restraining crack deformation, which led to a more significant decrease in K_{I}.

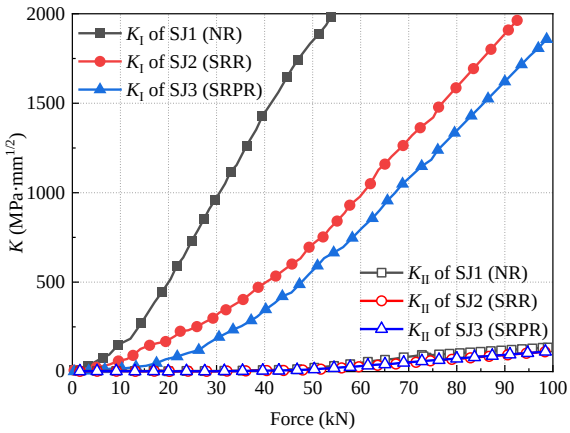

Fig. 5 The stress intensity factors under 0° (pure tension load)

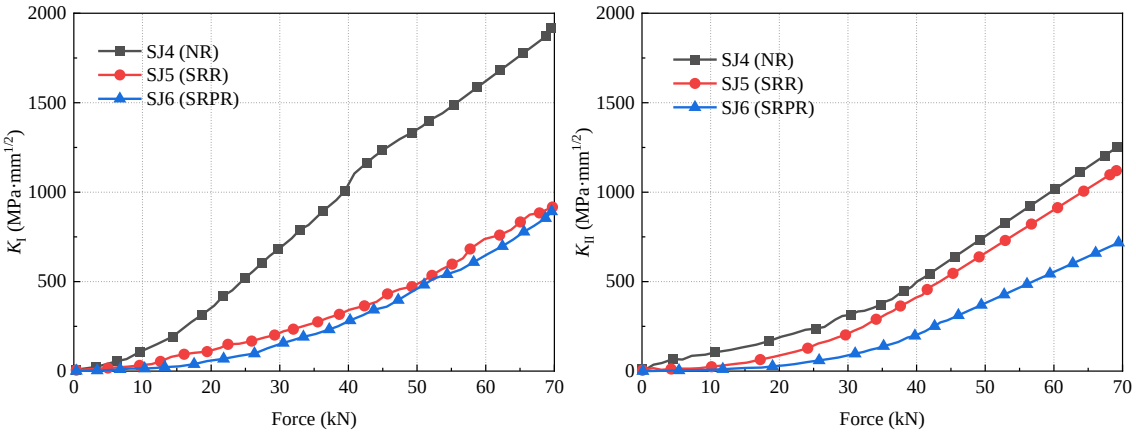

(a) K_I (b) K_{II}

Fig. 6 The stress intensity factors under 45° (tension-shear mixed load)

2.3.2. Tension-shear mixed load

Under tension-shear mixed load, the crack tip experienced tension and shear stresses simultaneously. As observed, K_I of SJ4 increased rapidly, while that of SJ5 and SJ6 exhibited slow growth. The reduction in K_I was approximately consistent for both the SRR and SRPR. K_{II} values, which remained relatively small, were minimally affected by SRR, as the trend of K_{II} curve growth of SJ4 and SJ5 was almost consistent. Benefiting by the steel plate, the shear resistance effect of SRPR was more obvious, manifested as K_{II} values of SJ6 reduced by a certain amount.

2.3.3. Pure shear load

As depicted in Fig. **7**, the pure shear load could be divided into two stages. When the load was small, K_I values were close to zero, indicating that the specimens were experiencing predominantly uniaxial shear stress. The K_{II} values decrease after maintenance. SRPR showed more reduction in the values of K_{II}. Once the load exceeded 38kN, both K_I and K_{II} exhibited a significant increased, which indicated that load mode has gradually shifted pure shear load to tension-shear mixed load. And the maintenance effect gradually decreased at this stage. The shear resistance of SRPR was slightly better.

At lower loads, both SRR and SRPR exhibited a certain shear resistance. As the external load increased, uniaxial pure shear load became unsustainable and turned to tension-shear mixed load with larger angles. SRPR demonstrated a more robust maintenance effect compared to SRR.

2.4. Stress analysis

2.4.1. Finite element model

The above experimental findings illustrated the effects of SRR and SRPR on reducing the stress intensity factors at the crack tip of CTS specimens under different loading angles. Numerical calculations were performed by using ABAQUS software to analyze the stress characteristics in these specimens. The loading condition was simplified to as a plane stress state and the specimens were assumed to be isotropic. The dimensions and material constants of the model were consistent with the specimens. The model was meshed using solid element type C3D8R with a grid size of 1mm, and the boundary conditions of the model are shown in Fig. **8**. The elastic modulus of the whole model was taken to be 2.06 × 10^5 MPa and the Poisson's ratio was 0.3.

The prefabricated crack was formed by extended finite element method and mesh refinement at the crack tip was conducted. In the models of specimens with SRR and SRPR, components such as steel-rods, steel plate, high-strength bolts and washers were modelled according to reference[15].To achieve loading at different angles, the external load was distributed according to the following equation [7].

$$\begin{aligned} F_1 &= F_6 = F\left(\frac{1}{2}\cos\alpha + \frac{m}{l}\sin\alpha\right) \\ F_2 &= F_5 = F\sin\alpha \\ F_3 &= F_4 = F\left(\frac{1}{2}\cos\alpha - \frac{m}{l}\sin\alpha\right) \end{aligned} \tag{2}$$

Where l and m are geometrical parameters, here are 80 mm and 62 mm respectively; α is the loading angle; F is the external load.

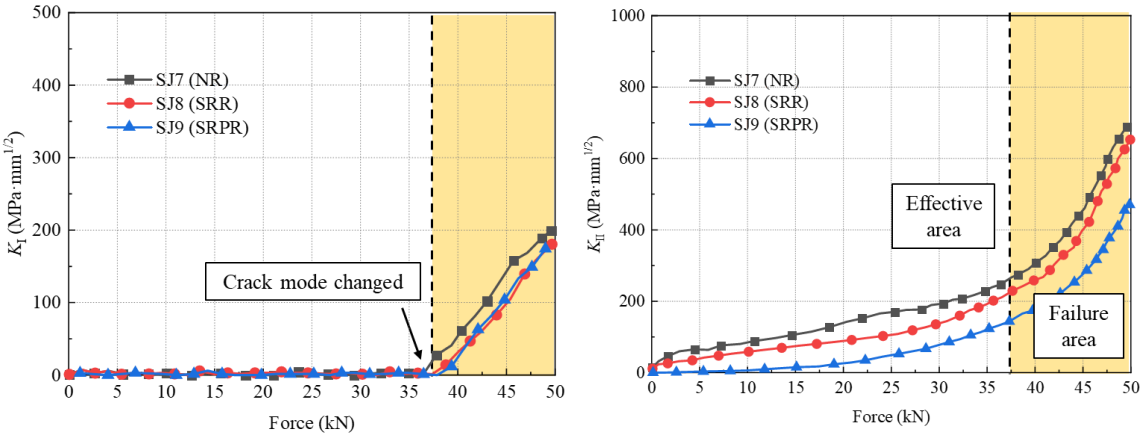

(a) K_I (b) K_{II}

Fig. 7 The stress intensity factors under 90° (pure shear load)

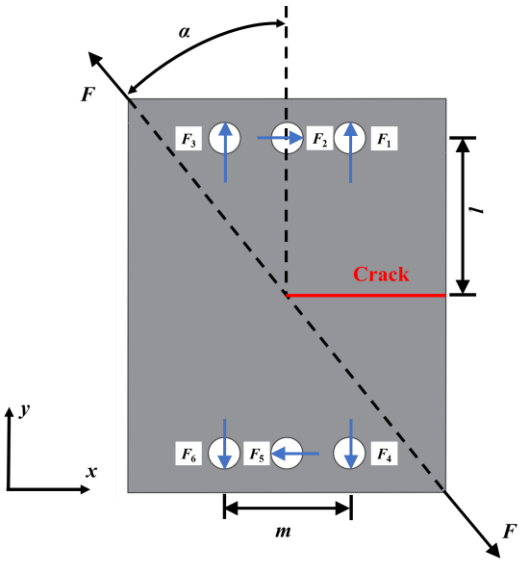

(a) Boundary conditions

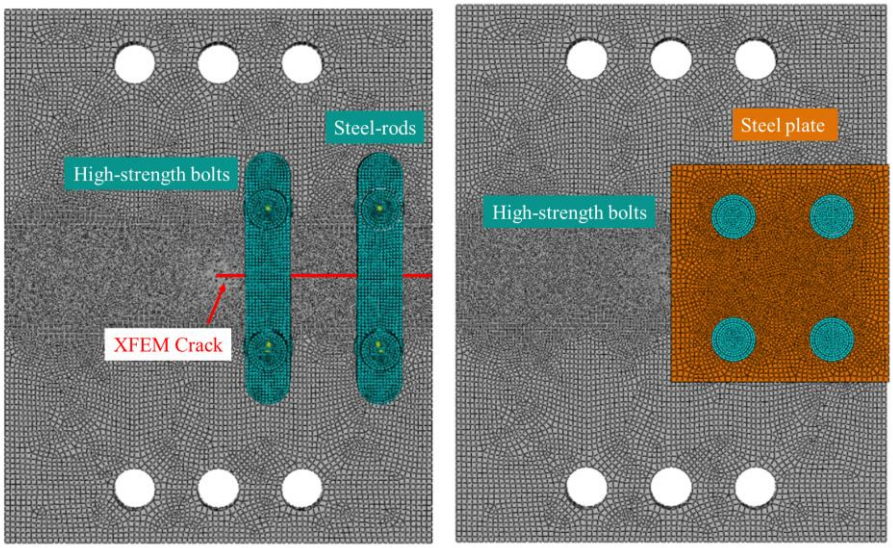

(b) Assembly and Meshing

Fig. 8 Finite element model (SRR and SRPR)

2.4.2. Model verification

For the NR specimens with edge crack, previous studies have provided a calculation method for the stress intensity factors at the crack tip [19], as shown in Eq. (3).

$$K_{\mathrm{I}}=\frac{F\cos\alpha}{Wt}\sqrt{\pi a}\,\frac{1}{(1-\frac{a}{W})}\sqrt{\frac{0.26+2.65(\frac{a}{W-a})}{1+0.55(\frac{a}{W-a})-0.08(\frac{a}{W-a})^2}}$$

$$K_{\mathrm{II}}=\frac{F\sin\alpha}{Wt}\sqrt{\pi a}\,\frac{1}{(1-\frac{a}{W})}\sqrt{\frac{-0.23+1.4(\frac{a}{W-a})}{1-0.67(\frac{a}{W-a})+2.08(\frac{a}{W-a})^2}} \quad (3)$$

Where a is the crack length, here is 80 mm; W and t are the width and the thickness of CTS specimen, here are 160 mm and 6 mm respectively.

Taking the model of NR specimen under a load of 40kN, the stress intensity factors K_{I} and K_{II} at the crack tip with different loading angles were calculated. And the theoretical results were obtained by Eq. (3), seen in Table 2. As shown, the error between the numerical results and theoretical results was within 6%, indicating the rationality and feasibility of the finite element model and loading form.

Table 2
Comparisons of stress intensity factors obtained by numerical and theoretical methods

Loding angle α /°	Stress intensty factors	Numerical results / MPa·mm$^{1/2}$	Theoretical results / MPa·mm$^{1/2}$	Error /%
0	K_{I}	904.2	929.4	2.71
	K_{II}	25.5	0	/
45	K_{I}	626.1	657.2	4.73
	K_{II}	343.8	325.4	5.65
90	K_{I}	19.2	0	/
	K_{II}	472.6	460.2	2.69

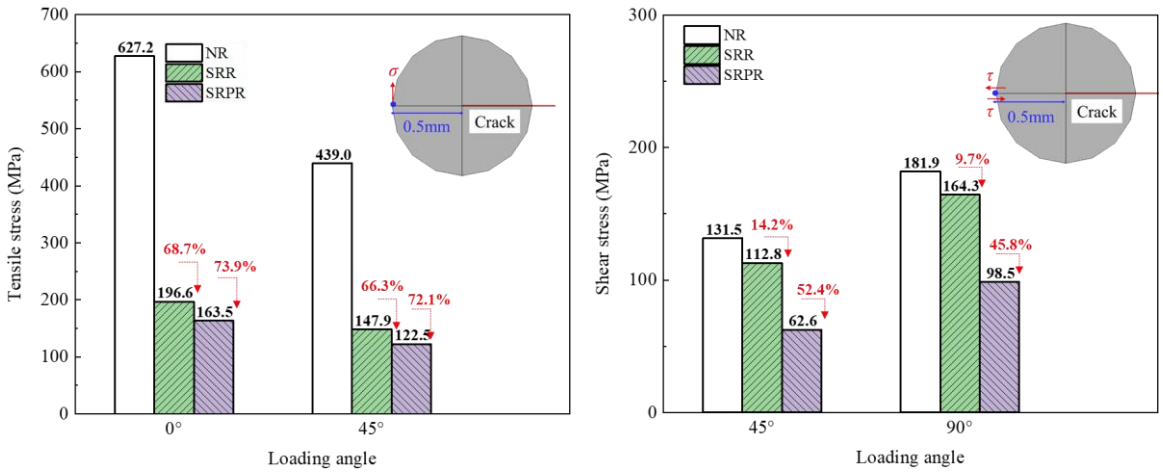

(a) Tensile stresses (b) Shear stresses

Fig. 9 Stresses at the crack tip

2.4.3. Stress characteristics

The stress conditions at the crack tip under various loading angles were investigated. Due to stress singularity, the stress values at the crack tip node tended to approach infinity. Therefore, tensile stresses and shear stresses under 0°, 45°, 90° were extracted at a node located 0.5 mm away from the crack tip, seen in Fig. **9**.

As depicted, both SRR and SRPR were effective in reducing tensile stresses at the crack tip. Compared to SRR, the adoption of SRPR resulted in a further reduction in tensile stress by 5.2% and 5.8% when subjected to pure tension load and tension-shear load mixed load, respectively. Meanwhile, SRR had little effect on reducing shear stress, while SRPR reduced shear stress at the crack tip by nearly half. SRPR achieved a better maintenance effect under shear load, which was consistent with the experimental results.

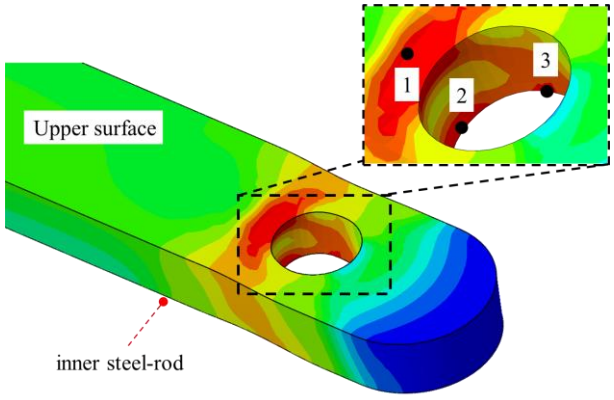

Fig. 10 Mises stress distribution of inner steel-rod

To analyze the stress characteristics of steel-rods under tension-shear mixed load, a force of 100 kN was applied to the model shown in Fig. **8**. The load was incrementally increased from 0 kN to 100 kN in 20 steps, with increments of 5 kN. During the simulation process, notable stress concentrations were observed at both the upper and lower surfaces of inner steel-rod. The locations with high stress concentrations were identified as Point 1, 2, and 3, as illustrated in Fig. **10**, and were potential failure locations for steel-rod.

The mises stress variations at these designated points were extracted, as shown in Fig. **11**. As the applied load increased, the mises stresses also increased, indicating that steel-rod's participation in bearing the load. With further loading, Point 1 yielded, followed by Point 3, while the stress at Point 2 remained relatively low. Upon Points 1 and 3 entered the plastic phase, the stress at Point 2 rapidly increased and reached the yield strength. Point 1 reached the ultimate strength first, leading to damage to the upper surface and failure of steel-rod.

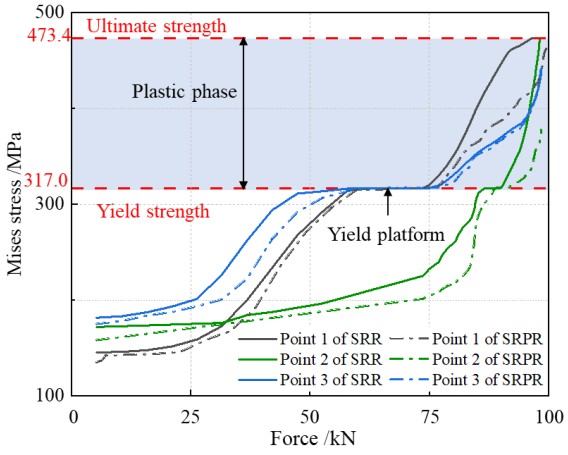

Fig. 11 Stress variation curves of points

It was observed that the stress characteristics at these three points on inner steel-rods of both SRR and SRPR were similar, and steel-rods exhibited similar failure laws, given in Fig. **12**. The overall stresses on inner steel-rod of SRPR were lower than those of SRR. A higher external load on steel-rod of SRPR was required to reach the yield strength.

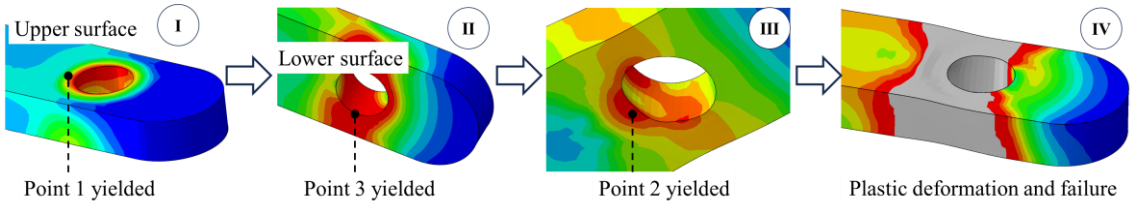

Fig. 12 Failure mode of inner steel-rod

3. Simulation of reinforcement on U-rib

3.1. Segmental model

In the previous study, the roles of SRR and SRPR in hindering crack propagation in flat plate specimens with short cracks was through static testing. Numerical simulations were carried out to evaluate the maintenance effect of these two configurations on long cracks in real bridges. Following the modelling method described in existing research [20], a solid segmental model containing only pavement, deck, U-rid and diaphragm was established by ABAQUS software, as shown in Fig. **13**. The overall dimensions of the model were 12 808 × 4 200 × 1 200 mm. The thickness of pavement and deck was 48 mm and 12 mm respectively. The size of the 7 U-ribs was 300 × 6 × 280 mm, they were spaced 700 mm apart and numbered from 1# to 7#. Five diaphragms, each with an 8 mm thickness and 3200 mm space, were labeled from A to E in turn. The elastic modulus of pavement was 1 000 MPa, while that of the rest was 2.06 × 10^5 MPa. The Poisson's ratio of the model was 0.3.

The global grid of the model was 50 mm, and the meshes in the crack region were refined to 2.5 mm. A long crack was inserted in the U-rib-deck weld at the 4# U-rib located between diaphragms B and C, with the crack shape shown in Fig. **14**. The cracked body was generated using contour integral method, and twenty degenerative elements were introduced at the crack tip, each with a mesh size of 0.1 mm. All translational degrees of freedom for the deck and diaphragms were restricted. A sub-model containing two U-ribs was created to ensure the accuracy of the calculations.

The load amplitude was determined using Fatigue Load Model III, as specified by the Chinese standard [22]. The spacing between the two lateral axles is 2 000 mm, which exceeds the spacing of three U-ribs. Additionally, the spacing between the second and third axles of the vehicle is 6 000 mm, approximately equivalent to the spacing of three transverse diaphragms. The transverse stress influence line for the orthotropic bridge deck is relatively short [23], so the superimposed stress effects between the lateral axles and the front and rear axles could be disregarded. A biaxial moving load was applied to the model and the distance of front and rear axles was 120 mm. The wheel load area measured 600 × 200 mm with a pressure of 0.5 MPa, as illustrated in Fig. **14**.

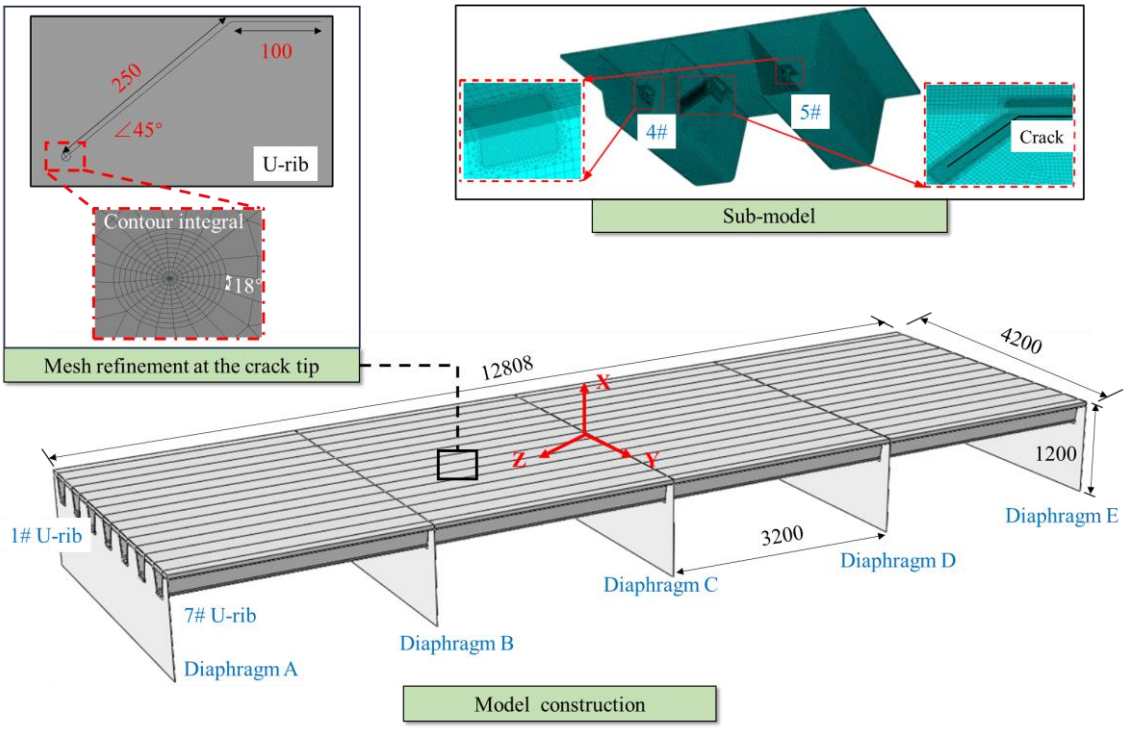

Fig. 13 Segmental finite element model with a long crack (Unit: mm)

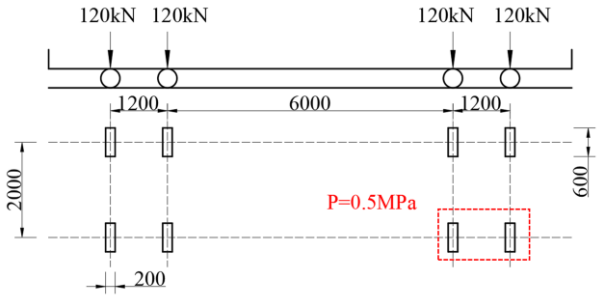

Fig. 14 Load mode (Unit: mm)

3.2. Characteristics of crack

Current practical tests indicate that the most unfavorable working condition is when the vehicle load is directly applied above the crack [24]. Therefore, the biaxial moving load was applied above the long crack mentioned in Fig. **14**. The deformation of the crack under this load case was studied. As the crack can be divided into two parts: an oblique crack and a horizontal crack, two local coordinate systems for these two parts were established respectively, seen in Fig. **15**, where the *x* direction represented the out-of-plane direction, and the *y* direction represented the in-plane direction. Points A and A' were set at the middle of the oblique crack, Points B and B' were set at the ends of horizontal crack. Before loading, Points A and A' coincided, as did Points B and B'. Under the applied loads, mutual extrusion and dislocation were clearly observed. This deformation significantly weakened the mechanical performance and reduced the local stiffness of U-ribs, thereby seriously affecting the structural safety of the steel box girder. Here, the maximum displacement differences in the x and y directions between A and A' were recorded as ΔX_A and ΔY_A, similar to ΔX_B and ΔY_B.

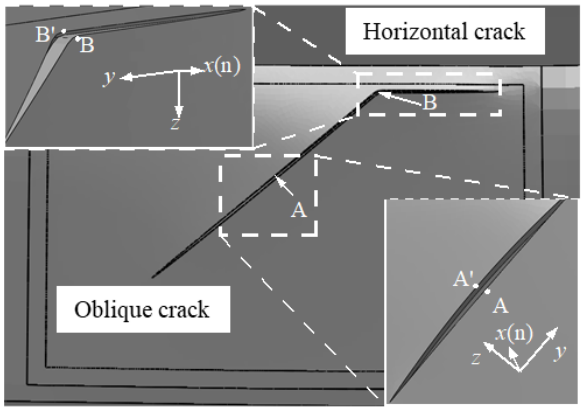

Fig. 15 Deformation of the crack zone

3.3. Reinforcement schemes

Regarding the oblique crack on U-rib as the research object, two reinforcement schemes were proposed: (1) SRR; (2) SRPR. Considering the length of crack, five couples of steel-rods with a 40 mm spacing were arranged on the sub-model, as shown in Fig. **16**a. A 210 × 100 × 6 mm steel plate was positioned over the U-rib crack, with inner steel-rods arranged on the inner side of U-rib, as shown in Fig. **16**c. The materials of steel-rods, steel plate, high strength bolts, spring washers and round shims were specified as Q345qD steel. A pretightening force with the value of 17.8kN was applied on bolts. A friction coefficient of 0.35 was set for the contact surfaces between components.

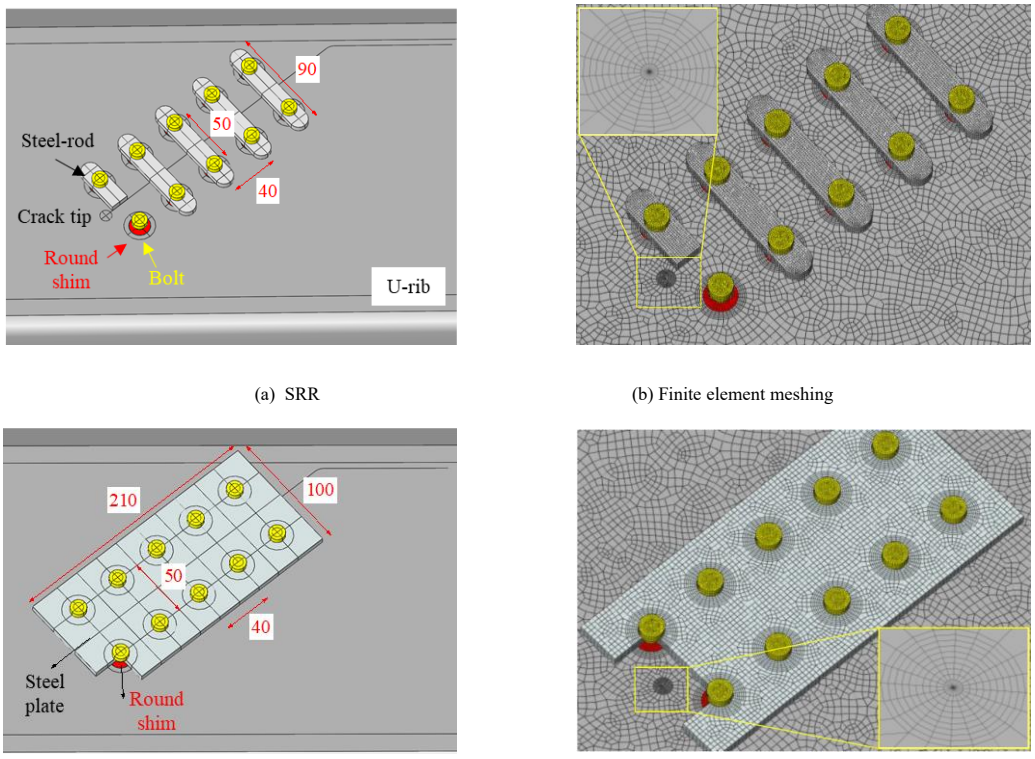

(a) SRR

(b) Finite element meshing

(c) SRPR

(d) Finite element meshing

Fig. 16 Two reinforcement schemes (Unit: mm)

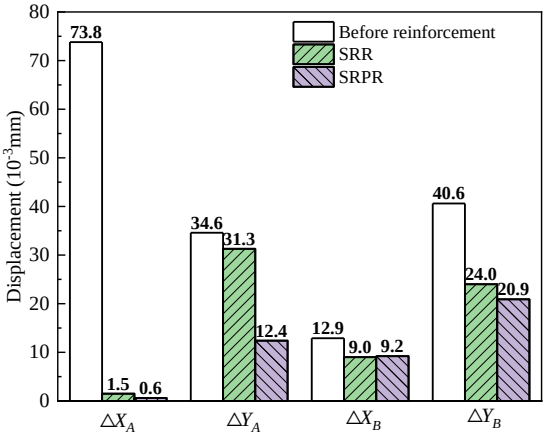

Fig. 17 Maximum displacement differences before and after reinforcement

3.4. Effect Analysis

3.4.1. Deformation

Fig. **17** illustrates the reduction in ΔX_A after applying the SRR and SRPR, resulting in reductions of 98.0% and 99.2%, respectively. These schemes were highly effective in almost completely restraining out-of-plane deformation. For ΔY_A, SRPR reduced it by 64.2%, while SRR only achieved a 9.5% reduction, which indicated that SRPR was more effective at limiting the in-plane deformation of oblique fatigue crack. ΔX_B was small before reinforcement, both of SRR and SRPR could decrease the value of ΔX_B to a certain extent. And ΔY_B was reduced by 40.1% and 48.5% respectively, out-of-plane and in-plane deformation of horizontal crack were limited.

3.4.2. Stress intensity factors

Fig. **18** displays the maximum stress intensity factors on both sides of the crack under the most unfavorable working condition. It was observed that the simulation results for both sides had no significant difference. SRPR and SRR substantially reduce K_{I} on both sides, providing nearly equal tensile resistance. However, K_{II} was almost unchanged after SRR while it decreased by approximately 35% after SRPR. The steel plate effectively restrained the in-plane deformation of the crack and reduced the concentration of stress at the crack tip. It was shown that SRPR offered superior shear resistance compared to SRR, aligning with the experimental results.

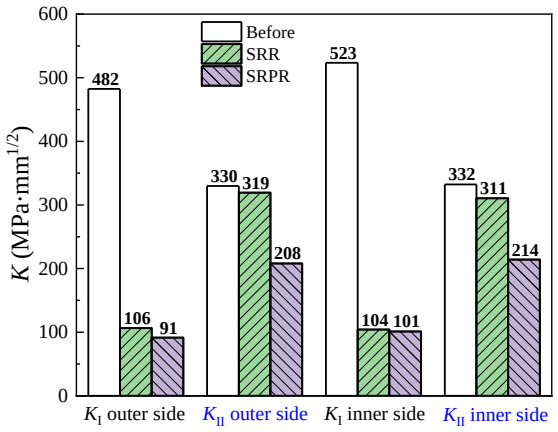

Fig. 18 Maximum K at two sides of crack under Load Case T6

4. Field maintenance and monitoring

4.1. Project of field monitoring

The simulation results indicate that the use of steel-rods and steel plates demonstrated excellent shear resistance, proving to be an effective solution for retrofitting long fatigue cracks in U-ribs. To study the maintenance effect in real bridge, field reinforcement and monitoring were conducted. The background bridge is a steel box girder suspension bridge with a main span exceeding 1,300 meters, which has been in operation for over 20 years. The average daily traffic volume on the bridge has surpassed 100,000 vehicles. The increasing traffic volume has contributed to significant fatigue problems. The fatigue crack in question initiated from the weld joint of U-rib, then forked and propagated obliquely along the U-rib base metal. As vehicle passed over the crack, obvious dislocations were observed on the surface. The length of the crack on the base metal surface was approximately 180mm. Fig. **19** gives the strengthening scheme.

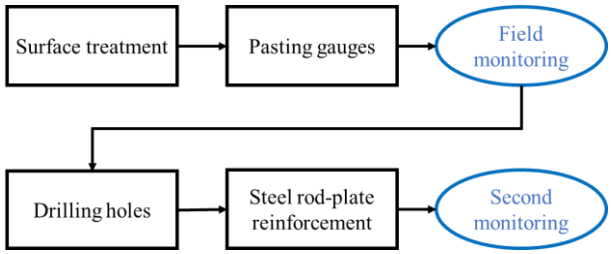

Fig. 19 Scheme of construction

Before attaching the strain gauges, the surface underwent polishing to remove the coating. Six holes, each with 18 mm diameter, were drilled on double sides of the crack body by magnetic drill, as depicted in Fig. **20**b. The strain gauges were installed in a vertical arrangement following the crack tip. To ensure comprehensive maintenance that considered operational constraints and the specific crack characteristics, steel-rods and steel plate were utilized simultaneously, seen in Fig. **20**c. The strain data near the crack tip was recorded using a strain indicator operating at a frequency of 256Hz, and the strain records are converted into stresses by using Hooke's law $\sigma = E\,\varepsilon$. For the material of steel box girder in the studied bridge, the Young's modulus E is 2.10×10^5MPa, and the Poisson's ratio is 0.3. Data acquisition occurred over a 1-hour period both before and after maintenance.

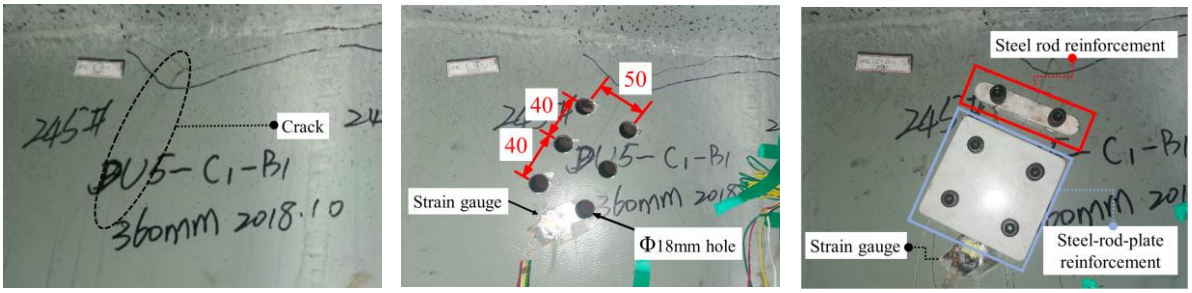

(a) Before maintenance (b) Drilling holes (c) After maintenance

Fig. 20 Diagram of reinforcement in real bridge

4.2. Stress range spectrum

The stress range spectrum, which was based on collected strain data, underwent analysed. To calculate the stress range spectrums, the rain-flow counting method [25] was employed for processing the stress data. After rain-flow computation, the final stress range spectrum is presented in Fig. **21**.

The stress range spectrum for a 1-hour duration was analysed based on the obtained data. The stress amplitudes below 5MPa were excluded from consideration, as the low-stress random amplitudes made only a minimal contribution to the fatigue damage, which were mainly caused by other factors, such as wind, temperature gradient, etc. It was observed that the number of cycles at high stress ranges decreased obviously after maintenance, while the low stress ranges increased. The maximum tensile-compressive stress amplitude reduced from 70 MPa to 50 MPa, marking a 28% decrease. Additionally, the maximum shear stress amplitude reduced from 80 MPa to 60 MPa, with a fall of 25%. These results clearly indicated the positive impact of the maintenance.

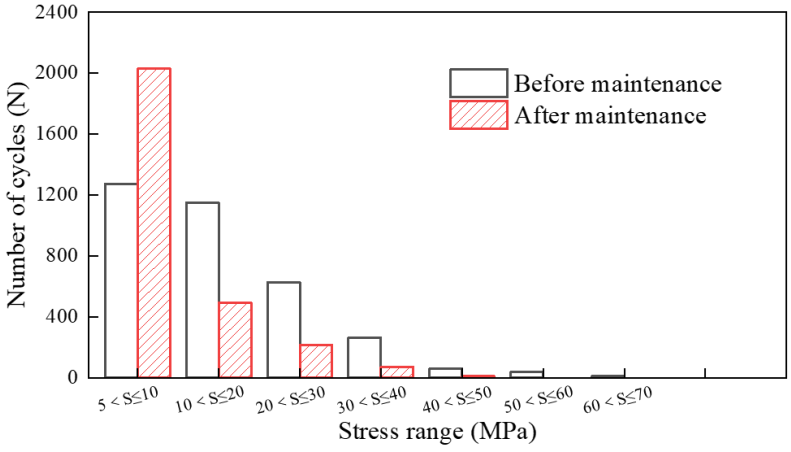

(a) Tensile and compressive stress range spectrum

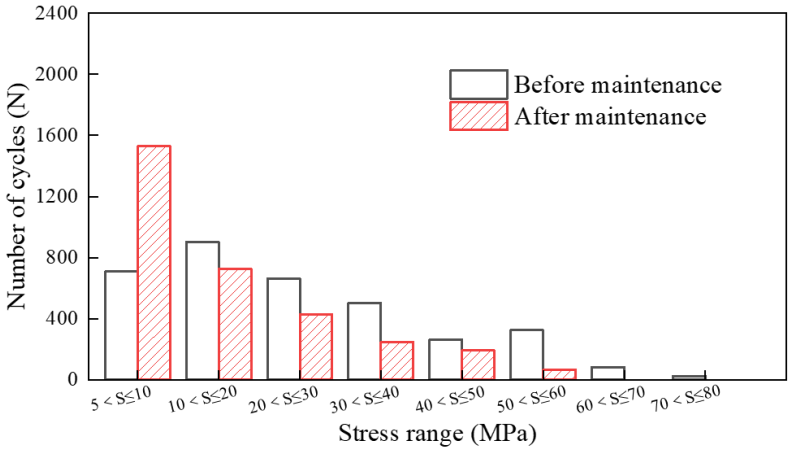

(b) Shear stress range spectrum

Fig. 21 Stress range spectrums obtained within 1 hour

5. Conclusions

(1) Both steel-rod reinforcement (SRR) and steel-rod-plate reinforcement (SRPR) significantly enhanced tensile capacity. Under tension load, these two configurations relieved the stress concentration and reduced K_I. When subjected to a tension-shear mixed load, SRR exhibited minimal shear resistance, whereas SRPR demonstrated a more substantial shear performance. The steel-rods have similar stress characteristics and damage forms, which were manifested by the hole edge reaching yield and plastic damage.

(2) SRPR effectively constrained both out-of-plane and in-plane deformations of oblique cracks in U-rib-to-deck welded joint, reducing the stress intensity factors at the crack tip. While SRR had limited effectiveness in preventing crack deformation.

(3) As indicated by the analysis of the real bridge monitoring results, the method that using steel-rods and steel plates improved the stress conditions at the crack tip. A significant reduction in the number of cycles at high tensile and shear stress ranges was observed, while an increase in the cycles at low stress ranges occurred. As a result, the fatigue crack propagation was effectively suppressed.

Acknowledgements

The research reported herein has been conducted as part of the research projects granted by the National Natural Science Foundation of China under (Grant No. 52308166 and 52378153), the Fundamental Research Funds for the Central Universities under (Grant No. B230201034 and B230204003). The assistances are gratefully acknowledged.

References

[1] Fisher, J.W. and Roy, S., "Fatigue of steel bridge infrastructure", Structure and Infrastructure Engineering, 7, 457-475, 2011. https://doi.org/10.1080/15732479.2010.493304

[2] Jong, F.B.P., "Overview fatigue phenomenon in orthotropic bridge decks in The Netherlands", 2004 Orthotropic Bridge Conference, Sacramento, 489-512, 2004.

[3] Gao, T., Yuanzhou, Z.Y., Ji, B.H. and Xie, Z., "Vision-based fatigue crack automatic perception and geometric updating of finite element model for welded joint in steel structures", Computer-aided Civil and Infrastructure Engineering, 1-17, 2024. https://doi.org/10.1111/mice.13166

[4] Patel, A.B. and Pandey, R.K., "Fatigue crack growth under mixed-mode loading", Fatigue & Fracture of Engineering Materials & Structures, 4(1), 65-77, 2007.

[5] Fang, L., Fu, Z.Q., Ji, B.H. and Kainuma, S., "Research on mixed mode crack drilling under out-of-plane shear in steel bridge deck", International Journal of Fatigue,156, 106679, 2022. https://doi.org/10.1016/j.ijfatigue.2021.106679

[6] Yao, Y., Ji, B.H., Fu, Z.Q., Zhou, J. and Wang, Y.X., "Optimization of stop-hole parameters for cracks at diaphragm-to-rib weld in steel bridges", Journal of Constructional Steel Research, 162, 105747,2019. https://doi.org/10.1016/j.jcsr.2019.105747

[7] Gong, H., Jin, Z.G., Yang, F.P., and Mao, W.T., "Analysis of stop-hole effects on mode I-II fatigue crack behavior for Q420 steel using experiments, FEM and variable length RNN approaches", Theoretical and Applied Fracture Mechanics, 124, 103823, 2023. https://doi.org/10.1016/j.tafmec.2023.103823

[8] Yamada, K., Ishikawa, T. and Kakiichi, T., "Rehabilitation and improvement of fatigue life of welded joints by ICR treatment", Advanced Steel Construction. 11(3), 294–304, 2015. https://doi.org/10.18057/IJASC.2015.11.3.4

[9] Yuanzhou, Z.Y., Ji, B.H., Fu, Z.Q., Kainuma, S. and Tsukamoto, S., "Fatigue crack retrofitting by closing crack surface", International Journal of Fatigue. 119(Feb), 229-237, 2019. https://doi.org/10.1016/j.jcsr.2017.12.015

[10] Yuanzhou, Z.Y., Ji, B.H., Wang, Q.D., and Fu, Z.Q., "Investigation on crack behaviours by closing its surface using impact treatment", Journal of Constructional Steel Research, 156 (May), 1-8, 2019. https://doi.org/10.1016/j.jcsr.2019.01.009

[11] Miki, C., "Fatigue damage in orthotropic steel bridge decks and retrofit works", International Journal of Steel Structures, 6(4), 255-267, 2006.

[12] Fu, Z.Q., Wang, Q.D., Ji, B.H. and Yuanzhou, Z.Y., "Rewelding repair effects on fatigue cracks in steel bridge deck welds", Journal of Performance of Constructed Facilities, 31(6), 04017094, 2017. https://ascelibrary.org/doi/10.1061/%28ASCE%29CF.1943-5509.0001083

[13] Jiang, F., Ding, Y.L., Song, Y.S., Geng, F.F. and Wang, Z.W., "CFRP strengthening of fatigue cracks at U-rib to diaphragm welds in orthotropic steel bridge decks: Experimental study, optimization, and decision-making", Structures, 43, 1216-1229, 2022. https://doi.org/10.1016/j.istruc.2022.07.039

[14] Wang, C.S, Zhai, M.S., Duan, L. and Wang, Y.Z., "Cold reinforcement and evaluation of steel bridges with fatigue cracks", Journal of Bridge Engineering, 23(4), 04018014, 2018. https://doi.org/10.1061/(ASCE)BE.1943-5592.0001219

[15] Meng. C., Yuanzhou, Z.Y., Ji. B.H., Chen, Z.Z. and He, B., "Static analysis on fatigue crack retrofitting using steel-rod reinforcement method", Thin-Walled Structures, 198, 111687, 2024. https://doi.org/10.1016/j.tws.2024.111687

[16] Richard, H.A. and Benitz, K., "A loading device for the creation of mixed mode in fracture mechanics", International Journal of Fracture, 22,55–58, 1983. https://doi.org/10.1007/BF00942726

[17] Rittel, D., "A hybrid experimental-numerical investigation of dynamic shear fracture", Engineering Fracture Mechanics. 72(1), 73-89, 2005. https://doi.org/10.1016/j.engfracmech.2004.01.013

[18] Zhou, G.P. and Chen. H., "Influence of strain gauge position on the calculation of dynamic stress intensity factors", Journal of Harbin Engineering University, 41(12) 1772-1778, 2020. (in Chinese). http://dx.doi.org/10.11990/jheu.201906086

[19] Wright, W.J., "Fracture toughness requirements for highway bridges: past and future trends", Progress in Structural Engineering and Materials, 4(1) 96-104, 2010. https://doi.org/10.1002/pse.99

[20] Richard, H.A., "Some theoretical and experimental aspects of mixed mode fractures", Proceedings of the 6th International Conference on Fracture, New Delhi, India, 3337-3344, 1984.

[21] Fu, Z.Q., Ji, B.H., Ye, Z. and Wang, Y.X., "Fatigue evaluation of cable-stayed bridge steel deck based on predicted traffic flow growth", KSCE Journal of Civil Engineering, 21(4), 1400-1409, 2017. https://doi.org/10.1007/s12205-016-1033-0

[22] Ministry of Transport of the People's Republic of China, Specifications for Design of Highway Steel Bridge: JTG-D64, 2015. (In Chinese).

[23] Ji, B.H., Chen, X., Liu, R. and Yang, M.Y., "A numerical study on the fatigue effect of trough-deck plate weld joint to steel bridge deck system", Progress in Steel Building Structures, 16(6), 56-62, 2014. (In Chinese). https://doi.org/10.13969/j.cnki.cn31-1893.2014.06.007

[24] Wang, Y.X., Fu, Z.Q., Ge, H.B., Ji, B.H. and Hayakawa, N., "Cracking reasons and features of fatigue details in the diaphragm of curved steel box girder", Engineering Structures, 201, 109767, 2019. https://doi.org/10.1016/j.engstruct.2019.109767

[25] Matsuiski, M. and Endo, T., "Fatigue of metals subjected to varying stress", Japan Society of Mechanical Engineering, 96, 100-103,1968.

Advanced Steel Construction – Vol. 21 No. 1 (2025) 83–94
DOI:10.18057/IJASC.2025.21.1.8

AN INNOVATIVE STEEL INTERLOCKING TIE SYSTEM FOR COMPOSITE WALLS IN MODULAR INTEGRATED CONSTRUCTION

Xiao-Kang Zou [1], Ming-Yang Li [2], Wen-Jie Lu [1,*], Jiang Huang [3], Jun Shi [3] and Yao-Peng Liu [4]

[1] *Structures Research Hub, China State Construction Engineering (Hong Kong) Ltd., Hong Kong, China*
[2] *School of Civil Engineering, Southwest Jiaotong University, Chengdu, China*
[3] *China State Construction Engineering (Hong Kong) Ltd., Hong Kong, China*
[4] *School of Civil Engineering and Transportation, South China University of Technology, Guangzhou 510641, China*
** (Corresponding author: E-mail: wenjie.lu@cohl.com)*

ABSTRACT

This paper proposes an innovative steel interlocking tie system for composite walls in reinforced concrete Modular Integrated Construction (MiC), eliminating the need for tie bolts penetrating precast sidewalls. This design facilitates complete factory interior fitting and minimizes on-site disruption to internal finishes. Experimental tests for the proposed steel interlocking system have been conducted and the advanced finite element models for the investigation of the system have been developed. Six case studies comparing density-based topology optimization and empirical optimization using finite element analysis are presented. The empirical optimization demonstrates high computational efficiency, as it does not require elaborate iterative analysis and produces a design comparable to that from topology optimization. The final optimized shape has 49.8% of the weight of the initial design and an average mechanical performance difference of 3.02% compared to the topology optimization.Six case studies comparing density-based topology optimization and empirical optimization using finite element analysis reveal that empirical optimization achieves comparable mechanical performance with significantly reduced computational cost and time. Furthermore, the system's adaptability is demonstrated through adjustments to interlocking tie dimensions accommodating to accommodate varying tying positions and wall thicknesses, effectively controlling wall deformations and meeting strength and stiffness requirements under the requirements of certain wall deformations, strength and stiffness. A successful real-world application in a Hong Kong MiC project is also presented, offering and offers practical guidance for future MiC implementations.

ARTICLE HISTORY

Received: 2 October 2024
Revised: 21 December 2024
Accepted: 22 December 2024

KEYWORDS

Modular integrated construction (MiC);
Interlocking tie system;
Finite element analysis;
Topology optimization

1. Introduction

In recent years, Hong Kong has encountered several challenges, including labor shortages, high construction costs, and significant demands for development in the construction industry. Since 2017, the Modular Integrated Construction (MiC) method has been increasingly adopted to alleviate pressure on the local construction market. This approach shifts many construction processes to prefabrication factories, significantly reducing both the duration and complexity of on-site construction.

Two primary structural systems are common in reinforced concrete MiC: column-beam frame system and shear wall system. Column-beam frame systems are prevalent in low-rise MiC modules, where adjacent modules connect with each other solely at column-beam joints using horizontal and vertical bolts. Shear wall systems, offering greater stiffness than column-beam frame systems, are typically favored in high-rise MiC modules. Although predominantly used in high-rise constructions, shear wall systems can also be beneficial in low-rise constructions due to their reduced impact on interior architectural design compared to column-beam frame systems.

This paper focuses on the shear wall structural system in reinforced concrete MiC, where shear walls are formed between adjacent modules. During on-site installation, the narrow gap between modules is filled with cast-in-situ concrete, creating a composite wall. To prevent deformation of the precast sidewalls during concrete pouring, tie rods penetrating the sidewalls are typically used to, counteracting the horizontal pressure of the wet concrete. However, this method compromises interior finishes, requiring extensive on-site repair and decoration, thus limiting its application only to projects with minimal interior design requirements, such as public housing.

Hu and Xia (2023), Ji et al. (2022), Duan et al. (2022) and Pan et al. (2023) proposed an alternative method where precast sidewalls directly resist the lateral pressure of the poured concrete without the need for tie rods. This method requires thicker precast walls to withstand the concrete pressure, consequently increasing module weight and complexity of transportation and lifting, while reducing usable interior space.

To optimize sidewall thickness and minimize disruption to factory-finished interiors, Li et al. (2023) and Yao et al. (2023) developed a composite wall system with a rebar truss tying mechanism. The rebar truss is half embedded in one precast sidewall, with the other half protruding outside the precast sidewall. By welding couplers to the protruded rebar truss to connect with tie rods, this system eliminates penetrations in one sidewall but still requires tie rods to penetrate through the other sidewall before concrete pouring. Poon et al. (2023) further refined this by embedding slotted steel angles into all the precast sidewalls, and then inserting wedge connectors into the slots from the top of the gap between two MiC modules before concrete pouring. However, the constructability and potential slippage at these slotted connections require further investigation.

To preserve interior finishes while resisting lateral pressure on thin precast sidewalls during concrete pouring, Zou et al. (2024) proposed a novel interlocking tie system for MiC composite wall construction. This new system enabling complete factory finishing and protecting interior decorations during on-site module connections, replaces the traditional through-wall tie rods. It also avoids the need for thicker sidewalls, resulting in lighter modules, increased usable space, simplified lifting, and the potential for larger module dimensions within site lifting capacity limits, ultimately enhancing occupant comfort.

To optimize the aforementioned wall tie, balancing material cost and performance requirements, the original design can be refined by adjusting material grade, geometry, and thickness. Optimization can be achieved through various methods, including manual adjustment based on numerical simulations and topology optimization. In topology optimization, the density-based method is prevalent, aiming to minimize compliance (maximize global stiffness) within a fixed domain by determining the material density of each finite element.

This optimization problem, which involves a complex integer programming formulation with variables proportional to the number of elements, can be efficiently tackled using homogenization (Bendsøe, 1989). This approach determines effective material properties for elements with microscopic voids, where the void size is related to the element density, thereby converting discrete variables into continuous ones. A crucial element of this method is the interpolation scheme that links material properties to the element density. The Solid Isotropic Material with Penalization (SIMP) method (Bendsøe, 1989; Zhou and Rozvany, 1991) is widely adopted. SIMP penalizes the element density variable to reduce element stiffness, introducing a penalty factor p (usually $p > 3$) to minimize intermediate densities, often referred to as "gray" regions, and encourage clear solid-void solutions. Although SIMP lacks a direct physical interpretation, its simplicity and effectiveness have led to its widespread use in commercial software like ANSYS.

Other topology optimization techniques go beyond the density-based method. Evolutionary Structural Optimization (ESO) (Xie and Steven, 1993, 1997) discretely adds or removes elements, and avoids intermediate densities. However, its heuristic, non-sensitivity-based criteria have been criticized for potentially leading to suboptimal solutions. Boundary variation methods, such as level set (Osher and Sethian, 1988) and phase-field (Chen, 2002) methods, define the boundary shape implicitly, often resulting in smooth boundaries that require little post-processing. Despite their advantages, these methods can

encounter difficulties when applying practical manufacturing constraints.

Note that topology optimization requiring iterative solutions of system equations demands substantial computational resources, particularly for large-scale, refined finite element models. Consequently, empirical structural optimization combined with finite element analysis, despite its potential inconsistency, is often preferred in practice for its efficiency. Therefore, this study employs both topology and empirical optimization approaches.

Based on previous systematic optimization techniques (Zou et al., 2007, 2023), this study explores both empirical and topology optimization of an innovative interlocking tie system for Modular Integrated Construction (MIC), previously successfully deployed in a real-world project. This paper also introduces the underlying mechanism of the proposed tie system. To evaluate the efficacy and reliability of empirical optimization, both empirical and density-based topology optimization are applied to interlocking tie design, and their results are compared. The broader applicability of the interlocking ties within MIC is also explored. Finally, the successful implementation of this system in a Hong Kong MiC project is presented.

2. Mechanism of the proposed interlocking tie system

The innovative interlocking tie system (Fig. 1) comprises H-shaped steel embeds, hooks, and loops, working in conjunction with MiC sidewalls to resist the lateral pressure of wet concrete during the cavity filling process between adjacent modules. The hooks and loops, featuring serrated contact surfaces (Fig. 1c), are welded to the embeds. Tie spacing is determined by factors such as lateral pressure magnitude, the loaded area per tie, and its tensile capacity.

Fig. 2 presents two MiC modules with interlocking tie system. The composite wall construction procedure is as follows:

1) Embeds are installed in the sidewalls of prefabricated modules.
2) Hooks are welded to the embeds' end plates, and loops, within loop holders, are welded to the opposing end plates.
3) The n^{th} module is installed on-site.
4) Wall reinforcement is placed between the modules. The $(n+1)^{th}$ module's loops are raised with ropes and secured to the top of the module.
5) The $(n+1)^{th}$ module is installed on-site.
6) The ropes are cut, releasing the loops to engage the hooks (Enlarged view in Fig. 2b).
7) Concrete is poured into the gap between the n^{th} and $(n+1)^{th}$ modules.

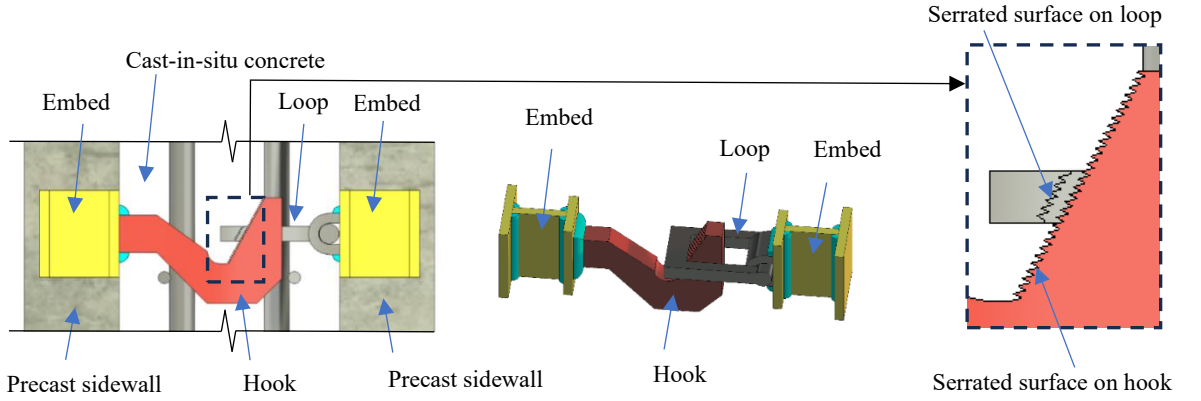

(a) Section view (b) 3D view (c) Enlarged view of interlocking details

Fig. 1 Interlocking tie system for composite walls in MiC

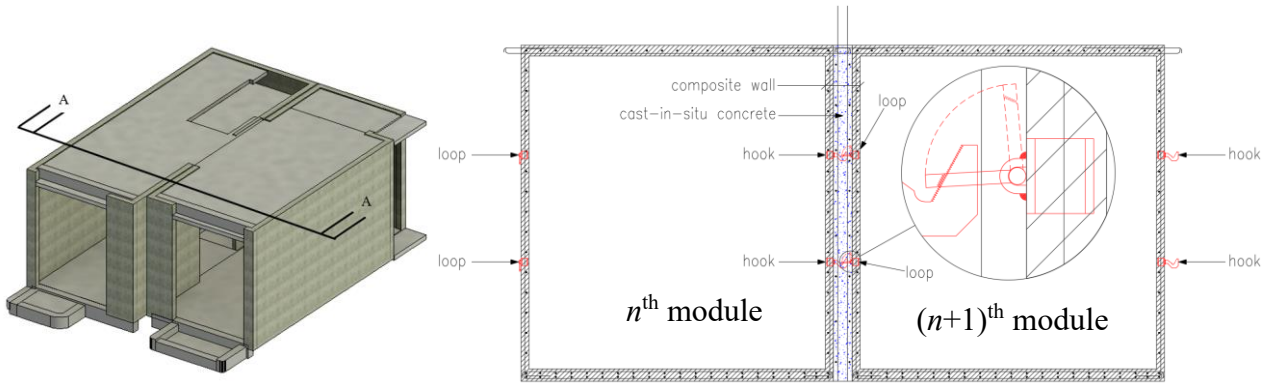

(a) BIM model (3D view) (b) Section A-A

Fig. 2 Two adjacent MiC modules with interlocking tie system

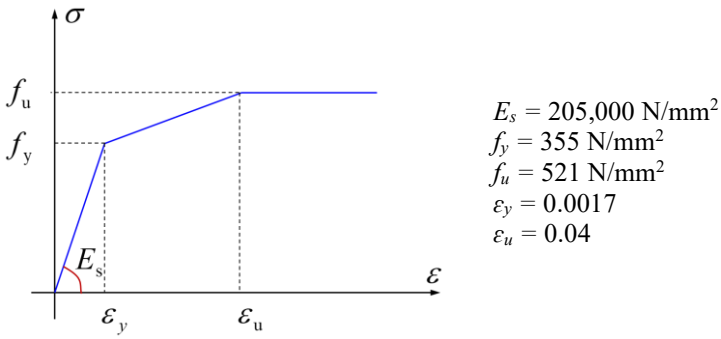

E_s = 205,000 N/mm^2
f_y = 355 N/mm^2
f_u = 521 N/mm^2
ε_y = 0.0017
ε_u = 0.04

Fig. 3 Stress-strain relationship for steel material

3. Development of finite element model

In this paper, finite element analysis (FEA) models using ANSYS software were developed to investigate the behavior of the proposed interlocking tie system.

3.1. Material model of steel

The adopted S355 steel was modeled using a multilinear kinematic hardening rule (Fig. 3). The Young's modulus E_s, yield strain ε_y, ultimate strain ε_u and their corresponding yield strength f_y and ultimate strength f_u are determined from experimental tests, as illustrated in Fig. 3.

3.2. Design loads for interlocking tie system

According to the design concrete pressure envelope (Fig. 4) and the following Eq. (1) in CIRIA Report 108 (Clear and Harrison, 1985), the concrete fluid pressure acting on the sidewall of the module experiences a linear increase to P_{max} at a depth of P_{max}/D, and keeps this value to the bottom level.

$$P_{max} = \min\{D\left[C_1\sqrt{R} + C_2K\sqrt{H - C_1\sqrt{R}}\right], Dh\}, \text{ in kN/m}^2 \quad (1)$$

in which, C_1 is the coefficient dependent on the size and shape of formwork; C_2 is the coefficient dependent on the constituent materials of the concrete; D is the weight density of concrete; H is the vertical form height; h is the vertical pour height; R is the rate at which the concrete rises vertically up the form; K is the temperature coefficient taken as $(\frac{36}{T+16})^2$; T is the concrete temperature at placing.

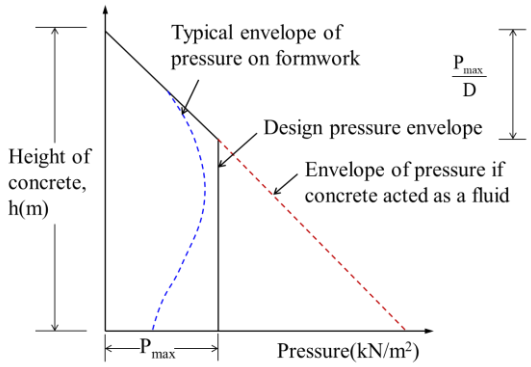

Fig. 4 Concreting pressure recommended in CIRIA report 108

In this paper, the lateral concreting pressure P_{max} can be determined by Eq. (1) and the associated parameters are given in Table 1. The distribution of concreting pressure for designing the proposed interlocking tie system is shown in Fig. 5.

Table 1
Parameters for determination of concreting pressure in this paper

Parameter	C_1	C_2	D kN/m³	H m	H m	T °C	K	R m/hr	P_{max} kPa	P_{max}/D m
Value	1.0	0.3	24.0	2.925	2.925	30	0.612	1.0	30.11	1.25

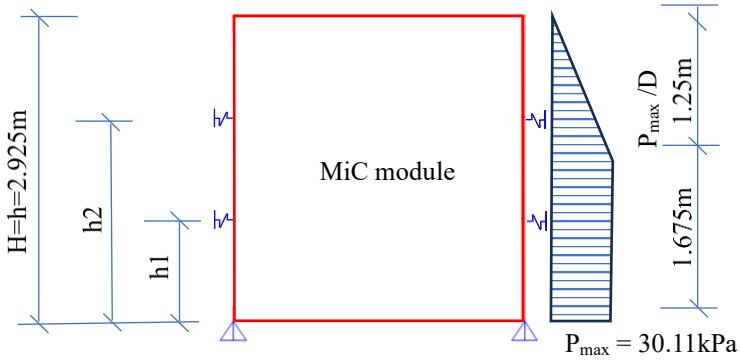

Fig. 5 Concreting pressure for designing interlocking tie system

Assuming a maximum spacing of 1.0 m vertically and horizontally for the interlocking ties, the tensile force F acting on each tie can be estimated using Eq. (2) below.

$$F = P_{max} \times \text{Loaded Area} \quad (2)$$

Taking the loaded area as 1.0m×1.0m, the tensile force F is calculated to be 30.11 kN. To estimate preliminary interlocking tie dimensions, a simplified method is used to assess key sections under combined axial, bending, and shear forces in accordance with local design codes. A worst-case unfactored tensile force F is applied to the top of the hook (Fig. 6a), and sections I-I through IV-IV (Fig. 6a, Table 2) are adjusted to meet code requirements. For the loop, F is applied to the left end (Fig. 6b). These preliminary dimensions (Fig. 6a and 6b) serve as the starting point for member size optimization.

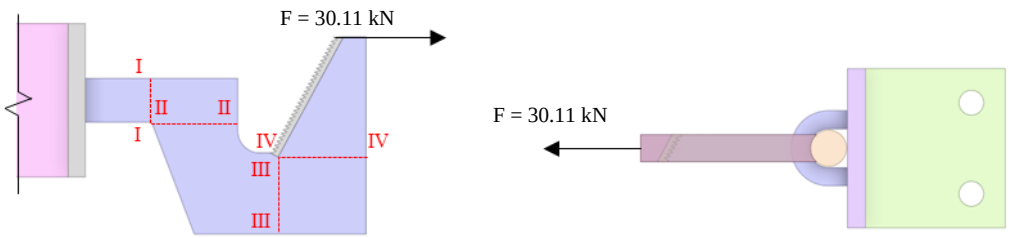

(a) Sketch of hoop component (b) Sketch of loop component

Fig. 6 Sketch of the main components of interlocking tie

Table 2
Dimensions of interlocking tie before optimization

Cross-section	Section width (mm)	Section thickness (mm)
I-I	20	30
II-II	40	30
III-III	40	30
IV-IV	40	30
Weight = 1.65 kg		

Note: The locations of cross-section I-I to IV-IV are shown in Fig. 6a.

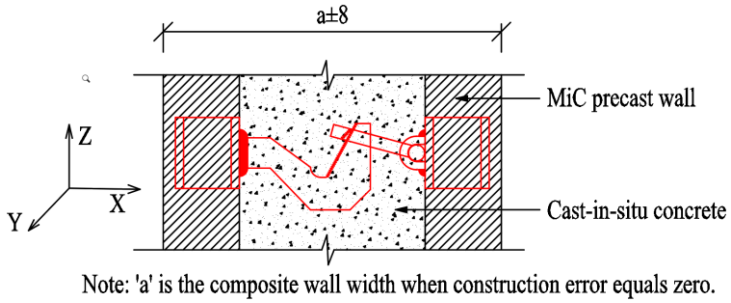

Fig. 7 Allowable construction tolerance in X direction for the interlocking tie system

3.3. Construction tolerances

Construction tolerances must be considered for embed installation, hook/loop welding (factory), and module placement (on-site). Based on practical experience, ±3 mm and ±5 mm tolerances are allocated for factory fabrication and on-site installation, respectively. Therefore, a total tolerance of ±8 mm is incorporated into the tie system design in the X-direction (Fig. 7), with similar consideration in the perpendicular horizontal Y-direction.

3.4. Finite element modeling

The concrete, steel, and rebar were modeled using a 10-node tetrahedral element in ANSYS, with three translational degrees of freedom (UX, UY and UZ) per node. The element supports plasticity, creep, swelling, stress stiffening, large deflections, and large strains. Specifically, it was used to model the steel plate in the wall tie analysis.

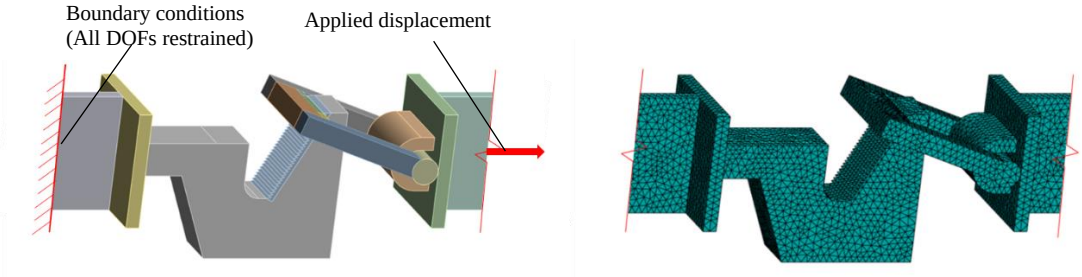

(a) Boundary conditions and applied displacement (b) Meshing details

Fig. 8 Finite element model of the interlocking tie

The interlocking tie, consisting of a hook, loop, and embedded end plates (see Fig. 6 and Table 2), connects via interlocking serrated surfaces. To simulate tensile loading, one end is fixed, while the other is displaced longitudinally until failure. Displacement restraints are applied to the left end, and a tensile displacement is applied incrementally to the right-end plate (Fig. 8a). Mesh details are shown in Fig. 8b.

The reaction force at the fixed (left) end is recorded during right-end displacement. The interlocking mechanism is modeled by coupling nodes at the serrated contact surfaces, assuming full contact and no relative movement. The loop shaft is modeled as a frictionless revolute joint.

To protect interior finishes, a maximum allowable horizontal deformation of 4 mm per sidewall during concrete pouring is considered reasonable, resulting in a total allowable deformation of 8 mm (4 mm × 2) for analysis and design.

3.5. Validation of finite element model

Experimental tensile tests were conducted to validate the finite element model developed in Section 3.4. Fig. 9 compares the force-displacement curves from both the numerical model and experiments. While the numerical model overestimates the initial stiffness (up to 8 mm displacement), likely due to the slippage of the sawtooth contact part of the specimen during the initial test loading, it accurately predicts the wall tie behavior after 8 mm, corresponding to full serration engagement. Therefore, the numerical model is deemed suitable for studying the wall tie's mechanical properties.

The validated numerical model can therefore be used for subsequent structural optimization. The physical test showed interlocking tie failure at 21 mm displacement, with rupture occurring at the loop corner (Fig. 10a). The equivalent plastic strain distribution (Fig. 10b) confirms strain concentration at the observed rupture location. Since the hook remained largely elastic during failure, indicating inefficient material usage, optimizing its shape could improve material utilization.

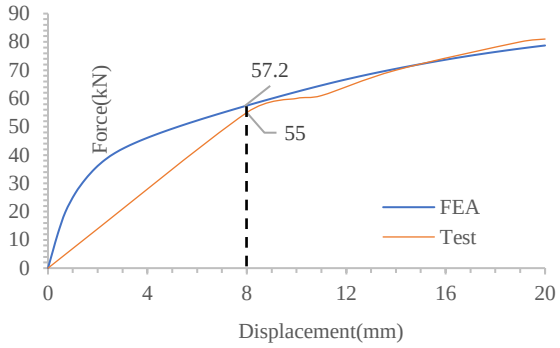

Fig. 9 Force-displacement curves from FE model and tensile test

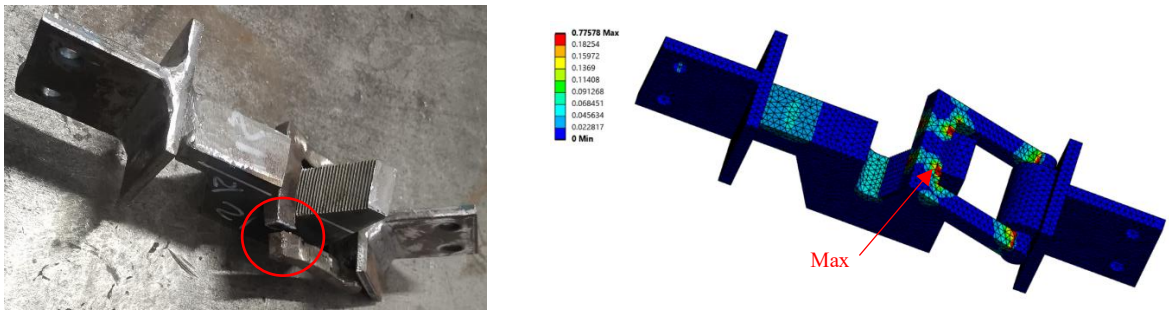

(a) Failure mode in experimental test (b) Equivalent plastic strain in FE model

Fig. 10 Failure of interlocking tie: experimental vs. numerical

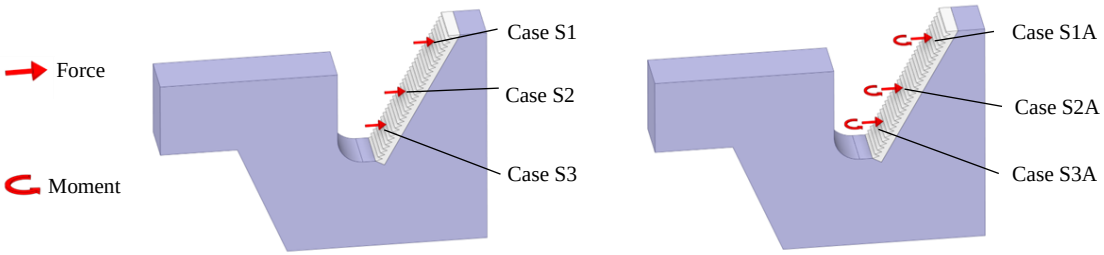

(a) Load cases without eccentricity (b) Load cases with eccentricity

Fig. 11 Critical load cases considered in optimization

4. Optimization of interlocking tie

4.1. Critical load cases for optimization

The optimization objective is to minimize the interlocking tie size while maintaining deformation within the allowable limit u_{max} under a factored applied tensile load F^d of 34.6 kN = 1.15 × F in Eq. (2). As shown in Fig. 11, based on different locking positions and eccentricities, six critical load cases are considered and listed in Table 3.

Table 3
Definition of six critical cases considered

Locking Position	Without Eccentricity	With Eccentricity
Upper	Case S1	Case S1A
Center	Case S2	Case S2A
Lower	Case S3	Case S3A

4.2. Methodology for optimization

The optimization aims to minimize wall tie volume while maintaining sufficient strength. Starting with an initial volume (V_{ini}), the design volume is iteratively reduced. The optimization converges when the minimum reaction force across all six load cases (at u_{max} displacement) equals the target applied load F^d.

Note that the initial hook design (Section 3.2) was modified by reducing the thickness from 30 mm to 20 mm and increasing the root height to 30 mm. This adjustment aimed to reduce overall stiffness and strength while preserving strength at the critical weak point.

Density-based topology optimization is employed in each iteration to determine the optimal shape for a given volume, minimizing structural compliance (and thus displacement) within the design domain under the prescribed loading.

The classical compliance minimization problem for single load case is given below:

$$\min_{\rho}[c(\rho)] = U^{T}K(\rho)U \tag{3}$$

$$\text{Subject to: } K(\rho)U = F \tag{4}$$

$$\sum_{e=1}^{N} v_e \rho_e \leq V \tag{5}$$

$$\rho_{min} \leq \rho_e \leq 1, e = 1 \cdots N \tag{6}$$

where ρ is the vector of element design densities; ρ_e represents the density of each element; U is the displacement vector; F is the force load vector; c is the objective function which represent compliance here; $K(\rho)$ is the global stiffness matrix which varies according to ρ; v_e is the volume of each element and N is the total number of elements; V represents the volume limitation, where $V = v_f V_0$, V_0 is the volume of design domain and v_f is the fraction of the remaining volume.

Eq. (3) presents the objective function, which minimizes compliance (strain energy) to maximize overall stiffness. Eq. (4) enforces force equilibrium. Eq. (5) constrains the total element volume (V). Eq. (6) defines the upper and lower bounds for element densities.

The relationship of stiffness K and element density ρ is given by Solid Isotropic Material with Penalization (SIMP) method, introduced by Bendsøe (1989):

$$\mathrm{K}(\rho) = \sum_{e=1}^{N} \mathrm{K}_e(E_e) \tag{7}$$

$$E_e = {\rho_e}^p E^0 \tag{8}$$

in which E_e is the isotropic material property (Young's modulus in this case); p is the power-law factor used to penalize intermediate densities between 0 and 1, typically set to 3.

Eq. (7) represents the assembly of the global stiffness matrix. Eq. (8) defines the penalized proportional material properties of the elements.

For multiple load cases, the objective function is defined as the sum of the compliances for each case, as shown in Eq. (9), using the individual compliance calculations from Eq. (3):

$$\min_{\rho}[C(\rho)] = \sum_{i=1}^{N_c} c_i(\rho) \tag{9}$$

where $c_i(\rho)$ is the compliance of case i calculated using Eq. (3); and N_c is the number of load cases considered. In this paper, N_c is taken as 6, as shown in Table 3.

4.3. Empirical optimization method

The empirical optimization presented here is based on FEA results, iteratively removing material from regions exhibiting low stress and strain, as illustrated in Fig. 12.

The empirical optimization procedure is as follows:

1) Perform FEA on the initial design (Section 4.2) to identify the optimization region and determine F_{min} (the minimum reaction force across all load cases).
2) Divide the design boundary into movable and immovable segments.
3) Adjust the movable segments (via translation or rotation) while maintaining overall shape integrity, and update the FE models.
4) Perform FEA on the updated model and calculate F_{min}. Compare F_{min} with the target reaction force F_{tar} (equal to the applied load F^d from Section 4.1).
5) Repeat steps 3 and 4 until the difference between F_{min} and F_{tar} is less than 5%.
6) Compare the current volume (V_i) with the previous volume (V_{i-1}). If the difference is less than 5%, the optimization converges; otherwise, adjust the boundary based on FEA results and reaction forces, and return to step 3.

The flow chart is shown in Fig. 13.

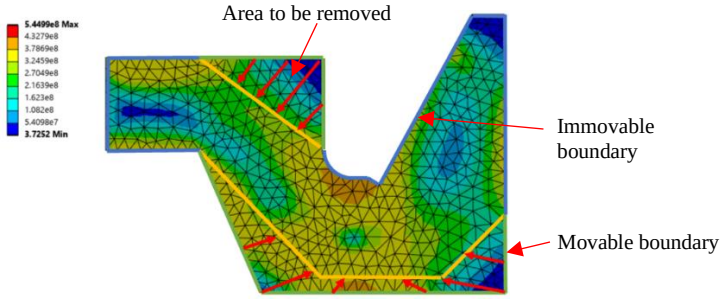

Fig. 12 Region under low stress to be removed

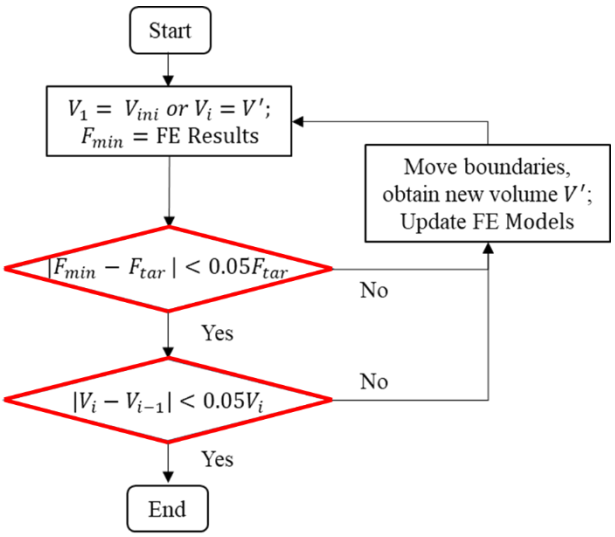

Fig. 13 Flow chart for empirical optimization

4.4. Topology optimization method

A topology optimization, employing the density-based method (Eqs. 3 to 9) within ANSYS's structural optimization module, was conducted to validate the accuracy and efficiency of the empirical optimization results. A convergence accuracy of 0.1% was used for each iteration. To ensure manufacturability with a single-directional cut and prevent the formation of voids, an extrusion constraint along the y-axis with a minimum member size of 20 mm was applied (Fig. 14).

The topology optimization process iteratively performs FEA on shapes generated with varying mass retention percentages. The objective is to identify the minimum volume shape that satisfies the design requirements. Since topology optimization results in a discrete distribution of element densities, producing a non-smooth boundary, post-processing (smoothing and linearization) is necessary to create a manufacturable component.

The topology optimization procedure is as follows:

1) Starting with the initial design (Section 4.2), define the optimization and excluded regions. Apply load cases and manufacturing constraints (minimum member size and extrusion direction).
2) For the first cycle, set the initial volume retention ratio (V_{ini}) to 90% and the volume reduction step size ($V_{st,ini}$) to 5%. Subsequent cycles update V_f (volume retention ratio) and V_{st} (step size).
3) Employ the topology optimization algorithm (Eqs. 3 to 9) to calculate compliance and update element densities. Interpret the resulting material distribution as the updated design.
4) Perform FEA on the updated model and compare F_{min} with F_{tar}. If $F_{min} < F_{tar}$, reduce V_f by V_{st}. If $F_{min} > F_{tar}$, reduce the step size to $V_{st}' = 0.5V_{st}$.
5) Repeat steps 3 and 4 until the difference between F_{min} and F_{tar} is less than 5%.
6) Compare the current volume fraction ($V_{f,i}$) with the previous ($V_{f,i-1}$). If the difference is less than 5%, the optimization converges; otherwise, reduce the step size to $V_{st}' = 0.5V_{st}$ and return to step 2.

The topology optimization procedure is illustrated in Fig. 15.

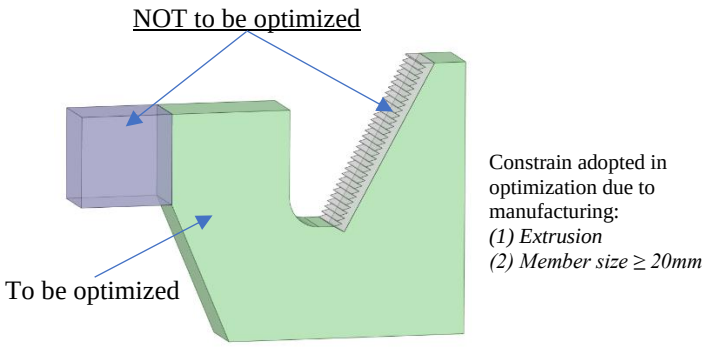

Fig. 14 Settings for topology optimization

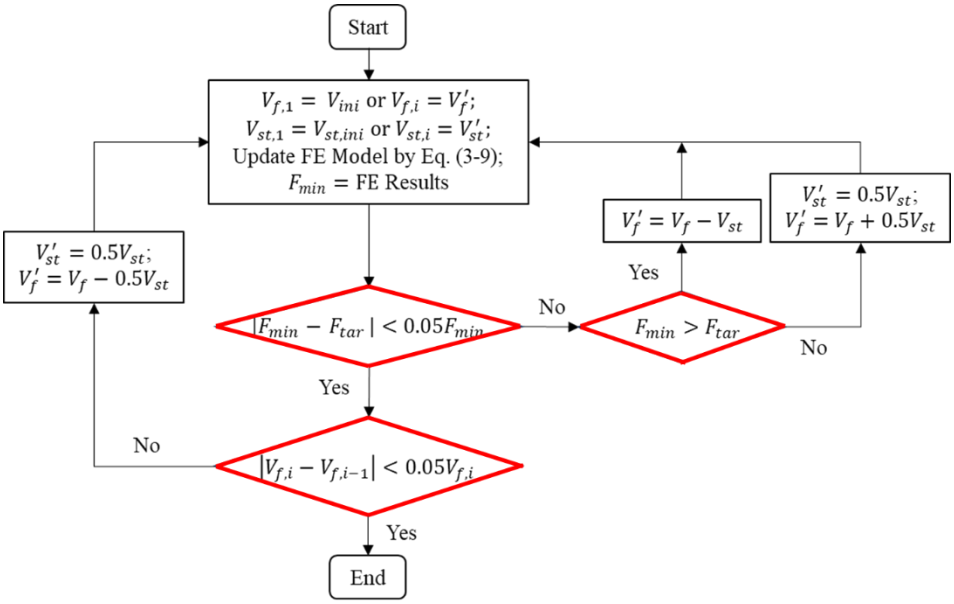

Fig. 15 Flow chart for topology optimization

4.5. Result comparison between two optimization methods

4.5.1. Optimization history

The steel weight and reaction force for achieving design loads during optimization in two different methods are shown in Fig. 16.

The empirical optimization converged in 6 cycles, while the topology optimization required 9 cycles. The final design, based on a linearization of the Cycle 8 and Cycle 9 results, weighs 814 g, a value between the weights of those two cycles.

The stress distribution during optimization processing is demonstrated in Table 4.

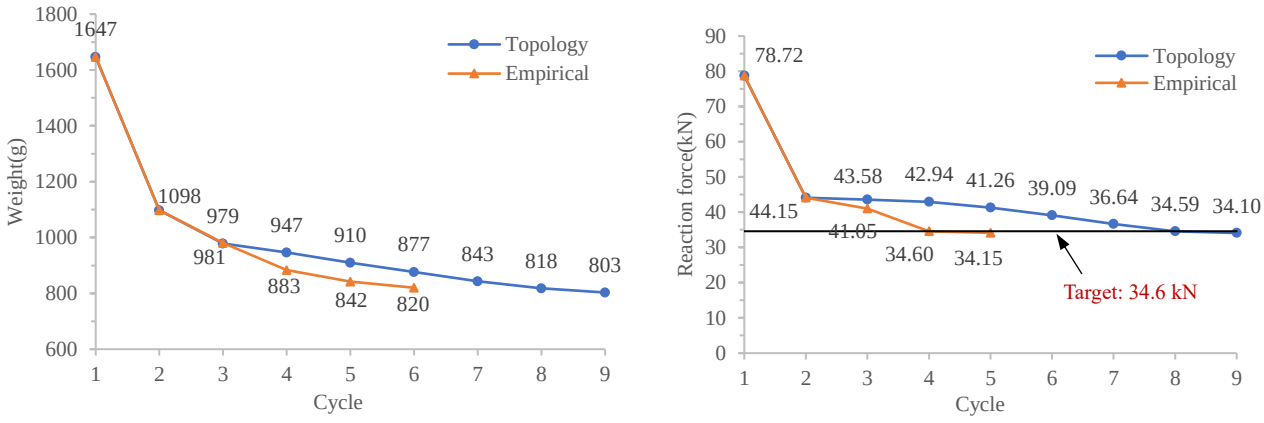

(a) Steel weight

(b) Reaction force

Fig. 16 History of two optimization methods

Table 4
Stress distribution for representative cycles in topology optimization method

Equivalent stress	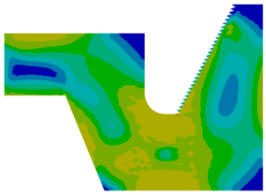	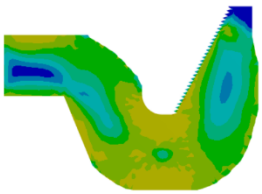	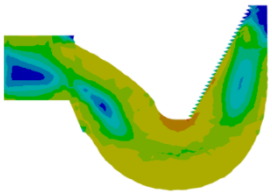	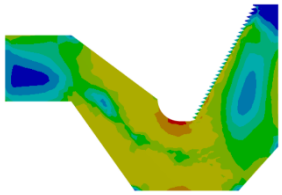
Cycle No.	2	3	9	Final

4.5.2. Comparison of steel weight

The designs from both empirical and topology optimization are shown in Fig. 17. The empirical optimization design weighs 820 g, which is 49.8% of the initial weight. In contrast, the topology optimization design weighs 814 g, representing 49.4% of the initial weight.

4.5.3. Comparison of section dimensions

Fig. 17 illustrates the differences between the results of the two optimization methods. Although the overall shape remains consistent, the dimensions of the cross-sections have changed, particularly in sections II'-II' and III'-III'. The maximum difference in cross-sectional area is 9.1%.

4.5.4. Comparison of stress distribution

The stress distribution of original design is compared against that of the topology optimization and empirical optimization in Fig. 18.

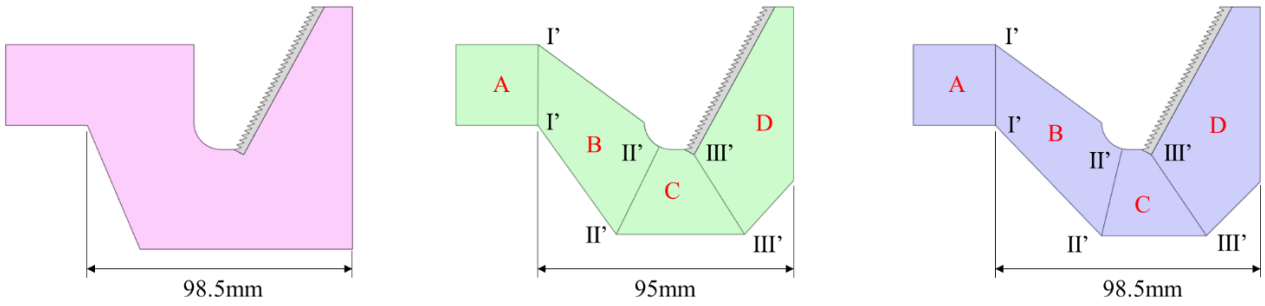

(a) Original design (b) Topology optimization (c) Empirical optimization

Fig. 17 Dimensions of interlocking tie before and after optimization

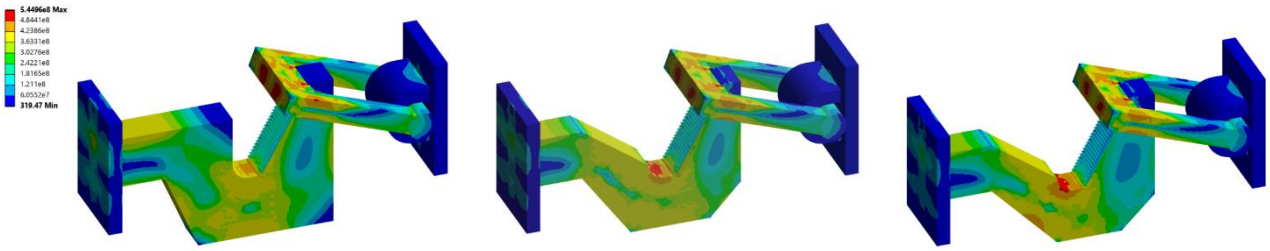

(a) Original design (b) Topology optimization (c) Empirical optimization

Fig. 18 Stress comparison before and after optimization

4.5.5. Comparison of load-deflection curves

Finite element analysis (FEA) was conducted on both optimization schemes using the validated model. As shown in Fig. 19, the two schemes yield almost identical weights and similar mechanical properties, with an average tensile force difference of 3.02% at 8 mm displacement and a maximum difference of 6.5% in Case S1A. The primary distinction between the schemes is the location of yielding, attributed to variations in cross-section dimensions.

This demonstrates that empirical optimization is acceptable for practical engineering, as it saves computational effort and converges faster while maintaining accuracy comparable to topology optimization algorithms.

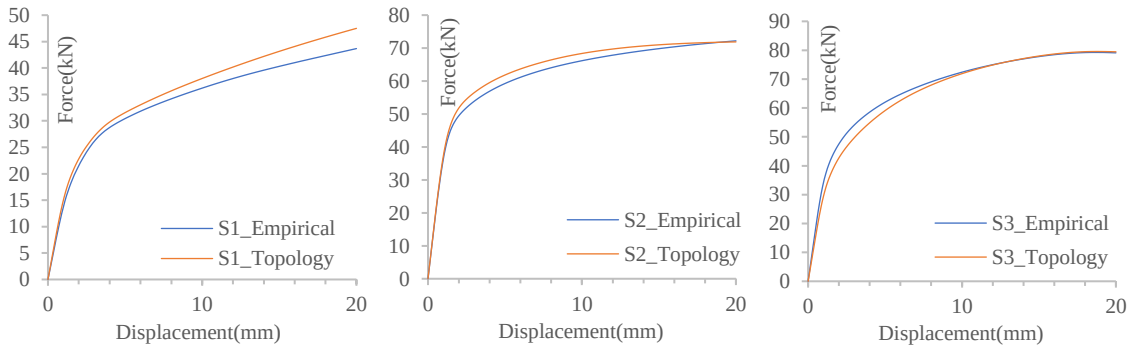

(a) Case S1 (b) Case S2 (c) Case S3

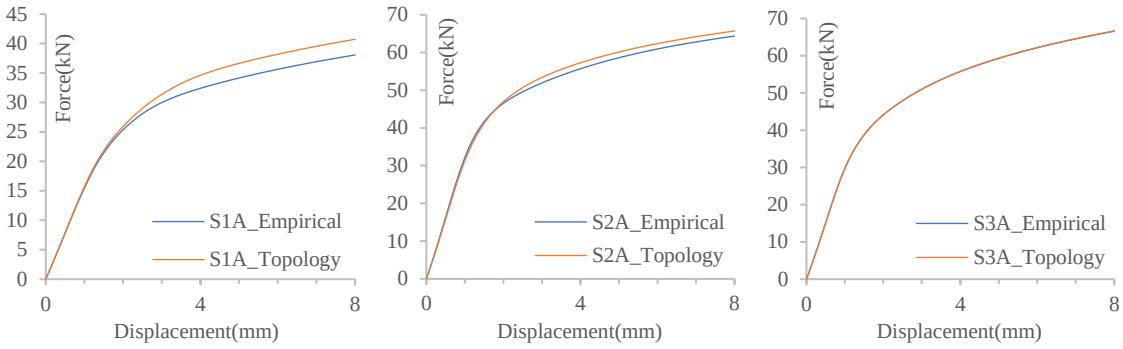

(a) Case S1A (b) Case S2A (c) Case S3A

Fig. 19 Load-deflection curves from empirical and topology optimization methods

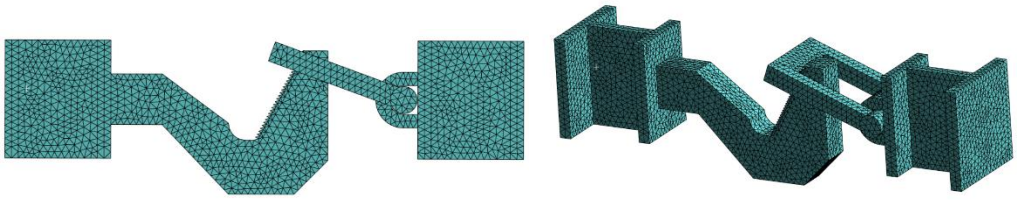

(a) Section view (b) 3D view

Fig. 20 Final optimized shape of the interlocking tie

4.5.6. Final optimized shape of interlocking tie

The optimized shape and finite element model are shown in Fig. 20. The model uses the shape obtained through the empirical optimization procedure outlined in Section 4.3 and follows the model settings described in Section 3.6.

4.5.7. Verification test against numerical analysis – Case S1

Additional experimental tensile test for Case S1 after empirical optimization was conducted. The force-displacement curves in Fig. 21 indicate that the numerical results closely match the tensile test after 5 mm of displacement. Initially, during the first 5 mm, the numerical model shows higher stiffness than the experimental test, as the idealized contact assumed in the FE model does not fully account for the slippage of the sawtooth contact part of the specimen during the initial loading. Fig. 22 compares the deformed shapes of the test sample with the numerical model.

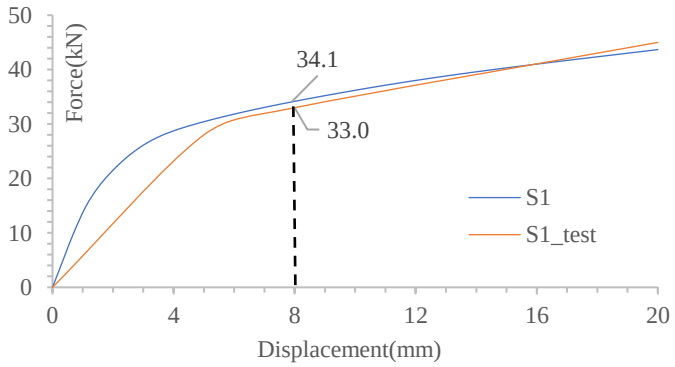

Fig. 21 Force-displacement curves for Case S1 (empirical optimization)

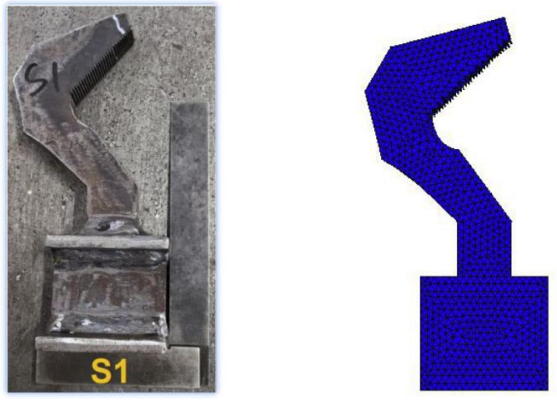

(a) Deformed shape after testing (b) Deformed shape from FEA

Fig. 22 Comparison of deformed shapes for Case S1 (empirical optimization)

5. Influence of tie location and wall thickness

5.1. Effect of interlocking tie location along the height of composite wall

According to the analysis in Section 3, changes in height due to position variation primarily influence the force change in the wall tie. This section focuses on the design of the interlocking tie when the height h_2 is 2.0 m. When the height changes to h_2 = 2.0 m, the tension force reduces to about 85% of that at h_1=1.0m.

To meet lower stiffness and load-carrying capacity requirements, the hook size can be reduced while maintaining its basic shape. When the required tensile force at an 8 mm displacement along X-axis is reduced to about 85% of the final scheme, the size-reduced hook is shown in Fig. 23. This hook weighs 568.8 g, which is 76.6% of the weight in the empirical optimization scheme.

The force-displacement curves for six critical load cases from numerical analysis are shown in Fig. 24. It can be seen that the overall trend of the curve is similar to the scheme before the position change. However, the tension is reduced by approximately 14% when the displacement reaches 8 mm.

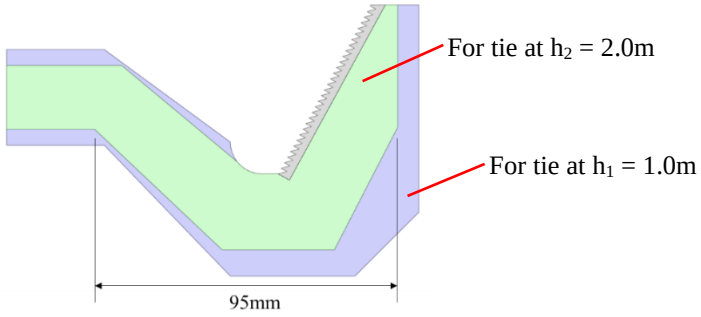

Fig. 23 Design of interlocking tie at different locations

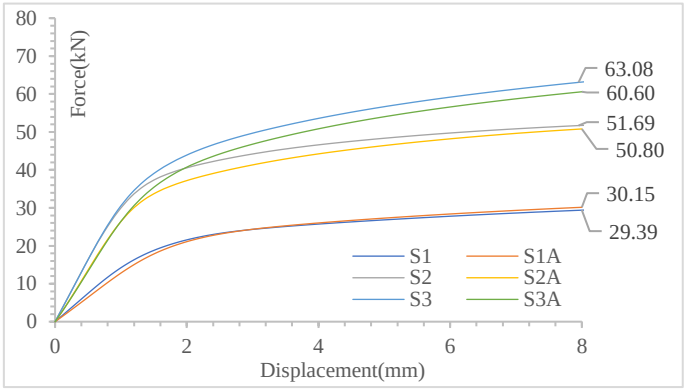

Fig. 24 Force-displacement curves of interlocking tie for h_2 = 2.0 m

5.2. Effect of wall thickness

As shown in Fig. 25, the hook shape in the 250 mm and 500 mm wall thickness schemes matches the empirical optimization scheme but is truncated at the bottom to accommodate the wall thickness while retaining the sawtooth area.

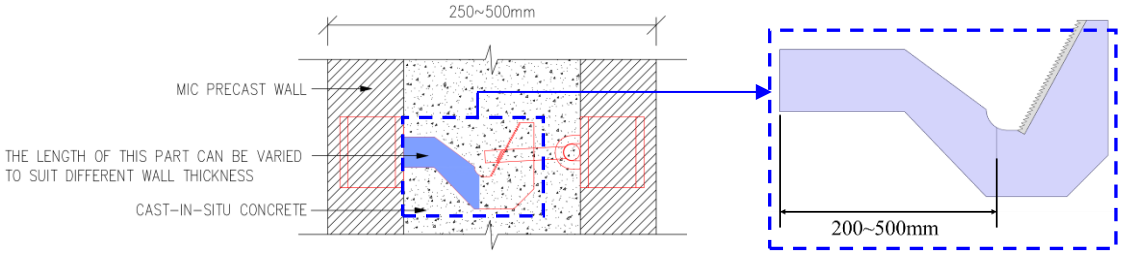

Fig. 25 Dimensions of interlocking tie for different wall-thicknesses (250 to 500 mm)

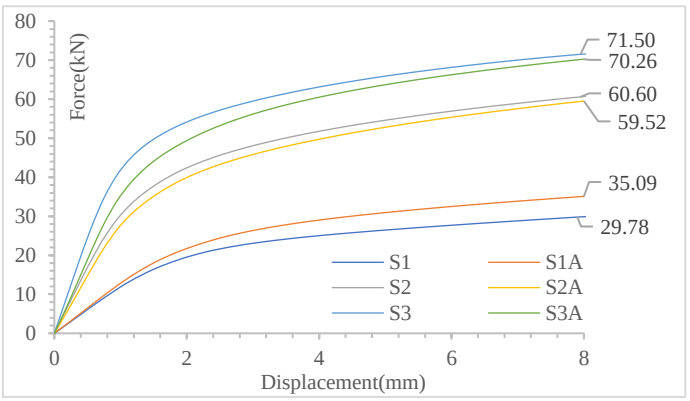

Fig. 26 Force-displacement curves of six load cases (wall thickness = 250mm)

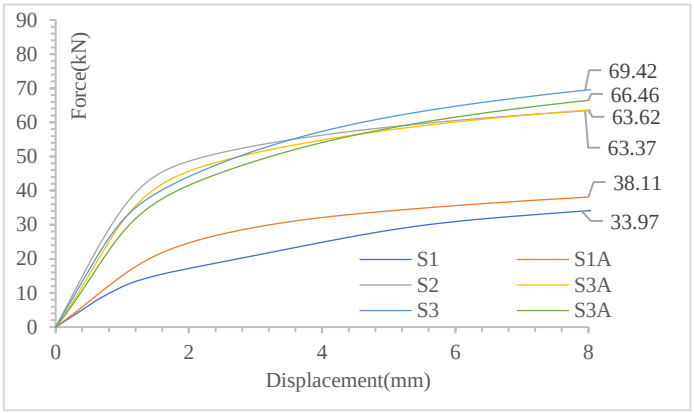

Fig. 27 Force-displacement curves of six load cases (wall thickness = 500mm)

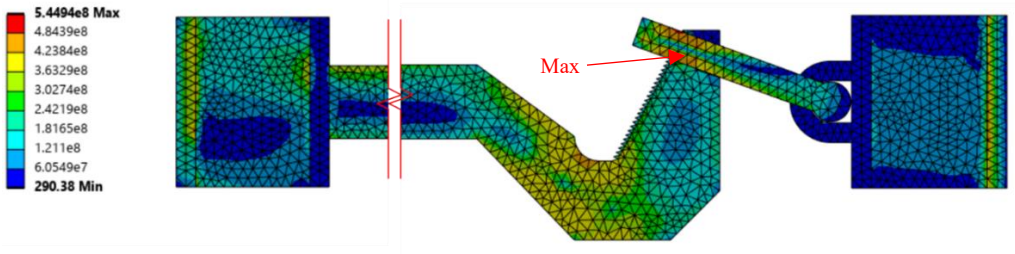

Fig. 28 Stress distribution at 8mm displacement for different wall thickness 250~500mm (S1)

As shown in Fig. 26, for a wall thickness of 250 mm, the tensile force of the wall tie at 8 mm displacement is 96.1% of that in the empirical scheme. The reduction in strength is primarily due to the increased moment on the support plates, caused by the change in the lever arm.

As shown in Fig. 27, for a wall thickness of 500 mm, the tensile force of the wall tie at 8 mm displacement is nearly identical to that in the empirical scheme. This is because the root of the hook is relatively strong compared to other parts of the system and remains elastic under the 8 mm displacement load. The typical stress distribution of the interlocking tie in different wall thickness for Case S1 is shown in Fig. 28.

6. Application in a Hong Kong MiC project

After the optimizations, the design of the interlocking tie system was finalized and incorporated into a four-story reinforced concrete MiC project in Hong Kong, as shown in Fig. 29. The optimized dimensions facilitated easier manufacturing and installation in the factory, minimizing conflicts with on-site rebar placement. The complete design received approval from local regulatory authorities. The project consisted of 106 MiC modules, including 90 composite walls, and featured a total of 1,048 inner tie sets. With the deformation of the sidewalls effectively controlled by the inner ties, the on-site concrete pouring for each composite wall proceeded successfully.

In comparison to the traditional method of using through-bolts to penetrate precast sidewalls, the use of inner ties resulted in a time savings of approximately one month and a reduction in construction costs by several million HKD for this project.

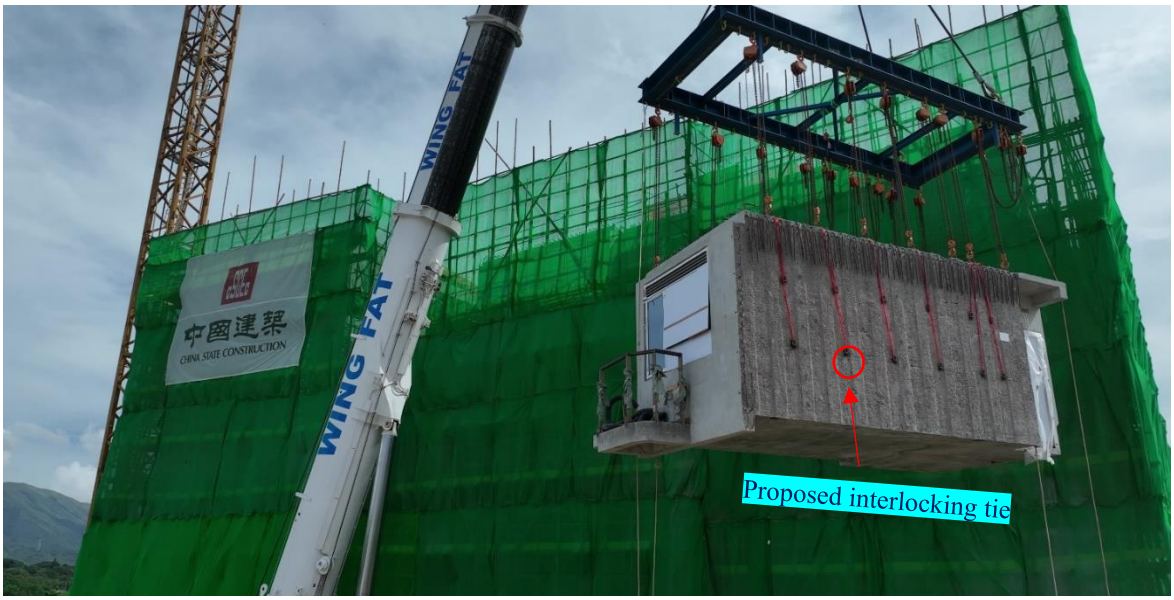

Fig. 29 Proposed interlocking ties adopted in a MiC building

7. Conclusions

This paper introduces an innovative interlocking tie system to address the challenge of securing prefabricated sidewalls during concrete casting in composite walls for reinforced concrete modular integrated construction (MiC) projects. The study utilizes topology optimization via software ANSYS to refine the interlocking tie design, providing detailed descriptions of the optimization processes. This approach minimizes material usage while improving manufacturing and installation efficiency. A comparison between topology optimization results and those from empirical optimization based on finite element analysis (FEA) reveals an average difference in mechanical properties of less than 5%. This demonstrates that empirical optimization is a viable and resource-efficient alternative in engineering practice.

To accommodate project-specific variations such as interlocking tie positioning and wall thickness, the study investigates interlocking ties with lower bearing capacities and varying wall thicknesses. The results show that interlocking ties can effectively control sidewall deformation across various scenarios through simple dimensional adjustments.

The optimized interlocking tie system was successfully implemented in a real MiC project in Hong Kong, providing a valuable reference for future initiatives. This innovative system could enhance the rate of interior decoration in high-rise buildings. The dimensions of the interlocking ties can be customized to accommodate various wall thicknesses and heights above floor level.

In the future, through further fire resistance and durability tests, this system may also be used for permanent tie connections between precast sidewalls and cast-in-situ walls, thus enhancing the overall stiffness of the structure and further reducing the total thickness of the structural walls.

Acknowledgments

The R&D funding support for “Research on Key Connections of Reinforced Concrete Modular Integrated Construction Structures” from China State Construction Engineering (Hong Kong) Limited is gratefully acknowledged. We would like to express our sincere gratitude to Dr Jianwei HE from NIDA Technology Co., Ltd. for providing valuable suggestions for this research. We would also like to extend our heartfelt thanks to Zhongcai HE, Chenghua HE, Daniel KAN, Yang ZHANG and Chimun LO for site supervision during MiC construction in a Hong Kong project. Lastly, we would like to thank Haoyue QIAO for proofreading.

References

[1] Bendsøe, M.P. (1989). Optimal shape design as a material distribution problem. Structural Optimization, 1:193–202.

[2] Bendsøe, M.P., Sigmund, O. (1999). Material interpolation schemes in topology optimization. Archive of Applied Mechanics, 69:635-654.

[3] Bendsoe, M.P., Sigmund, O. (2004). Topology optimization: theory, methods and applications. Springer, Berlin.

[4] Chen, L.Q. (2002). Phase-field models for microstructure evolution. Annual Review of Materials Research, 32:113-140.

[5] Clear, C. A., Harrison, T. A. (1985). CIRIA Report 108 - Concrete Pressure on Formwork. Construction Industry Research and Information Association, London.

[6] Deaton, J.D., Grandhi, R.V. (2014). A survey of structural and multidisciplinary continuum topology optimization: post 2000. Structural and Multidisciplinary Optimization, 49:1-38.

[7] Duan, L.J., Yu, Y.S., Wang, T., et al. (2022). Experimental research on mechanical behavior of Prefabricated Prefinished Volumetric Construction connections. Journal of Qingdao University of Technology, vol. 43, no. 5, pp. 1-7.

[8] Hu, H.S., Xia, H.J. (2023). A type of modular shear wall structure and its construction method. CN115807499B[P], 2023-04-25.

[9] Ji, J., Huang, G.X., Feng, Z.H., et al. (2022). A type of composite modular integrated construction structure. CN115045534A[P], 2022-09-13.

[10] Kobayashi, M.H. (2010). On a biologically inspired topology optimization method. Communications in Nonlinear Science and Numerical Simulation, 15(3):787-802.

[11] Li, Z., Wang, Q., Zhang, J.Y., et al. (2023). A type of MiC building with mixed wall structures. CN219794297U[P], 2023-10-03.

[12] Osher, S., Sethian, J.A. (1988). Fronts propagating with curvature dependent speed: algorithms based on the Hamilton-Jacobi formulation. Journal of Computational Physics, 79(1):12-49.

[13] Pan, W., Wang, Z., Zhang, Y., et al. (2023). Horizontal connection joint and construction method of multi-story and high-rise concrete MiC buildings. CN116084591A[P], 2023-05-09.

[14] Poon, C.M., Ma, M.C., Li, Z., et al. (2023). A type of concrete MiC structural system and its construction mete hod. CN117127714A[P], 2023-11-28.

[15] Rozvany, G.I.N., Zhou, M., Birker, T. (1992). Generalized shape optimization without homogenization. Structural Optimization, 4:250-252.

[16] Stolpe, M., Svanberg, K. (2001). An alternative interpolation scheme for minimum compliance topology optimization. Structural and Multidisciplinary Optimization, 22:116-124.

[17] Svanberg, K. (1987). The method of moving asymptotes—a new method for structural optimization. International Journal for Numerical Methods in Engineering, 24:359-373.

[18] Svanberg, K. (2002). A class of globally convergent optimization methods based on conservative convex separable approximations. SIAM Journal on Optimization, 12(2):555-573.

[19] Xie, Y.M., Steven, G.P. (1993). A simple evolutionary procedure for structural optimization. Computers & Structures, 49(5):885-896.

[20] Xie, Y.M., Steven, G.P. (1997). Evolutionary structural optimization. Springer.

[21] Yao, J., Huang, M.Y., Zeng, Z.X., et al. (2023). A type of concrete MiC module. CN219527957U[P], 2023-08-15.

[22] Zhou, M., Rozvany, G.I.N. (1991). The COC algorithm, Part II: topological, geometrical and generalized shape optimization. Computer Methods in Applied Mechanics and Engineering, 89:309-336. https://doi.org/10.1016/0045-7825(91)90046-9

[23] Zhou, M., Rozvany, G.I.N. (2001). On the validity of ESO type methods in topology optimization. Structural and Multidisciplinary Optimization, 21:80-83.

[24] Zillober, C. (1993). A globally convergent version of the method of moving asymptotes. Structural Optimization, 6:166-174.

[25] Zou, X.K., Huang, J., Lu, W.J., et al. (2024). A New Composite Wall Inner Tie System Applied in Reinforced Concrete Modular Integrated Construction. Proceedings of the 10th International Conference on Construction Engineering and Project Management, pp. 85-92, Jul. 29-Aug.1, Sapporo.

[26] Zou, X.K., Chan, C.M., Li, G., Wang, Q. (2007). Multi-objective Optimization for Performance-Based Design of Concrete Structures. Journal of Structural Engineering, vol. 133, vol. 10, pp. 1462-1474.

[27] Zou, X.K., Zhang, Y., Liu, Y.P., Shi, L.C., Kan, D. (2023). Design and Construction of High-Performance Long-Span Steel Transfer Twin Trusses Applied in One Hospital Building in Hong Kong. Buildings, vol. 13, no. 3:751.